



I. R. IRAN

ISSN: 2423-7167

e-ISSN: 1735-9244



International Journal of Engineering

Journal Homepage: www.ije.ir



TRANSACTIONS C: ASPECTS

Volume 36, Number 06, June 2023

Materials and Energy Research Center

INTERNATIONAL JOURNAL OF ENGINEERING

Transactions C: Aspects

DIRECTOR-IN-CHARGE

H. Omidvar

EDITOR IN CHIEF

G. D. Najafpour

ASSOCIATE EDITOR

A. Haerian

EDITORIAL BOARD

- | | | | |
|------|--|-------|--|
| S.B. | Adeloju, Charles Sturt University, Wagga, Australia | A. | Mahmoudi, Bu-Ali Sina University, Hamedan, Iran |
| K. | Badie, Iran Telecomm. Research Center, Tehran, Iran | O.P. | Malik, University of Calgary, Alberta, Canada |
| M. | Balaban, Massachusetts Ins. of Technology (MIT), USA | G.D. | Najafpour, Babol Noshirvani Univ. of Tech., Babol, Iran |
| M. | Bodaghi, Nottingham Trent University, Nottingham, UK | F. | Nateghi-A, Int. Ins. Earthquake Eng. Seis., Tehran, Iran |
| E. | Clausen, Univ. of Arkansas, North Carolina, USA | S. E. | Oh, Kangwon National University, Korea |
| W.R. | Daud, University Kebangsaan Malaysia, Selangor, Malaysia | M. | Osanloo, Amirkabir Univ. of Tech., Tehran, Iran |
| M. | Ehsan, Sharif University of Technology, Tehran, Iran | M. | Pazouki, MERC, Karaj, Iran |
| J. | Faiz, Univ. of Tehran, Tehran, Iran | J. | Rashed-Mohassel, Univ. of Tehran, Tehran, Iran |
| H. | Farrahi, Sharif University of Technology, Tehran, Iran | S. K. | Sadrnezhaad, Sharif Univ. of Tech, Tehran, Iran |
| K. | Firoozbakhsh, Sharif Univ. of Technology, Tehran, Iran | R. | Sahraeian, Shahed University, Tehran, Iran |
| A. | Haerian, Sajad Univ., Mashhad, Iran | A. | Shokuhfar, K. N. Toosi Univ. of Tech., Tehran, Iran |
| H. | Hassanpour, Shahrood Univ. of Tech., Shahrood, Iran | R. | Tavakkoli-Moghaddam, Univ. of Tehran, Tehran, Iran |
| W. | Hogland, Linnaeus Univ, Kalmar Sweden | T. | Teng, Univ. Sains Malaysia, Gelugor, Malaysia |
| A.F. | Ismail, Univ. Tech. Malaysia, Skudai, Malaysia | P. | Tiong, Nanyang Technological University, Singapore |
| M. | Jain, University of Nebraska Medical Center, Omaha, USA | X. | Wang, Deakin University, Geelong VIC 3217, Australia |
| M. | Keyanpour rad, Materials and Energy Research Center, Karaj, Iran | H. | Omidvar, Amirkabir Univ. of Tech., Tehran, Iran |

EDITORIAL ADVISORY BOARD

- | | | | |
|-------|--|-------|---|
| S. T. | Akhavan-Niaki, Sharif Univ. of Tech., Tehran, Iran | A. | Kheyroddin, Semnan Univ., Semnan, Iran |
| M. | Amidpour, K. N. Toosi Univ of Tech., Tehran, Iran | N. | Latifi, Mississippi State Univ., Mississippi State, USA |
| M. | Azadi, Semnan university, Semnan, Iran | H. | Oraee, Sharif Univ. of Tech., Tehran, Iran |
| M. | Azadi, Semnan University, Semnan, Iran | S. M. | Seyed-Hosseini, Iran Univ. of Sc. & Tech., Tehran, Iran |
| F. | Behnamfar, Isfahan University of Technology, Isfahan | M. T. | Shervani-Tabar, Tabriz Univ., Tabriz, Iran |
| R. | Dutta, Sharda University, India | E. | Shirani, Isfahan Univ. of Tech., Isfahan, Iran |
| M. | Eslami, Amirkabir Univ. of Technology, Tehran, Iran | A. | Siadat, Arts et Métiers, France |
| H. | Hamidi, K.N.Toosi Univ. of Technology, Tehran, Iran | C. | Triki, Hamad Bin Khalifa Univ., Doha, Qatar |
| S. | Jafarmadar, Urmia Univ., Urmia, Iran | | |

TECHNICAL STAFF

M. Khavarpour; M. Mohammadi; V. H. Bazzaz, R. Esfandiar; T. Ebadi

DISCLAIMER

The publication of papers in International Journal of Engineering does not imply that the editorial board, reviewers or publisher accept, approve or endorse the data and conclusions of authors.

CONTENTS

Transactions C: Aspects

A. Hassanjani-Roshan, M. R. Vaezi, H. Koohestani, F. Cheraghi	Investigating the Effect of Ultrasound Intensity on the Magnetic Properties of Magnetite Nanostructures Synthesized by Sonochemical Method	1034-1039
V. K. Patil, V. R. Pawar, S. P. Kulkarni, T. A. Mehta, N. R. Khare	Real Time Emotion Recognition with AD8232 ECG Sensor for Classwise Performance Evaluation of Machine Learning Methods	1040-1047
M. Farhoodi, A. Toloie Eshlaghy, M. R. Motadel	A Proposed Model for Persian Stance Detection on Social Media	1048-1059
N. Asgarkhani, M. Seifollahi, S. M. Abbasi	Effect of Aging Treatment on Microstructure and Mechanical Properties of Al _{0.7} CoCrFeNi High Entropy Alloy	1060-1065
M. Hashempour, M. Kolahdoozan	Numerical Modeling of Sediment-flow around Obstacle Inspired by Marine Sponges: Considering Body Configurations	1066-1074
A. Iraj	Evaluating Finn-Byrne Model in Liquefaction Analysis of Quay Wall and Cantilevered Retaining Wall Models	1075-1091
K. Gaurav, A. Kumar, P. Singh, A. Kumari, M. Kasar, T. Suryawanshi	Human Disease Prediction using Machine Learning Techniques and Real-life Parameters	1092-1098
M. Hooshmand, H. Yaghobi, M. Jazaeri	Irradiation and Temperature Estimation with a New Extended Kalman Particle Filter for Maximum Power Point Tracking in Photovoltaic Systems	1099-1113
S. Singh, S. Patel	Potential Use of Fly Ash for Developing Angular-shaped Aggregate	1114-1120
H. A. Goaz, H. A. Jabir, M. A. Abdulrehman, T. S. Al-Gasham	Evaluation of lightweight Concrete Core Test Including Steel Bars	1121-1128
S. Howldar, B. Balaji, K. Srinivasa Rao	Design and Qualitative Analysis of Hetero Dielectric Tunnel Field Effect Transistor Device	1129-1135
X. Xie, B. Zheng	Application of Ultra-sensitive Pillar-enhanced Quartz Crystal Resonators for Airborne Detection of Nanoparticles: A Theoretical Study	1136-1142
Z. Zhang, G. Fu, D. Xu	A Dynamic Model for Laminated Piezoelectric Microbeam	1143-1149

M. Torkashvand, N. Shamami, H. Bigdeli	The Equipment Scheduling and Assignment Problem in the Overhaul Industry	1150-1165
N. Kazemifard, L. Bashir, D. Rahmani	A Novel Hybrid Model for Technology Strategy Formulating in High-tech Industries under Uncertainty: A Case Study	1166-1178
A. Yavari, H. Hassanpour	Election Prediction Based on Messages Feature Analysis in Twitter Social Network	1179-1184
G. Kumar, N. P. Mandal	Experimental Analysis of Square Position on Variable Displacement Electrohydraulic Actuation System by Open Loop Control	1185-1192
S. Syamsuir, B. Soegijono, S. D. Yudanto, B. Basori, M. K. Ajiriyanto, D. Nanto, F. B. Susetyo	Electrolyte Temperature Dependency of Electrodeposited Nickel in Sulfate Solution on the Hardness and Corrosion Behaviors	1193-1200



Investigating the Effect of Ultrasound Intensity on the Magnetic Properties of Magnetite Nanostructures Synthesized by Sonochemical Method

A. Hassanjani-Roshan^a, M. R. Vaezi^b, H. Koohestani^{*a}, F. Cheraghi^c

^a Faculty of Materials and Metallurgical Engineering, Semnan University, Semnan, Iran

^b Materials and Energy Research Center (MERC), Karaj, Iran

^c Department of material science and engineering, Sharif University of Technology, Tehran, Iran

PAPER INFO

Paper history:

Received 02 February 2023

Received in revised form 02 March 2023

Accepted 03 March 2023

Keywords:

Ultrasonic Irradiation
Fe₃O₄ Nanostructures
Sonochemical Process
Magnetic Properties
Sonication Power

ABSTRACT

In this article, the synthesis of magnetite nanostructures was successfully carried out by the sonochemical process. In this method, stoichiometric amount of iron chlorides (FeCl₃·6H₂O and FeCl₂·4H₂O), ammonia (NH₃) and polyvinylpyrrolidone (PVP) were used to synthesize pure Fe₃O₄ nanoparticles. The effect of initial sonication power of the ultrasonic device on the size and morphology of the final products as one of the effective parameters was investigated. For this, the initial power of the sonicator was evaluated at 90, 70, 50 and 30 W at 40°C. Characterization of Fe₃O₄ nanoparticles was done by transmission electron microscope (TEM) and X-ray powder diffraction (XRD) and its magnetic properties were investigated by vibrating sample magnetometer (VSM). Investigation of the XRD pattern after annealing showed that pure Fe₃O₄ phase was successfully formed during the sonochemical process. TEM images determined the size of Fe₃O₄ nanoparticles to be 10-50 nm. The results showed that increasing the initial power of the system reduced the particle size and improved the magnetic properties of nanoparticles.

doi: 10.5829/ije.2023.36.06c.01

1. INTRODUCTION

The materials properties depend on the kind and situation of atoms in the structure. When the materials dimension approaches molecular and atomic size, the ratio of area to volume increases considerably. Therefore, the behavior of nanomaterials is substantially different from bulk microstructures [1-3].

Iron oxide nanoparticles with various structures, known as very important nanomaterials, have been used broadly in many fields such as electrical topics, magnetism, medicine, chemical, dying and the food industry. Fe₃O₄ nanostructures have various applications in fabricating sensors, shape memory alloys, rechargeable lithium batteries and drug delivery because of their unique chemical and magnetic characteristics [4, 5]. These nanomaterials attracted to magnets have been studied as drug delivery factors. Fe₃O₄ nanoparticles

have attracted much attention from researchers due to their superparamagnetic properties, and containing both Fe(II) and Fe(III) ions, which makes it superior to other types of iron oxides [6].

Fe₃O₄ nanoparticles are also used in infectious diseases, encapsulating medicine, active drug delivery, applied sensors, diagnostic cells, hyperthermia, making genes and imaging of the body and determining the diseases via increasing the image contrast in MRI as well. This kind of particle ought to be enough small in order to prevent them to be deposited and also remaining invisible against the phagocytosis systems [3, 7]. Despite the weak and strong points of iron oxides in practical applications, superparamagnetic iron oxides and super paramagnetic iron nanoparticles are the only magnetic nanoparticles used in medical applications [8]. Materials magnetic properties result from the electrons magnetic moments. Each electron has a magnetic moment in the atom that

*Corresponding Author Institutional Email:
h.koohestani@semnan.ac.ir (H. Koohestani)

comes from two sources: one is related to the orbital motion around the nucleus (electron orbit magnetic moment), and another is associated with the electron spinning around its axis (electron spin magnetic moment) [9]. Furthermore, each electron can be a small permanent magnet using its orbit and spin magnetic moments [10]. The relation between the properties and the grain size is a very important issue in magnetic materials. In the case of soft magnetic materials, the area under the hysteresis curve significantly decreases with reducing the size of grains even if it can be disappeared completely [11, 12].

So far, various synthesis methods have been mentioned for the synthesis of magnetite nanoparticles, including the sol-gel process, chemical vapor deposition (CVD), hydrothermal technique, pulsed laser evaporation, electron irradiation, and reactive sputtering [12-15]. However, chemical processes are often used because it is an easy, repeatable and cost-effective methods, and among them, chemical bath deposition (CBD) and sonochemical processes are more useful [16-18]. In previous works, Fe₃O₄ nanoparticles have been synthesized by the sonochemical method. The results have shown that ultrasonic radiation causes cavitation in an aqueous medium, which leads to the formation, growth, and collapse of microbubbles [19, 20]. Therefore, the quality and properties of the synthesized product will be affected. In this work, the effect of ultrasound intensity on the structural and Fe₃O₄ properties of magnetite nanoparticles synthesized by the sonochemical method will be investigated.

2. MATERIALS AND EXPERIMENTS

2. 1. Materials In this work iron chlorides (FeCl₃.6H₂O, FeCl₂.4H₂O), ammonia (NH₃) and polyvinylpyrrolidone (PVP) were purchased from Merck.

2. 2. Synthesis The synthesis of magnetite nanoparticles was done according to the previous method [18]. In this method, FeCl₃.6H₂O (0.4 M, 50 ml) and FeCl₂.4H₂O (0.2 M, 50 ml) are used as starting precursors and PVP as a surfactant, and ammonia (0.8 M, 50 ml) is also used. NH₃ was added dropwise to the resulting aqueous solution. Process sonication was provided using the Misonix sonicator model S-4000 sonicator through direct ultrasonic irradiation with an initial power of 10, 30, 50 and 70 W for about 30 min and a temperature of 40 °C. Then the solution was exposed to ultrasound for 60 min to complete the sonochemical process. The influence of ultrasonic power on the structure and morphologic properties of nanoparticles has been studied and samples I, II, III, and IV are prepared under different conditions listed in Table 1.

After completing the procedure and appearing precipitations, the obtained solution is put in the

TABLE 1. The process conditions of ultrasonic device for synthesizing magnetite nanoparticles

Sample Code	Initial Power (W)	Ultrasonic Waves Intensity (W/cm ²)	Imported Energy into the Solution (kJ)
I	30	52	123
II	50	65	150
III	70	78	185
IV	90	94	202

centrifuge system at 1000 rpm for 15 min to separate precipitations containing nanoparticles. After collection, the final precipitated particles were filtered and washed with methanol and distilled water to remove by-products. Then all the samples were air-dried at room temperature and calcined at 500 °C for 60 min to obtain crystalline iron oxide nanoparticles.

2. 3. Characterizations Crystal phases of Fe₃O₄ nanoparticles were characterized by X-ray diffraction (Siemens D-5000, with Cu K α radiation). The morphology of the synthesized samples was studied by TEM analysis (ZEISS, Germany). Their magnetic properties were measured with a vibrating sample magnetometer system (AGSM model, \pm 0.001 emu/g).

3. RESULTS AND DISCUSSIONS

The primary product without annealing has a completely amorphous structure [18, 21]. This is due to the collapse of high-temperature bubbles in some parts of the solution where the bubbles are present, so as the temperature decreases rapidly, the particles do not have enough time to crystallize. Under these conditions, the reactants carry out intense interactions in a very short period of time. Cavitation events lead to increased heating and cooling rates to more than 10¹⁰ Ks⁻¹ [22, 23]. Hence, after TGA/DTA analysis in previous work and determining the crystallinity temperature, the samples were heat-treated at 500 °C for about 1 h to gain a calcined powder and also to get the required peaks for phase and structure analysis [18]. It can be seen in Figure 1 which is related to the diffraction of Fe₃O₄ nanoparticles, all peaks are associated with Fe₃O₄ nanoparticles and there are not any peaks associated with impurities. The sharp peaks with high intensity show the high crystallinity of the prepared nanopowder via sonochemical method.

Considering the pattern, it can be found that there is a direct relation between ultrasonic intensity and flatness of peaks. As much as the initial power is raised, flatness of peaks is also increased, although the crystallite size will be decreased, in sequence. Using the XRD patterns and Scherer equation, the size of the crystals was determined [24]:

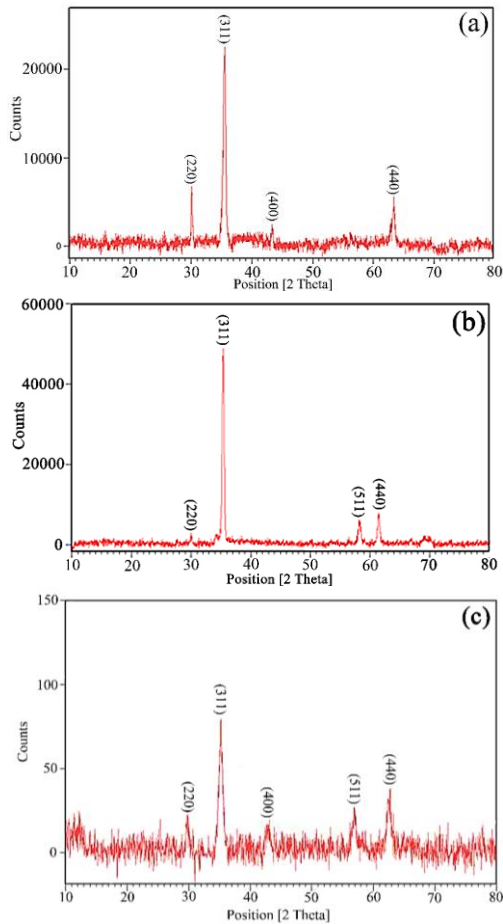


Figure 1. XRD patterns of the samples (a) I, (b) II, and (c) IV

$$D = \frac{k\lambda}{\beta \cdot \cos\theta} \quad (1)$$

where k is constant (0.89 for spherical particles), D is the crystallite size (nm), λ is the wavelength of the X-ray beam ($\lambda = 0.15406$ nm for Cu $K\alpha$ radiation), β is the full width at half maximum for the diffraction peak under consideration (in radians), according to measurements, the mean size of crystals is about 8 nm, 14 nm, and 17 nm for initial powers of 90, 50 and 30 W, respectively. Ultrasonic waves disperse the suspension solution into smaller droplets. In this way, it reduces the kinetics of particle growth and the amount of aggregation and stops crystal growth. This leads to reduced crystallinity, cluster decomposition [25]. The ultrasonic process is more effective than the magnetic field in the particle growth step, and the bubbles formed in this process break more particles into smaller particles [23].

Figure 2 shows TEM images of Fe_3O_4 nanostructures prepared via sonochemical process with different powers. Fe_3O_4 nanoparticles have spherical morphology with smooth geometry and high degree of crystallinity.

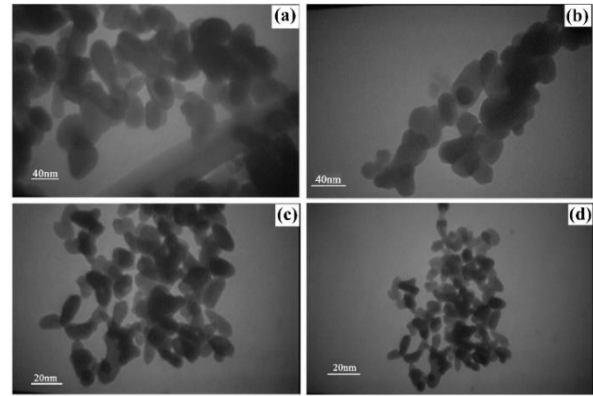


Figure 2. TEM images of Fe_3O_4 nanoparticles at initial powers: (a) I, (b) II, (c) III, (d) IV

The gained size of nanoparticles is shown in Table 2. Cavitation promotes the local reaction, heating, and severe stirring through the heat transfer of gas bubbles. Therefore, by accelerating the nucleation process, the concentration of seeds increases. This phenomenon leads to the relaxation and interface defects and the formation of nanoparticles [22].

Since the temperature and solution concentration are constant for all samples in this research, these factors have not influenced the results and the only effective factor is ultrasonic wave intensity. By increasing the initial power, the bubbles are formed with more energy. Furthermore, the sonochemical influences of this kind of bubbles will increase. These bubbles have more energy so they have more sonochemical influences on the solution [26-28].

According to Table 1, by increasing the initial power from 30 to 50 W at constant temperature of 40 °C, the intensity of the ultrasonic waves has increased from 52 W/cm^2 to 94 W/cm^2 . This increase is due to the expansion of energetic bubbles or the increase in the solution viscosity due to precipitation formation.

The VSM analysis is used in order to determining the effect of the ultrasonic waves intensity on the magnetic properties of the prepared nanostructures via sonochemical technique. Figure 3 shows the hysteresis curves of the prepared nanostructures, and their results are listed in Table 3.

TABLE 2. The average size of obtained Fe_3O_4 nanostructure measured from TEM images

Sample Code	The size of particles (nm)
I	50
II	35
III	20
IV	10

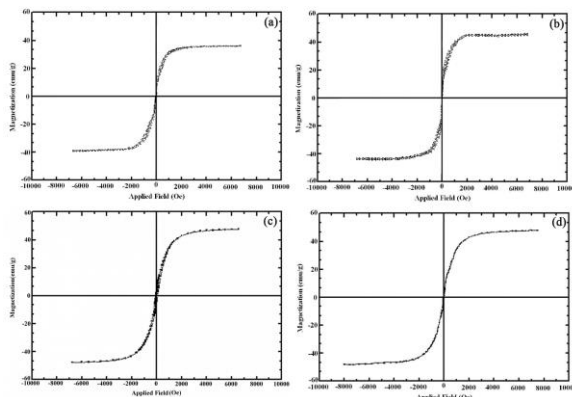


Figure 3. VSM spectra of the synthesized samples: (a) I, (b) II, (c) III, (d) IV

TABLE 3. Magnetic properties of the samples synthesized via sonochemical processing with different intensity of ultrasonic waves

Sample Code	Initial power (W)	M (emu/g)	H _C (Oe)
I	30	38	1100
II	50	43	1000
III	70	47	800
IV	90	50	-

It can be seen that by increasing the power and the intensity of ultrasonic waves, the magnetism of particles has decreased. Reduction in the particle size results in raising coercivity to a maximum amount (IV), then it will be decreased until it will be closed to zero. Yadav et al. [29] showed that increasing of the ultrasonic power input in the synthesis of MnFe_2O_4 increases the saturation magnetization and negligible surface spin canting.

The main reason for this situation is that the magnetization of the multi-domain nanoparticles can be changed with the motion of the domain walls. In this case, nanoparticles with small sizes consist of one domain, but larger particles that are composed of several domains minimize the static magnetization energy. The approximate range for the critical particle size above which the magnetic nanoparticle is not single-domain is from a few to several tens of nanometers, which is higher than the typical domain wall dimension in the magnetic material. The nature of the domain structure has a strong influence on the hysteresis behaviour of magnetic nanoparticles. By decreasing the ultrasonic frequency, the nucleation rate accelerates due to an increase in the magnitude of the shock wave caused by the cavitation collapse. Therefore, magnetization improves as the crystallite size decreases [30].

Considering the XRD and TEM results of obtained samples have been prepared via the sonochemical process, it is clear that decreasing the particle and crystallite sizes tends to reduce the coercivity to zero.

Therefore, by controlling the particle size in the nano dimension, it is possible to change the coercivity easily. After removing the magnetic field, the magnetic properties are disappeared approximately in this kind of nanostructure. If permanent magnets will be necessary, nanopowders should keep their magnetite properties even in absence of a magnetic field. Consequently, the hysteresis loop should be large, which means that H_c and M_r should be high, but the hysteresis loop of the nanostructures obtained via the sonochemical process is small. It is an important point that declares a good relationship between the properties and the grain size of materials. In soft magnetic materials decreasing the grain size tends to reduce the area under the hysteresis graph significantly, even if it may disappear completely such as in sample IV. Fuentes-García et al. [31] synthesized magnetite nanoparticles by a one-step sonochemical method. The results showed that the obtained nanomaterials with improved properties have a good potential to be used as magnetic hyperthermia agents.

4. CONCLUSIONS

In this work, the sonochemical process was used as a new and advanced technique with direct ultrasonic waves irradiating on the solution for the synthesis of iron oxide (Fe_3O_4) nanostructures. Then, the effect of the intensity of ultrasonic waves on the properties of Fe_3O_4 nanoparticles was investigated. The obtained nanoparticles have an amorphous structure resulting from the collapse of cavitation bubbles as enormous cooling rate. Because it prevents their crystallization during quenching and also the quick decrease of temperature around the nanoparticles. Therefore, to obtain crystallite nanoparticles, they must be calcined. The significant results of this work relate to the size, morphology, structure, purity and magnetic properties of the prepared materials. The size of crystallites is about 8 nm to 17 nm and the particle size considering the average size of particles is 10-50 nm which put them in a super small iron oxide nanoparticles group with a diameter of less than 50 nm. It can be seen that increasing the initial power of the system reduces the grain size with which the magnetic properties of particles have increased. Synthesized magnetite nanoparticles have a spherical morphology with smooth geometry and a degree of crystallinity, which are very useful and practical in various fields.

5. REFERENCES

1. Kim, E.H., Ahn, Y. and Lee, H.S., "Biomedical applications of superparamagnetic iron oxide nanoparticles encapsulated within chitosan", *Journal of Alloys and Compounds*, Vol. 434, (2007), 633-636, DOI:10.1016/j.jallcom.2006.08.311.

2. Tjong, S. and Chen, H., "Nanocrystalline materials and coatings", *Materials Science and Engineering: R: Reports*, Vol. 45, No. 1-2, (2004), 1-88, DOI:10.1016/j.mser.2004.07.001.
3. Kuchibhatla, S.V., Karakoti, A., Bera, D. and Seal, S., "One dimensional nanostructured materials", *Progress in Materials Science*, Vol. 52, No. 5, (2007), 699-913, DOI:10.1016/j.pmatsci.2006.08.001.
4. Wang, X., Liao, Y., Zhang, D., Wen, T. and Zhong, Z., "A review of Fe₃O₄ thin films: Synthesis, modification and applications", *Journal of Materials Science & Technology*, Vol. 34, No. 8, (2018), 1259-1272, DOI:10.1016/j.jmst.2018.01.011.
5. Ali, A., Hira Zafar, M.Z., ul Haq, I., Phull, A.R., Ali, J.S. and Hussain, A., "Synthesis, characterization, applications, and challenges of iron oxide nanoparticles", *Nanotechnology, Science and Applications*, Vol. 9, (2016), 49, DOI: 10.2147/NSA.S99986.
6. Suslick, K.S., Hyeon, T. and Fang, M., "Nanostructured materials generated by high-intensity ultrasound: Sonochemical synthesis and catalytic studies", *Chemistry of Materials*, Vol. 8, No. 8, (1996), 2172-2179, DOI:10.1021/cm960056l.
7. Salouti, M. and Ahangari, A., "Nanoparticle based drug delivery systems for treatment of infectious diseases, InTech London, UK, Vol. 552, (2014).
8. Dulińska-Litewka, J., Łazarczyk, A., Hałubiec, P., Szafranski, O., Karnas, K. and Karewicz, A., "Superparamagnetic iron oxide nanoparticles-current and prospective medical applications", *Materials*, Vol. 12, No. 4, (2019), 617, DOI: 10.3390/ma12040617.
9. Kusch, P. and Foley, H., "The magnetic moment of the electron", *Physical Review*, Vol. 74, No. 3, (1948), 250, DOI:10.1103/PhysRev.74.250.
10. Bahadur, D., Giri, J., Nayak, B.B., Sriharsha, T., Pradhan, P., Prasad, N., Barick, K. and Ambashtha, R., "Processing, properties and some novel applications of magnetic nanoparticles", *Pramana*, Vol. 65, No. 4, (2005), 663-679.
11. Raming, T., Winnubst, A.J., van Kats, C.M. and Philipse, A., "The synthesis and magnetic properties of nanosized hematite (α -Fe₂O₃) particles", *Journal of Colloid and Interface Science*, Vol. 249, No. 2, (2002), 346-350, DOI:10.1006/jcis.2001.8194.
12. Azizi, A., Yourdkhani, A., Koohestani, H., Sadmezhaad, S. and Asmatulu, R., "Fe₅₀Co₅₀ nanoparticles via self-propagating high-temperature synthesis during milling", *Powder Technology*, Vol. 208, No. 3, (2011), 623-627, DOI:10.1016/j.powtec.2010.12.030.
13. F Hasany, S., H Abdurahman, N., R Sunarti, A. and Jose, R., "Magnetic iron oxide nanoparticles: Chemical synthesis and applications review", *Current Nanoscience*, Vol. 9, No. 5, (2013), 561-575, DOI:10.1680/bbn.12.00014.
14. Ayuk, E., Ugwu, M. and Aronimo, S.B., "A review on synthetic methods of nanostructured materials", *Chemistry Research Journal*, Vol. 2, No. 5, (2017), 97-123.
15. Wani, I.A., Nanomaterials, novel preparation routes, and characterizations, in Nanotechnology applications for improvements in energy efficiency and environmental management. 2015, IGI Global, 1-40. DOI: 10.4018/978-1-4666-6304-6
16. Ekwealor, A. and Ezema, F., "Effects of precursor concentration on the optical and structural properties of Fe₂O₃ thin films synthesized in a polymer matrix by chemical bath deposition", *Journal of Ovonic Research*, Vol. 9, No., (2013), 35-43.
17. Ghanbari, D., Salavati-Niasari, M. and Ghasemi-Kooch, M., "A sonochemical method for synthesis of Fe₃O₄ nanoparticles and thermal stable pva-based magnetic nanocomposite", *Journal of Industrial and Engineering Chemistry*, Vol. 20, No. 6, (2014), 3970-3974, DOI:10.1016/j.jiec.2013.12.098.
18. Hassanjani-Roshan, A., Vaezi, M.R., Shokuhfar, A. and Rajabali, Z., "Synthesis of iron oxide nanoparticles via sonochemical method and their characterization", *Particuology*, Vol. 9, No. 1, (2011), 95-99, DOI:10.1016/j.partic.2010.05.013.
19. Gedanken, A., "Using sonochemistry for the fabrication of nanomaterials", *Ultrasonics Sonochemistry*, Vol. 11, No. 2, (2004), 47-55, DOI:10.1016/j.ultsonch.2004.01.037.
20. Shin, N., Saravanakumar, K. and Wang, M.-H., "Sonochemical mediated synthesis of iron oxide (Fe₃O₄ and Fe₂O₃) nanoparticles and their characterization, cytotoxicity and antibacterial properties", *Journal of Cluster Science*, Vol. 30, No. 3, (2019), 669-675, DOI: 10.1007/s10876-019-01526-7.
21. Pinkas, J., Reichlova, V., Zboril, R., Moravec, Z., Bezdecka, P. and Matejkova, J., "Sonochemical synthesis of amorphous nanoscopic iron (iii) oxide from Fe(acac)₃", *Ultrasonics Sonochemistry*, Vol. 15, No. 3, (2008), 257-264, DOI:10.1016/j.ultsonch.2007.03.009.
22. Fuentes-García, J., Santoyo-Salzar, J., Rangel-Cortes, E., Goya, G.F., Cardozo-Mata, V. and Pescador-Rojas, J.A., "Effect of ultrasonic irradiation power on sonochemical synthesis of gold nanoparticles", *Ultrasonics Sonochemistry*, Vol. 70, (2021), 105274, DOI:10.1016/j.ultsonch.2020.105274.
23. Eskandari, M.J. and Hasanzadeh, I., "Size-controlled synthesis of Fe₃O₄ magnetic nanoparticles via an alternating magnetic field and ultrasonic-assisted chemical co-precipitation", *Materials Science and Engineering: B*, Vol. 266, (2021), 115050, DOI:10.1016/j.mseb.2021.115050.
24. Fotukian, S.M., Barati, A., Soleymani, M. and Alizadeh, A.M., "Solvochemical synthesis of CuFe₂O₄ and Fe₃O₄ nanoparticles with high heating efficiency for magnetic hyperthermia application", *Journal of Alloys and Compounds*, Vol. 816, (2020), 152548, DOI:10.1016/j.jallcom.2019.152548.
25. Fouad, D.E., Zhang, C., Mekuria, T.D., Bi, C., Zaidi, A.A. and Shah, A.H., "Effects of sono-assisted modified precipitation on the crystallinity, size, morphology, and catalytic applications of hematite (α -Fe₂O₃) nanoparticles: A comparative study", *Ultrasonics Sonochemistry*, Vol. 59, (2019), 104713, DOI:10.1016/j.ultsonch.2019.104713.
26. Wang, X.K., Chen, G.H. and Guo, W.L., "Sonochemical degradation kinetics of methyl violet in aqueous solutions", *Molecules*, Vol. 8, No. 1, (2003), 40-44, DOI:10.3390/80100040.
27. Avvaru, B. and Pandit, A.B., "Experimental investigation of cavitation bubble dynamics under multi-frequency system", *Ultrasonics Sonochemistry*, Vol. 15, No. 4, (2008), 578-589, DOI:10.1016/j.ultsonch.2007.06.012.
28. Gielen, B., Marchal, S., Jordens, J., Thomassen, L., Braeken, L. and Van Gerven, T., "Influence of dissolved gases on sonochemistry and sonoluminescence in a flow reactor", *Ultrasonics Sonochemistry*, Vol. 31, (2016), 463-472, DOI:10.1016/j.ultsonch.2016.02.001.
29. Yadav, R.S., Kuřitka, I., Vilcakova, J., Jamatia, T., Machovsky, M., Skoda, D., Urbánek, P., Masař, M., Urbánek, M. and Kalina, L., "Impact of sonochemical synthesis condition on the structural and physical properties of MnFe₂O₄ spinel ferrite nanoparticles", *Ultrasonics Sonochemistry*, Vol. 61, (2020), 104839, DOI:10.1016/j.ultsonch.2019.104839.
30. Koizumi, H., Uddin, M.A. and Kato, Y., "Effect of ultrasonic irradiation on γ -Fe₂O₃ formation by co-precipitation method with Fe³⁺ salt and alkaline solution", *Inorganic Chemistry Communications*, Vol. 124, (2021), 108400, DOI:10.1016/j.inoche.2020.108400.
31. Fuentes-García, J.S.A., Carvalho Alavarse, A., Moreno Maldonado, A.C., Toro-Córdova, A., Ibarra, M.R. and Goya, G.F.n., "Simple sonochemical method to optimize the heating efficiency of magnetic nanoparticles for magnetic fluid hyperthermia", *ACS Omega*, Vol. 5, No. 41, (2020), 26357-26364, DOI:10.1021/acsomega.0c02212.

Persian Abstract

چکیده

در این مقاله، سنتز نانوذرات مگنتیت با فرآیند سونوشیمیایی با موفقیت انجام شد. در این روش از مقدار استوکیومتری کلریدهای آهن ($\text{FeCl}_2 \cdot 4\text{H}_2\text{O}$) و ($\text{FeCl}_3 \cdot 6\text{H}_2\text{O}$)، آمونیاک (NH_3) و پلی وینیل پیرولیدون (PVP) برای سنتز نانوذرات خالص Fe_3O_4 استفاده شد. تاثیر توان امواج آتراسونیک اولیه بر اندازه و مورفولوژی محصولات نهایی به عنوان یکی از پارامترهای موثر مورد بررسی قرار گرفت. برای این کار، توان اولیه دستگاه سونیکاتور در ۹۰، ۷۰، ۵۰ و ۳۰ وات در دمای ۴۰ درجه سانتیگراد ارزیابی شد. شناسایی نانوذرات Fe_3O_4 با استفاده از میکروسکوپ الکترونی عبوری (TEM) و پراش پرتو ایکس (XRD) و خواص مغناطیسی آن توسط مغناطیس سنج نمونه ارتعاشی (VSM) بررسی شد. بررسی الگوی XRD پس از کلسینه کردن نشان داد که فاز Fe_3O_4 خالص با موفقیت در فرآیند سونوشیمیایی تشکیل شد. تصاویر TEM اندازه نانوذرات Fe_3O_4 را ۱۰-۵۰ نانومتر تعیین کردند. نتایج نشان داد که افزایش توان اولیه سیستم باعث کاهش اندازه ذرات و بهبود خواص مغناطیسی نانوذرات می‌شود.



Real Time Emotion Recognition with AD8232 ECG Sensor for Classwise Performance Evaluation of Machine Learning Methods

V. K. Patil^{*a}, V. R. Pawar^b, S. P. Kulkarni^a, T. A. Mehta^a, N. R. Khare^a

^a Department of Electronics & Telecommunication Engineering, AISSMS Institute of Information Technology, Pune, India

^b Department of Electronics & Telecommunication Engineering, Bharti Vidyapeeth College of Engineering, Pune, India

PAPER INFO

Paper history:

Received 31 August 2022

Received in revised form 11 December 2022

Accepted 13 December 2022

Keywords:

Emotion Recognition
Machine Learning
Support Vector Machine
Naive Bayes
Electrocardiogram
Heart Rate Variability

ABSTRACT

Emotions are the accelerators of human intellect and innovation and creativity, so the ability to recognize emotions is in high demand. Real-time hardware has hurdles of Noise and hardware factors as compared to simulations. An electrocardiogram (ECG) sensor (AD8232), a temperature sensor (LM35), and a signal processing circuit is hardware of the proposed real-time emotion identification. The RR intervals are calculated from the ECG data. Emotions prediction using machine learning makes use of RR intervals and body temperature as features. One of the four emotions (namely 1. Happy 2. Stressed 3. Neutral 4. Sad.) is visualized at the serial port of the processor by using WESAD benchmark dataset and the HRV, serial, and pickle libraries. This article's innovation factors are (1) Use of ECG for emotion detection rather than disease detection with Emotion induction method, RR interval capturing and design of RR interval GUI for real time capture of temperature and ECG (2) Display of current emotion on Arduino serial port. (3) Measurement of Class performance using F1 score, macro average, and weighted average instead of general term accuracy. (4) Use of the probability based Navies Bayes as compared to traditional KNN, SVM, Random Forest methods (5) Class wise performance for example Navies Bayes' specificity or accuracy is lower than SVM's (0.96), but its recall or sensitivity is higher (0.97) vs. (0.94) for stress. In this article, we presented performance parameters in terms of interactive computations, tabular form and graphical display.

doi: 10.5829/ije.2023.36.06c.02

1. INTRODUCTION

Emotions have a major impact on many aspects of human life and actions [1]. The strategies and desired outcomes of organizations are linked to people's emotions [2]. Hence, emotion detection research is in demand. The subjects respond with different levels of emotions to the same set of stimuli [3]. Thus, challenging aspect of emotion recognition is behavioral uncertainty. Emotions can be detected using various signal processing algorithms. Table 1 shows variety of modalities for emotion like facial expressions, biomedical sensors [4]. The speech-based and facial expression emotion identification methods may be representing different emotions than the actual [5]. Emotion recognition using biosensors linked to the subject's body is proportional to

emotions and behavioral patterns [6-9]. Wearable technology [6, 9] is now developed from labs to doorsteps. Biological signals (like electrocardiogram (ECG)) which were used for clinical diagnosis [10] can be utilized to detect emotions [11].

Emotions identified with Wearables have the benefit that emotions cannot be suppressed nor be hidden in physiological parameter traits. Real-time emotions can be predicted using a physiological benchmark database [12, 13] and machine learning techniques. The reason to use Machine learning algorithms instead of deep learning is twofold. First reason is, while multiple ECG classifiers are available for disease identification, Support Vector Machine (SVM), K Nearest Neighbor (KNN), and Random Forest [14-19] are employed for emotion categorization with real-time ECG. Second reason is real

*Corresponding Author Institutional Email:
varshapatil101@gmail.com (V. K. Patil)

TABLE 1. Modalities of Emotion Recognition and drawbacks

Sr No.	Modality used	Drawback
1	Speech-based emotion identification	speaker's emotion may be hidden or not expressed accurately and is available only for the time till the speaker speaks. The accuracy is low ranging from 44% to 83.5%[5]
2	Facial expressions-based method	it may possibly miscommunicate the level, depth, and underpinned message of emotions[7].

time ECG signals are to be classified hence hardware AD8232 is also to be evaluated with structured limited benchmark dataset WESAD instead of just concentrating on simulation approach. The proposed research aims to develop real-time affective computing with ECG biosensors and Navies bayes machine learning algorithms to classify emotions.

In this article, we propose a comparative approach to ECG based emotion detection using Navies Bays and SVM. The Navies bayes is chosen because it is based on probability rules, and in emotion recognition probability of getting one of the emotions: 1 Happy, 2 Stressful. 3rd: Angry, 4th: Sad.) can be predicted with proposed experimentation. SVM is chosen because for emotion classification with ECG signals it has been proved the best classifier in the literature validated these experiments with performance matrices F1 score, accuracy, etc. (see Table 2).

2. LITERATURE REVIEW

Biosensors [10] such as optical sensors, Electrochemical biosensors, and Oxygen sensors are available and can further be utilized in Gephi software for use of ECG for disease prediction. An emotion recognition system [20] is designed with IoT and machine learning techniques with temperature and heart rate parameters [20] to recognize human emotions. A wearable emotion recognition device was used in [9, 11, 21] auto capture the data from a heart rate [21] and other biosignals. Another study approach [4, 21] looked at the solution of emotion detection as emotion extraction using skin conductance, skin temperature, ECG, EMG, and EEG data. Schmidt et al. [12] proposed a WESAD a publicly available dataset for stress detection. Haag, et al. [21] uses a way to teach computers to identify emotions by feeding them signals from a variety of biosensors. The literatures [21, 22] demonstrates EEG signal processing

TABLE 2. SVM KNN, Random forest are the Popular Methods for emotion Recognition with ECG

Sr No.	ECG features	Emotions recognized	Machine learning techniques used	Remark/factor
1	Heart rate HRV) [14]	Emotions: Happy exciting Calm Tense	K-NN [14] PSO-SVM Random forest	90.51667% 81.707%
2	Weighted Mean Filter to improve the Baseline Reduction	Relax, Joy, fear idenficaton ¹	SVW, CART, KNN	92%
3	ECG values converted with DCT and sampled frequency domain	The optimal number of features 75, Emotions Happy, calm, relax, and Tense [23]	PSO-SVM Random forest K-NN, SVM, Random Forest [24]	Recognition_rate (Avg) 90%, 51.667%, 81.707%, 82.483%
4	Respiration Inhale-Exhale Temperature	Happy, Sad, Fear	[18]	75%
5	Time and frequency-based ECG signal processing [15]	Unhappiness, pleasure, and pride	SVW, CART, KNN [15, 19]	
6	ECG feature extraction with signal processing techniques like analysis with the article is providing ECG classification [16]	ECG classification only no emotion classified	filtering, differentiation transform, and principal component	99.71 predictivity
7	demonstrates emotion recognition with DCT and IIR signal processing. [17]		SVM, KNN, particle swarm optimization method	0.889
8	demonstrates emotions classified with using a Convolutional neural self supervised network for unlabelled ECG data. [25]	Three databases named AMIGOS, DREAMER, and WESAD	Neural Network	0.966

¹ <https://docs.arduino.cc/resources/datasheets/A000066-datasheet.pdf>

techniques based on SVM and Time-frequency domain respectively. Butkevičiūtė et al. [22] proposed the detection of pulse variations and provides a precise output that indicates the emotional conditions with ECG electrodes. Our proposed research is also using the AD8232 for ECG capturing [22, 26].

Shin et al. [27] proposed an actual time interface with human-targeted emotion which mixes the ratio of ECG and EEG signals. Goshvartpour et al. [13] proposed a method of Matching Pursuit (MP) algorithm for emotions. Bulagang et al. [28] proposed a method of ECG and EDG/ GSR as input traits to categorize feelings. Hui et al. [6] proposed a method of emotion detection with contactless approaches and touch and skin-penetrating electrodes. Hasnul et al. [25] proposed a method that specializes in emotion recognition research based on electrocardiograms (ECGs) as an unimodal and multimodal method Xianhai [29] proposed a technique related to the emotional sample reputation method as a standard neural network classifier to examine ECG statistics with wavelet coefficients. Fernández [8], Zenonos et al. [30], Patil et al. [31] proposed methods to discover the possibility of gadgets for mood reputation for work environments [8, 24] is showing a machine learning approach for predictivity of ECG classification. Some articles consider ECG signal correlation and time-frequency domain statistical characteristics [19, 32]. Data [33] modified weighted mean filter to improve the baseline eduction approach for emotion recognition in the article [3].

3. MATERIAL AND DATA

3.1. Material As shown in Figure 1, The proposed framework consists of hardware of microcontroller, An ECG measuring sensor (AD 8232), pulse sensor, temperature sensor (LM35) and software elements of machine learning algorithms, driver programs, and performance measurement programs written in python.

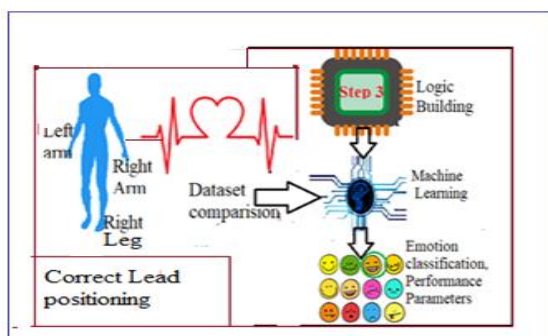


Figure 1. Conceptualization of proposed system arrangement

3.2. Dataset The Wearable Emotion and Stress Affect Dataset (WESAD) in CSV format is used [12]. Dataset is split between 70 percent training and 30 percent testing. The dataset contains, self reports and collection of 1Hz heartbeat data from the Raspbian device on the chest. and temperature data sampled at 4Hz collected using the wristband device. physiological data from 15 subjects collected during the lab research. Figure 2 shows logical flowchart for RR interval extraction on hardware for duration of 2 minutes interval.

3.3. Choice and Positioning of Biosensors In the market, 3,4,5,6, and 12 leads ECG models are available. AD8232 is a portable, low-cost, 3 lead ECG with 80 dB CMRR. AD8232 is having inbuilt well designed signal conditioning modules¹ and has capability of extraction, amplification, and filtration of cardiac bio signal potentials in the noisy condition. The low-pass signal processing circuits built in the AD 8232 remove powerline interface noise³. The ECG sensor detects heartbeat rhythm and pace [26].

Three electrical leads namely, Right Arm [RA] and Right Arm [LA] Right ankle measure the ECG. LM35 is attached to a finger or wrist. From Captured ECG signals, noise is removed with low pass filter and power line inference by thresholding, The output of Sensor and Graphical User Interface is shown in Figures 3 and 4. To capture real time emotions, WESAD [12] serves as the reference dataset.

3.4. Method Ten volunteers of age group 20 to 22 are chosen in such a way that they do not have any mental illness or heart disease. The video induction method of 12 minute duration for emotion induction is used.

The real time ECG data capturing is done for 2 minute per sample. For each volunteers, 6 samples of 2 minutes are collected. Thus for ten volunteers 60

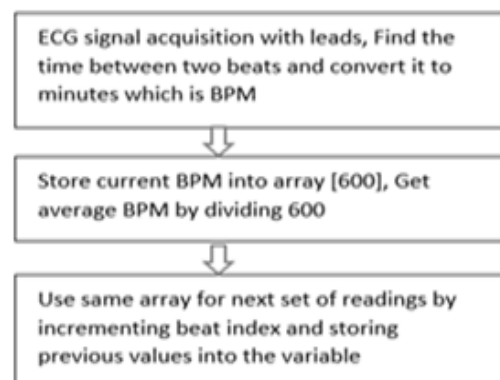


Figure 2. AD 8232 based RR interval determination (600 is array size, in which current peaks are stored and refreshed)

¹ <https://www.analog.com/media/en/technical-documentation/data-sheets/ad8232.pdf>

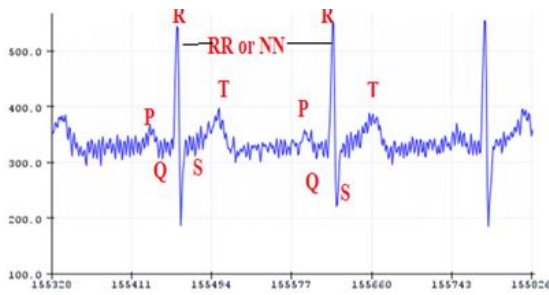


Figure 3. The output waveform of the proposed system wave showing real-time showing QRS complex, RR interval



Figure 4. The GUI design for captured heartbeat

samples of each 2 minute duration are collected. Hence we have 600 samples, From these collected samples. We have processed data in real time. For real time implementation Arduino processor¹ with an Analog to Digital Converter resolution of 10 bits is used. The recorded ECG range will range from 0 to 1023 and the real time graphs are available at serial port.

4. RESULTS

4. 1. Platform Used For machine learning part Python HRV, serial, pickle libraries, and WESAD benchmark dataset are used for data acquisition. Arduino output is seen and transferred to machine learning from serial port. The possible ECG Feature extraction methods are listed in Table 3.

4. 2. PQRST Waveform and RR interval ECG waveform typically forms the typical shape called as the PQRST². The visualization of the waveform is in Table 4. A peak detection method is used as a first step. This method is comparing each time series data and storing the largest number as a latest peak. The difference between newer peak and the previous peak in time domain is called as RR interval. The current peak value is compared a newest peak value [34] and is selected as R feature to calculate:

$$\text{Heart Rate} = [(60000)] / (\text{R-R interval}) \tag{1}$$

4. 3. ECG based Emotion Classification with Machine Learning

For ECG based disease classification, variety of ECG classifiers like Neural network, particle swarm algorithms are available. For emotion detection with ECG classifiers SVM, KNN, Random forest are popular methods (Table 1).

We have proposed navies bays classifier for solving the emotion classification multiclass problem because The navies bays classifier is probability based. From Litturature, we know that, SVM [27] is the best candidate with better accuracy hence we are proposing SVM to compare with navies bays classifier.

TABLE 3. List of important ECG features. Out of these features, RR interval is selected as feature

Summary of ECG features: A: Time Domain, B.Frequency Domain and Poincare plots		
A.Time domain Features of ECG		
1	HR - M	Mean of heart rate
2	SDR_R	Standard deviation of interbeat (msec) Interval, $SDR_R = \sqrt{\frac{1}{N-1} * \sum_{k=1}^N (R_{Rk} - R_R) \wedge 2}$
3	RM_square_SD	- $SDNN = \sqrt{\text{succesive NN interval difference}}$ (msec)
4	RR(50)	- (Number of NN interval pairs) > 50 milliseconds
5	PrR_R(50)	- (The % of numbers of pairs of NN) > 50
	$MeanR_R$	$MeanR_R = \frac{1}{N} * \sum_{k=1}^N (R_{Rk})$
B.Frequency domain Features of ECG(R paeak detection)(Power spectral Density)		
1	Power_SD range less than 0.04 Hz,	power distribution across frequency of area/energy
C.Poincare plot		
Poincare plot is the roatational transformation for the X axis is the RR interval with t points, and the Y axis repersents the t+1 points interval		

¹ <https://docs.arduino.cc/resources/datasheets/A000066-datasheet.pdf>

² <https://www.svms.org/anns.html>

TABLE 4. Visualization of the PQRST points, and significance (we have captured the peaks of PQRST for getting RR interval)

Points on the ECG	Source/ Remark	Duration/ Remark	Visualization of PQRST and Selected feature is RR or NN Interval
p	Depolarization is source of the P wave . stimulation of the both sides of atriais	Duration P < 0.12 sec	
QRS-complex	concurrent movement of the both ventricles	QRS duration is less than 0.10 sec	
ST SEGMENT	QRS complex and T wave are in concave upward direction	Patterns of downward direction or horizontal of ST segment describe depression.	

4. 4. Support Vector Machine The SVM approach is used to categorize emotions into four categories: neutral, stress, happy, and sad. The SVM method's goal is to find or decision boundary for categorizing n-dimensional space so that additional data points can be easily classified in the future.

A scatterplot is graph showing the relationship between two variables in the dataset.

Figure 5 shows a output of the SVM Scatterplot with heart rate on X axis and temperature on Yaxis. The preliminary observation shows that neutral and happy are well classified in the scatterplot. Neutral to happy. Stress and sad emotions seem to be in close vicinity. The Table 5 shows values of ranges observed in scatterplot.

The very first step posted by us for ECG Machine learning emotion classifier approach is to make the subjects calm down to a neutral state, and then use 12 minutes of video induction method.

Figure 6 shows the output of neutral emotion labels from the serial monitor of the processor by applying the SVM algorithm to ECG and temperature features. The output label neutral (Base) state is captured when the subjects are instructed to be in the relaxed position.

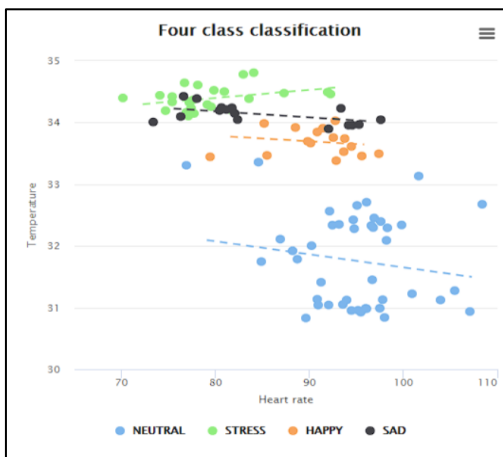


Figure 5. SVM scatterplot :four classes of emotions

TABLE 5. The SVM scatter plot Analysis

Emotion class	Indicated by (dot) colour	SVM	
		Heart rate Range	Temp. Range
Neutral	Blue	85 - 110 BPM	30 - 33°C
Stress	Green	70 - 100 BPM	34°C
Happy	Orange	80 - 100 BPM	33 - 34°C.
Sad	Black	75 – 100 BPM	34 - 34.5°C

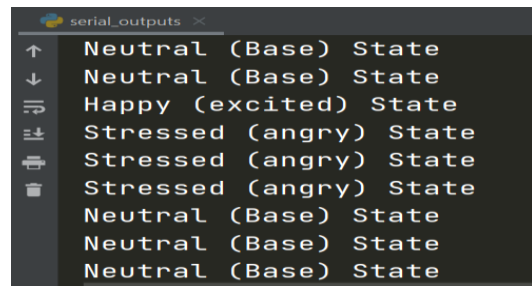


Figure 6. Labeled Neutral Emotions at output at initial instances

Navies Bayes

A naive Bayes classifier is based on the Bayes theorem and is a type of supervised learning. It suggests that the existence (or lack) of one feature of a class is not related to the existence (or lack) of any other feature. For real-time emotion recognition with ECG, the navies bays classifier used is probability-based prediction. As the emotions are totally random events. prediction with probability-based method is a suitable method.

The formula for Bayes' theorem is given as:

$$P(P|Q) = P(Q|P) \times P(P) / P(Q) \tag{2}$$

Performance Parameters Comparison for SVM and Navies Bayes Emotion Classiifies

Machine learning performance working in order to get predictions of the output is evaluated by numbers called its Performance Parameters. While defining these

parameters True Pos abbreviation is used for True Positive and False Neg False abbreviation is used for False Negative. Some of the calculations of performance parameters are done for understanding purpose as listed below.

a) Hamming Loss The proposed method is related to multiclass emotion classification, So calculation of accuracy will not truly support accuracy of model predictions. Hence, here Hamming loss term (with range 0 to 1) is useful.

Lesser value of hamming loss indicates a better classifier.

$$\text{Hamming loss} = \frac{\text{wrongly predicted labels}}{\text{(Total labels)}} \quad (3)$$

b) Specivity

$$\text{Specitivity} = \frac{\text{True Neg}}{\text{(False pos)+(True neg)}} = 1/3+5=0,125 \quad (4)$$

c) Sensitivity or Precision

$$\text{Sensitivity or precision} = \frac{\text{True pos}}{\text{(True pos)+(False Pos)}} \quad (5)$$

e.g. for Stress emotion class with navies bayes is calculated as Precision=201/ (201+34)=0.86

d) Recll e.g., for sad emotion class:

$$\text{Recall} = \frac{\text{True pos}}{\text{(True pos)+(False neg)}} = \frac{128}{128+11} = 0.92 \quad (6)$$

e) F1-Score F1 Score can be described as the harmonic mean of the model's precision and recall.

$$\text{F1Score} = 2 \times \frac{\text{(Precision)*(\text{Re call})}}{\text{(Precision)+(\text{Recall})}} \quad (7)$$

e.g., for sad emotion class:

$$\text{F1 Score} = 2 * \frac{0.94*0.92}{0.9+0.92} = 0.93 \quad (8)$$

f) Macro-average It is the basic mean of all class:

$$\text{Macro avg} = \frac{\text{F1-Score of all emotion class}}{\text{Total number of emotion class}} \quad (9)$$

$$\text{Macro - avg} = \frac{1+1+0.93+0.96}{4} = 0.97 \quad (10)$$

g) Weighted-average The weighted-average F1 score is the mean of all per-class F1 scores with respect to each class's support.

$$\text{Weighted}_{\text{avg}} = \frac{\text{(F1-Score)} \times \text{Support}}{\text{Sum of Support}} \quad (11)$$

$$\text{Weighted}_{\text{avg}} = \frac{1*0.446+1*0.133+0.93*0.139+0.96*0.234}{0.961} = 0.97077 \approx 0.98 \quad (12)$$

As per the above calculations and interpretation analysis, for the proposed setup with the SVM and Navies Bayes The performance of proposed system in Table 6, Figure 7 is at par with the previous literature described in Table 1. The comparisons of SVM and

TABLE 6. Comparison of performance factors for Navies byes and SVM (70 %Training and 30% testing split)

Predicted Class	Method	Precision	Recall	F1 score	Support	Remark	
Sad	SVM	0.94	0.92	0.93	139	Parameters are defined with definations and calculations in previous section	
	Navies Bayes	0.99	0.73	0.83	139		
Stress	SVM	0.96	0.97	0.96	234		
	Navies Bayes	0.86	1.00	0.92	234		
Neutral	SVM	1.00	1.00	1.00	446		The Scatterplot in Figure also shows all 6 readings classified correctly
	Navies Bayes	1.00	1.00	1.00	446		
Happy	SVM	1.00	1.00	1.00	133		
	Navies Bayes	1.00	0.99	1.00	133		

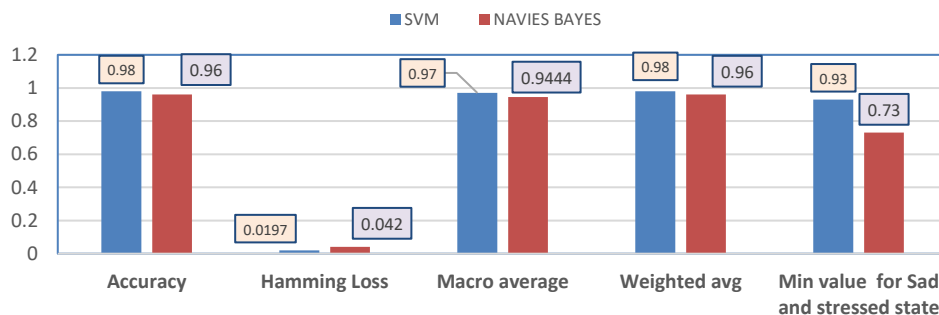


Figure 7. Comparison of performance factors for Navies and SVM 70 % training and 30 % testing split

Navies Bayes for emotion detection showS SVM has better accuracy of 98 percent and less Hamming Loss of 0.0197 as compared to Navies Bays values of 96 percent and 0,042 Hamming loss values. SVM proved better with less loss and better accuracy.

5. CONCLUSION

In this paper, the successful implementation of human emotion detection and classification from physiological signals is done. Apart from ECGs use for disease diagnosis, ECG signal can be used for emotion detection on hardware. We have classified the real time readings of 12 minute video induction into six 2 minute sample time. As per the peak values and disitance among peaks, four different emotion classes based on the ranges of different heart rate and temperature values are categorised. with machine learning algorithms.

5. 1. Strengths of Experimentation

1. Visualization of PQRST waveforms, Peaks, RRinterval, Scatterplot, comparison of output classes for SVM and Navies Bayeson real time data on the hardware is most challanging part which is successfully implemented. Real time body parameters heart rate, and body temperature are the two features are considered for ML algorithms instead of only ECG RR interval consideration.
2. Classwise precision, F1score, micro weights changes were not discussed till now, But we have presented them in interactive manner of calculations, tabluar form (Table 6) and graphical display.Hence, Thus strength is of this research is the Analysis of the emotion's classification by emotion classwise consideration of performance matrix
3. Primary contribution of this research is successful implementation of real-time affective computing with RR interval feature on hardware despite of noise and harware parameters, simulation is always easy than Hardware implementation.

5. 2. The Limiation The limitation of this study is the signal acquired are not compared with medical standard equipment because ECG in proposed study is not used for dignostic study.

5. 3. Future Scope

1. Additional body parameters such as SpO₂, skin conductance can be used for detecting human emotions.
2. Portable wearable devices can be created with the inclusion of mentioned body parameters to be employed in gaming zones or parental controls for gaming PCs.

3. Comparision of ECG aquisition readings with standard medical equipment before emotion classification.

6. REFERENCES

1. Lewis, K., "The influence of emotions on our shopping habits", *Siegel Institute Ethics Research Scholars*, Vol. 1, No. 1, (2017), 3. <https://digitalcommons.kennesaw.edu/siers/vol1/iss1/3>
2. Brundin, E., Liu, F. and Cyron, T., "Emotion in strategic management: A review and future research agenda", *Long Range Planning*, Vol. 55, No. 4, (2022), 102144. <https://doi.org/10.1016/j.lrp.2021.102144>
3. Shu, L., Xie, J., Yang, M., Li, Z., Li, Z., Liao, D., Xu, X. and Yang, X., "A review of emotion recognition using physiological signals", *Sensors*, Vol. 18, No. 7, (2018), 2074. <https://doi.org/10.1016/j.lrp.2021.102144>
4. Dzedzickis, A., Kaklauskas, A. and Bucinskas, V., "Human emotion recognition: Review of sensors and methods", *Sensors*, Vol. 20, No. 3, (2020), 592. <https://doi.org/10.3390/s20030592>
5. Basharirad, B. and Moradhaseli, M., "Speech emotion recognition methods: A literature review", in AIP Conference Proceedings, AIP Publishing LLC. Vol. 1891, (2017), 020105.
6. Hui, T.K. and Sherratt, R.S., "Coverage of emotion recognition for common wearable biosensors", *Biosensors*, Vol. 8, No. 2, (2018), 30. doi: 10.3390/bios8020030.
7. Barrett, L.F., Adolphs, R., Marsella, S., Martinez, A.M. and Pollak, S.D., "Emotional expressions reconsidered: Challenges to inferring emotion from human facial movements", *Psychological Science in the Public Interest*, Vol. 20, No. 1, (2019), 1-68. <https://doi.org/10.1177/1529100619832930>
8. Fernández-Caballero, A., Martínez-Rodrigo, A., Pastor, J.M., Castillo, J.C., Lozano-Monator, E., López, M.T., Zangróniz, R., Latorre, J.M. and Fernández-Sotos, A., "Smart environment architecture for emotion detection and regulation", *Journal of Biomedical Informatics*, Vol. 64, (2016), 55-73. doi: 10.1016/j.jbi.2016.09.015.
9. Shu, L., Yu, Y., Chen, W., Hua, H., Li, Q., Jin, J. and Xu, X., "Wearable emotion recognition using heart rate data from a smart bracelet", *Sensors*, Vol. 20, No. 3, (2020), 718. <https://doi.org/10.3390/s20030718>
10. Roshani, S., Coccia, M. and Mosleh, M., "Sensor technology for opening new pathways in diagnosis and therapeutics of breast, lung, colorectal and prostate cancer", *medRxiv*, Vol., No., (2022), 2022.2002. 2018.22271186. doi: 10.28991/HIJ-2022-03-03-010
11. Egger, M., Ley, M. and Hanke, S., "Emotion recognition from physiological signal analysis: A review", *Electronic Notes in Theoretical Computer Science*, Vol. 343, (2019), 35-55. doi: 10.1016/j.entcs.2019.04.009.
12. Schmidt, P., Reiss, A., Duerichen, R., Marberger, C. and Van Laerhoven, K., "Introducing wesad, a multimodal dataset for wearable stress and affect detection", in Proceedings of the 20th ACM international conference on multimodal interaction. (2018), 400-408.
13. Goshvarpour, A., Abbasi, A. and Goshvarpour, A., "An accurate emotion recognition system using ecg and gsr signals and matching pursuit method", *Biomedical journal*, Vol. 40, No. 6, (2017), 355-368.
14. Valderas, M.T., Bolea, J., Laguna, P., Vallverdú, M., Bailón, R. , "Human emotion recognition using heart rate variability analysis with spectral bands based on respiration", in In 2015 37th Annual International Conference of the IEEE Engineering in Medicine

- and Biology Society (EMBC). Vol. 343, (2015 of Conference), 6134-6137.
15. Dissanayake, T., Rajapaksha, Y., Ragel, R. and Nawinne, I., "An ensemble learning approach for electrocardiogram sensor based human emotion recognition", *Sensors*, Vol. 19, No. 20, (2019), 4495. <https://doi.org/10.3390/s19204495>
 16. Rodríguez, R., Mexicano, A., Bila, J., Cervantes, S. and Ponce, R., "Feature extraction of electrocardiogram signals by applying adaptive threshold and principal component analysis", *Journal of applied research and technology*, Vol. 13, No. 2, (2015), 261-269. doi: 10.1016/j.jart.2015.06.008.
 17. Manullang, M.C.T., Simanjuntak, J. and Ramdani, A.L., "Implementation of ad8232 eeg signal classification using peak detection method for determining rst point", *Indonesian Journal of Artificial Intelligence and Data Mining*, Vol. 2, No. 2, (2019), 61-66. doi: 10.24014/ijaidm.v2i2.7593.
 18. Dhuheir, M., Albaseer, A., Baccour, E., Erbad, A., Abdallah, M. and Hamdi, M., "Emotion recognition for healthcare surveillance systems using neural networks: A survey", in 2021 International Wireless Communications and Mobile Computing (IWCWC), IEEE. (2021), 681-687.
 19. Patil, V.K. and Pawar, V.R., "How can emotions be classified with eeg sensors, ai techniques and iot setup?", in 2022 International Conference on Signal and Information Processing (IConSIP), IEEE. (2022), 1-6.
 20. Londhe, S. and Borse, R., "Emotion recognition based on various physiological signals-a review", *ICTACT Journal on Communication Technology*, Vol. 9, No. 3, (2018), 1815-1822. doi: 10.21917/ijct.2018.0265.
 21. Haag, A., Goronzy, S., Schaich, P. and Williams, J., "Emotion recognition using bio-sensors: First steps towards an automatic system", in Affective Dialogue Systems: Tutorial and Research Workshop, ADS 2004, Kloster Irsee, Germany, June 14-16, 2004. Proceedings, Springer., (2004), 36-48.
 22. Butkeviciūtė, E., Michalkovič, A. and Bikulčienė, L., "Eeg signal features classification for the mental fatigue recognition", *Mathematics*, Vol. 10, No. 18, (2022), 3395. <https://doi.org/10.3390/math10183395>
 23. Sun, B. and Lin, Z., "Emotion recognition using machine learning and eeg signals", *arXiv preprint arXiv:2203.08477*, (2022). <https://doi.org/10.48550/arXiv.2203.08477>
 24. Kumar, S. and Sahoo, G., "A random forest classifier based on genetic algorithm for cardiovascular diseases diagnosis (research note)", *International Journal of Engineering, Transactions B: Applications*, Vol. 30, No. 11, (2017), 1723-1729. doi: 10.5829/ije.2017.30.11b.13.
 25. Hasnul, M.A., Aziz, N.A.A., Alelyani, S., Mohana, M. and Aziz, A.A., "Electrocardiogram-based emotion recognition systems and their applications in healthcare—a review", *Sensors*, Vol. 21, No. 15, (2021), 5015. <https://doi.org/10.3390/s21155015>
 26. Bravo-Zanoguera, M., Cuevas-González, D., Reyna, M.A., García-Vázquez, J.P. and Avitia, R.L., "Fabricating a portable eeg device using ad823x analog front-end microchips and open-source development validation", *Sensors*, Vol. 20, No. 20, (2020), 5962. <https://doi.org/10.3390/s20205962>
 27. Shin, D., Shin, D. and Shin, D., "Development of emotion recognition interface using complex eeg/ecg bio-signal for interactive contents", *Multimedia Tools and Applications*, Vol. 76, (2017), 11449-11470. <https://doi.org/10.1007/s11042-016-4203-7>
 28. Bulang, A.F., Weng, N.G., Mountstephens, J. and Teo, J., "A review of recent approaches for emotion classification using electrocardiography and electrodermography signals", *Informatics in Medicine Unlocked*, Vol. 20, (2020), 100363. <https://doi.org/10.1016/j.imu.2020.100363>
 29. Xianhai, G., "Study of emotion recognition based on electrocardiogram and rbf neural network", *Procedia Engineering*, Vol. 15, (2011), 2408-2412. <https://doi.org/10.1016/j.proeng.2011.08.452>
 30. Zenonos, A., Khan, A., Kalogridis, G., Vatsikas, S., Lewis, T. and Sooriyabandara, M., "Healthyoffice: Mood recognition at work using smartphones and wearable sensors", in 2016 IEEE International Conference on Pervasive Computing and Communication Workshops (PerCom Workshops), IEEE. (2016), 1-6.
 31. Patil, V.K., Hadawale, O., Pawar, V.R. and Gijre, M., "Emotion linked aiot based cognitive home automation system with sensorvisual method", in 2021 IEEE Pune Section International Conference (PuneCon), IEEE. (2021), 1-7.
 32. Zhang, Z., Wang, X., Li, P., Chen, X. and Shao, L., "Research on emotion recognition based on eeg signal", in Journal of Physics: Conference Series, IOP Publishing. Vol. 1678, (2020), 012091.
 33. Emami, N. and Kuchaki Rafsanjani, M., "Extreme learning machine based pattern classifiers for symbolic interval data", *International Journal of Engineering, Transactions B: Applications*, Vol. 34, No. 11, (2021), 2545-2556. doi: 10.5829/IJE.2021.34.11B.17.
 34. Tivatansakul, S. and Ohkura, M., "Emotion recognition using eeg signals with local pattern description methods", *International Journal of Affective Engineering*, Vol. 15, No. 2, (2016), 51-61.

Persian Abstract

چکیده

احساسات شتاب دهنده عقل و نوآوری و خلاقیت انسان هستند، بنابراین توانایی تشخیص احساسات بسیار مورد تقاضا است. سخت‌افزار بلادرنگ در مقایسه با شبیه‌سازی‌ها دارای موانعی از نظر نویز و عوامل سخت‌افزاری است. یک سنسور الکتروکاردیوگرام (ECG) (AD8232) (LM35)، و یک مدار پردازش سیگنال سخت‌افزاری برای شناسایی احساسات بلادرنگ پیشنهادی است. فواصل RR از داده‌های ECG محاسبه می‌شود. پیش‌بینی احساسات با استفاده از یادگیری ماشین از فواصل RR و دمای بدن به عنوان ویژگی استفاده می‌کند. یکی از چهار احساس (یعنی ۱. خوشحال ۲. استرس ۳. خستگی ۴. غمگین). در پورت سریال پردازنده با استفاده از مجموعه داده‌های معیار WESAD و کتابخانه‌های HRV، سریال و ترشی تجسم می‌شود. عوامل نوآوری این مقاله عبارتند از (۱) استفاده از ECG برای تشخیص احساسات به جای تشخیص بیماری با روش القای احساسات، ضبط فاصله RR و طراحی رابط کاربری گرافیکی بازه RR برای ضبط زمان واقعی دما و (2) ECG نمایش احساسات فعلی در پورت سریال آردوینو. (۳) اندازه‌گیری عملکرد کلاس با استفاده از امتیاز FI، میانگین کلان، و میانگین وزنی به جای دقت اصطلاح عمومی. (۴) استفاده از ناویس بیز مبتنی بر احتمال در مقایسه با روش‌های سنتی SVM، KNN، جنگل تصادفی (۵) عملکرد علاقه‌کلاس برای مثال ویژگی یا دقت Navies Bayes کمتر از SVM (0.96) است، اما فراخوانی آن حساسیت آن بالاتر است. (۰.۹۷) در مقابل (۰.۹۴) برای استرس. در این مقاله، پارامترهای عملکرد را از نظر محاسبات تعاملی، شکل جدولی و نمایش گرافیکی ارائه کردیم.



A Proposed Model for Persian Stance Detection on Social Media

M. Farhoodi^a, A. Toloie Eshlaghy^{*a}, M. R. Motadel^b

^a Department of Information Technology Management, Science and Research Branch, Islamic Azad University, Tehran, Iran

^b Central Tehran Branch, Islamic Azad University, Tehran, Iran

PAPER INFO

Paper history:

Received 09 January 2023

Received in revised form 16 January 2023

Accepted 17 January 2023

Keywords:

Stance Detection

Data Augmentation

Fake News

Machine Learning

Deep Learning

Transfer Learning

Multi-Classifer Fusion

ABSTRACT

Stance detection is a recent research topic that has become an emerging paradigm of the importance of opinion-mining. It is intended to determine the author's views toward a specific topic or claim. Stance detection has become an important module in numerous applications such as fake news detection, argument search, claim validation, and author profiling. Despite considerable progress made in this regard in languages like English, unfortunately, we have not made good progress in some languages such as Persian, where we are confronted with a lack of datasets in this area. In this paper, two solutions are used to address this issue: 1) the use of data augmentation and 2) the application of different learning approaches (machine learning, deep learning, and transfer learning) and a meaningful combination of their outcomes. The results show that each of these solutions can not only enhance stance detection performance, but when both are combined, a very significant improvement in the results is achieved.

doi: 10.5829/ije.2023.36.06c.03

1. INTRODUCTION

Social media plays a significant role in the number of people accessing news over the last few decades. With increasing public access to social media, a lot of dubious and incorrect content is being produced and shared for beneficial purposes. Nowadays, people often use social media to express their opinions on published content [1]. These stances together can prepare valuable information to get an overview of some important news or rumors. Automatic stance detection is a strongly motivated mining operation on social media and networks [2]. Stance detection aims to determine the author's point of view (such as a favor, neutral or against) toward a post, a claim or a new one [3]. It has become a key component in many applications such as claims validation, fake news detection, argument search, and author profiling, etc. [4].

The stance detection requires a large amount of labeled data. Research shows that most papers have worked on stance detection in English language [5-7] and that many of the prepared datasets are also in the same language [8-10]. Nevertheless, for stance detection in low data resource languages, it is necessary to use

techniques that are data independent or that may increase the amount of data without generating new labeled data. These techniques are known as data augmentation.

As well, stance detection is an issue of classification. In general, classification is used in many applications such as news topic identification, author detection, etc. But the results of these classifiers are sometimes different, and the samples misclassified by different classifiers are usually not the same in a lot of experiments. This is due to a variety of reasons, such as the use of different training sets, the use of different features, or the use of different parameters to adjust the algorithm used in each of these individual classifiers. Multi-classifiers are typically used to solve this problem. In this paper, we examined the impact of data augmentation methods on the accuracy of detecting Persian stance on social media. In addition, after applying a variety of learning approaches including machine learning, deep learning, and transfer learning, we attempted to fuse their results to determine the final output.

This paper is organized as follows: Section 2 provides an overview of the research. Section

*Corresponding Author Email: toloie@gmail.com
(A. Toloie Eshlaghy)

3 gives a detailed explanation of our approach and the proposed model. Section 4 sets out the results achieved. Finally, Section 5 outlines the findings and future work.

2. RELATED WORKS

In recent studies, stance detection can be categorized into various types:

1) Target-specific stance detection: It tries to detect the stance expressed in a text toward a particular target (e.g., a person, a social movement, an organization, a product, or a policy) [11], which most research has focused on it [12, 13].

2) Multi-target stance detection: It aims to detect the opinions of social media users with respect to two or further targets [10, 14]. Conforti et al. [9] stated that because in numerous applications, there are many natural dependencies between targets, target-specific models are not effective and should be focused on multi-target stance detection.

3) Claim-based stance detection: It is an appropriate technique to investigate the veracity of the news. Its aim to detect the stance in a part of the text or comment toward a claim [15]. Therefore, claim-based stance detection has been extensively used for rumor detection [6, 16, 17].

In recent years, most research has concentrated on social media posts and tweets. In general, the stance detection approaches can be separated into four main kinds [3]: 1) feature-based machine learning approaches which often apply machine learning algorithms like decision tree, logistic regression, SVM¹, etc. for learning [18], 2) deep learning methods which usually use deep neural networks (such as RNN² or LSTM³) [19-23]. Some of the common features used in these approaches are vector representation of words, i.e. Word2Vec and Glove, phrase embedding, n-grams of words or letters, 3) transfer learning which has made significant progress in NLP technology due to the development of large language models using contextualized word embedding based on Transformer architecture [24] and applied by most research [24, 25], and 4) ensemble learning approaches that use more than one classifier to get the final result of the stance detection [13, 20].

In addition, despite the increasing popularity of the stance detection task, almost existing approaches are limited to using the textual features of social media posts, overlooking the social nature of the task. But a limited number of studies focused on contextual features [26, 27].

However, most researches have focused on the English language. Of course, in recent times, many studies have been conducted on other languages other

than English, like Russian [28], Indian [13], Italian [18], Zulu [29], and recently Persian [21, 25].

Since a significant amount of data is needed for automatic stance detection, therefore, in low data resources languages such as the Persian language in which there is not enough labeled data, it is necessary to use approaches to increase data. These techniques are called data augmentation.

Data augmentation methods increase the number of instances in the train data by generating different versions of actual datasets without explicitly collecting new data [30]. Data augmentation methods are designed to increase system efficiency in addition to increasing the data.

The strategy of data augmentation in natural language processing is a complex task because of the inherent complexities of language. We cannot substitute each word with a synonym, and even if we do, the context will be different. An increase in data can take place at various levels: letter level, word level, phrase level, and document level. On the other hand, data augmentation techniques are usually performed in different methods: from rule-based methods [31] to model-based methods [32], which can be very complex. Implementing rule-based methods is much easier, but may not lead to significant improvements. Model-based methods have important effects on performance, but are more challenging to develop and use. On the other hand, the distribution of the generated augmented data should not be too similar or differ too much from the original dataset. Because it can lead to overfitting or poor performance through effective data augmentation approaches that should aim for a balance.

A review of the studies shows that almost all research on stance detection has employed individual classifiers. Numerous studies in other fields have shown that the results of multiple classifiers can outperform better than the best individual classifier and improve the system performance [33]. In other words, when there is high variability among single classifiers, Multiple Classifier Systems (MCSs) can generally achieve greater classification accuracy than any individual classifier [34]. In recent years, many application areas have adopted several methods of merging classifiers, such as object tracking [35], human action recognition [36], risk analysis [37], fault diagnosis [38], face recognition [39] and so on.

3. PROPOSED APPROACH and IMPLEMENTATION DETAILS

In this section, a Persian stance detection approach will be presented. The methodology depicted in Figure 2.

¹ Support Vector Machine

² Recurrent Neural Network

³ Long Short-Term Memory

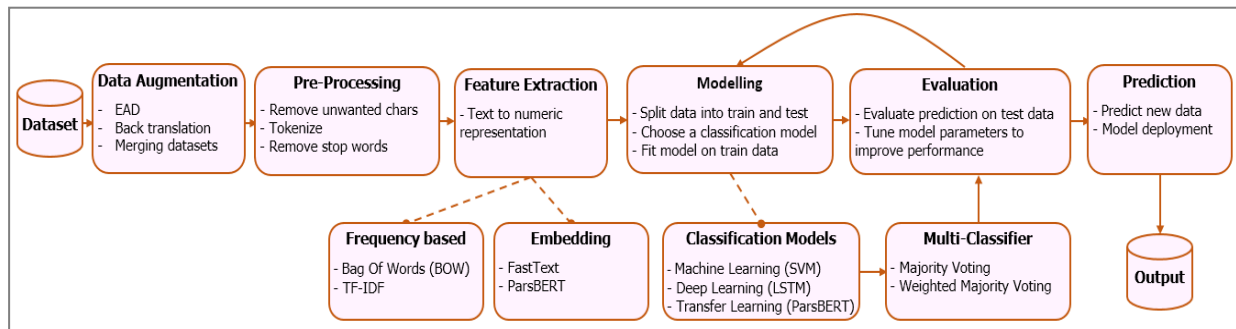


Figure 1. Flow diagram illustrating the methodology of this study

In our approach, data augmentation was used to the original dataset in various ways and the different augmented data were produced, which are illustrated in Figure 3 with letters A to E.

3. 1. Data Augmentation As mentioned above, a large amount of labeled data is needed for stance detection. In languages with low data resources such as Persian language, this amount of data does not exist. Thus, one way to increase the accuracy, enhancement the amount of data by using data augmentation methods.

Data augmentation techniques refer to strategies that enlarge the data in size or amount artificially without explicitly collecting new data [30]. Some of the data augmentation techniques are [40]:

1) Paraphrasing-based methods: these methods try to make minor changes in sentences without changing the semantics of the sentences and enter the changed sentences as new examples into the database; so, the augmented data transfer very similar information as the original sentences.

Back-translation is the most common method in these categories which consists of three steps: 1) each text sample in the dataset is translated to the default language,

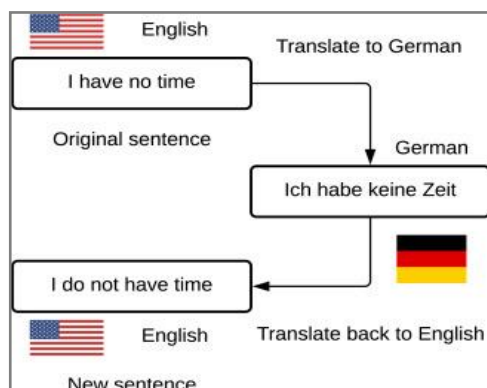


Figure 2. An example of the back-translation method

2) translated samples are back-translated to the original language, and 3) duplicate samples are removed from the mixture of the two-source dataset and the created data. This method lets to the production of textual data of different rewording to the real text while keeping the original context and meaning [41]. Figure 2 shows an example of two steps 1 and 2 (in this example, the original data is in English).

3) Noising-based methods: This method focuses to add low noise to the data with a little change so that the meaning of the increased data is very similar to the source data [40]. One of the most common methods in this category is EDA¹, which consists of four simple but powerful operations. These operations include synonym replacement, random insertion, random swapping, and random deletion of words [19].

4) Sampling-based methods: Corresponding to the data distribution, we can add new samples. For example, it is possible to create a larger dataset by merging the original dataset and a similar dataset in another language.

3. 2. Pre-processing Texts published in cyberspace such as posts on social media or web contain a lot of noise. As the performance of machine learning models is dependent upon data quality in addition to the quantity and variety of the data [42, 43], therefore cleaning the data and normalizing them is necessary thing. In this process, after tokenizing the text, sequences such as punctuation marks, numbers, additional spaces, stop words, and undesirable characters were removed in the text.

3. 3. Feature Extraction Since machine learning or deep learning algorithms are only able to understand numerical data instead of textual data, it is necessary to make the text meaningfully for them. Therefore, they must be expressed numerically. For this purpose, some algorithms such as TF-IDF, Word2Vec, etc. enable words to be expressed numerically to solve such problems. So, we used the following two approaches for feature extraction:

¹ Easy Data Augmentation

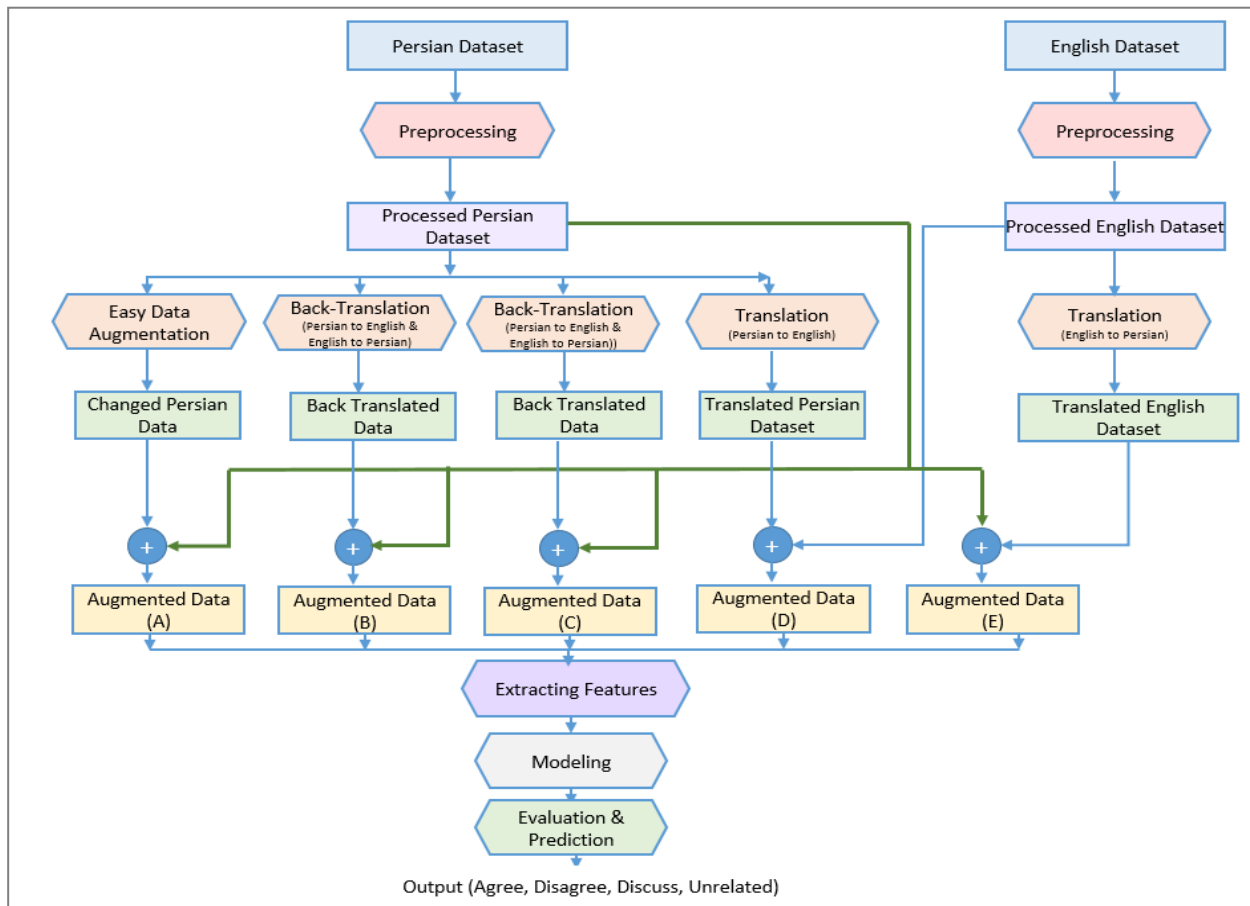


Figure 3. Proposed methodology for data augmentation

3.3.1. Frequency-based In this approach, each word in the text is represented by its frequency as follows:

- Bag of words (BoW): displays the number of occurrences of each bag that is created for each word without considering the word order within the text [44].
- TFIDF: is a statistical measure used to determine the mathematical significance of words in documents [44].

3.3.2. Embedding In word embedding, each word is represented in a continuous vector space. In this space, all words with semantic or syntactical similarity must be placed in the same area [45]. In this paper, we used two pre-trained embeddings as described below:

-FastText embedding: This method is based on the skip-gram model which learns to predict a target word near to the specific word and represents each word as a bag of character n-grams [46-48]. In this approach due to the use of n-gram word tokenization, for misspelled words, unusual words, or words that did not exist in the train data, an embedding is provided. This model is presented by Facebook and learned using Wikipedia 2017, UMBC web base corpus, and statmt.org news

datasets that contains 16 billion tokens. The embedding dimension is 300, the vocabulary is 1 million words [45].

- BERT embedding: Bidirectional Encoder Representations from Transformers (BERT) is another of the strongest document and word representations [47]. It is a transformer that includes an attention mechanism that learns the contextual relationships between words in a given sentence [48]. Under this approach, depending on the context, the same word may have a different embedding. Just like fastText, it is possible to embed rare words. In this paper, we use Pars-BERT that is a Persian language model based on BERT architecture and includes over 3.9 million documents, 73 million sentences, and 1.3 billion words with many writing styles on many topics [49].

3.4. Modeling At this step, the following tasks were carried out:

- Divide the data into train and test: in this regard, 80% of the data is considered to be train data and the rest as test data. As well, we used k-fold cross-validation and set k=10. On the other hand, since the samples are unbalanced, i.e., the amount of instances per class is not

equal, the stratifiedKfold library in Python has been used to shuffle the data in a balanced way.

- Select classification models: three different approaches were used for modeling: machine learning (such as SVM, Decision Tree, logistic regression, etc.), deep learning (LSTM), and transfer learning (ParsBERT).

- Fit models on training data: In this step, we trained our models on train data, that is, we passed the data into the model so that the model can update its internal mathematical variables and be prepared to predict. In other words, during fitting, we can pass various parameters like batch-size, epochs, learning rate, etc.

3. 5. Multi-classifier fusion

In this step, we suggested a multi-classifier fusion model for Persian stance detection. As mentioned previously, the results of individual classifiers, because of the algorithm, the results obtained from them are different. Multiple classifiers therefore combine several individual classifiers for better results. Multiple classifiers use different methods to fuse the results of each classifier, but majority voting is the most popular approach where each classifier "vote" for a particular class, and the class with the most votes is predicted by the multi-classifier system [50]. Under the majority voting approach, all individual classifiers have the same "authority" to classify correctly no matter how well they perform [51]. To solve this problem, weighting methods have been suggested, which are more appropriate to solve the problems that the member's classifiers perform the same task. In this approach, the output of each classifier is usually weighted according to its calculated accuracy on the train-data [52].

In this paper, we tried to use traditional majority and weighted majority voting methods to achieve the final results. Figure 4 shows the proposed model of the stance detector based on multi-classifier fusion. As described in this figure, first the texts in the dataset are preprocessed and then the desired features are extracted. In the next step, these features are used in the relevant classifier. As we know, in the machine learning approach, the SVM algorithm is used because it performs better (see 4.C in this article). In the deep learning approach, the LSTM is used and finally, in the transfer learning approach, the Pars-BERT transformer is used. In the next step, the results of these three classifiers are fused using both majority and weighted majority voting methods, and finally returns a specific stance as the final result.

3. 6. Evaluation For evaluating the performance of our approaches, we use Accuracy and F1-measure. Accuracy measures the proportion of the number of correct predictions relative to the total samples and F1-

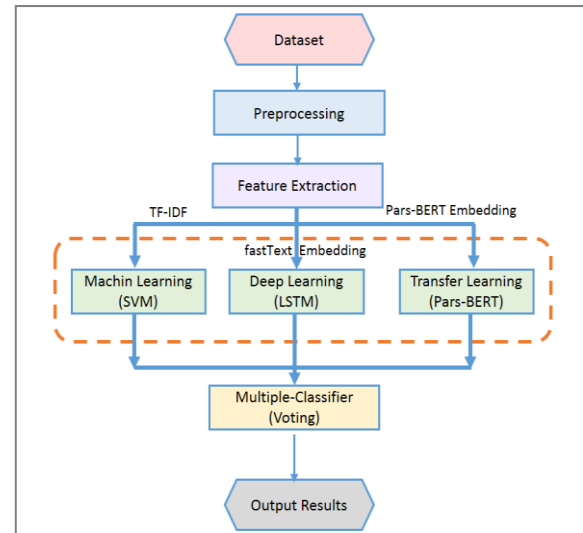


Figure 4. The Proposed model for multiple classifier fusion

measure determines the harmonic mean of precision and recall and is calculated as Equation (1):

$$F - Measure = \frac{2 * Precision * Recall}{Precision + Recall} \quad (1)$$

3. 7. Prediction

Once the model is trained on data, it should be capable of predicting new data. In this respect, we obtained 20% of the data set as test data and applied the relevant algorithms to it. Test results are given in the following section.

4. EXPERIMENTAL RESULTS

4. 1. Dataset

In the current research, we used two datasets in Persian and English languages. In the following we describe each of them:

4. 1. 1. Persian Dataset¹

This dataset includes 534 claims gathered from Shayeaat² and Fakenews³ and includes of two parts [21]: the first part consists of claims with news headlines and the second one includes claims with the body text of the articles. The labels of each news headline or article's body are:

- Agree: The article expresses that the claim is right, without any kind of cover and quotation.
- Disagree: The article expresses that the claim is wrong, without any kind of cover and quotation.
- Discuss: The article does not get any argument about the right or wrong of the claim.
- Unrelated: The claim is not reported in the article.

The first part of this data set, which contains the pair (news headline, claim), includes 2029 examples, and the

¹ <https://github.com/majidzarharan/persian-stanceclassification>

² Shayeaat.ir

³ Fakenews.ir

second part, which contains the pair (article's body, claim), includes 1997 examples. Table 1 shows the distribution of labels in each section.

4. 1. 2. English Dataset This dataset is presented in SemEval-2017-Task8 and contains 297 rumors -which are collected around 8 events taken from the urgent news-along with 5271 response tweets, which is a total of 5568 pairs (tweets and tweet responses). This dataset is separated into two parts, training data, and test data. The tag set distributions in each of the parts of this data provided in Table 2.

This dataset used the tree-based conversation consisting of tweets that replied to the rumor tweet, directly or indirectly [53]. The labels of stances in this dataset are Support, Deny, Query, and Comment (SDQC). Therefore, this dataset aims to detect the stance of reply tweets toward a rumor tweet (that can be direct or nested responses). Figure 5 presents an example of the tree structure for tweets. In this figure, user1 and user3 directly respond to user0's tweet, but user2 has expressed his opinion in response to user1's post.

4. 2. Results of Applying Data Augmentation Techniques

First, we present experimental results on the Persian dataset (without increased data) in two parts (1, 2) in Table 3. Next, we look at the effects of the application of each of the data augmentation methods on the performance of the algorithm used.

4. 2. 1. Easy Data Augmentation (EDA) Karande et al. [26] proposed that all operations of the EDA technique were examined on the Persian dataset. It has shown that a combination of such operations would be more appropriate to these data. So, in this paper, we used the combination of these operations on the Persian dataset. The experimental findings are given in Table 4.

TABLE 1. Distribution of labels in the Persian dataset

	Agree	Disagree	Discuss	Unrelated	Total
Part 1 (Headline-Claim Stance)	405	164	802	658	2029
Part 2 (Article-Claim Stance)	137	206	1068	586	1997

TABLE 2. Distribution of labels in the English dataset

	Support	Deny	Query	Comment
Train	910	344	358	2907
Test	94	71	106	778

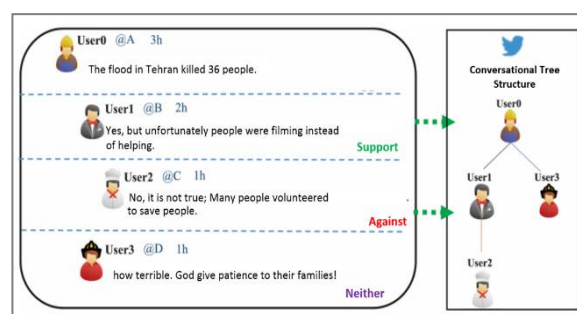


Figure 5. The tree structure of social media conversational

4. 2. 2. Back-translation For the back-translated data augmentation, in the current study, we have considered English as the target language. Table 5 provides the results of this approach.

4. 2. 3. Merging the Persian Dataset and English Dataset To accomplish this, we have implemented the following steps:

TABLE 3. Results on the original dataset

Data	Size	Feature	Accuracy	Precision	Recall	F-Measure
Part 1 (Headline-Claim)	2029	BOW	0.41	0.40	0.41	0.40
		TFIDF	0.53	0.53	0.53	0.53
Part 2 (Article-Claim)	1997	BOW	0.55	0.50	0.55	0.51
		TFIDF	0.83	0.83	0.83	0.83

TABLE 4. Results of EDA on the Persian dataset

Data	Size	Feature	Accuracy	Precision	Recall	F-Measure
Part 1 (Headline-Claim)	4058	BOW	0.52	0.52	0.51	0.52
		TFIDF	0.77	0.77	0.77	0.76
Part 2 (Article-Claim)	3994	BOW	0.63	0.61	0.63	0.61
		TFIDF	0.80	0.80	0.80	0.79

TABLE 5. Results of back-translation on the Persian dataset

Data	Size	Feature	Accuracy	Precision	Recall	F-Measure
Part 1 (Headline-Claim)	3998	BOW	0.49	0.48	0.49	0.48
		TFIDF	0.67	0.67	0.67	0.66
Part 2 (Article-Claim)	4058	BOW	0.46	0.45	0.46	0.45
		TFIDF	0.62	0.62	0.62	0.62

- First, we reviewed the stance detection datasets and chose one that was similar to Persian dataset. The sense of similarity here is that, first, both datasets were developed for the same purpose (here, to stance detection of a text, news, or a tweet reply toward to a claim or tweet). Second, the two datasets have the same tags or, if differentiated, the tags can be mapped to each other.

Some research was carried out on the preparation of dataset for stance detection in Persian. Tutek et al. [21] did the only work which was explained in part A of this section. One of the English datasets that may be regarded as equivalent is the one that was published in SemEval 2017-task 8. Its type is based on claims which its labels can be mapped to each other. Explanations of the English dataset can be found in part A.2 of this section.

- As the Persian dataset does not reflect the tweet tree conversation, we also tried to select only the top level of the English dataset tree structure. Thus, the size of our English dataset has been reduced to 3272 instances.

- At the next step, the English dataset labels were mapped to the Persian dataset as follows:

Agree \approx *Support*
Disagree \approx *Deny*
Discuss \approx *Query*
Unrelated \approx *Comment*

- The final step is to translate the English dataset is translated into Farsi and add it to the Persian dataset. The experimental findings for augmented data are shown in Table 6.

4. 2. 4. Comparison of Data Augmentation Methods

Figure 6 presents the results for each method of data augmentation on original dataset. The results indicate that the best method to increase the quality of stance detection performance is to merge the original dataset with a similar dataset in another language, which increases the diversity of data. If such a dataset is not found in other languages or is not accessible, the next best method is EDA method, which also shows a good improved algorithm performance. Back translation method though increased the accuracy, but compared to the other two methods, it does less improvement in the algorithm.

4. 3. Results of Applying Different Learning Approaches

As discussed above, we used three learning approaches: 1) machine learning, 2) deep learning, and 3) transfer learning. The results of the implementation of each of these methods are given

TABLE 6. Results on the augmented dataset

Data	Size	Feature	Accuracy	Precision	Recall	F-Measure
Translated English dataset + part1	5301	BOW	0.77	0.79	0.77	0.78
		TFIDF	0.81	0.81	0.80	0.81
Translated English dataset + part2	5269	BOW	0.66	0.64	0.66	0.63
		TFIDF	0.87	0.88	0.87	0.87

**Figure 6.** Comparison of data augmentation methods

below.

4. 3. 1. Machine Learning Approach

In this step, we used different supervised algorithms for stance detection in two parts of the original dataset. In Table 7, the relevant algorithms are given along with the results obtained from each. As the results show, the SVM algorithm shows a higher accuracy than other algorithms.

For the augmented dataset (for example the D dataset), the same algorithms were implemented and the results in Table 8 demonstrated that, again, SVM performed best.

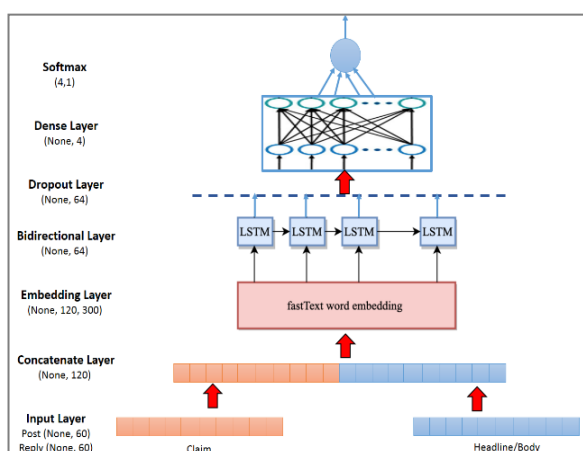
TABLE 7. Results of machine learning algorithms on original dataset

	Part 1 (Headline-Claim)				Part 2 (Article-Claim)			
	BOW		TFIDF		BOW		TFIDF	
	Acc.	F1	Acc.	F1	Acc.	F1	Acc.	F1
Logistic Regression	0.40	0.39	0.53	0.52	0.51	0.47	0.64	0.61
Decision Tree	0.41	0.40	0.52	0.53	0.49	0.48	0.44	0.44
SVM	0.40	0.38	0.53	0.53	0.51	0.47	0.65	0.63
Random Forest	0.40	0.39	0.51	0.52	0.49	0.47	0.50	0.46
KNN	0.39	0.36	0.40	0.38	0.49	0.45	0.49	0.46
Ada-boost	0.43	0.38	0.50	0.46	0.52	0.39	0.52	0.42

TABLE 8. Results of machine learning algorithms on augmented dataset

	Part 1 (Headline-Claim)				Part 2 (Article-Claim)			
	BOW		TFIDF		BOW		TFIDF	
	Acc.	F1	Acc.	F1	Acc.	F1	Acc.	F1
Logistic Regression	0.77	0.78	0.80	0.80	0.74	0.70	0.85	0.84
Decision Tree	0.78	0.77	0.81	0.81	0.81	0.80	0.80	0.80
SVM	0.77	0.78	0.82	0.82	0.83	0.83	0.86	0.86
Random Forest	0.77	0.78	0.81	0.81	0.81	0.81	0.83	0.82
KNN	0.73	0.70	0.74	0.70	0.76	0.73	0.81	0.79
Ada-boost	0.60	0.61	0.72	0.67	0.72	0.69	0.69	0.68

4. 3. 2. Deep Learning Approach In this phase, LSTM deep neural network classifiers were used. LSTM is an RNN model which overcomes the vanishing gradient and is used to model sequential data tasks. It is capable of efficiently capturing long-range dependencies. The designed network architecture is presented in Figure 7.

**Figure 7.** The schematic of our deep learning model

Since in our dataset, a tag is assigned for each pair of (claim and news headline) or (claim and news body), therefore, the neural network here takes two inputs. In the second layer, the two inputs are concatenated. After that, it enters the embedding layer, which utilizes fastText embedding. Then there is the bi-directional layer in which LSTM is used. It is followed by a fully-connected network to map the outputs to the tag space. For optimizing the model, Adam optimizer [17] is used for 20 epochs. Batch size and embedding-dimension are respectively 16 and 300. We used the TensorFlow library [54] to implement this model. The hyper-parameters have been tuned by evaluation over the validation set to achieve the highest accuracy and F1-measurement. Table 9 provides the test results of applying this model to our primary and augmented dataset. As the results show, when the volume of the dataset increases, the algorithm can make predictions with higher accuracy.

4. 3. 3. Transfer Learning Approach In this paper, we used pre-trained BERT models to for applying transfer learning. The Pars-BERT model can be fine-tuned to a specific task. It involves matching the parameters of a pre-trained BERT model for a particular

TABLE 9. Results of deep learning model

	Part 1 (Headline-Claim)		Part 2 (Article-Claim)	
	Acc.	F1	Acc.	F1
Pars-BERT (Original dataset)	0.72	0.73	0.75	0.74
Pars-BERT (Augmented dataset)	0.95	0.94	0.97	0.96

task by using a low data resource [45]. Figure 8 presents the suggested network architecture.

Like the previous model, here we have two inputs for the neural network too. We used the base model of Pars-BERT and fine-tuned it using the stance detection corpus. Then it is followed by a fully-connected network to map the Pars-Bert's outputs to the tag space. The learning rate, batch size, and the number of epochs are set to $5e^{-05}$, 128 and 10, respectively. In addition, the epsilon is set to $1e^{-08}$. Adam was applied for optimizing the model.

Table 10 shows the test results of applying this model on our original and augmented dataset. As the results show, when the volume of the dataset increases, the algorithm can make predictions with higher accuracy.

4. 4. Results of Applying Multi Classifier Fusion

In this section, the results of the empirical test of the proposed model shown in Figure 3 are presented on the original dataset and augmented dataset. For a better comparison, Tables 11 and 12 show the test results of the individual classifiers first, and then the performance of the use of the multi-classifier fusion. Clearly, among individual classifiers, the use of transfer learning methods can produce good results. On the other hand, the findings show that the combination of classifiers may lead to a significant improvement. The amount of this improvement is higher when weighted majority voting is

TABLE 10. Results of the transfer learning model

	Part 1 (Headline-Claim)		Part 2 (Article-Claim)	
	Acc.	F1	Acc.	F1
LSTM (original dataset)	0.69	0.67	0.72	0.71
LSTM (augmented dataset)	0.86	0.87	0.94	0.94

TABLE 11. Comparison of results of multi-classifier versus individual classifier in the original dataset

Algorithm	Dataset	Part 1 (Headline-Claim)		Part 2 (Article-Claim)	
		Acc.	F1	Acc.	F1
Individual Classifier					
SVM		0.53	0.53	0.65	0.63
LSTM		0.69	0.67	0.72	0.71
Pars-BERT		0.72	0.73	0.75	0.74
Multiple-Classifer					
Majority Voting		0.76	0.77	0.78	0.77
Weighted Majority Voting		0.78	0.77	0.79	0.79

TABLE 12. Comparison of results of multi-classifier versus individual classifier in augmented data

Algorithm	Dataset	Part 1 (Headline-Claim)		Part 2 (Article-Claim)	
		Acc.	F1	Acc.	F1
Individual Classifier					
SVM		0.81	0.81	0.87	0.87
LSTM		0.86	0.87	0.94	0.94
Pars-BERT		0.95	0.94	0.97	0.96
Multiple-Classifer					
Majority Voting		0.95	0.95	0.98	0.97
Weighted Majority Voting		0.97	0.96	0.99	0.99

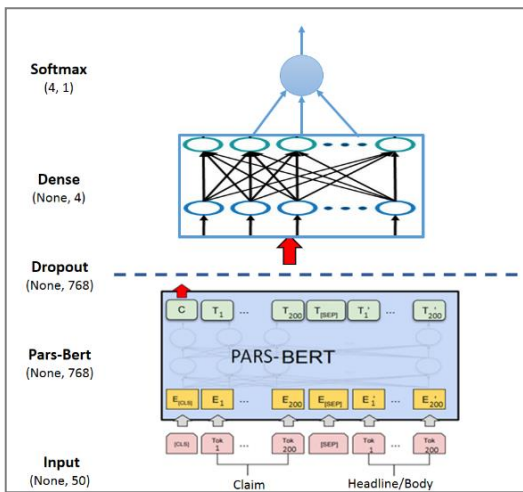


Figure 8. The schematic of our transfer leaning model

used. because in this case, it considers more weight to the classifier that has greater accuracy and increases the likelihood of its effectiveness in making the final decision.

As the results show, the use of transfer learning methods on the original data returns relatively good results. When the amount of data increases, the use of deep and transfer learning methods can make predictions with good accuracy and seek satisfaction. But as the above tables show, the use of multi-classifiers can perform better than the mentioned methods and provide quite acceptable accuracy. Therefore, according to the conditions, the following points can be considered:

- To improve the position detection accuracy, it is better to use similar data in another language, otherwise the EDA method is suitable.

- If similar data is not found in another language, it is better to use transfer learning methods.

- In any case, the use of multi-classifiers can lead to a good improvement.

4. 5. Comparison and Discussion As mentioned earlier by Tutek et al. [21] and Vaswani et al. [24] performed similar work in the field of Persian stance detection. Tutek et al. [21] used LSTM and Vaswani et al. [24] applied transfer learning and data augmentation on the dataset are discussed in this paper.

Table 13 compares the proposed model to the best models. As can be seen, multi-classifier fusion has a considerable impact on improving stance detection tasks

There are various advantages to the proposed model. Some of them are discussed below:

- It detects the stance by having only the content of a post and without extracting more features. This saves time and reduces computational costs.

-The size of the dataset can be increased without collecting more data and labelling them, which requires time, money and human resources.

- Combining the results of different classifier optimizes the use of the individual abilities and creates synergy.

-The proposed model is flexible in that other classifications may be used according to the subject and the intended application.

Unfortunately, no model is without disadvantages. Given below are some of the disadvantages of the proposed model:

- May not always have a dataset similar to the original dataset in another language. Of course, in this case, other methods of data augmentation should be used.

- It only uses content features to find the position. When interfacing with social networks, it is important to know which account answered the tweet. For example, the person who answers may be against the author of the tweet and thus reject the claims of that person, or it may be a bot, so user profiling can be a better help to identifying the stance.

TABLE 13. Comparison of the proposed model to the latest models presented for Persian stance detection

Model	Headline-Claim		Article-Claim	
	Accuracy	F1	Accuracy	F1
[21]	0.67	0.67	0.72	0.71
[24]	0.75	0.75	0.76	0.76
The proposed model (original dataset)	0.78	0.77	0.79	0.79
The proposed model (augmented data)	0.97	0.96	0.99	0.99

5. CONCLUSION AND FUTURE WORKS

In this paper first, we attempted to apply several data augmentation techniques to overcome the problem of the absence of data in stance detection in low data resource languages and to analyze the impact of each in improving the performance of algorithm. In this regard, we investigated Persian claimed-based stance detection and used various methods of data augmentation (including EDA, back translation, and merging similar datasets). The test results showed that if we can merge the source dataset with the similar dataset into other languages and create a bigger dataset, we achieve a significant improvement without spending time, money, and human resource in collecting data and labeling them. If such a dataset is unavailable or does not exist, a good improvement can be obtained by using the EDA technique.

Also, we proposed a model based on multi-classifier fusion for Persian stance detection, where, in addition to using different approaches such as machine learning, deep learning, and transfer learning to detection, the fusion of these classifiers' results is used to make the final decision. For this purpose, majority voting has been used and the results have shown that multi-classifier fusion can yield better results than the best classifier and improve the performance. Consequently, it may be concluded that multiple classification systems (MCS) are a good approach for stance detection. If we consider the accuracy of the classifiers as an efficient factor in the final decision to detect the Persian stance, we can achieve a significant improvement in the results.

So, our medal is innovative from two perspectives:

1. Use of the data augmentation method by combining the primary dataset and similar dataset in English and creating a larger dataset

2. Fusion of the individual classifier results through multi-classifiers.

Finally, the proposed model was also compared with the latest models presented in the field of Persian stance detection. While the proposed model has a significant improvement over related works, it also has limitations, which we will mention in the following and the future work that can be done to solve them.

As mentioned earlier, one of the limitations of this model is the use of content-only features, while contextual features such as user features and so on can also be used. Therefore, user profiling is one of the important tasks that can be addressed going forward.

Another thing that can be done to improve the model is to analyze the sentiment contained in the reply text of a tweet. For example, if someone answers "I'm sorry" to the tweet "Sanctions against Iran are increasing daily", analyzing the sentiment of the reply text can help identify the position.

In addition, one other thing that can be done to

improve the model is the detection of irony. Sometimes in social media spaces, people reply to a tweet with sarcasm, as its stance cannot be easily recognized. For example, if for the tweet "inflation has gone down by 20% this year", someone answers "don't get tired" It is unclear whether the stance of replier is to agree or disagree with that tweet. Therefore, the sarcasm detection module may also contribute to stance detection and be one of the tasks to focus on in the future.

6. REFERENCES

- Sobhani, P., "Stance detection and analysis in social media", Universite d'Ottawa/University of Ottawa, (2017),
- Dutta, S., Caur, S., Chakrabarti, S. and Chakraborty, T., "Semi-supervised stance detection of tweets via distant network supervision", in Proceedings of the fifteenth ACM international conference on web search and data mining., (2022), 241-251.
- Küçük, D. and Can, F., "A tutorial on stance detection", in Proceedings of the Fifteenth ACM International Conference on Web Search and Data Mining., (2022), 1626-1628.
- Schiller, B., Daxenberger, J. and Gurevych, I., "Stance detection benchmark: How robust is your stance detection?", *KI-Künstliche Intelligenz*, (2021), 1-13. doi: 10.1007/s13218-021-00714-w.
- Kochkina, E., Liakata, M. and Augenstein, I., "Turing at semeval-2017 task 8: Sequential approach to rumour stance classification with branch-ilstm", *arXiv preprint arXiv:1704.07221*, (2017). doi: 10.18653/v1/S17-2083.
- Yuan, C., Qian, W., Ma, Q., Zhou, W. and Hu, S., "Srlf: A stance-aware reinforcement learning framework for content-based rumor detection on social media", in 2021 International Joint Conference on Neural Networks (IJCNN), IEEE., (2021), 1-8.
- Zubiaga, A., Liakata, M., Procter, R., Wong Sak Hoi, G. and Tolmie, P., "Analysing how people orient to and spread rumours in social media by looking at conversational threads", *PLoS one*, Vol. 11, No. 3, (2016), e0150989. doi: 10.1371/journal.pone.0150989.
- Mohammad, S., Kiritchenko, S., Sobhani, P., Zhu, X. and Cherry, C., "Semeval-2016 task 6: Detecting stance in tweets", in Proceedings of the 10th international workshop on semantic evaluation (SemEval-2016), (2016), 31-41.
- Conforti, C., Berndt, J., Pilehvar, M.T., Giannitsarou, C., Toxvaerd, F. and Collier, N., "Will-they-won't-they: A very large dataset for stance detection on twitter", *arXiv preprint arXiv:2005.00388*, (2020). doi: 10.18653/v1/2020.acl-main.157.
- Sobhani, P., Inkpen, D. and Zhu, X., "A dataset for multi-target stance detection", in Proceedings of the 15th Conference of the European Chapter of the Association for Computational Linguistics: Volume 2, Short Papers., (2017), 551-557.
- Du, J., Xu, R., He, Y. and Gui, L., "Stance classification with target-specific neural attention networks", International Joint Conferences on Artificial Intelligence., (2017).
- Lai, M., Cignarella, A.T., Fariás, D.I.H., Bosco, C., Patti, V. and Rosso, P., "Multilingual stance detection in social media political debates", *Computer Speech & Language*, Vol. 63, (2020), 101075. doi: 10.1016/j.csl.2020.101075.
- Zotova, E., Agerri, R., Nuñez, M. and Rigau, G., "Multilingual stance detection in tweets: The catalonia independence corpus", in Proceedings of the Twelfth Language Resources and Evaluation Conference., (2020), 1368-1375.
- Swami, S., Khandelwal, A., Singh, V., Akhtar, S.S. and Shrivastava, M., "An english-hindi code-mixed corpus: Stance annotation and baseline system", *arXiv preprint arXiv:1805.11868*, (2018). doi: arXiv:1805.11868v1
- Darwish, K., Magdy, W. and Zanoua, T., "Trump vs. Hillary: What went viral during the 2016 us presidential election", in Social Informatics: 9th International Conference, SocInfo 2017, Oxford, UK, September 13-15, 2017, Proceedings, Part I 9, Springer. (2017), 143-161.
- Li, Y., He, H., Wang, S., Lau, F. and Song, Y., "Improved target-specific stance detection on social media platforms by delving into conversation threads", *arXiv preprint arXiv:2211.03061*, (2022). doi: arXiv:2211.03061.
- Derczynski, L., Bontcheva, K., Liakata, M., Procter, R., Hoi, G.W.S. and Zubiaga, A., "Semeval-2017 task 8: Rumoureal: Determining rumour veracity and support for rumours", *arXiv preprint arXiv:1704.05972*, (2017). doi: 10.18653/v1/S17-2006.
- Bar-Haim, R., Bhattacharya, I., Dinuzzo, F., Saha, A. and Slonim, N., "Stance classification of context-dependent claims", in Proceedings of the 15th Conference of the European Chapter of the Association for Computational Linguistics: Volume 1, Long Papers., (2017), 251-261.
- Cignarella, A.T., Lai, M., Bosco, C., Patti, V. and Paolo, R., "Sardistance@ evalita2020: Overview of the task on stance detection in italian tweets", in Proceedings of the Seventh Evaluation Campaign of Natural Language Processing and Speech Tools for Italian. Final Workshop (EVALITA 2020), Ceur., (2020), 1-10.
- Wei, P., Lin, J. and Mao, W., "Multi-target stance detection via a dynamic memory-augmented network", in The 41st International ACM SIGIR Conference on Research & Development in Information Retrieval., (2018), 1229-1232.
- Tutek, M., Sekulić, I., Gombar, P., Paljak, I., Čulinović, F., Boltužić, F., Karan, M., Alagić, D. and Šnajder, J., "Takelab at semeval-2016 task 6: Stance classification in tweets using a genetic algorithm based ensemble", in Proceedings of the 10th international workshop on semantic evaluation (SemEval-2016), (2016), 464-468.
- Zarharan, M., Ahangar, S., Rezvaninejad, F.S., Bidhendi, M.L., Pilevar, M.T., Minaei, B. and Eetemadi, S., "Persian stance classification data set", in TTO., (2019).
- Umer, M., Imtiaz, Z., Ullah, S., Mehmood, A., Choi, G.S. and On, B.-W., "Fake news stance detection using deep learning architecture (cnn-ilstm)", *IEEE Access*, Vol. 8, (2020), 156695-156706. doi: 10.1109/ACCESS.2020.3019735.
- Vaswani, A., Bengio, S., Brevdo, E., Chollet, F., Gomez, A.N., Gouws, S., Jones, L., Kaiser, Ł., Kalchbrenner, N. and Parmar, N., "Tensor2tensor for neural machine translation", *arXiv preprint arXiv:1803.07416*, (2018). doi: arXiv:1803.07416.
- Nasiri, H. and Analoui, M., "Persian stance detection with transfer learning and data augmentation", in 2022 27th International Computer Conference, Computer Society of Iran (CSICC), IEEE. (2022), 1-5.
- Karande, H., Walambe, R., Benjamin, V., Kotecha, K. and Raghu, T., "Stance detection with bert embeddings for credibility analysis of information on social media", *PeerJ Computer Science*, Vol. 7, (2021), e467. doi: 10.7717/peerj-cs.467.
- Khiabani, P.J. and Zubiaga, A., "Few-shot learning for cross-target stance detection by aggregating multimodal embeddings", *arXiv preprint arXiv:2301.04535*, (2023). doi: arXiv:2301.04535.
- Ren, Y., Liu, Y., Chen, J., Guo, X., Shi, J. and Jia, M., "News stance discrimination based on a heterogeneous network of social background information fusion", *Entropy*, Vol. 25, No. 1, (2022), 78. doi: 10.3390/e25010078.
- Lozhnikov, N., Derczynski, L. and Mazzara, M., "Stance prediction for russian: Data and analysis", in Proceedings of 6th

- International Conference in Software Engineering for Defence Applications: SEDA 2018 6, Springer., (2020), 176-186.
30. Dlamini, G., Bekkouch, I.E.I., Khan, A. and Derczynski, L., "Bridging the domain gap for stance detection for the zulu language", in Intelligent Systems and Applications: Proceedings of the 2022 Intelligent Systems Conference (IntelliSys) Volume 1, Springer., (2022), 312-325.
 31. Feng, S.Y., Gangal, V., Wei, J., Chandar, S., Vosoughi, S., Mitamura, T. and Hovy, E., "A survey of data augmentation approaches for nlp", *arXiv preprint arXiv:2105.03075*, (2021). doi: 10.18653/v1/2021.findings-acl.84.
 32. Yin, F., Yao, Z. and Liu, J., "Character-level attention convolutional neural networks for short-text classification", in Human Centered Computing: 5th International Conference, HCC 2019, Čačak, Serbia, August 5–7, 2019, Revised Selected Papers 5, Springer., (2019), 560-567.
 33. Liu, R., Xu, G., Jia, C., Ma, W., Wang, L. and Vosoughi, S., "Data boost: Text data augmentation through reinforcement learning guided conditional generation", *arXiv preprint arXiv:2012.02952*, (2020). doi: 10.18653/v1/2020.emnlp-main.726.
 34. Mi, A., Wang, L. and Qi, J., "A multiple classifier fusion algorithm using weighted decision templates", *Scientific Programming*, Vol. 2016, (2016). doi: 10.1155/2016/3943859.
 35. Liang, S., Han, D. and Han, C., "A novel diversity measure based on geometric relationship and its application to design of multiple classifier systems", *Acta Automatica Sinica*, Vol. 40, No. 3, (2014), 449-458. doi: 10.3724/SP.J.1004.2014.00449.
 36. Chen, S., Lu, X., Chen, X., Chen, M., Chen, J., Wang, D. and Zhu, S., "Object tracking with multi-classifier fusion based on compressive sensing and multiple instance learning", *Mathematical Problems in Engineering*, Vol. 2020, (2020), 1-17. doi: 10.1155/2020/1574054.
 37. Bagheri, M.A., Hu, G., Gao, Q. and Escalera, S., "A framework of multi-classifier fusion for human action recognition", in 2014 22nd International Conference on Pattern Recognition, IEEE., (2014), 1260-1265.
 38. Pan, Y., Zhang, L., Wu, X. and Skibniewski, M.J., "Multi-classifier information fusion in risk analysis", *Information Fusion*, Vol. 60, (2020), 121-136. doi: 10.1109/ICPR.2014.226.
 39. Huang, J.-T., Wang, M.-H., Li, W.-J. and Gu, B., "Multiple classifier fault diagnosis system based on dynamic weight", *Acta Electronica Sinica*, Vol. 40, No. 4, (2012), 734. doi: 10.3969/j.issn.0372-2112.2012.04.018.
 40. Yu, Z., Nam, M.Y., Sedai, S. and Rhee, P.K., "Evolutionary fusion of a multi-classifier system for efficient face recognition", *International Journal of Control, Automation and Systems*, Vol. 7, (2009), 33-40. doi: 10.1007/s12555-009-0105-z.
 41. Li, B., Hou, Y. and Che, W., "Data augmentation approaches in natural language processing: A survey", *AI Open*, Vol. 3, (2022), 71-90. doi: 10.1016/j.aiopen.2022.03.001.
 42. Beddiar, D.R., Jahan, M.S. and Oussalah, M., "Data expansion using back translation and paraphrasing for hate speech detection", *Online Social Networks and Media*, Vol. 24, (2021), 100153. doi: 10.1016/j.osnem.2021.100153.
 43. Maharana, K., Mondal, S. and Nemade, B., "A review: Data pre-processing and data augmentation techniques", *Global Transitions Proceedings*, (2022). doi: 10.1016/j.gltp.2022.04.020.
 44. Qader, W.A., Ameen, M.M. and Ahmed, B.I., "An overview of bag of words; importance, implementation, applications, and challenges", in 2019 international engineering conference (IEC), IEEE., (2019), 200-204.
 45. Aizawa, A., "An information-theoretic perspective of tf-idf measures", *Information Processing & Management*, Vol. 39, No. 1, (2003), 45-65. doi: 10.1016/S0306-4573(02)00021-3.
 46. d'Sa, A.G., Illina, I. and Fohr, D., "Bert and fasttext embeddings for automatic detection of toxic speech", in 2020 International Multi-Conference on: "Organization of Knowledge and Advanced Technologies"(OCTA), IEEE., (2020), 1-5.
 47. Joulin, A., Grave, E., Bojanowski, P., Douze, M., Jégou, H. and Mikolov, T., "Fasttext. Zip: Compressing text classification models", *arXiv preprint arXiv:1612.03651*, (2016). doi: arXiv:1612.03651.
 48. Devlin, J., Chang, M.-W., Lee, K. and Toutanova, K., "Bert: Pre-training of deep bidirectional transformers for language understanding", *arXiv preprint arXiv:1810.04805*, (2018). doi: arXiv:1810.04805.
 49. Vaswani, A., Shazeer, N., Parmar, N., Uszkoreit, J., Jones, L., Gomez, A.N., Kaiser, Ł. and Polosukhin, I., "Attention is all you need", *Advances in Neural Information Processing Systems*, Vol. 30, (2017). doi: 10.48550/arXiv.1706.03762.
 50. Farahani, M., Gharachorloo, M., Farahani, M. and Manthouri, M., "Parsbert: Transformer-based model for persian language understanding", *Neural Processing Letters*, Vol. 53, (2021), 3831-3847. doi: 10.1007/s11063-021-10528-4.
 51. Kuncheva, L.I., "Combining pattern classifiers: Methods and algorithms, John Wiley & Sons, (2014).
 52. Moreno-Seco, F., Inesta, J.M., De León, P.J.P. and Micó, L., "Comparison of classifier fusion methods for classification in pattern recognition tasks", in Structural, Syntactic, and Statistical Pattern Recognition: Joint IAPR International Workshops, SSPR 2006 and SPR 2006, Hong Kong, China, August 17-19, 2006. Proceedings, Springer., (2006), 705-713.
 53. Du, P., Xia, J., Zhang, W., Tan, K., Liu, Y. and Liu, S., "Multiple classifier system for remote sensing image classification: A review", *Sensors*, Vol. 12, No. 4, (2012), 4764-4792. doi: 10.3390/s120404764.
 54. Kingma, D.P. and Ba, J., "Adam: A method for stochastic optimization", *arXiv preprint arXiv:1412.6980*, (2014). doi: arXiv:1412.6980.

Persian Abstract

چکیده

تشخیص موضوع یک موضوع تحقیقاتی اخیر است که به یک پارادایم نوظهور نظیر کاوی با اهمیت تبدیل شده است که هدف آن تعیین دیدگاه نویسنده نسبت به یک موضوع یا ادعای خاص است. تشخیص موضوع به یک مؤلفه کلیدی در برنامه های مانند تشخیص اخبار جعلی، اعتبار سنجی ادعا، جستجوی استدلال، پروفایل نویسنده تبدیل شده است. با وجود پیشرفت قابل توجهی که در این زمینه در زبان های مانند انگلیسی صورت گرفته است، متأسفانه در برخی از زبان ها مانند فارسی که با کمبود دیتاست در این زمینه مواجه هستیم، پیشرفت خوبی نداشته ایم. در این مقاله از دو راه حل برای حل این مشکل استفاده شده است: (۱) استفاده از افزایش داده ها و (۲) اعمال رویکردهای مختلف یادگیری (مانند یادگیری ماشینی، یادگیری عمیق و یادگیری انتقال) و ترکیب معنی دار نتایج آنها. نتایج نشان می دهد که هر یک از این راه حل ها نه تنها می توانند به تنهایی منجر به بهبود عملکرد تشخیص موضوع شوند، بلکه زمانی که هر دو با هم ترکیب شوند، بهبود بسیار قابل توجهی در نتایج حاصل می شود.



Effect of Aging Treatment on Microstructure and Mechanical Properties of Al_{0.7}CoCrFeNi High Entropy Alloy

N. Asgarkhani, M. Seifollahi*, S. M. Abbasi

Faculty of Materials & Manufacturing Technologies, Malek Ashtar University of Technology

PAPER INFO

Paper history:

Received 25 January 2023

Received in revised form 15 March 2023

Accepted 16 March 2023

Keywords:

Al_{0.7}CoCrFeNi High Entropy Alloy

Aging

Microstructure

Hardness

Hot Compression

ABSTRACT

In this study, the effects of aging times and temperatures on the microstructure, hardness and compression strength of Al_{0.7}CoCrFeNi high entropy alloy have been investigated. The alloy was cast in a vacuum induction melting furnace, homogenized at 1250 °C for 6 h; then aged at 700 to 1000 °C for 2-8 h. The as-cast structure is dendritic and includes FCC(A1) and BCC(A2, B2) phases with the hardness of 497 HV. During ageing, B2 precipitates at the grain boundaries at 700 °C and the hardness increases about 7%. The ratio of BCC to FCC phases on the basis of XRD in as-cast alloy is approximately equal which is increased by ageing at 700 °C. At 800 °C, the formation of a destructive and hard phase of σ cause to increase the hardness to 543 HV and the ratio of (A2+B2)/A1 has decreased. At 1000 °C, the ratio of (A2+ B2)/A1 increases, and the peak intensity of σ decreases, so that the hardness value decreases to 385 HV. The results of hot deformation test showed that the alloy at the strain rate of 10⁻³ s⁻¹ and temperatures of 800, 900, 1000 and 1100 °C has a yield strength of 306, 179, 91 and 50 MPa, respectively.

doi: 10.5829/ije.2023.36.06c.04

1. INTRODUCTION

The high entropy alloys are known as solid solution alloys that have 5-13 elements with the same or almost the same atomic percentage (5-35%). Solid solutions with several elements due to high entropy tend to be stable at high temperatures. It is remarkable that these alloys have low diffusion rate, which causes the formation of nanometer precipitates, and severe lattice distortion due to the difference in atomic radii [1, 2].

AlCoCrFeNi high entropy alloys have the variety of eutectic microstructures including FCC and BCC phases. The ratio of FCC to BCC phases in these alloys has a direct effect on the mechanical properties. These alloys have excellent properties such as good corrosion resistance, high hardness and elevated yield strength even at high temperatures. σ phase is the other phase in the AlCoCrFeNi alloy [1, 3]. The amount of FCC, BCC and σ phases can be controlled with chemical composition justification and heat treatment. Due to the presence of five elements, this alloy is extremely non-

uniform and has dendritic structure. So, it requires high-temperature homogenization, which reduces the amount of segregation to a desirable extent and eliminates the dendritic structure [4-6].

Heat treatment process is an integral part of the industrial production components. Recent studies on high entropy alloys also show further research in this field required. Munitz et al. [7] assessed the effects of different aging temperatures on the microstructure of AlCoCrFeNi high entropy alloy. They found that aging for 3 hours at 650 °C, changes phases from BCC to σ and σ phase turns again to BCC at 975 °C. Wang et al. [8] examined the effects of aging at 600-1200 °C for 168 h on the microstructure of AlCoCrFeNi high entropy alloy. They found the formation of FCC phase was inhibited as a result of high rate of quenching, so the alloy maintain in solid solution manner. They also reported that after aging at temperatures of 800-1200 °C, nanometer-scale sediments and FCC phase precipitates from at the grain boundaries and cause to decrease in compressive strength and increase in ductility. Furthermore, Butler and

*Corresponding author email: m_seifollahi@mut.ac.ir (M. Seifollahi)

Weaver [9] reported the formation of coarse-grained microstructures consisting of FCC and BCC phases at 1050 °C/520 hr and stabilized FCC, BCC and σ phases at 700°C/ 1000 h. Most of the researches conducted in the field of manufacture and characterization of alloys with different compounds or the effect of alloying elements on the microstructure and properties. In the last two years, researches have done on the effects of heat treatment [10-12] and cold work [13-15], but none of them has fully examined the mechanisms of these processes. Homogenization provides the desired microstructure for the annealing process and subsequent aging leads to the development of the service operation. Although the researchers might be assess the effects of homogenization and aging of these alloys, so there is a research gap yet. In this research, the effects of aging and its mechanism on the microstructure and hardness of Al_{0.7}CoCrFeNi alloy were investigated.

2. MATERIALS METHOD

Al_{0.7}CoCrFeNi alloy was melted in a vacuum induction melting (VIM) furnace under a vacuum of 3.9×10^{-3} Pa. The chemical composition of Al_{0.7}CoCrFeNi alloy was measured using EDS analysis and the results are summarized in Table 1. Samples of $1 \times 1 \times 1$ cm³ were subjected to homogenization at 1250 °C for 6 h and oil quenched, then aged for 2, 4, 6 and 8 hours at temperatures of 700, 800, 900 and 1000 °C and water quenched. In order to study the microstructure, the samples were polished and etched in 10ml HCl+ 10ml HNO₃ + 10ml H₂O solution. The microstructure was examined by Olympus optical microscope and Vega-Tescan scanning electron microscopy equipped with EDS analysis. The hardness of the specimens was measured using a Easyway Vickers hardness testing machine under 30 kg load. Each hardness value is an average of five readings . The compression tests were performed at 800, 900 and 1100°C using Instron 8502 machine. The samples were 8mm in diameter and 12mm in length according to ASTM E209.

3. RESULTS AND DISCUSSION

Figures 1(a) and 1(b) show the optical microstructure of cast and homogenized (1250°C for 6 hours) Al_{0.7}CoCrFeNi alloy, respectively. As can be seen in

TABLE 1. Chemical composition of Al_{0.7}CoCrFeNi (at%) measured by EDS

Element	Al	Co	Cr	Fe	Ni
Nominal	17	20.75	20.75	20.75	20.75
Actual (EDS)	16.76	19.4	20.9	20.48	22.47

these figures, the casting microstructure consists of dendritic and interdendritic regions due to non-equilibrium solidification. After homogenization the microstructure becomes uniform without any dendritic morphology as a result of solid state diffusion mechanism. In Figure 1(b), the grain boundaries are perfectly clear.

DSC analysis was performed on the homogenized sample up to the temperature of 1000°C at a heating rate of 10°C/min for 100 min under argon gas and data are shown in Figure 2. At 500°C, a peak is observed which can be attributed to the precipitation of σ from the BCC phase. No other changes are observed due to the presence of FCC and BCC phases, which both are mixed together from the beginning and no other fuzzy transformation occurs. This is a feature of high entropy alloys that they are single-phase solid solution, and this phase is stable up to the high temperatures even close to melting temperatures [16].

Figure 3 shows the X-ray diffraction patterns of the as-cast and aged alloy at different temperatures for 4 h. The characteristic phase are summarized in Table 2. A1 and A2 are regular FCC and irregular BCC, respectively and both are rich of Co, Cr and Fe. B2 is BCC irregular phase and rich of Al and Ni.

According . Munitz et al. [7] and Wang et al. [10], it is expected that σ phase nucleated and grow at 700°C, but it is not observed in the XRD pattern. It seems that 4 hours at 700°C is insufficient. Of course, it is also possible that σ phase is formed at 700°C, but its amount is less than 5% that is not detectable with XRD analysis.

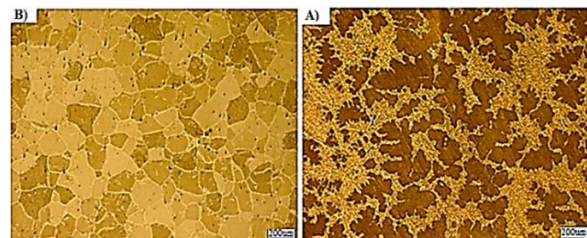


Figure 1. Optical microstructure of entropy alloy above AlCoCrFeNi (A): Casting (B): Homogenized at 1250 °C temperature for 6 hours and cooled in oil

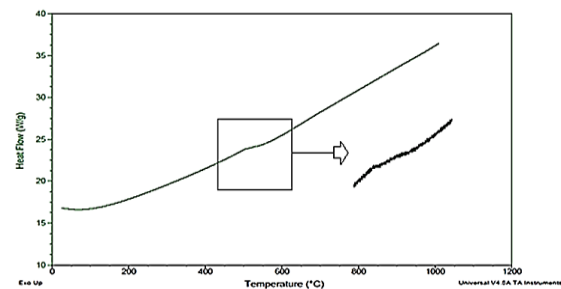


Figure 2. differential scanning calorimetry of Al_{0.7}CoCrFeNi high entropy alloy homogenized at 1250°C for 6 hours

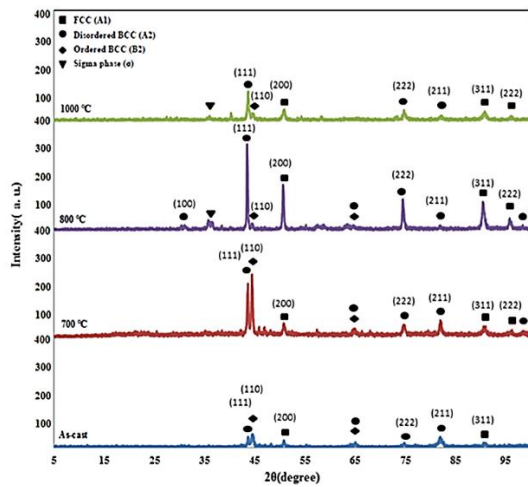


Figure 3. X-ray diffraction pattern of high entropy Al_{0.7}CoCrFeNi after different ageing at temperatures

TABLE 2. The characteristic of the phases measured by XRD

Heat treatment	Phases	BCC/FCC
As-cast	A1, A2, B2	1
700 °C	A1, A2, B2	2.5
800 °C	A1, A2, B2	1.7
1000 °C	A1, A2, B2, σ	2.2

As the temperature rises to 800 °C, the σ phase peak is observed in the XRD pattern. σ phase is considered harmful due to its brittle and fragile nature that forms due to the diffusion driving force increasing at 800 °C. It is possible that the formation of σ phase at 800 °C has led to the growth of FCC phase [3].

It is essential to note that dissolution of σ phase is expected at 1000 °C, and can be concluded that 4 hours is not sufficient to dissolve it. At 1000 °C the BCC/FCC ratio has been decreased due to the gradual dissolution of σ phase. Therefore, with increasing temperature up to above 1000 °C, the harmful σ phase gradually dissolves. Munitz et al. [7] reported that BCC phase converted to σ at 650 °C and to BCC again at 975 °C. σ Phase with the chemical composition of FeCr is harder than BCC and cause to hardness increase.

Figure 4 shows optical microstructure of the alloy aged at 700-1000 °C for 2-8 hours.

It is observed that after aging at 700 °C for 2h, the microstructure did not change significantly compared to the homogenized structure. The dark phase (BCC) and the white fingerprint phase (FCC) are clearly visible in the structure. At this temperature, the fraction of BCC phase is higher than FCC, which is in agreement with XRD results. It is observed that with increasing time from 2 to 8 hours, fingerprint phases tend to dissolve and join to the boundaries. Also, the thickness of the grain

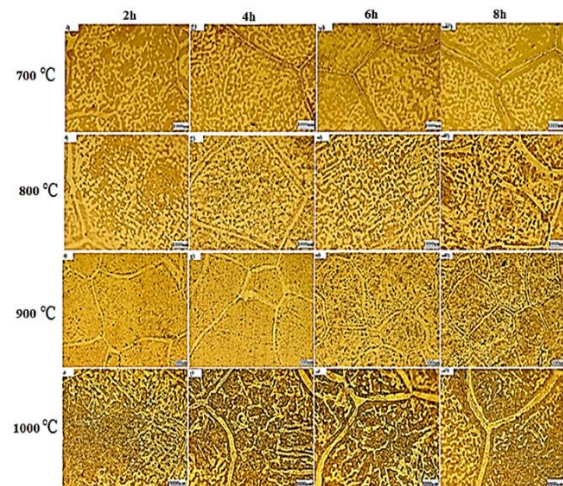


Figure 4. Optical microscopic images of AlCoCrFeNi entropy alloy after aging at temperatures of (700-1000 °C) (A: 2 h, B: 4 h, C: 6 h, D: 8) and cooled in water

boundaries decreases with times. A1 (rich of Co, Cr and Fe) is a dendrites phase after solidification which dissolves and its element diffuse toward grain boundaries during homogenizing and again diffuse into B2 phase with increasing time from 2 to 8 hours.

It is noteworthy that the grain boundaries changes during ageing in comparison to homogenization and some precipitates form on the grain boundaries. According to the results of XRD analysis and also literature [7, 17], it can be said that these precipitates are B2, which is formed after aging at the grain boundaries.

At 800 °C, according to the results of XRD analysis, microstructures include FCC, BCC and σ phases. σ phases are not visible due to their small size and volume fraction. The sediments of B2 are also observed in the middle of A1. It has been reported by Wang et al. [10] that Al can stabilize the BCC phase in high entropy alloys. In particular, Al stabilizes the regular BCC (B2) and Cr stabilizes the irregular BCC (A2). The Cr greatly increases the driving force of the σ phase formation. Also, the mobility of Cr in BCC phase is much higher than in FCC. Cr by increasing the driving force plays an important role in intensifying the precipitation rate of σ . Therefore, it is expected that σ forms directly from (Fe and Cr rich FCC phase) and (Fe and Cr rich irregular BCC phase). When Cr diffuses from BCC to σ phase, at the same time, Ni atoms diffuse into the Cr depleted zones and FCC phase formed.

The microstructure of alloy aged at 900 °C is included FCC, BCC and σ phases. As can be seen in Figure 4, the microstructure has dramatically changed. It is observed that phases A1, A2, B2 are completely intertwined with each other so around the grain boundaries are surrounded by A2 and B2. It is also observed that the grain boundaries are more thicker than of 800 °C, which

indicates an increase in FCC to BCC ratio due to the σ phase increasing (it will be discussed).

At 1000°C, there are also FCC, BCC and σ phases, according to Figure 4. As can be seen in this figure, the needle like B2 precipitate are seen in the microstructures as well as around the grain boundaries. The amount of σ has been decreased, which led to a decrease in FCC, and increase in BCC phase. It is appeared that precipitates within grain boundaries are also declined slightly.

Figure 5 shows SEM images of an AlCoCrFeNi high-entropy alloy after homogenizing and aging at the temperatures of 700-1000°C for 4 hours along with the line scan analysis of the elements.

As can be seen in Figure 5b, the depleted areas around the boundaries are disappearing in comparison to the homogenized state. In homogenized state (Figure 5(a)), the amount of Al and Ni at the grain boundaries decreases sharply, but it does not happen in aged sample due to the deposition of B2 inside A1 after aging.

Figure 5(c) shows the extensive amount of needle-like BCC phase, which are scattered throughout the microstructure. The BCC phase is appeared to accumulate and move toward boundaries as temperature rises. It is also observed that the fingerprint phases also tend to approach the boundaries. Until 700°C, the boundaries are free from dark BCC phases. As the temperature increases, due to BCC to σ phase transformation, the morphology of BCC phases changes from the coarse fingerprint to needle-like which indicates a decrease in BCC to FCC ratio. The results of

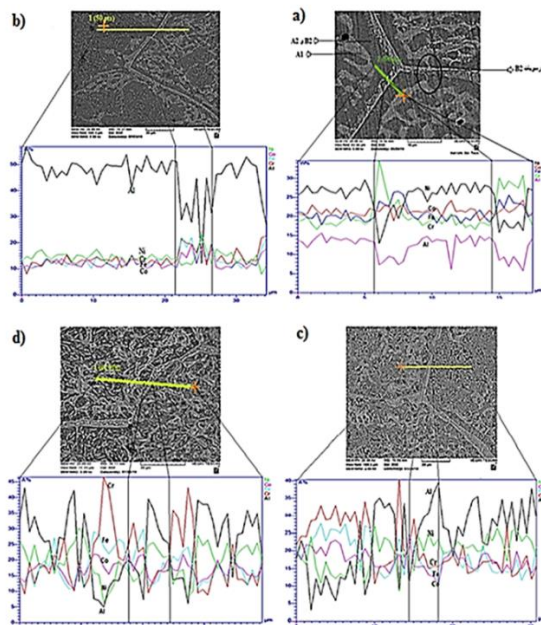


Figure 5. Electron microscopic images of an AlCoCrFeNi entropy alloy overgrown after aging at temperatures of 700 to 1000°C (a-d, respectively) for 4 hours and cooled in water with a linear analysis of the distribution of their elements

In Figure 5(c), Al, Co, Cr, Fe and Ni elements are scattered throughout the microstructure. At the grain boundaries, Al and Ni have increased and Co, Cr and Fe have slightly decreased. Therefore, it can be concluded that with increasing aging temperature to 900°C, B2 has penetrated more into the boundaries, which is also observed in Figure 5(c).

As can be seen in Figure 5(d), at 1000°C, B2 phase is scattered through the boundaries, and in fingerprint phases. So, it can be said that phase B2 has penetrated into phase A1. B2 appear to get more elongated at 1000°C. The results of linear element analysis also show that all the elements are mixed together and it is difficult to separate them from each other.

Figure 6 shows the variation of hardness during ageing from 700 to 1000°C. after ageing, hardness increase until 800°C and again started to decrease until 1000°C.

linear scan analysis indicate that needle like phases are rich of Al and Ni. Needle like BCC and B2 are enrich of Al and Ni, respectively. The different behavior between Al and Ni is related to the diffusion coefficient of the elements. Al has superior diffusion coefficient compared to Ni [18], so, Al has diffused to the grain boundaries more.

The fast increase in hardness is due to an increase in BCC to FCC ratio and possibly the precipitation of σ . At 800°C, the hardness increased to 543 HV, which is due to the formation of needle like B2 phase and σ . At 900 and 1000°C, the hardness decreased to 454 and 385 HV, respectively, which is due to the gradual dissolution of phase σ . The σ phase is a hard and brittle phase with FeCr composition. This phase precipitates with slow diffusion mechanism at 700°C cause to increases hardness. This phase tends to dissolve as the temperature rises and dissolves completely at 1250°C [18-21].

The flow curve of hot compression test of the alloy is shown in Figure 7. The results showed that the alloy at 800, 900, 1000 and 1100°C has a yield strength of 306, 179, 91 and 50 MPa, respectively. At the beginning of the deformation, with increasing strain, the stress increases linearly until it reaches the yield point. Then, as the strain increases, the density of dislocations increases and hardening occurs. As the deformation continues, the heat energy during the hot work leads to a smooth dynamic recovery mechanism. With increasing

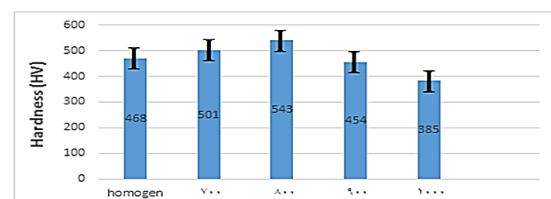


Figure 6. Chart of hardness changes of homogenized and aged samples at temperatures of 700, 800, 900 and 1000°C for 2, 4, 6, 8 hours and cooled in water

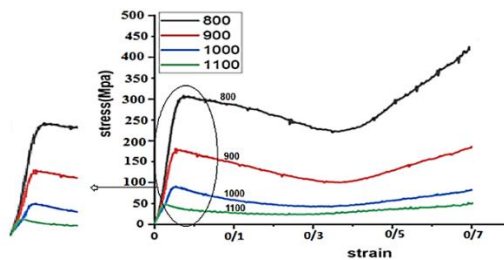


Figure 7. True compressive stress-strain diagram of alloy under different heat treatment conditions

temperature, the hardness gradually decreases and reaches to a stable state. In the early stages of deformation, the occurrence of recovery is not able to fully cope with the hardness and therefore the hardness increases. As the strain increases, the slope of the stress-strain curve increases and the stiffness decreases significantly. This process continues to reach the maximum point. In this case, the density of the dislocations is increased so the recovery overcomes the stiffness and the flow stress decreases to reach the steady state. In this case, the balance between the rate of dislocations formation and elimination occurred and the tension remains constant.

4. CONCLUSIONS

1. The results of XRD phase analysis show that the high entropy alloy of AlCoCrFeNi has 3 phases FCC (A1), BCC (A2, B2) and σ . The ratio of BCC and FCC phases in the as cast structure is approximately equal. After aging at 700°C, 800°C and 1000°C the ratio of BCC to FCC phase is about 2.5, 1.7 and 2.2, respectively
2. The peak at 500°C in the DSC thermal analysis results is attributed to the precipitation of phase σ from the BCC phase, which is re-dissolved at a temperature of about 1000°C.
3. After aging at 700°C, fingerprint phases tend to join the boundaries, and deposits of the B2 phase form within the boundaries.
4. At 800°C, fingerprint phases are mixed with borders and forms the needle-shaped sediments in phase B2 and also σ .
5. As a result of microstructure changes during aging, the hardness of the alloy changes from 467Hv in the as cast structure to 501, 543, 454 and 385Hv at aging temperature of 700, 800, 900 and 1000°C respectively.
6. The results of hot compression test showed that the alloy at 800, 900, 1000 and 1100°C has a yield strength of 306, 179, 91 and 50 MPa, respectively.

5. REFERENCES

1. Niu, P., Li, R., Yuan, T., Zhu, S., Chen, C., Wang, M. and Huang, L., "Microstructures and properties of an equimolar alccocrfeni

- high entropy alloy printed by selective laser melting", *Intermetallics*, Vol. 104, (2019), 24-32. doi: 10.1016/j.intermet.2018.10.018.
2. Vyas, A., Menghani, J. and Natu, H., "Metallurgical and mechanical properties of laser clad AlCoCrFeNi-10 high entropy alloy coating", *International Journal of Engineering, Transactions A: Basics*, Vol. 33, No. 7, (2020), 1397-1402. doi: 10.5829/IJE.2020.33.07A.27.
3. Murty, B.S., Yeh, J.-W., Ranganathan, S. and Bhattacharjee, P., "High-entropy alloys, Elsevier, (2019).
4. Shi, Y., Collins, L., Feng, R., Zhang, C., Balke, N., Liaw, P.K. and Yang, B., "Homogenization of AlCoCrFeNi high-entropy alloys with improved corrosion resistance", *Corrosion Science*, Vol. 133, (2018), 120-131. doi: 10.1016/j.corsci.2018.01.030.
5. Wei, L., Liu, X., Gao, Y., Peng, X., Hu, N. and Chen, M., "Phase, microstructure and mechanical properties evaluation of AlCoCrFeNi high-entropy alloy during mechanical ball milling", *Intermetallics*, Vol. 138, (2021), 107310. doi: 10.1016/j.intermet.2021.107310.
6. Zhao, C., Li, J., Liu, Y., Ma, X., Jin, Y., Wang, W.Y., Kou, H. and Wang, J., "Optimizing mechanical and magnetic properties of AlCoCrFeNi high-entropy alloy via fcc to bcc phase transformation", *Journal of Materials Science & Technology*, Vol. 86, (2021), 117-126. doi: 10.1016/j.jmst.2020.12.080.
7. Munitz, A., Salhov, S., Hayun, S. and Frage, N., "Heat treatment impacts the micro-structure and mechanical properties of AlCoCrFeNi high entropy alloy", *Journal of Alloys and Compounds*, Vol. 683, (2016), 221-230. doi: 10.1016/j.jallcom.2016.05.034.
8. Wang, R., Zhang, K., Davies, C. and Wu, X., "Evolution of microstructure, mechanical and corrosion properties of AlCoCrFeNi high-entropy alloy prepared by direct laser fabrication", *Journal of Alloys and Compounds*, Vol. 694, (2017), 971-981. doi: 10.1016/j.jallcom.2016.10.138.
9. Butler, T.M. and Weaver, M.L., "Investigation of the phase stabilities in AlNiCoCrFe high entropy alloys", *Journal of Alloys and Compounds*, Vol. 691, (2017), 119-129. doi: 10.1016/j.jallcom.2016.08.121.
10. Wang, W.-R., Wang, W.-L. and Yeh, J.-W., "Phases, microstructure and mechanical properties of AlCoCrFeNi high-entropy alloys at elevated temperatures", *Journal of Alloys and Compounds*, Vol. 589, (2014), 143-152. doi: 10.1016/j.jallcom.2013.11.084.
11. Toocharoen, S., Kaewkuekool, S. and Peasura, P., "The rejuvenation heat treatment of nickel base superalloy grade GTD111 after long-term service via the Taguchi method for optimization", *International Journal of Engineering, Transactions A: Basics*, Vol. 34, No. 4, (2021), 956-965. doi: 10.5829/IJE.2021.34.04A.22.
12. Azadi, M., Iziy, M., Marbout, A. and Rizi, M., "Investigation of the heat treatment effect on microstructures and phases of Inconel 713C superalloy", *International Journal of Engineering, Transactions A: Basics*, Vol. 30, No. 10, (2017), 1538-1544. doi: 10.5829/ije.2017.30.10a.15.
13. Gwalani, B., Soni, V., Lee, M., Mantri, S., Ren, Y. and Banerjee, R., "Optimizing the coupled effects of Hall-Petch and precipitation strengthening in an Al0.3CoCrFeNi high entropy alloy", *Materials & Design*, Vol. 121, (2017), 254-260. doi: 10.1016/j.matdes.2017.02.072.
14. Kuwabara, K., Shiratori, H., Fujieda, T., Yamanaka, K., Koizumi, Y. and Chiba, A., "Mechanical and corrosion properties of AlCoCrFeNi high-entropy alloy fabricated with selective electron beam melting", *Additive Manufacturing*, Vol. 23, (2018), 264-271. doi: 10.1016/j.addma.2018.06.006.
15. Tang, Z., Senkov, O.N., Parish, C.M., Zhang, C., Zhang, F., Santodonato, L.J., Wang, G., Zhao, G., Yang, F. and Liaw, P.K.,

- "Tensile ductility of an alcoxcrfeni multi-phase high-entropy alloy through hot isostatic pressing (HIP) and homogenization", *Materials Science and Engineering: A*, Vol. 647, (2015), 229-240. doi: 10.1016/j.msea.2015.08.078.
16. Zhao, C., Li, J., Liu, Y., Wang, W.Y., Kou, H., Beaugnon, E. and Wang, J., "Tailoring mechanical and magnetic properties of alcoxcrfeni high-entropy alloy via phase transformation", *Journal of Materials Science & Technology*, Vol. 73, (2021), 83-90. doi: 10.1016/j.jmst.2020.08.063.
 17. Strumza, E. and Hayun, S., "Comprehensive study of phase transitions in equiatomic alcoxcrfeni high-entropy alloy", *Journal of Alloys and Compounds*, Vol. 856, (2021), 158220. doi: 10.1016/j.jallcom.2020.158220.
 18. Vaidya, M., Trubel, S., Murty, B., Wilde, G. and Divinski, S.V., "Ni tracer diffusion in coxcrfeni and coxcrfemni high entropy alloys", *Journal of Alloys and Compounds*, Vol. 688, (2016), 994-1001. doi: 10.1016/j.jallcom.2016.07.239.
 19. Shivam, V., Basu, J., Pandey, V.K., Shadangi, Y. and Mukhopadhyay, N., "Alloying behaviour, thermal stability and phase evolution in quinary alcoxcrfeni high entropy alloy", *Advanced Powder Technology*, Vol. 29, No. 9, (2018), 2221-2230. doi: 10.1016/j.appt.2018.06.006.
 20. Joseph, J., Hodgson, P., Jarvis, T., Wu, X., Stanford, N. and Fabijanic, D.M., "Effect of hot isostatic pressing on the microstructure and mechanical properties of additive manufactured alcoxcrfeni high entropy alloys", *Materials Science and Engineering: A*, Vol. 733, (2018), 59-70. doi: 10.1016/j.msea.2018.07.036.
 21. Uporov, S., Bykov, V., Pryanichnikov, S., Shubin, A. and Uporova, N., "Effect of synthesis route on structure and properties of alcoxcrfeni high-entropy alloy", *Intermetallics*, Vol. 83, (2017), 1-8. doi: 10.1016/j.intermet.2016.12.003.

Persian Abstract

چکیده

در این پژوهش، اثر دما و زمان پیرسازی بر ریزساختار، سختی و استحکام فشاری آلیاژ آنتروپی بالای $\text{Al}_{0.7}\text{CoCrFeNi}$ مورد بررسی قرار گرفته است. آلیاژ به روش ذوب القایی تحت خلأ تولید و در دمای 1250°C به مدت ۲ ساعت همگن سازی شده است. سپس در دمای $700-1000^\circ\text{C}$ تحت عملیات پیرسازی قرار گرفته است. ساختار ریختگی به صورت دندریتی و شامل فازهای $\text{FCC}(\text{A}_1)$ و $\text{BCC}(\text{A}_2, \text{B}_2)$ با سختی 497 ویکرز است. پس از پیرسازی در دمای 700°C ، فاز B_2 رسوب کرده و نسبت فازهای BCC به FCC که در حالت ریختگی تقریباً برابر یک است، زیاد می‌شود. در 800°C ، فاز مخرب و سخت σ تشکیل شده و سختی به 543 ویکرز رسیده و نسبت $(\text{A}_2+\text{B}_2)/\text{A}_1$ کاهش می‌یابد. در 1000°C ، این نسبت، میزان σ و سختی تا 385 ویکرز کاهش می‌یابد. نتایج آزمایش فشار گرم نشان داد که آلیاژ دارای استحکام 306 ، 179 ، 91 و 50MPa به ترتیب در دماهای 800 ، 900 ، 1000 و 1100°C است.



Numerical Modeling of Sediment-flow around Obstacle Inspired by Marine Sponges: Considering Body Configurations

M. Hashempour, M. Kolahdoozan*

Department of Civil and Environmental Engineering, Amirkabir University of Technology, Tehran, Iran

PAPER INFO

Paper history:

Received 19 December 2022

Received in revised form 27 March 2023

Accepted 31 March 2023

Keywords:

Synthetic Sponge

Sediment Concentration

Fluid Hydrodynamics

OpenFOAM

Marine Environment

ABSTRACT

Coral reefs are exposed to extinction due to the sediment blocking through coral colonies. In this condition, there is no practical solution that originates from nature. Among all aquatic animals, marine tubular sponges have marvelous mechanisms. These natural creatures can inspire the design of a device for managing sediment-flow hydrodynamics. They suck flow from body perforation and pump water and undigested materials from the top outlet. Therefore, coinciding with receiving nutrients, the flow becomes circulated. This may help the momentum transfer through the coral colonies. In the current study, a synthetic sponge by motivating the tubular sponges was designed. Synthetic sponges' suction/pumping discharge was constant at 150 L/h. They have a body diameter of 8 and 15 cm and a height of 20 cm. The perforation area distribution changes to understand how it may influence sediment-flow hydrodynamics. The numerical modeling based on Reynolds Averaged Navier Stokes (RANS) equations and image processing technique (surface LIC) were deployed to determine the vortical flow patterns. Results confirmed that choosing the best body perforation configuration and area distribution can generate the dipole vortex. In this condition, a tornado combines with dipole and erodes the sediments to $\approx 30\%$ near the bed. Moreover, the sediment concentration reduces to $\approx 20\%$ in the water column at $X/D = 1$. In this condition, it can be observed that the emergence of specific vorticities and recirculations develops the suspension of particles. Therefore, the synthetic sponge with precise design can be practical for enhancing the momentum transferring and preventing pollutant blockage among coral colonies.

doi: 10.5829/ije.2023.36.06c.05

NOMENCLATURE

NOMENCLATURE		Greek Symbols	
\vec{U}	Mixture velocity	ρ	Mixture density (kg/m^3)
p	Pressure	α_m	Volume fraction of the mixture
g	Gravity (m/s^2)	α_1	Volume fraction of the air
S^*	Strain rate tensor	α_2	Volume fraction of the water
k	Turbulent kinetic energy per unit mass	α_3	Volume fraction of the sediment
I	Kronecker delta	μ	Mixture dynamic viscosity
D	Sponge body diameter	κ_{α_m}	Surface curvature of mixture
J	Sponge suction/pumping discharge (L/h)	σ	Surface tension
\bar{C}_0	Mean sediment concentration	τ	Reynolds stress tensor

1. INTRODUCTION

Coral reefs are the primary alive ocean ecosystems. They mainly exist in shallow waters and near the coasts. In this regard, they are prone to sedimentation and pollutant

accumulation [1]. Human civilization operations, global warming, increasing water temperature, and wave height cause coral reefs to be exposed to extinction [2]. It is anticipated that 90% of coral reefs will be annihilated by 2040 [3].

*Corresponding Author Institutional Email: mklhdzan@aut.ac.ir
(M. Kolahdoozan)

The coral reefs' death causes the migration of fishes and other aquatic animals, and then they will disappear forever due to losing their hometown and food resources. In addition, the extinction of the coral reefs causes harm to the coastlines and human residences via significant wave heights [1]. Various studies have focused on determining how corals influence flow and sediment hydrodynamics. A solution is expected to be provided for saving the coral reefs by learning from nature. Today it is believed that the branched corals' density is responsible for saturation velocity [4]. They stir the flow and enhance the momentum exchange to over 400% [5]. The passive vortices are in charge of the water stir phenomenon. They vanished where the loosely branched corals were presented [6]. An increase in turbulence directly influences the sedimentation/suspension rates of particles rear of the coral patch [7]. The reduction of velocity around corals causes sedimentation to be increased [8].

The tubular corals (sponges) also have interesting effects on flow hydrodynamics. A group called *Euplectella aspergillum* has mazed-helical ridges on the outer surface. This fabulous shape is the inspiration for engineering and structural designs. It totally suppresses the shedding behavior of Von-Karman street and moderates the uplift force. This leads to enhancing the sponge stability and preventing erosion of bed materials [9]. Removing the outer ridges causes the increase of vibration in the wake street due to the shear of the Boundary Layer (BL) [10]. The sponges suck flow from the body perforation (Ostia) and pump the water and undigested materials from the top outlet (Osculum). This function helps them to clean their residence, circulate flow, and receive nutrients without movement [11]. It may be interesting for controlling the sedimentation, nevertheless, the authors did not find any project or research that focuses on sponge planting for controlling sedimentation.

The yellow tube sponge (*Aplysina fistularis*) has a perforated-tubular shape. When it is lower than 20 cm, it has one column. By growing and reaching over 20 cm, it proliferates [12]. Figure 1 shows the yellow tube sponge compared to the *Staghorn coral* and *Giant barrel sponge* [13].

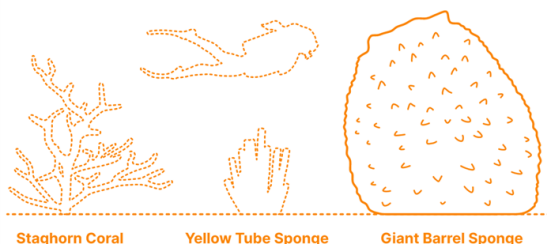


Figure 1. Yellow tube sponge versus Staghorn coral and Giant barrel sponge [13]

A singular tube of one cluster of yellow tube sponges has a 3-15 cm diameter. But a cluster diameter reaches up to 84 cm [14]. The body perforation has an average diameter of 270 μm [12, 15]. This sponge has various suction/pumping discharges within a day. The suction/pumping discharge varies with sponge size, pollutant/sediment concentration, water temperature, etc. [16, 17]. Figure 2, illustrates the yellow tube sponge dimensions [13, 14].

The innovation of the current study is inspiring the marine tubular sponges to design a new structure for enhancing the momentum transfer through the coral colonies. In this structure that will be called the *synthetic sponge* from now on, the physical shape and suction/pumping mechanism of natural tubular sponges were enthused. Numerical modeling was employed to investigate how the synthetic sponge can manage sediment-flow hydrodynamics and sediment concentration.

2. COMPUTATIONAL METHODS AND DETAILS

InterMixingFoam solver of OpenFOAM V.1812® was deployed for numerical modeling purposes. In continue, the details of the modeling, mesh generation, validation, and scenario preparation are presented.

2. 1. Basic Numerical Solution and Equations

The interMixingFoam solver is based on the Three-Fluid-Mixture (TFM) theory. Three phases (i.e., air, water, and sediment) are considered as fluids. The equations consist of phases concentrations and the relative velocity between water and sediment [18, 19].

$$\alpha_m = \alpha_2 + \alpha_3 \quad (1)$$

$$\alpha_1 = 1 - \alpha_m \quad (2)$$

where α_m , α_1 , α_2 , and α_3 are volume fractions of the mixture, air, water, and sediment, respectively. By using Reynolds Averaged Navier Stokes (RANS) equations, the governing equations of fluid flows (continuity and momentum) can be expressed as follows [20, 21]:

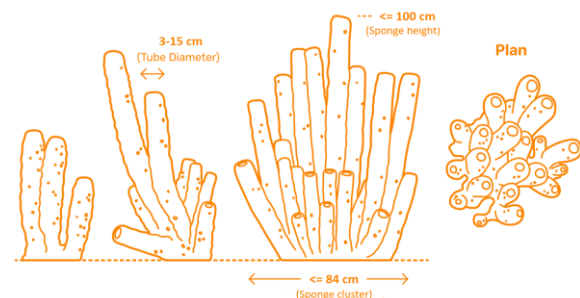


Figure 2. Yellow tube sponge dimensions [13, 14]

$$\nabla \cdot \bar{U} = 0 \tag{3}$$

$$\frac{\partial \rho \bar{U}}{\partial t} + \nabla \cdot (\rho \bar{U} \bar{U}) = \nabla \cdot (\mu \nabla U + \rho \tau) - \nabla p + \rho g + \sigma \kappa_{\alpha_m} \nabla \alpha_m \tag{4}$$

where \bar{U} is mixture velocity, p is pressure, ρ is mixture density, μ is mixture dynamic viscosity, g is gravitational acceleration, κ_{α_m} is surface curvature of the mixture, σ is surface tension [20], and τ is Reynolds stress tensor defined by the Boussinesq approximation as follows.

$$\tau = \frac{2}{\rho} \mu_t S^* - \frac{2}{3} k \delta \tag{5}$$

where μ_t is turbulent viscosity, S^* is strain rate tensor, k is turbulent kinetic energy per unit mass, and δ is Kronecker delta.

The two-equation of k- ω Shear Stress Transport (k- ω SSt) was deployed as a turbulence closure model. See the OpenFOAM manual for the details of the interMixingFOAM solver and k- ω SSt equations [22].

2. 2. Validation The Coleman [23] experiments were carried out for validation (Case No. 2). The 0.91 kg of sediment with a particle diameter of 105 mm was injected into a rectangular channel. The channel had $15 \times 0.356 \times 0.4$ m (L \times W \times H) dimensions. Figure 3 shows the accuracy of the validation of velocity and concentration. The RMSE of concentrations and longitudinal velocities were $4.45E-5$ and $0.0.069$, respectively. Correlation coefficients between measured and computed data of concentrations and longitudinal velocities were 0.99 and 0.96 respectively. Therefore, the validation is acceptable.

2. 3. Model Setup Some scenarios were defined to investigate the effects of a synthetic sponge on sediment-flow hydrodynamics and concentration. The further details are as follows.

2. 3. 1. Synthetic Sponge The synthetic sponge has a perforated cylindrical shape that uses suction and

pumping functions. The suction is done by body perforation, and the top outlet performs pumping. Figure 4 shows the synthetic sponge shape and mechanism versus the natural sponge. It is also worth to pay attention that the current study’s goal is not simulating a natural tubular sponge. The main goal is to understand how a structure inspired by a tubular sponge influences sediment-flow hydrodynamics. The synthetic sponge has a larger perforation diameter and significant suction/pumping discharge compared to the natural one.

2. 3. 2. Scenarios Five scenarios were designed to investigate the effects of synthetic sponges on sediment-flow hydrodynamics (Table 1). The perforation area distribution (the cumulative of the body pores area to the lateral area of the sponge) varies between 0.02-0.375. This range was chosen to facilitate the production of a synthetic sponge in the laboratory. In addition, since the body diameter of a single tube of the sponge has 0.03-0.15 m, the body diameter of the synthetic sponge (D) also was 0.08 and 0.15 m [25]. A natural sponge’s height, when a single tube exists and before the emergence of branches, is less than 0.2 m [25]. Thus the synthetic sponge height (h) in all scenarios was 0.2 m.

The suction/pumping discharge of natural sponge also varies between 0.018-2.1 L/h [25]. Nevertheless, due to practical limitations, the suction/pumping discharge of synthetic sponge (J) was kept constant and equal to 150 L/h. The mean sediment concentration (\bar{C}_0) and velocity (\bar{U}_0) also were 0.000325 and 0.54 m/s, respectively. They

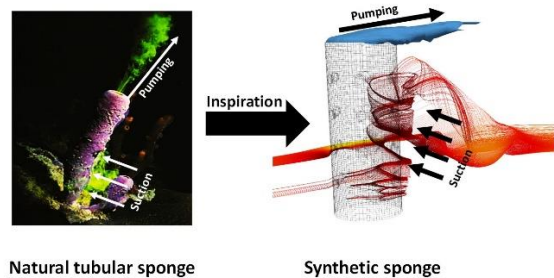


Figure 4. The natural tubular sponge [24] versus synthetic sponge

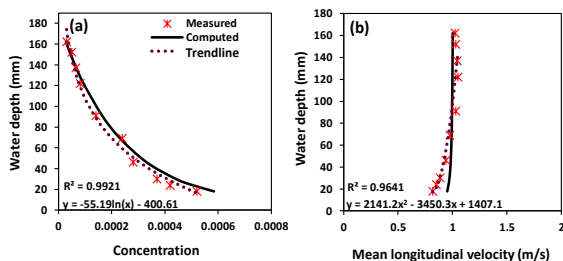


Figure 3. The accuracy of the numerical modeling: (a) concentration and (b) mean longitudinal velocity

TABLE 1. Scenarios of the numerical study

Scenario	Perforation area distribution	Perforation diameter (m)	Body diameter (m)	Pores vertical distance (m)
M1	0	0	0.08	0
M2	0.0375	0.010	0.08	0.04
M3	0.0843	0.015	0.08	0.057
M4	0.375	0.010	0.08	0.015
M5	0.02	0.010	0.15	0.052

were chosen based on Coleman's [23] experiments about dilute sediment transport and Palau Salvador et al. [26] experiments, respectively.

2.3.3. Mesh Generation The channel has $2.32 \times 0.356 \times 0.4$ m (L \times W \times H) dimensions. The sponge/rigid cylinder was located 0.32 m from upstream. The sponge was designed by CATIA V.5R21 software. The mesh generation also was prepared by SnappyHexMesh. The explicit surface and edge refinement levels were set to 1 and (0 2), and the unstructured boundary layer was set around the sponge. It is important to pay attention that the mesh sizes were selected based on the mesh independence analysis. Table 2 shows the mesh independence analysis. As can be observed, in the C3 scenario the percentage change is about 1 % and also has an acceptable size for capturing the vortices. Figure 5 shows the mesh and computational domain as well.

2.3.4. Boundary Conditions, Turbulence Model, and Solution Procedure The y^+ is the dimensionless quantity for the distance from the wall up to the center of the first grid cell. It is necessary to be checked to ensure the correct modeling of the flow near the bed. When it comes to the near-wall treatment, three options exist:

1. use wall function $\rightarrow 30 < y^+ < 300$
2. insensitive wall functions $\rightarrow 1 < y^+ < 300$
3. resolve the boundary layer $\rightarrow y^+ < 6$

The use of wall functions allows using coarser grids [27]. In the current study, to prevent the computational cost and ensure the correct flow conditions, OpenFOAM special wall function was deployed. The y^+ parameter computes by the following equation [28]:

$$y^+ = \frac{y \cdot u_\tau}{\nu} \quad (6)$$

where u_τ is the friction velocity, y is absolute distance from the wall, and ν is kinematic viscosity. The y^+ in the current study was between 30-200. Therefore, the OpenFOAM wall function provides desired accuracy. The velocity boundary conditions are defined in Table 3.

A K- ω SSt was used as a turbulence closure model. This model shows higher accuracy in detecting the flow separation downstream. k and ω coefficients were set to 0.11 and 0.85, respectively. The maximum CFL number, deltaT, and run-time also were 0.5, 0.001, and 80 seconds, respectively.

3. RESULTS AND DISCUSSION

In the current study, the Surface Line Integral Convolution (SurfaceLIC) was coupled with OpenFOAM. The SurfaceLIC is an image processing technique. It visualizes vector fields through the combination of noises and streaking (by black lines). However, additional image optimization is necessary to achieve the high accuracy of re-circulation zones [29]. In the current study, both LIC and color were used to enhance the contrast. Anti-aliasing (AA) was performed to prevent pixelation. A uniform noise texture was applied on flow sections to visualize the streaks of velocity vectors better. The noise texture and grain size were 128 and 2, respectively.

3.1. The Surface Line Integral Convolution at $Z/h=0.25$

Based on Figure 6, downstream of the rigid

TABLE 2. Mesh sensitivity analysis

Case No.	Mesh size (x \times y \times z) m	$ \bar{U} $ (at $X/D = 1$)	$\left \frac{ \bar{U}_{casei+1} - \bar{U}_{casei} }{ \bar{U}_{casei} } \right \times 100$
C0	0.013 \times 0.02 \times 0.016	0.2427	-
C1	0.026 \times 0.02 \times 0.008	0.2494	2.76
C2	0.026 \times 0.01 \times 0.016	0.2473	0.84
C3	0.013 \times 0.01 \times 0.008	0.2502	1.17
C4	0.0065 \times 0.01 \times 0.004	0.2809	12.25
C5	0.013 \times 0.005 \times 0.004	0.2980	6.07
C6	0.0065 \times 0.005 \times 0.008	0.2557	14.19

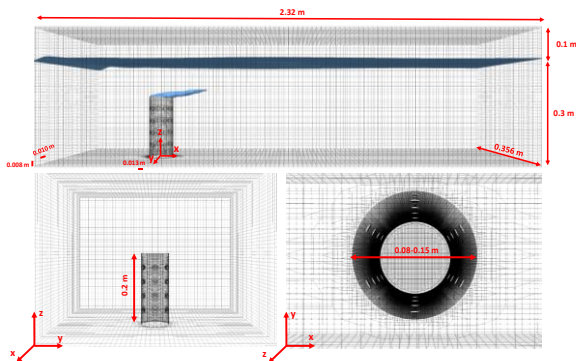


Figure 5. Computational domain and mesh structures

TABLE 3. Velocity boundary conditions

Boundary	Velocity boundary condition
Channel inlet	fixedValue
Channel outlet	zeroGradient
Channel bottom	no-slip
Sponge/Cylinder wall	no-slip
Top of the channel	pressureInletOutletVelocity
Sponge perforation	flowRateInletVelocity (Discharge)
Sponge outlet	flowRateOutletVelocity (Velocity)

cylinder (M1 scenario), small re-circulation bubbles emerge. It is worth noting that the re-circulation bubble (re-circulation zone) consists of a stationary vortex, i.e., the vortex does not move. In this zone, the air core does not exist and the streamwise velocity component is negative. The bubbles are the erosive zones. The size of bubbles is less than when a rigid cylinder exposed the pure current. The presence of sediment causes energy extraction from the water. So the velocity and consequently, the size of the re-circulation bubble reduces. Another research also observed this for dense and dilute sediment-concentrated fluids [30]. The S marks in Figure 6, indicate the location of the bubbles' foci [31]. Foci were detected attached to the cylinder toe at $X/D \approx 0.51$.

By replacing the rigid cylinder with the synthetic sponge, it was observed that whenever the perforation area and pores' vertical distance are small (M2 scenario), the streamlines do not separate in downstream. In this regard, the re-circulation bubble vanishes. In the M3 scenario, an asymmetric wake emerges by reducing the suction velocity. A primary wake bubble with a foci location of ($X/D \approx 0.8, Y/D \approx -0.98$) was detected near the sponge toe. The emergence of the primary bubble is due to the attaching of the shear layer rolling to the sponge's rear surface [31].

In the M4 scenario, a steady pattern generates when the perforation area distribution reaches 0.375. In this condition, two symmetric and counter-rotating re-circulation bubbles emerge downstream with core coordinates of ($X/D \approx 1.1, Y/D \approx 1.1$) and ($X/D \approx 1.1, Y/D \approx -0.98$). The generation of two recirculation bubbles can be due to the dipole generation, less sediment concentration in the water column, and flow suction by

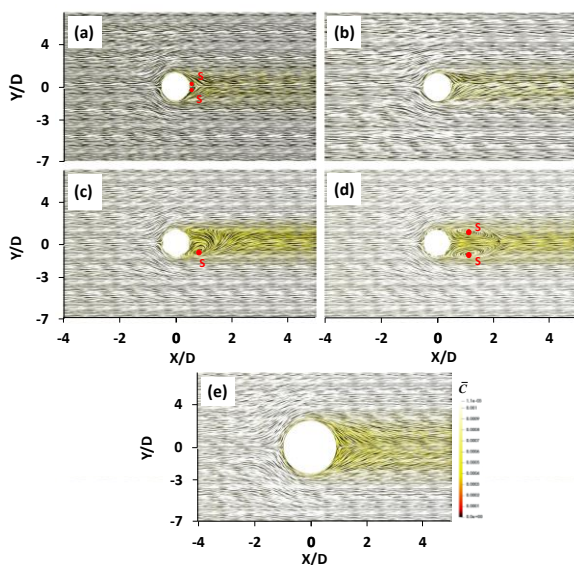


Figure 6. SurfaceLIC at $Z/h = 0.25$ for: (a) M1, (b) M2, (c) M3, (d) M4, and (e) M5

body perforation. In the M5 scenario, the conditions are nearly the same as in M2. But the sediment concentration downstream is much higher than in the M2 scenario. The reason will be discussed by vortical detection in future sections.

3. 2. The Surface Line Integral Convolution at $Y/D = 0$

For detecting the vertical concentration and flow hydrodynamics, image processing was deployed at a vertical surface in $Y/D = 0$ (Figure 7) downstream, a *quadrupole* vortex emerges. Its re-circulation core is at ($X/D = 0.6, Z/h = 0.64$). Since the sediment concentration near the bed is high, the up-wash and down-wash interact at a higher elevation. So a stagnation point (SP) emerges at ($X/D = 0.9, Z/h \approx 0.3$). Meanwhile, for M2 and M3, the suction makes the *quadrupole* unstable and turns it into a *six-vortices* type. The *six-vortices* type was detected recently [32, 33]. It is a transitional condition between *dipole* and *quadrupole*. The *six-vortices* pattern can be identified by increasing the pores' vertical distance and diameter (Figure 7(c)). Nevertheless, a stagnation point occurs at ($X/D = 0.7, Z/h = 0.47$).

In the M4 scenario, the increase in a perforation area distribution reduces the concentration downstream of the sponge. Consequently, the downwash interacts upwash near the bed (Figure 7(d)).

Therefore, the six-vortices or quadrupole vanishes, and the dipole emerges. A dipole has the potential to generate a tornado (spiral) adjacent to the sponge. The suction via pores disturbs the downward flow pattern and consequently, a tornado occurs. In this condition, coinciding with the suction mechanism, a spiral pulls the sediment out from the bed. It transfers particles to higher water elevations, where the flow velocity is much more significant. Figure 8 is the 3D- modeling of streamlines which displays the *tornado* generation by sponge.

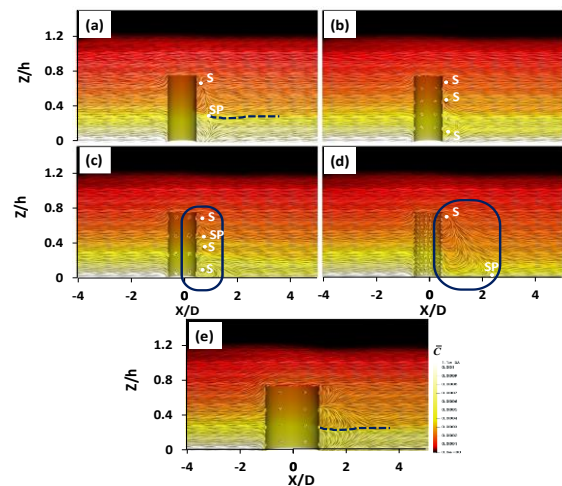


Figure 7. SurfaceLIC at $Y/D = 0$ for: (a) M1, (b) M2, (c) M3, (d) M4, and (e) M5

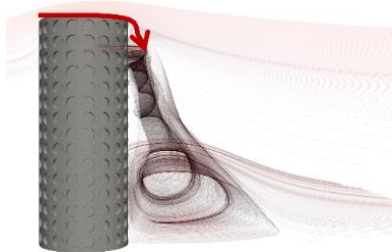


Figure 8. Tornado (Spiral) generation adjacent to the sponge in the M4 scenario

A similar tornado was observed downstream of a finite-height cylinder with $H/D = 1.12$ in low Reynolds number ($Re_D = 16000$) [32]. Nevertheless, the origin of the tornado is near the trailing edge of the synthetic sponge. Whereas, the origin of the tornado explained by Kirkil and Constantinescu [32] is near the bed. The difference in location is due to the cylinders' aspect ratios (AR) and relative boundary layer thickness (δ/h). The visualizations has been found by Zhang et al. [34]. However, due to using RANS modeling, the tornado's dimension can not accurately be captured.

Figure 9 confirms that at $X/D = 1$, the M4 scenario causes $\approx 20\%$ reduction in sediment concentration compared to the M1 scenario (Figure 9(a)). In addition, it causes $\approx 11\%$ and $\approx 30\%$ sediment erosion compared to the rigid cylinder, at $Z/h = 0.6$ and $Z/h = 0.2$, respectively (Figures 9(b) and 9(c)). It is worth pointing out that herein *erosion* and *sedimentation* means sediment concentration decrease and increase, respectively.

In scenario M5, the suction effects become weak by reducing the pore area distribution to the lowest value among all scenarios. Therefore unique vortical patterns were not captured by surfaceLIC. As a result, a 2% increase in sediment concentration at $X/D = 1$ can be observed. Near the bed ($Z/h = 0.2$) and at $Z/h = 0.6$, the sediment concentration also is higher than when a rigid cylinder presents ($\approx +6\%$). Thus, it can be concluded that designing the perforation configuration and sponge body size is essential for managing the vortical flow and preventing sedimentation through the channel.

3. 3. The Surface Line Integral Convolution at $X/D = 1$

For understanding the sedimentation/erosion patterns, the surfaceLIC was deployed at $X/D = 1$. through a vertical surface (Figure 10).

In the M1 scenario, two clockwise and counter-clockwise patterns were detected. This was similarly detected in M2-M5 scenarios. They are known as Counter Rotating Vortex Pairs (CRVP). The CRVP generation makes an eroded ridge in the $Y/D = 0$. So the circulation pattern causes lateral sedimentation in the channel.

Besides, the extension of the horse-shoe vortex (EHV) legs can be identified on both sides of the rigid

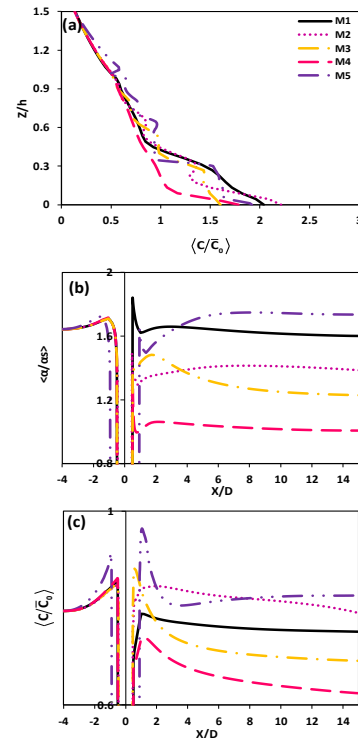


Figure 9. Concentration distribution at (a) $X/D = 1$, (b) $Z/h = 0.2$, and (c) $Z/h = 0.6$.

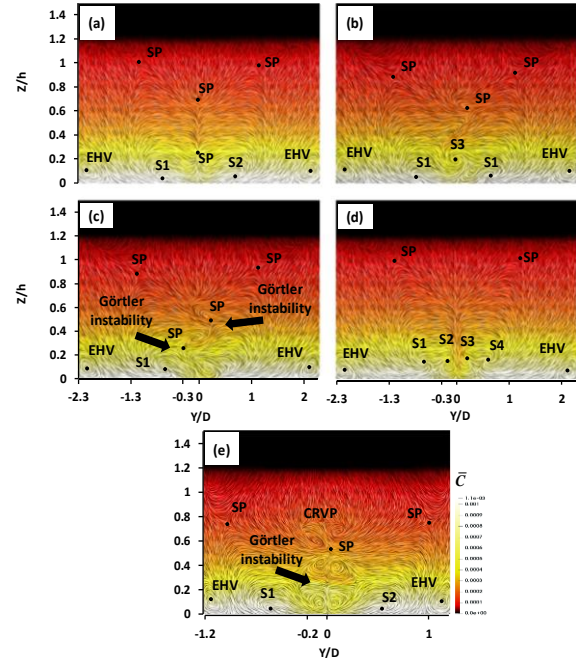


Figure 10. SurfaceLIC at $X/D = 1$ for: (a) M1, (b) M2, (c) M3, (d) M4, and (e) M5

cylinder/sponges. They are not precisely the downstream horse-shoe vortex or upstream vortices [35]. The horse-shoe vortex that continues downstream from the cylinder

helps sediment deposition in outer zones. In Figure 10(c), CRVP and similar mushroom vortex¹ can be detected. A mushroom vortex is often realized behind concave walls or along streamlines with a curvature form [36]. By reducing the perforation area distribution and pores' vertical distance (M5 scenario), the Görtler instability changes into the large dual mushrooms. The CRVP and the two-mushrooms generation disturb the sediment concentration and cause the suspended sediment through the water column. So, the results of Figure 9 were achieved.

It is also essential to pay attention that, based on Xu et al. [37], the pressure increase is the reason for changing the Görtler instability to completely round mushrooms. Nevertheless, Based on Figure 11, the place of perforations influences the fluid streamlines and the vortices generation. So, it is necessary to design the synthetic sponge's perforation configuration accurately to reach the best flow management.

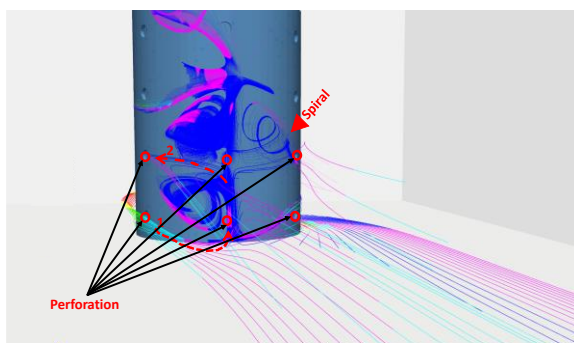


Figure 11. Streamline situations in the M5 scenario

4. CONCLUSION

In the current study, the marine tubular sponges were inspired to design a synthetic sponge. The synthetic sponge has a perforated tubular structure that sucks flow from the body perforation and pumps it from the top mouth. The numerical modeling based on RANS equations and image processing techniques were deployed to understand how synthetic sponges can influence sediment-flow hydrodynamics. Results confirmed that the perforation diameter, perforation area distribution, and perforation configuration influence the re-circulation bubble and vortices generation downstream of the sponge. The rigid cylinder causes quadrupole generation; meanwhile, sponges make it unstable. In this condition, regarding the sponge's characteristics *six-vortices* and a *dipole* generate.

The dipole and large tornado generation downstream of the sponge in the M4 scenario, reduce the sediment concentration to $\approx 20\%$ in the water column. The CRVP

production causes sedimentation in laterals and makes an eroded ridge in the middle of the channel.

Overall, it can be concluded that designing a device based on tubular sponges can influence sediment concentration through the water column. It can enhance sediment transport and momentum exchange. Therefore, the present design is anticipated to be practical for enhancing pollutant, sediment, and food transport through the coral colonies.

5. REFERENCES

1. Woodroffe, C.D. and Webster, J.M., "Coral reefs and sea-level change", *Marine Geology*, Vol. 352, (2014), 248-267. <https://doi.org/10.1016/j.margeo.2013.12.006>.
2. Fabricius, K.E., "Effects of terrestrial runoff on the ecology of corals and coral reefs: Review and synthesis", *Marine Pollution Bulletin*, Vol. 50, No. 2, (2005), 125-146. <https://doi.org/10.1016/j.marpolbul.2004.11.028>.
3. Nace, T. *Nearly all coral reefs will disappear over the next 20 years, scientists say.* 2020; Available from: <https://www.forbes.com/sites/trevornace/2020/02/24/70-90-percent-of-coral-reefs-will-disappear-over-the-next-20-years-scientists-say/?sh=5259cd1d7d87>.
4. Jr, J. and Graus, R., "Water flow and hydromechanical adaptations of branched reef corals", *Bulletin of Marine Science*, Vol. 25, (1975), 112-125.
5. Hossain, M.M. and Staples, A.E., "Passive vortical flows enhance mass transport in the interior of a coral colony", *Physics of Fluids*, Vol. 31, No. 6, (2019), 061701. DOI: 10.1063/1.5094076.
6. Hossain, M.M. and Staples, A.E., "Mass transport and turbulent statistics within two branching coral colonies", *Fluids*, Vol. 5, No. 3, (2020), 153. <https://doi.org/10.3390/fluids5030153>.
7. Folkard, A.M., "Hydrodynamics of model *Posidonia oceanica* patches in shallow water", *Limnology and Oceanography*, Vol. 50, No. 5, (2005), 1592-1600. <https://doi.org/10.4319/lo.2005.50.5.1592>.
8. Bartzke, G., Siemann, L., Büssing, R., Nardone, P., Koll, K., Hebbeln, D. and Huhn, K., "Investigating the prevailing hydrodynamics around a cold-water coral colony using a physical and a numerical approach", *Frontiers in Marine Science*, Vol. 8, (2021). DOI: 10.3389/fmars.2021.663304.
9. Fernandes, M.C., Saadat, M., Cauchy-Dubois, P., Inamura, C., Sirota, T., Milliron, G., Haj-Hariri, H., Bertoldi, K. and Weaver, J.C., "Mechanical and hydrodynamic analyses of helical strake-like ridges in a glass sponge", *Journal of The Royal Society Interface*, Vol. 18, No. 182, (2021), 20210559. <https://doi.org/10.1098/rsif.2021.0559>.
10. Qun, L.K., Abu, A., Kato, N., Muhamad, P., Tan, L.K. and Kang, H.S., "Performance of two- and three-start helical strakes in suppressing the vortex-induced vibration of a low mass ratio flexible cylinder", *Ocean Engineering*, Vol. 166, (2018), 253-261. <https://doi.org/10.1016/j.oceaneng.2018.08.008>.
11. Region, P. and Leys, S.P., "Effects of sediment on glass sponges (porifera, hexactinellida) and projected effects on glass sponge reefs. (2013). *DFO Canadian Science Advisory Secretariat Research Document, 74*.
12. Rickborn, A.J., "The spatial ecology of a coral reef sponge, *Aplysina fistularis*." (2014). Ph.D. Dissertations, Boston University

¹ secondary Görtler instability

13. Maddock, B. *Yellow tube sponge*. 2021; Available from: <https://www.dimensions.com/>.
14. Rickborn, A.J., "The spatial ecology of a coral reef sponge, *Aplysina fistularis*", Arizona State University, school of arts and sciences, Boston University, MA, (2010).
15. Machalowski, T., Rusak, A., Wiatrak, B., Haczkiwicz-Leśniak, K., Popiel, A., Jaroszewicz, J., Żak, A., Podhorska-Okołów, M. and Jesionowski, T., "Naturally formed chitinous skeleton isolated from the marine demosponge *Aplysina fistularis* as a 3d scaffold for tissue engineering", *Materials*, Vol. 14, No. 11, (2021), 2992. <https://doi.org/10.1016/j.carbpol.2021.118750>.
16. Morganti, T.M., Ribes, M., Yahel, G. and Coma, R., "Size is the major determinant of pumping rates in marine sponges", *Frontiers in Physiology*, Vol. 10, (2019), 1474-1474. DOI: 10.3389/fphys.2019.01474.
17. Strehlow, B., Jorgensen, D., Webster, N., Pineda, M.C. and Duckworth, A., "Using a thermistor flowmeter with attached video camera for monitoring sponge excurrent speed and oscular behaviour", *PeerJournal*, Vol. 4, (2016). DOI: 10.7717/peerj.2761.
18. Ebtahaj, I., Azimi, H. and Bonakdari, H., "Numerical analysis of sediment transport in sewer pipe", *International Journal of Engineering, Transactions B: Applications*, Vol. 28, No. 11, (2015), 1564-1570. DOI:10.5829/idosi.ije.2015.28.11b.03.
19. Jafarmadar, s., "The effects of pressure difference in nozzle's two phase flow on the quality of exhaust mixture", *International Journal of Engineering, Transactions B: Applications*, Vol. 26, No. 5, (2013), 553-562. DOI: 10.5829/idosi.ije.2013.26.05b.12.
20. Rodríguez-Ocampo, P., Ring, M., Fontes, J., Alcerreca-Huerta, J., Mendoza, E. and Silva, R., "Cfd simulations of multiphase flows: Interaction of miscible liquids with different temperatures", *Water*, Vol. 12, (2020), 2581. DOI: 10.3390/w12092581.
21. Trimulyono, A., Chrismianto, D., Samuel, S. and Aslami, M.H., "Single-phase and two-phase smoothed particle hydrodynamics for sloshing in the low filling ratio of the prismatic tank", *International Journal of Engineering, Transactions B: Applications*, Vol. 34, No. 5, (2021), 1345-1351. DOI: 10.5829/ije.2021.34.05b.30.
22. Ltd., O. *Openfoam manual*. 2022; Available from: <https://www.openfoam.com/documentation/>.
23. Coleman, N., "Effects of Suspended Sediment on the Open-Channel Velocity Distribution", *Water Resources Research*, Vol. 22, No. 10, (1986) 1377-1384. <https://doi.org/10.1029/WR022i010p01377>
24. BIRD, J. *Sponges*. 2014; Available from: <https://www.youtube.com/watch?v=m8a0oNsDEx8>.
25. Hashempour, M. and Kolahdoozan, M., "Three-dimensional modeling of dilute sediment concentration around the synthetic sponge inspired by the tubular sponge mechanism", *Ocean Engineering*, Vol. 271, 113799. <https://doi.org/10.1016/j.oceaneng.2023.113799>
26. Palau-Salvador, G., Stoesser, T., Fröhlich, J., Kappler, M., Rodi, W., "Large Eddy Simulations and Experiments of Flow Around Finite-Height Cylinders", *Flow, Turbulence and Combustion*, Vol. 84, No. 2, (2009). DOI: 10.1007/s10494-009-9232-0
27. Introductory OpenFOAM® Course From 14th to 18th July, 2014. Wolf dynamics. University of Genoa, DICCA.
28. Jones, D., Chapuis, M., Liefvendahl, M., Norrison, D. and Widjaja, R., "Rans simulations using openfoam software., (2016).
29. Cabral, B. and Leedom, L.C., "Imaging vector fields using line integral convolution", in Proceedings of the 20th annual conference on Computer graphics and interactive techniques, Anaheim, Association for Computing Machinery., (1993 of Conference), 263-270.
30. Selim, T., Hesham, M. and Elkiki, M., "Effect of sediment transport on flow characteristics in non-prismatic compound channels", *Ain Shams Engineering Journal*, Vol. 13, No. 6, (2022), 101771. <https://doi.org/10.1016/j.asej.2022.101771>.
31. Heidarinejad, G. and Delfani, S., "Direct numerical simulation of the wake flow behind a cylinder using random vortex method in medium to high reynolds numbers", *International Journal of Engineering*, Vol. 13, No. 3, (2000), 33-50.
32. Kirkil, G. and Constantinescu, G., "Effects of cylinder reynolds number on the turbulent horseshoe vortex system and near wake of a surface-mounted circular cylinder", *Physics of Fluids*, Vol. 27, No. 7, (2015), 075102. DOI: 10.1063/1.4923063.
33. Zhang, D., Cheng, L., An, H., Zhao, M., "Direct numerical simulation of flow around a surface-mounted finite square cylinder at low Reynolds numbers", *Physics of Fluids*, Vol. 29, (2017), 045101. DOI: 10.1063/1.4979479.
34. Summer, D., "Flow above the free end of a surface-mounted finite-height circular cylinder: A review", *Journal of Fluids and Structures*, Vol. 43, (2013), 41-63. <https://doi.org/10.1016/j.jfluidstructs.2013.08.007>.
35. Sau, A., Hwang, R., Sheu, T. and Yang, W., "Interaction of trailing vortices in the wake of a wall-mounted rectangular cylinder", *Physical Review E, Statistical, Nonlinear, and Soft Matter Physics*, Vol. 68, (2003), 056303. DOI: 10.1103/PhysRevE.68.056303.
36. Chen, Q., Yang, Z. and Wu, H., "Evolution of turbulent horseshoe vortex system in front of a vertical circular cylinder in open channel", *Water*, Vol. 11, No. 10, (2019), 2079. DOI:10.3390/w11102079.
37. Xu, D., Liu, J., Wu, X., "Görtler vortices and streaks in boundary layer subject to pressure gradient: excitation by free stream vortical disturbances, nonlinear evolution and secondary instability", *Journal of Fluid Mechanics*, Vol. 900, (2020). DOI: 10.1017/jfm.2020.438

Persian Abstract

چکیده

صخره‌های مرجانی به واسطه محبوس شدن ذرات رسوبی در بین کلونی‌های مرجانی مستعد انقراض هستند. در این شرایط راهکار عملی که خواستگاه آن از طبیعت باشد وجود ندارد. در میان تمام موجودات آبی، اسفنج‌های دریایی لوله‌ای سازوکار خارق‌العاده‌ای دارند که می‌توانند برای مدیریت هیدرودینامیک جریان‌های رسوبی الهام بخش باشند. آن‌ها آب را از حفرات بدنه مکش کرده و سپس همراه با مواد غذایی جذب نشده از دهانه بالایی خود به درون ستون آب پمپاژ می‌کنند. در این فرآیند، همزمان با جذب مواد غذایی چرخش جریان نیز صورت می‌گیرد. در مطالعه حاضر، یک اسفنج مصنوعی با الهام گرفتن از اسفنج‌های دریایی استوانه‌ای طراحی شد. اسفنج مصنوعی ارائه شده دارای قابلیت مکش/پمپاژ با دبی ۱۵۰ لیتر بر ساعت بوده است. این اسفنج دارای قطر بدنه ۸ و ۱۵ سانتیمتر و ارتفاع ۲۰ سانتیمتر است. همچنین سطح توزیع حفرات در سناریوهای مختلف تغییر داده شد تا اثرات آن بر هیدرودینامیک جریان رسوبی بررسی شود. مدلسازی عددی بر پایه معادلات متوسط‌گیری شده زمانی به همراه پردازش تصویر جهت شناسایی جریان‌های گردابه‌ای بکار گرفته شد. نتایج نشان داد که انتخاب اندازه بدنه و نحوه آرایش حفرات روی آن می‌تواند منجر به شکل‌گیری یک گردابه دو قطبی شود. در این شرایط، گردابه دو قطبی با یک گرداب همراه شده که می‌توانند غلظت رسوب را در نزدیک بستر تا ۳۰ درصد کاهش دهد. همچنین این اسفنج غلظت رسوب را در ستون آب و در مختصات $X/D=1$ به میزان ۲۰ درصد کاهش می‌دهد. در این شرایط، مشاهده گردید که تشکیل گردابه‌های منحصربفرد منجر به توسعه قابلیت تعلیق ذرات رسوبی می‌شود. بنابراین طراحی دقیق یک اسفنج مصنوعی می‌تواند برای بهبود انتقال مومنتوم و ممانعت از گرفتادن ذرات در میان کلونی‌های مرجانی موثر باشد.



Evaluating Finn-Byrne Model in Liquefaction Analysis of Quay Wall and Cantilevered Retaining Wall Models

A. Irajy*

Engineering faculty of Khoy, Urmia University of Technology, Urmia, Iran

PAPER INFO

Paper history:

Received 11 January 2023

Received in revised form 31 March 2023

Accepted 03 April 2023

Keywords:

Finn-Byrne Model

Liquefaction

Numerical Modeling

Quay Wall

Cantilevered Retaining Wall

ABSTRACT

Two centrifuge tests on a quay wall and a cantilevered retaining wall with saturated granular backfills were simulated using Finn-Byrne model. Capabilities of Finn-Byrne model in liquefaction analysis of the quay wall and the cantilevered retaining wall were evaluated. The quay wall model subjected to a horizontal acceleration time history and the cantilevered retaining wall model subjected to a horizontal and a vertical time history. The constitutive model is a linear elastic – perfectly plastic model. Hooke's elasticity and Mohr-coulomb criterion for the yield surface were assumed for the backfill material behavior. The excess porewater pressure generation, acceleration, wall lateral displacement, lateral earth pressures, deformation pattern, and backfill settlements were monitored and compared with centrifuge tests' results. The results showed that the adopted model is suitable for stability and displacement analyses of the quay walls and cantilevered retaining walls. However, a care should be taken when assessing the backfill settlements and dynamic earth pressure behind the wall stem. The rest of the results showed a good agreement with the centrifuge tests' results.

doi: 10.5829/ije.2023.36.06c.06

NOMENCLATURE

K	Bulk modulus (kPa)	K	Hydraulic conductivity (m/s)
G	Shear modulus	$\Delta\varepsilon_{vd}$	Incremental volume decrease
ϕ	Friction angle	ε_{vd}	Irrecoverable volume strain
C	Cohesion	γ	Cyclic shear strain
D_r	Relative density	C_1	Finn-Byrne model constant
γ	Unit weight (kN/m ³)	C_2	Finn-Byrne model constant
n	Porosity		

1. INTRODUCTION

Liquefaction is a catastrophic phenomenon in civil engineering that has become a major topic among engineers and researchers. Many researchers investigated the effect of liquefaction on geo-structures [1-3]. Some of them evaluated liquefaction potential [4-5] and showed how to mitigate that [6]. Predicting liquefaction via numerical models is a challenge and a complicated issue among geotechnical engineers. The Finn-Byrne model is a numerical model that introduces a formulation for porewater pressure generation in liquifiable soil media. This model was extensively employed for liquefaction analysis in different geo-

structures such as earth dams, ground sites, element tests, tunnels, and sheet pile walls for stability and displacement analyses in research and practice. The use of the Finn-Byrne model in liquefaction analyses of cantilevered retaining walls and quay walls is rare in the literature. This paper shows the capability and limitations of the Finn-Byrne model in liquefaction analysis of cantilevered retaining walls and quay walls. For this purpose, two centrifuge tests on a cantilevered retaining wall and a quay wall with saturated granular backfills were numerically simulated via the Finn-Byrne model and the results compared with those of the centrifuge tests. Quay walls and cantilevered retaining walls are two types of the geo-structures that are common in practice

*Corresponding Author Email: a.irajy@uut.ac.ir (A. Irajy)

and may be subjected to seismic loads while the backfill is saturated. Because the backfill is usually granular and likely saturated, the liquefaction and excess porewater pressure in the backfill and under the foundation could affect the walls significantly and produce undesirable displacements. Quay walls are constructed in wharves. This type of structures should sustain wave loads in stormy weather and ice loads in winter. They should have durability against salty water and cold and hot temperatures. Cantilevered retaining walls are constructed to support soil mass in slopes and abutments of the bridges, soil mass in wharves, and backfills supporting railroads and highways. The backfill may be saturated when groundwater table rises because of heavy rains or tidal effects near the shorelines.

Byrne [7] introduced the Finn-Byrne model. This model is a modified and simple model to predict porewater pressure generation via coupling cyclic shear strain and volume strain. Byrne [7] examined the model via numerical modeling of cyclic triaxial tests with strain control. The tests had been reported by NRC [8]. The predicted porewater pressures were greater than the measured porewater pressures. The model was then evaluated by modeling cyclic load controlled undrained tests [9] and assessing liquefaction resistance that was satisfactory.

Many researchers used the Finn-Byrne model to perform liquefaction analysis of geo-structures. Vargas et al. [10] performed liquefaction analysis of an irregular site ground using the Finn-Byrne model. Sudevan et al. [11] performed an uplift numerical analysis of an underground structure in a saturated loose sand under a dynamic load using the Finn-Byrne model and compared results with results of a centrifuge test and those of a numerical simulation using Wang model conducted by Chian et al. [12]. The developed excess porewater pressure at around of the structure using the Finn-Byrne model was in good agreement with the centrifuge test and was more accurate than numerical results via the Wang model. They observed that the Finn-Byrne model overestimated the amount of the structure uplift by 25% and the Wang model underestimated that by 10 %. Masini and Rampello [13] assessed the behavior of large homogeneous earth dams under strong seismic loads using the Finn-Byrne model. They showed that neglecting excess porewater pressures during seismic loading can underestimate the dam settlements significantly. Chou et al. [14] used Finn and UBCSAND models and calibrated them for simplified liquefaction analysis. They emphasized that the simple analytical procedures with associated numerical simulations are mostly used for liquefaction mitigation solutions. They concluded that the Finn model cannot model stress-strain and stress paths observed in the laboratory tests. However, it provided reasonable excess porewater pressures. The relationship between Cyclic Resistance

Ratio (CRR) predicted by the Finn model and the number of load cycles was reasonable. Banerjee et al. [15] performed numerical simulation of undrained cyclic triaxial tests using the Finn-Byrne and PM4SAND models. Both models predicted porewater pressure generation and cyclic stress paths well. However, the predicted stress-strain behavior was not good by both models. The Finn-Byrne model lacked in predicting the post-liquefaction behavior. Singh and Chatterjee [16] carried out liquefaction analysis of a cantilever sheet pile wall using the Finn-Byrne model. Various researchers conducted experimental methods to identify the failure modes and influential parameters on seismic response of quay walls [17-18] and some of them investigated only the seismic behavior [19-21]. Numerical seismic analysis and design of quay walls with saturated backfill is a challenge to engineers as it includes some of complexities such as proper prediction of excess porewater pressures and its effect on quay wall displacement and backfill deformation. Some researchers used advanced constitutive models to study seismic response of quay walls [22-24]. Madabhushi and Zeng [22] performed numerical analysis for centrifuge models on quay walls using advanced Pastor-Zienkiewicz Mark III model. They used fully coupled solid-fluid simulation. Yang et al. [23] performed numerical analysis of several centrifuge tests on quay wall under earthquake loads. They used a multiple-yield surface plasticity concept for the constitutive model. They conducted parametric study by changing permeability and soil relative density to assess amount of liquefied backfill and its effect on lateral spreading. They found that backfill permeability and dynamic properties are the parameters affecting the seismic behavior of quay walls significantly. Dakoulas and Gazetas [24] used advanced Pastor-Zienkiewicz elastoplastic constitutive model to simulate the seismic behavior of a quay wall from Rokko Island. They compared the numerical results with the results from Mononobe-Okabe theory. Abu Taiyab et al. [25] studied numerically and experimentally the effect of densification of loose sand around quay wall toe to mitigate damage to quay wall during earthquake loads. They used an elastoplastic multimechanism model called Hujoux model as the constitutive model. They found that the displacement of gravity quay wall is mainly because of shear strain occurred in the foundation. They also concluded that the densification of sand at the toe could prevent damage to quay wall considerably.

Wu [26] simulated the seismic behavior of San Fernando dam during the San Fernando Earthquake on 1971. A modified Martin-Finn-Seed model was used to predict the excess porewater pressure. Wu [26] predicted deformations and liquefied zones and compared them with the behavior observed in the Dam. The model underestimated vertical and horizontal displacements. However, the liquefactions zones were successfully

assessed. Wang et al. [27] simulated an earth dam, a water front slope, and a rockfill dam under earthquake load to assess deformations and liquefaction using a bounding surface hypoplasticity model with nine model parameters. They predicted accelerations, wall deflections, and porewater pressure generations well. They underpredicted and overpredicted the vertical settlement and horizontal displacement of the crest, respectively. Dewoolkar et al. [28] employed program Diana-Swandyne II to simulate liquefaction behavior of the backfill in a cantilevered retaining wall model tested in a centrifuge apparatus. They used an advanced dynamic constitutive model, Pastor-Zienkiewicz Mark III model [29], for the backfill behavior. They underestimated the backfill settlement and predicted the excess porewater pressure well. Twelve parameters should be determined for the Pastor-Zienkiewicz Mark III model. The program Diana-Swandyne II was developed by Chan [30]. A bounding surface plasticity model with thirteen parameters was employed by Andrianopoulos et al. [31] to assess liquefaction in two projects. They evaluated liquefaction response in a Nevada sand layer with free-field condition in the first case. They assessed the performance of a rigid foundation on liquifiable Nevada sand in the second case. They investigated the excess porewater pressure in two cases. The settlement was assessed in the second case that was mostly underpredicted. Chakraborty and Popescu [32] evaluated numerically the liquefaction potential in heterogeneous and homogenous soil layers. A simple frame of a structure was on the soil layers. The results showed that the excess porewater pressure in the heterogeneous soil layer was more than that of the homogenous layer. Kamai and Boulanger [33] used advanced bounding surface plasticity PM4SAND model to simulate liquefaction in a centrifuge test. The testing model consisted of two symmetrical slopes. There was an open channel between the symmetrical slopes. This model needs 11 parameters. They predicted lateral spreading, void redistribution, and dissipation patterns of the centrifuge test well.

Several researchers employed advanced dynamic elastoplastic constitutive models to assess liquefaction in different geo-structures. Validating these models and calibrating the large number of model parameters are time-consuming and boring works. Employing advanced constitutive models for numerical analysis of quay walls and cantilevered retaining walls under seismic loads may not be of interest to engineers as their use may be time-consuming and not cost-effective. For example, the Pastor-Zienkiewicz Mark III needs twelve parameters, the Hujeux model needs 22 parameters, and the PM4SAND needs 19 parameters. Determination of these number of parameters may be impractical for engineering problems. The present research uses and evaluates a simple constitutive model along with simple Finn-Byrne

formulation to assess its capability for simulation of two centrifuge tests on a gravity quay wall and a cantilevered retaining wall during seismic loads. The constitutive model employed in this research and the Finn-Byrne formulation require 5 parameters, which all have physical interpretations: shear modulus, bulk modulus, cohesion, friction angle, and relative density. The numerical procedure deployed here in this study does not consider water hydrodynamic pressure for numerical modeling of the quay wall model for simplicity; however, this can be added in future works.

2. METHODOLOGY

Two centrifuge tests on a quay wall and a cantilevered retaining wall from the literature were selected to be simulated numerically via the Finn-Byrne model. The model XZ9 was selected for quay wall simulation and the model MMD12 was selected for cantilevered retaining wall simulation using the Finn-Byrne model. Nevada sand was used as the backfill for both of the quay wall and cantilevered retaining wall models. Some of the soil parameters were reported in the literature and the rest were calibrated via the reported element tests. FLAC was used to simulate both of the centrifuge tests numerically. A linear elastic – perfectly plastic constitutive model employed in the numerical models for both of the models. The elastic behavior and the yield surface obey Hook's elasticity and Mohr-Coulomb's law, respectively. The Finn-Byrne model was employed to predict the porewater pressure generation during seismic loads. Both of the centrifuge tests used absorbing materials at both sides of the models. Therefore, free field boundaries were used at both sides in the numerical models. Porewater pressures, accelerations, and the top lateral displacement of the quay wall model were assessed. Porewater pressures, accelerations, dynamic lateral earth pressures behind the wall, wall deflections, dynamic thrust and its point of action were evaluated and compared with those of the centrifuge test of the cantilevered retaining wall. These comparisons revealed abilities and shortcomings of the Finn-Byrne model in numerical simulation of the quay walls and cantilevered retaining walls at the similar conditions. The results of the numerical model of the cantilevered retaining wall model via the Finn-Byrne model compared with those of a numerical model conducted by an advanced and complicated constitutive model to show the effectiveness of the Finn-Byrne model compared to more complex models.

3. QUAY WALL

3. 1. Centrifuge Test of Quay Wall Zeng [17] reported three centrifuge tests of gravity quay walls in

prototype scale performed at the Cambridge Geotechnical Centrifuge Center, i.e. XZ6, XZ7, and XZ9. The tests were conducted under acceleration of 80g. The relative densities of backfill for XZ6, XZ7, and XZ9 were 52.4 %, 25.8 % and 32.7 %, respectively. The backfill of XZ7 was dry and of the rest were saturated.

To investigate the effect of excess porewater pressure the model with lower relative density i.e. XZ9 was selected for simulation and assessment of the numerical model. Saturated loose granular material was used as the backfill. Figure 1 shows configuration of model XZ9 with the locations of porewater pressure transducers, accelerometers, and one LVDT. Figure 2 shows input motion history applied to the base of the model.

The soil used as the backfill was Nevada sand and its experimental tests were reported by Earth Technology Corporation [34]. Table 1 shows soil parameters used in the numerical model. All parameters except bulk and shear moduli were reported by Zeng [17] and Madabhushi and Zeng [22]. Bulk and shear moduli were calibrated using element tests on Nevada sand in VELACS project [34].

3. 2. Numerical Model The present work uses FLAC ITASCA to simulate the centrifuge model. FLAC

uses finite difference method for numerical simulation and was used by many researchers in geotechnical numerical modeling [35, 36]. A linear elastic – perfectly plastic constitutive model was assumed for the soil medium. Hooke’s elasticity was applied. The yield surface is Mohr-coulomb criterion and Finn-Byrne formulation was employed to predict pore pressure generation under dynamic loads. Finn-Byrne parameters are defined based on relative density.

Martin et al. [37] proposed a simple relationship between the volumetric strain and shear strain to simulate liquefaction. Finn and Byrne [38] developed this approach for drained condition. Finn et al. [39] developed this model by computing excess porewater pressure using volume constraints with an elastic rebound modulus. The tangent stiffness was dependent on shear strain and excess porewater pressure. Finn et al. [40] extensively developed this procedure. Then Byrne [7] introduced a simple method to calculate porewater pressure generation per Equation (1):

$$\frac{\Delta\varepsilon_{vd}}{\gamma} = C_1 \exp\left(-C_2\left(\frac{\varepsilon_{vd}}{\gamma}\right)\right) \tag{1}$$

$\Delta\varepsilon_{vd}$ is incremental volume decrease; ε_{vd} is irrecoverable volume strain; γ is cyclic shear strain; C_1 and C_2 are

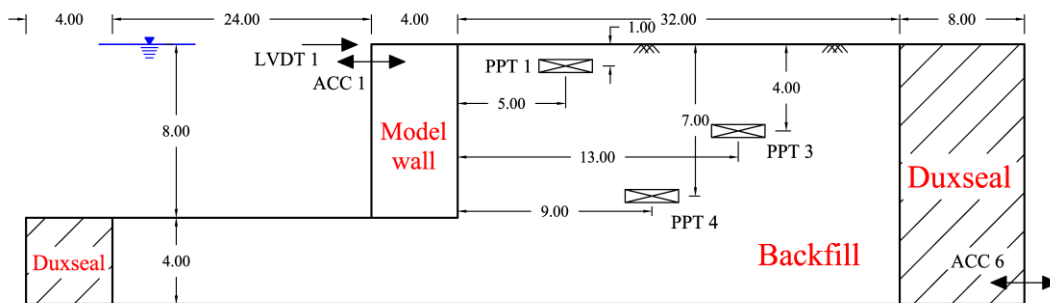


Figure 1. Model configuration of test XZ9 (dimensions in meter)

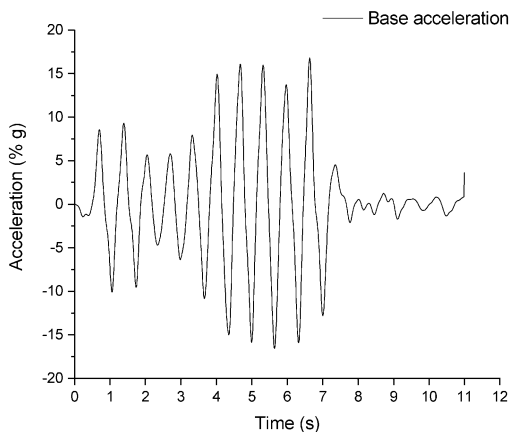


Figure 2. Acceleration history applied to model base

constants. This formulation shows an empirical relationship between the increment of volume decrease and the cyclic shear strain. When the volumetric strain, ε_{vd} , is accumulated the incremental volumetric strain, $\Delta\varepsilon_{vd}$, decreases. The shear-induced volumetric strain increases with increasing number of cycles. When the primary effect i.e. irrecoverable volume strain occurs during a complete strain cycle, the secondary effect i.e. the porewater pressure increases.

Byrne [7] suggested the following equation to calculate C_1 :

$$C_1 = 7600(D_r)^{-2.5} \tag{2}$$

where D_r is relative density and C_2 can be estimated as $\frac{0.4}{C_1}$ for many cases.

TABLE 1. Soil parameters

Bulk modulus (K) (kPa)	Shear modulus (G) (kPa)	Friction angle (ϕ) ($^{\circ}$)	Cohesion (C) (kPa)	Relative density (D_r) (%)	Unit weight (γ) (kN/m ³)	Porosity (n)	Hydraulic conductivity (K) (m/s)
68993	7213	31.3	0.0	32.7	14.9	0.433	6.6×10^{-5}

The wall's material is an aluminum alloy and its behavior was assumed linear elastic. Aluminum Elasticity modulus was assumed 68.9 GPa and unit weight was assumed 27.0 kN/m³. Because of the buoyancy effect submerged unit weight of the wall was applied in the numerical model, i.e. 17.0 kN/m³ and bulk modulus of the water was assumed 2×10^6 kPa and 5% Rayleigh damping has been applied to the backfill.

The centrifuge model benefits Duxseal material at both sides to absorb reflecting waves (See Figure 1). The numerical model uses free field boundaries at both side boundaries. In the free-field boundaries, the waves traveling from the main structure to the boundaries are absorbed properly. To simulate quiet boundaries, viscous dashpots are used along the lateral boundaries. Unbalanced forces of the free-field boundary are applied to the main boundary. The free-field method provides a boundary that behaves as an infinite boundary. Figure 3 shows boundary condition and mesh of the numerical model.

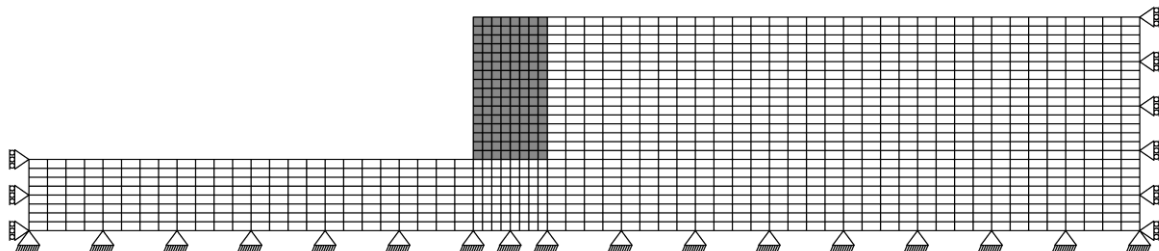
3. 3. Results Figure 4 shows lateral displacement of quay wall top predicted by the numerical model at LVDT1 and compares it with the centrifuge test results. The numerical model predicted reasonably the residual displacement and displacement history of centrifuge test response after the second 5.

Figures 5(a), 6(a), and 7(a) illustrate excess porewater pressures generated at measurement points PPT1, PPT3, and PPT4 during the seismic excitation. The numerical model shows an increasing trend in porewater pressures at points PPT3 and PPT4 and matches reasonably well with observed porewater pressures in the centrifuge test. While residual porewater pressures from numerical model matches with centrifuge tests, in early stages of excitation, a negative excess porewater pressure is observed in numerical model at PPT1. The volumetric strain history by the numerical model at PPT1 is

illustrated in Figure 5(b). A significant expansive volumetric strain occurred after second 1.5, which is resulted in negative excess porewater pressure. Then the contractive volumetric strain increases the porewater pressure. The expansive volumetric strain at PPT1 in early stages of the excitation can be from sudden displacement of quay wall due to lack of hydrodynamic pressure consideration in the numerical model. PPT1 is at the closer distance from the quay wall compared to PPT3 and PPT4. Therefore, a little expansive volumetric strain is observed at PPT1 while PPT3 and PPT4 does not show considerable expansive strain. The contractive volumetric strain is assumed positive and the expansive volumetric strain is assumed negative.

Figure 8(a) shows settlement and tilting of the quay wall after application of seismic loading in the centrifuge test reported by Zeng [17]. This figure shows 1.16 m lateral displacement of the wall while wall top lateral displacement measured during centrifuge tests (see Figure 4) shows 0.8 m lateral displacement at the end of seismic loading. Zeng [17] has not justified this difference. It seems lateral displacement of 1.16 m occurred several seconds after the end of loading and lateral spreading was not stopped after the end of excitation. Therefore, quantitative comparison of Figures 8(a) and 8(b) might not be possible. However, Figure 8(b) illustrates failure mode of settlement and tilting from numerical study conducted herein which is very similar to what observed in the centrifuge test.

Figure 9 shows the potential failure surface in the backfill for the quay wall model. The potential failure surface was not reported in the centrifuge test. The angle between the potential failure surface and the vertical line is about 46° in the numerical model. However, this angle was reported for two other centrifuge models with similar geometry and similar source for the backfill. These angles were 40.4° and 55.7° for models XZ7 and XZ6, respectively.

**Figure 3.** Boundary conditions and mesh for numerical model

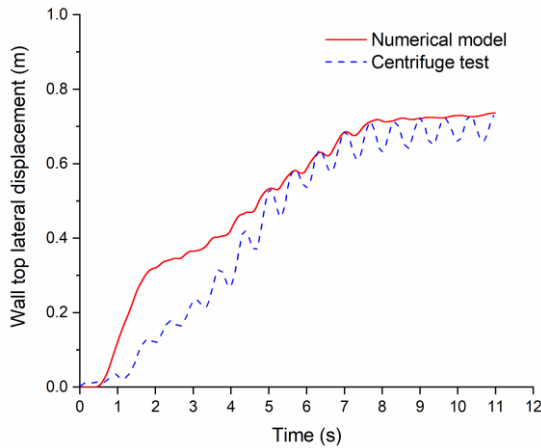


Figure 4. Top lateral displacement of quay wall at LVDT1, numerical versus centrifuge test results

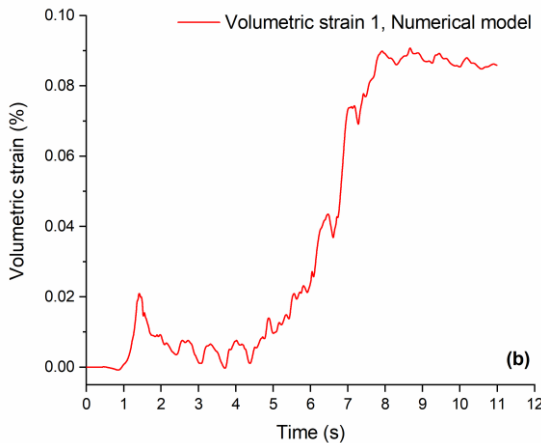
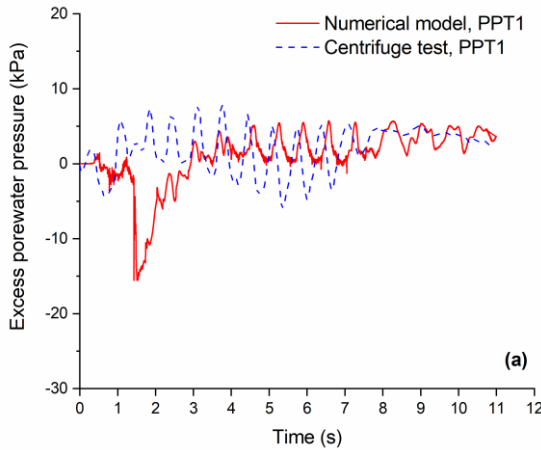


Figure 5. (a) Excess porewater pressure history at PPT1, numerical versus centrifuge test results, (b) Volumetric strain history from numerical model at PPT1

Figure 10 shows measured and predicted acceleration history via the Finn-Byrne model at ACC1.

The predicted acceleration history is reasonable but is not as good as the excess porewater pressures and displacement history of the wall. It can be from this point that the hydrodynamic load of the water was not applied to the quay wall.

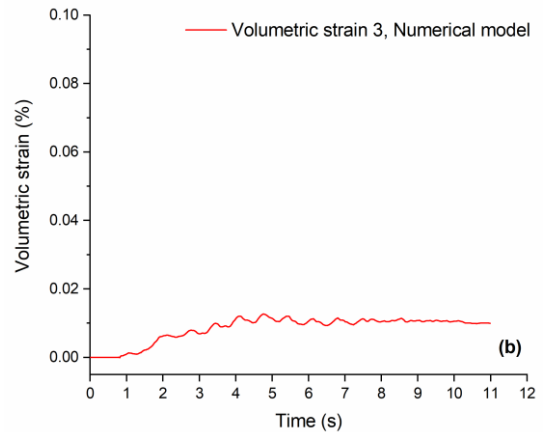
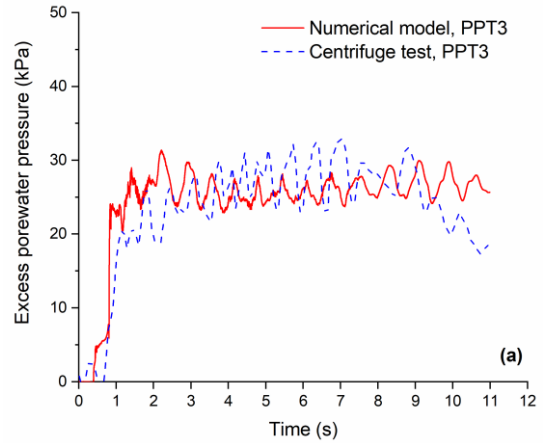
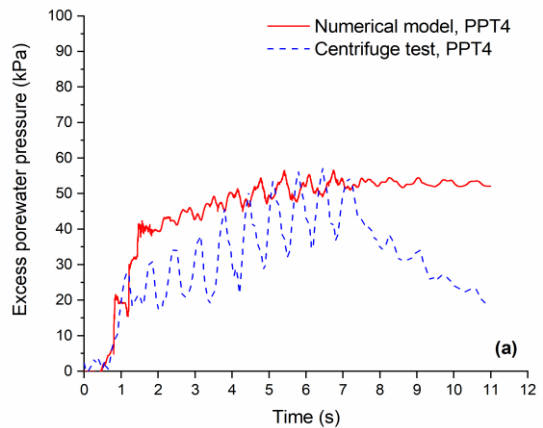


Figure 6. (a) Excess porewater pressure history at PPT3, numerical versus centrifuge test results, (b) Volumetric strain history from numerical model at PPT3



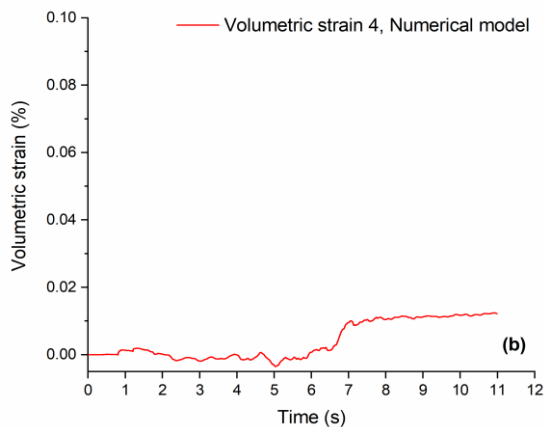


Figure 7. (a) Excess porewater pressure history at PPT4, numerical versus centrifuge test results, (b) Volumetric strain history from numerical model at PPT4

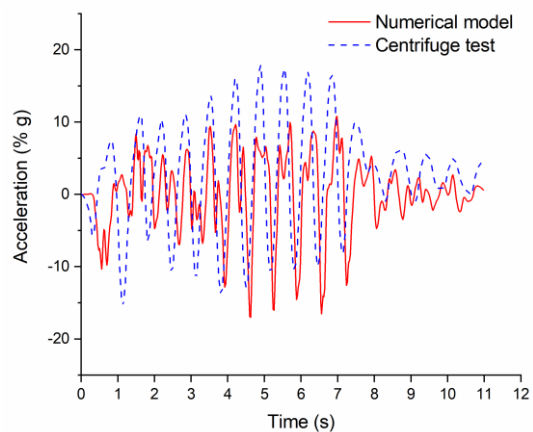


Figure 10. Measured and predicted acceleration history using Finn-Byrne model at ACC1

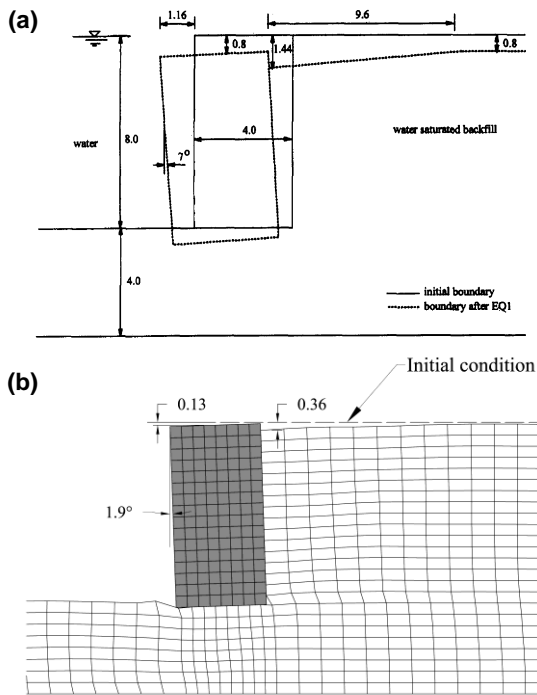


Figure 8. (a) Quay wall after application of seismic loading in centrifuge test (adapted from Zeng [17]) (b) Quay wall after application of seismic loading in numerical model

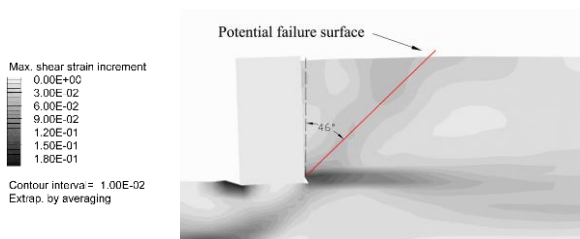


Figure 9. Potential failure surface in quay wall numerical model

4. CANTILEVERED RETAINING WALL

4. 1. Centrifuge Test

Dewoolkar et al. [41] carried out several centrifuge tests to evaluate seismic behavior of cantilevered retaining wall models with saturated and liquifiable backfill. A 400 g-ton centrifuge apparatus was used to perform the tests. The model MMD12 was used to simulate numerically via the Finn-Byrne model. The pore fluid used in the centrifuge tests was metolose water. Figure 11 shows configuration of the centrifuge test.

The backfill was Nevada sand No. 100. The relative density of the sand was 60%. Specific gravity was 2.67 and D_{50} was 0.1 mm. The minimum and maximum dry unit weights of the backfill were 13.87 and 17.33 kN/m^3 , respectively. The wall was connected to the base rigidly. To make an absorbing boundary at the right side of the centrifuge model a duxseal panel was used at the behind of the backfill. T6061-T6 aluminum was used as the material for the wall. Poisson's ratio and young's modulus of the wall were 0.3 and 69×10^6 kPa, respectively. The density was 2787.7 kg/m^3 . Scaling factor for the centrifuge model was 60. The model was subjected to an acceleration of 60 g in the centrifuge apparatus. 2% by weight metolose powder was mixed with deaired and distilled water and was used as the pore fluid in the soil medium. The metolose powder made the water 60 times more viscous than the water. Figure 12 shows horizontal and vertical input motions subjected to the testing model.

4. 2. Numerical Modeling

FLAC was used for numerical simulation of the centrifuge test on the cantilevered retaining wall model. Yield surface was defined using the Mohr – Coulomb criterion. Soil behavior before the plastic deformation is linear elastic based on Hooke's elasticity. Excess porewater pressure in the numerical model was computed based on the Finn-

Byrne formulation. Table 2 shows soil parameters for the numerical model. The triaxial element tests conducted on Nevada sand were used to calibrate the soil parameters. The relative density of soil samples was 60 % [34]. Dewoolkar et al. [41] reported density of 2787.7 kg/m^3 and elasticity modulus of $69 \times 10^6 \text{ kPa}$ for the wall material which were used in the numerical model.

Elastic behavior was assumed for the wall stem. The scale factor of N was applied to reduce the soil hydraulic conductivity reported in Table 6. The reduced hydraulic conductivity was used in the numerical model to simulate the high viscosity of the fluid. Changing the fluid viscosity cannot be done in the numerical model. Density of the fluid used in the numerical model was 1000.0 kg/m^3 . The bulk modulus of the fluid used in the

numerical model was $2 \times 10^6 \text{ kPa}$. Rayleigh damping of 5% was used in the numerical model. The friction angles between the backfill and the wall stem and between the backfill and the base were assumed $2/3\Phi$. (Φ = the backfill friction angle). Figure 13 illustrates mesh, geometry, and boundary conditions of the numerical model.

4. 3. Numerical Modeling By Dewoolkar et al.

Dewoolkar et al. [28] simulated numerically the MMD 12 centrifuge test. They used an advanced dynamic elastic-plastic constitutive model, Pastor-Ziekiewicz Mark III model, for soil behavior. This model was developed using the generalized plasticity theory by

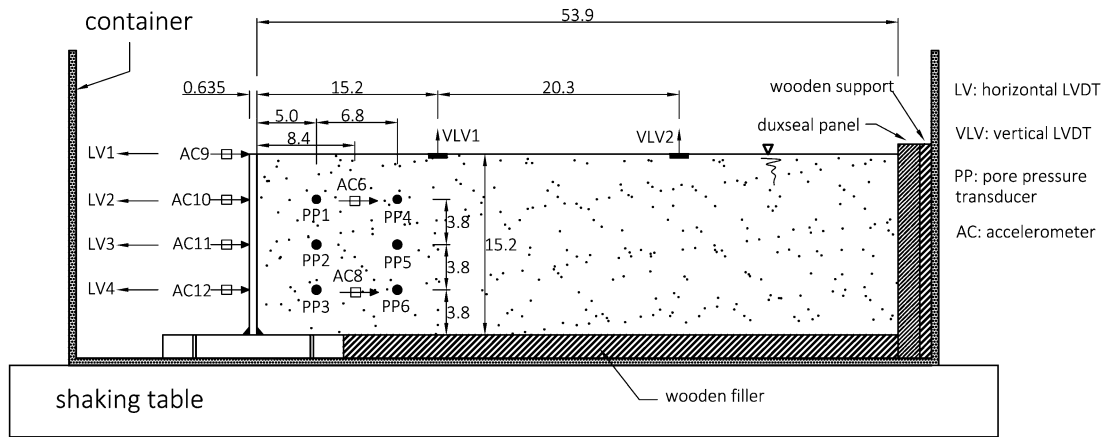


Figure 11. Configuration for centrifuge test of cantilevered retaining wall [41]

TABLE 2. Soil parameters of Nevada sand No. 100 used in numerical simulation

Bulk modulus (K) (kPa)	Shear modulus (G) (kPa)	Friction angle (ϕ) ($^\circ$)	Cohesion (C) (kPa)	Relative density (D_r) (%)	Unit weight (γ) (kN/m ³)	Porosity (n)	Hydraulic conductivity (K) (m/s)
22027	5291	40.3	0.0	60	15.76	0.398	5.6×10^{-5}

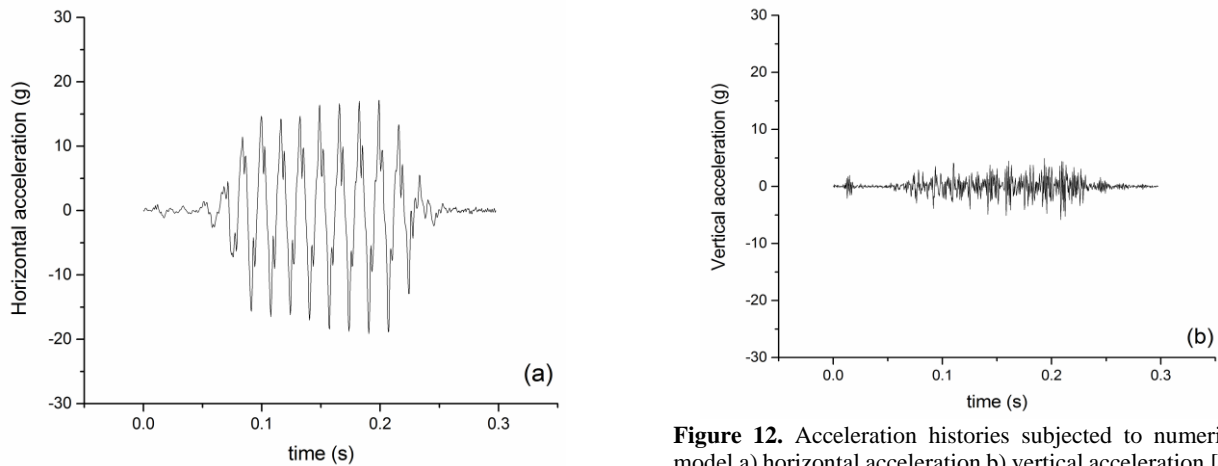


Figure 12. Acceleration histories subjected to numerical model a) horizontal acceleration b) vertical acceleration [41]

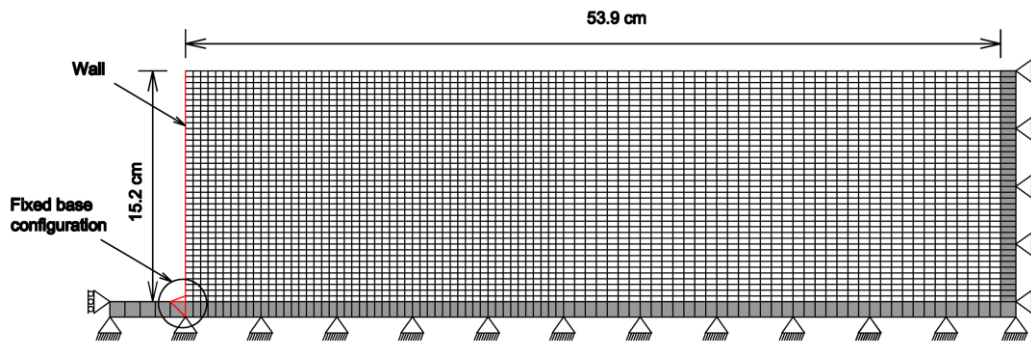


Figure 13. Mesh, geometry, and boundary conditions of the numerical model

pastor et al. [29]. The Pastor-Zienkiewicz mark III model is an advanced non-linear elastic - plastic soil model that was developed based on the generalized plasticity theory. This model can predict static and dynamic behavior of soil materials in drained and undrained conditions. This model is a well-established nonlinear model without explicit statement of yield and potential surfaces; instead, gradient vectors of the yield and potential surfaces are used. The elastic moduli in this model are dependent on mean effective stress. Several researchers used and developed this model for seismic analyses [42-44]. The adopted constitutive model in the present research uses linear elastic behavior while the Pastor-Zienkiewicz mark III model uses a non-linear elastic behavior. The size of the yield surface of the adopted model is constant while that changes in the Pastor-Zienkiewicz mark III model. The latter benefits from loading and unloading plastic moduli while the adopted model uses only a constant elastic modulus during loading and unloading. The loading and unloading tangent stiffness in the adopted model are the same while they are defined via different formulas in the Pastor-Zienkiewicz mark III model.

The Pastor-Zienkiewicz mark III model needs twelve parameters to be defined for fully dynamic analysis. The results of the numerical model using the Pastor-Zienkiewicz Mark III reported here and compared with the results of the Finn-Byrne model.

4. 4. Results Figures 14 and 15 show predicted and measured normalized porewater pressures at points PP1, PP2, PP3, PP4, PP5, and PP6. The porewater pressures were normalized to the atmospheric pressure of 101.325 kPa. Figure 14(b) compared the predicted porewater pressures by Pastor-Zienkiewicz Mark III model with those by Finn-Byrne model. As seen in all results from the Finn-Byrne model, the start of excess porewater pressures is at the beginning of the excitation whereas in the centrifuge test is at about 0.1 s. As mentioned, a constitutive model with linear elastic and perfectly plastic behavior was applied for the backfill.

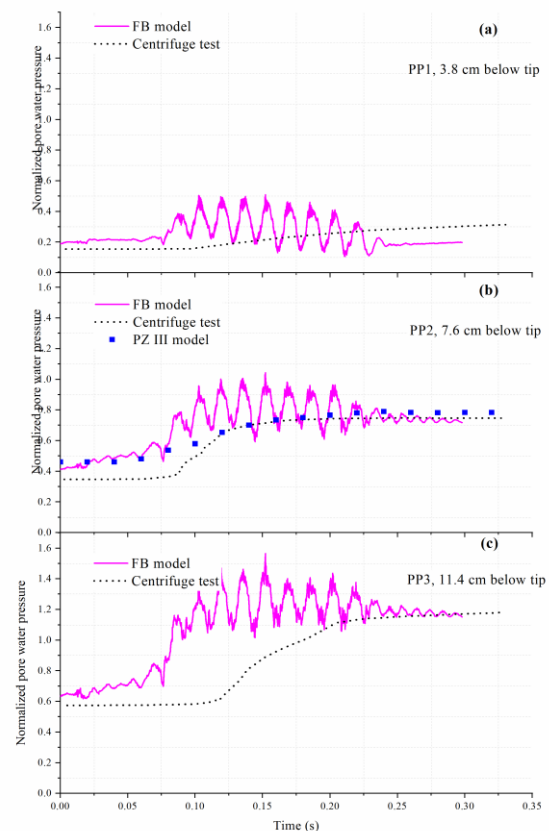


Figure 14. Comparison between measured and computed normalized porewater pressures using Finn-Byrne model and Pastor-Zienkiewicz Mark III model at PP1, PP2, and PP3

When the input motion is applied to the numerical model, the behavior of the backfill is elastic at low accelerations at the beginnings of the seismic load. No plastic deformation is observed at early stages and the waves are not damped and quickly conveyed to the above layers and produces excess porewater pressures at the beginnings of the seismic load. According to the general plastic behavior of the geo-materials, plastic deformation

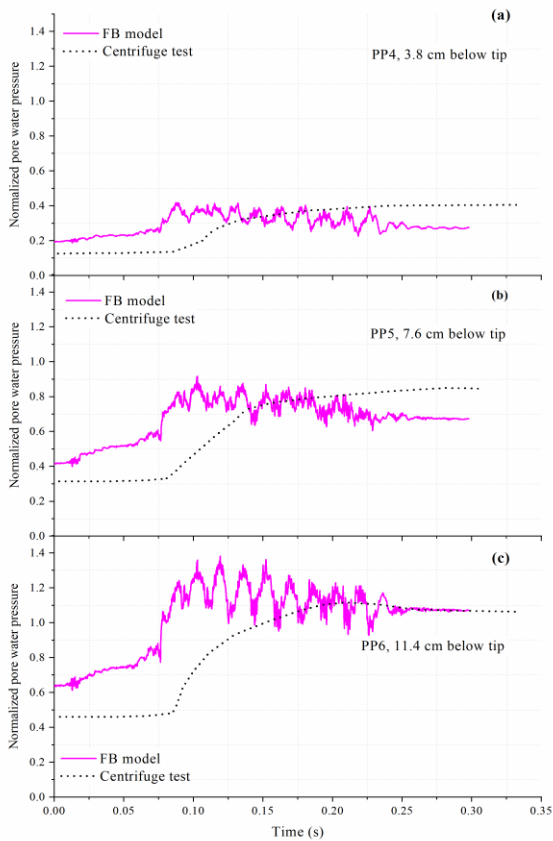


Figure 15. Comparison between measured and computed normalized porewater pressures using Finn-Byrne smodel at PP4, PP5, and PP6

can be observed at the beginnings of the seismic loads even with low amplitudes of acceleration. Therefore, the accelerations at the early stages are damped in the bottom layers and the excess porewater pressure cannot be observed at the top layers.

A good agreement was observed between the residual porewater pressures of the numerical model and the centrifuge test at PP2, PP3, and PP6. The discrepancy between the residual normalized porewater pressures of the numerical model and the centrifuge test at PP1, PP4, and PP5 is about 0.1 to 0.15.

Figure 16 shows measured and predicted acceleration histories at AC6 and AC8 in the backfill. Figure 17 shows measured and predicted acceleration histories at AC9, AC10, AC11, and AC 12 on the wall stem. The agreement between the measured and computed accelerations is very good at AC8 in the backfill and at AC11 and AC12 on the wall stem. This is because that these points are at the lower levels in comparison to AC6, AC9, and AC10. The predicted accelerations at AC9 and AC10 are reasonable. The computed accelerations at AC6 are not in good agreement with the measured amplitudes. This can be attributed to the type of soil constitutive model adopted for the backfill.

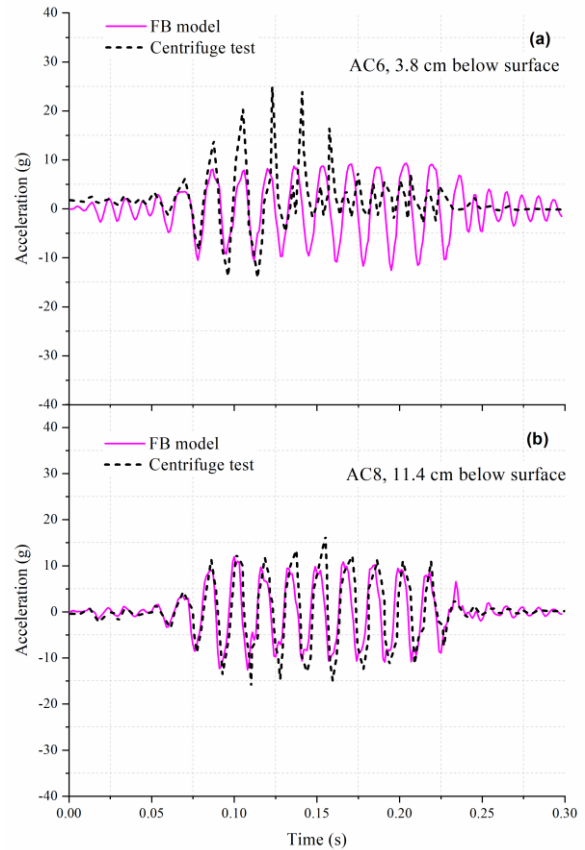


Figure 16. Comparison between measured and computed accelerations using Finn-Byrne model at AC6 and AC8 in the backfill

Figures 18 and 19 show observed and predicted normalized lateral earth pressures behind the wall stem using the Finn-Byrne model. The lateral earth pressures at EP4, EP5, EP6, and EP10 were well predicted.

The lateral earth pressures at EP2 and EP3 were not predicted well. This can be attributed to mostly elastic response of the soil medium at locations close to the backfill surface behind the wall. Plastic deformation can occur from the start of the seismic load. The plastic deformation is one of the main reasons for damping in the soil medium. It seems that the elastic-perfectly plastic constitutive model and Finn-Byrne model cannot simulate damping in the soil medium and large oscillations are seen in the predicted values.

The predicted lateral earth pressures at EP8 and EP9 are a little more than those of the measured amounts, however, they are reasonable. This discrepancy can also be from the mostly elastic behavior of the medium at these locations.

Figure 20 show measured and predicted wall deflections normalized to the wall height at LV1, LV2, LV3, and LV4. The predicted wall deflections at the end of seismic load at all locations match reasonably with the observed deflections in the centrifuge test.

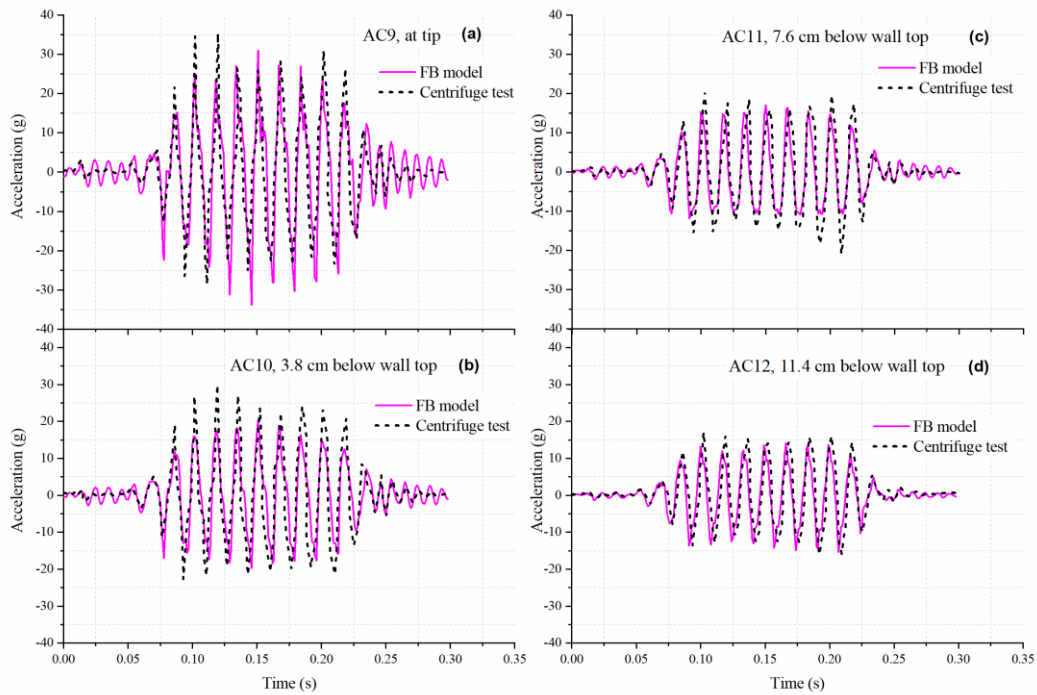


Figure 17. Comparison between measured and computed accelerations using Finn-Byrne model at AC9, AC10, AC11, and AC12 on the wall stem

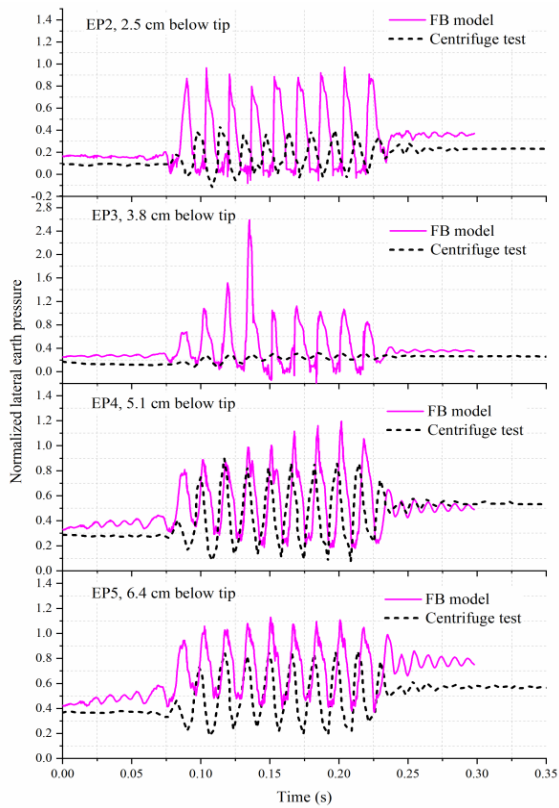


Figure 18. Measured and computed normalized lateral earth pressures using Finn-Byrne model at EP2, EP3, EP4, and EP5

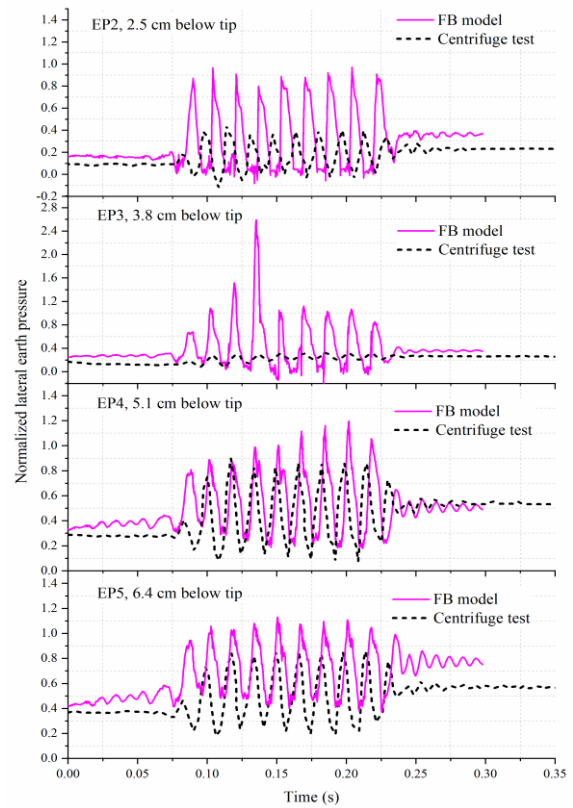


Figure 19. Measured and computed normalized lateral earth pressures using Finn-Byrne model at EP6, EP8, EP9, and EP10

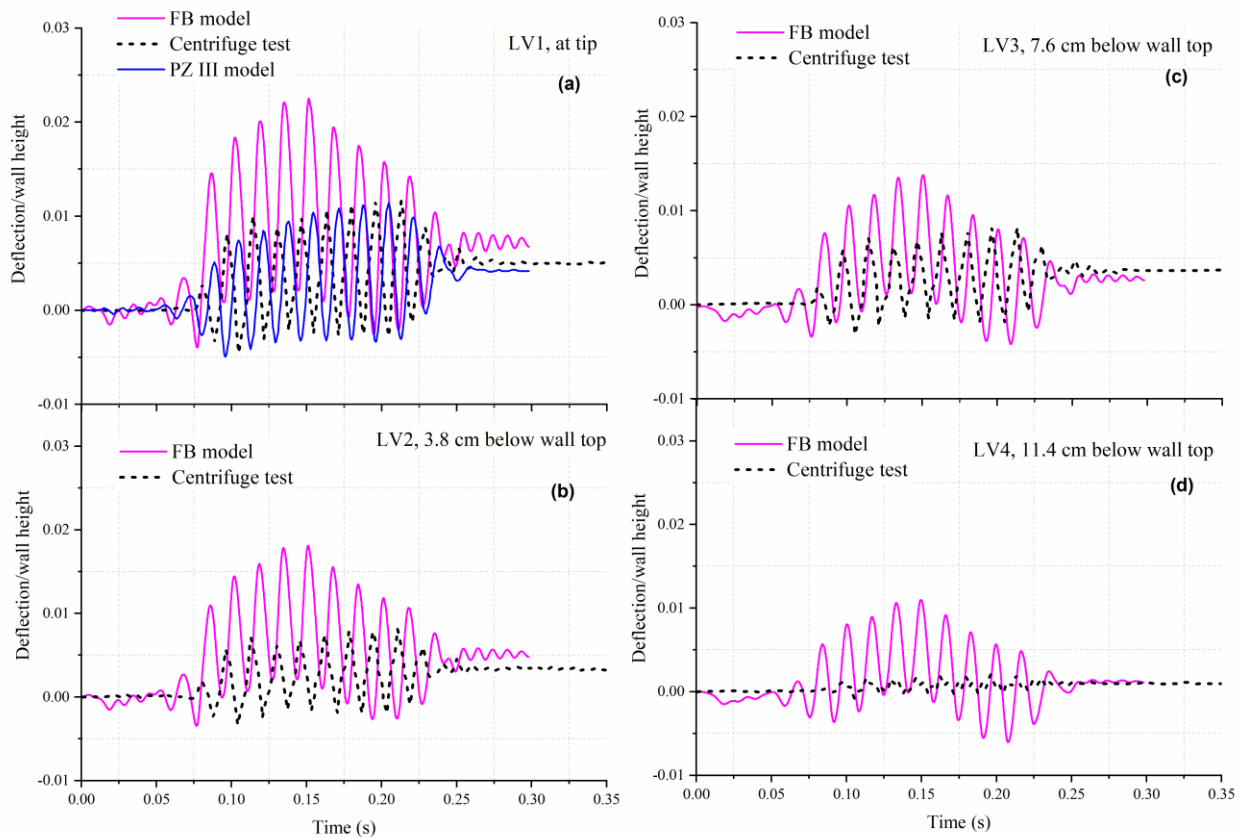


Figure 20. Measured and computed normalized wall deflections using Finn-Byrne model and Pastor-Zienkiewicz mark III model at LV1, LV2, LV3, and LV4

The predicted deflections during the seismic loading are greater than those of the centrifuge test. The deflection increases before 0.15 s and decreases after 0.15 s. This is because of the application of the baseline correction method. This method is used to correct raw input motions. In the seismic simulation of the structures, it may be observed a residual displacement or velocity at the end of seismic loads. This phenomenon is because of the nonzero output of the integral of the velocity time history. In this method, a low frequency velocity time history is added to the raw velocity time history. The integral of the corrected velocity time history, i.e., the final displacement should be zero. The residual predicted deflection matches reasonably with that of the centrifuge test. Figure 21 shows raw and corrected horizontal displacement time histories in the centrifuge test. The predicted deflections via Finn-Byrne model are consistent with the corrected horizontal time history in the centrifuge test (see Figures 20 and 21).

Figure 22 illustrates measured and predicted dynamic lateral thrust on the wall normalized to static thrust and point of action of the lateral total thrust. The point of action of the lateral total thrust was normalized to the

wall height. The thrust increase due to the shaking at the end of excitation was 60 % in the centrifuge test while this increase in the numerical model was 75 %. The discrepancy is about 25% of the centrifuge test. The point of action of the total thrust was predicted well.

Figure 23 shows predicted and measured backfill settlement of the model. The numerical results were predicted via the Finn-Byrne model and Pastor-Zienkiewicz mark III model. As seen, the Finn-Byrne model cannot predict the settlement well. Dewoolkar et al. [28] predicted the backfill settlement via the Pastor-Zienkiewicz mark III model. As shown, the Finn-Byrne model is simple compared to the Pastor-Zienkiewicz mark III model and requires fewer parameters, however, the Finn-Byrne model predicted the settlement better than the Pastor-Zienkiewicz mark III model. The number of parameters for Pastor-Zienkiewicz mark III is twelve and for the Finn-Byrne model with elastic-perfectly plastic model is five. Note that Dewoolkar et al. [28] argued that the parameters of the Pastor-Zienkiewicz mark III model were calibrated so that the prediction of excess porewater pressures was better than the prediction of the settlement.

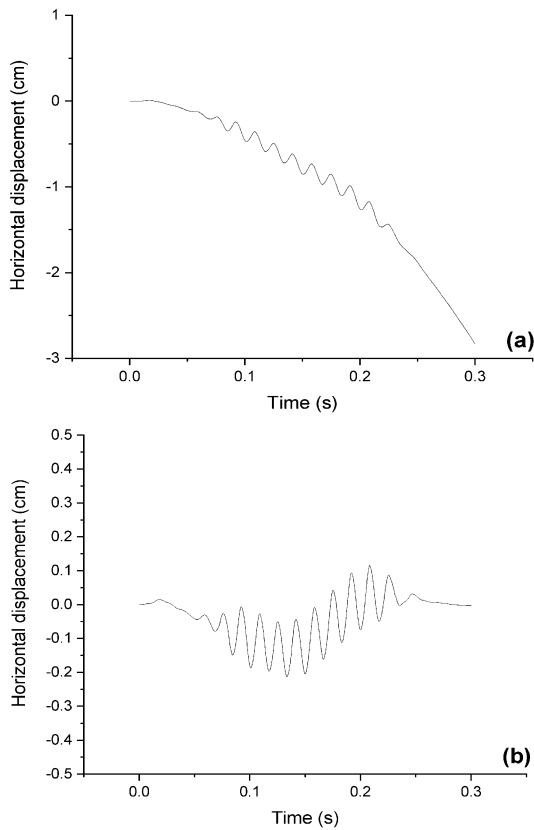


Figure 21. Time history of horizontal displacement in the centrifuge test (a) raw (b) corrected

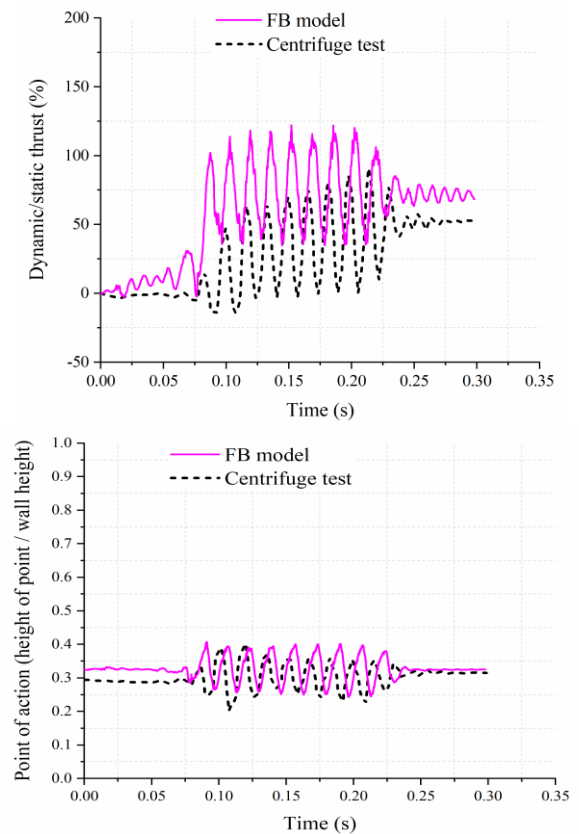


Figure 22. Measured and predicted dynamic thrust and its point of action (a) dynamic thrust normalized to static thrust (b) point of action for total thrust

5. DISCUSSION

Liquefaction in quay walls and cantilevered retaining walls may produce undesirable displacements and cause problems during the service period. Evaluating displacements and excess porewater pressures due to the liquefaction is yet a difficult job. The Finn-Byrne is a simple and relevant model to evaluate the liquefaction behavior. The literature review shows that the Finn-Byrne model was employed to assess the liquefaction behavior in different geo-structures. However, a few researches can be found to assess liquefaction behavior in quay walls and cantilevered retaining walls via the Finn-Byrne model. The present research was conducted to fill this research gap as the present topic is of interest to researchers and engineers.

The present work uses a constitutive model with linear elastic and perfectly plastic behavior with Mohr-Coulomb criterion for yield surface and the Finn-Byrne model for porewater pressure generation. Therefore, the behavior of the soil medium may be purely elastic at the beginnings of the seismic loads. The pure elastic behavior decreases material damping in the soil medium.

Based on the soil media behavior observations, the plastic behavior may be seen even under the light loads.

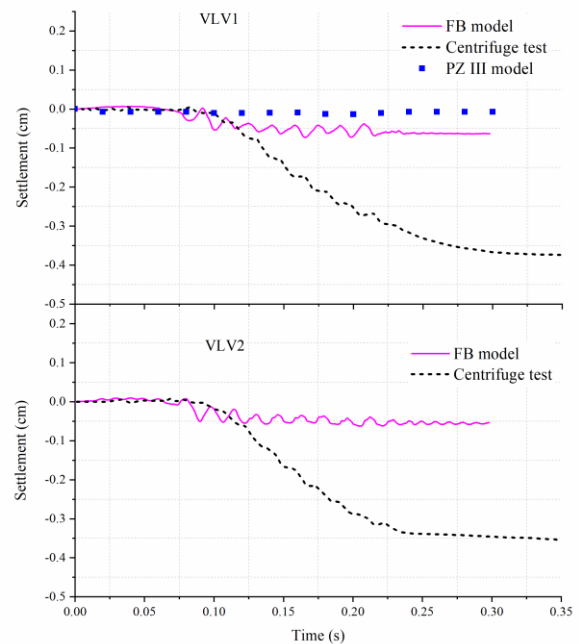


Figure 23. Measured versus predicted backfill settlement via Finn-Byrne model and Pastor-Zienkiewicz mark III model at VLV1 and VLV2

Therefore, the employed model cannot show material damping at the beginnings of the seismic excitations. The start of excess porewater pressures from the onset of the seismic excitation at the numerical model of cantilevered retaining wall is attributed to the shortcoming of the adopted constitutive model with the Finn-Byrne model in material damping simulation. When the plastic deformation starts in the numerical model, the maximum excess porewater pressures can be simulated well by the Finn-Byrne model for both of the quay wall and cantilevered retaining wall models. The residual porewater pressures were predicted well at some locations and not well for some other locations. The shortcoming of the Finn-Byrne model at the post-liquefaction stages were reported in the literature.

The predicted accelerations for both models are generally reasonable and the Finn-Byrne model may be recommended for acceleration amplification analysis in quay walls and cantilevered retaining walls with similar conditions.

The Finn-Byrne model computed the lateral displacement of the quay wall model satisfactorily. An abrupt displacement computed by the numerical model in the first couple of seconds is due to lack of water hydrodynamic pressures from passive side of the wall. The wall moves easier in the absence of water hydrodynamic pressure. The Finn-Byrne model computed the residual deflection of the cantilevered retaining wall stem reasonably. An increase in then a decrease in deflection was observed during the seismic load that was because of the influence of the baseline correction to the raw input motion. Large oscillations observed in the predicted deflection time history. This is due to the elastic-perfectly plastic behavior of the material and the weakness of the model in simulating the material damping.

The computed settlements via the Finn-Byrne model and Pastor-Zienkiewicz mark III were not satisfactory. The prediction of the Finn-Byrne model was better than that of the Pastor-Zienkiewicz mark III model. Note that the latter is more complicated than the Finn-Byrne model and needs more model parameters.

According to the results of the numerical model for the quay wall and cantilevered retaining wall models, the capability of the Finn-Byrne model in predicting excess porewater pressures in the backfill, accelerations, and lateral wall stem displacement is good. The results showed that the backfill settlements and dynamic earth pressures predicted via the numerical model did not match as well as the lateral displacements, excess pore water pressures, and accelerations with the results of the centrifuge test.

The poor prediction of the backfill settlement via the Finn-Byrne model shows that the adopted constitutive model cannot simulate volumetric strains properly during seismic loads. This is also true for the advanced Pastor-

Zienkiewicz mark III model. The sudden drop in the predicted excess porewater pressure at PPT1 in the quay wall model shows the weakness of the adopted constitutive model in predicting volumetric strain. The Finn-Byrne model predicted the lateral displacement of the quay wall well and the residual lateral deflection of the cantilevered retaining wall reasonable.

When the values of the lateral displacements of the walls are desired, the Finn-Byrne model may be recommended for the displacement analysis. However, when the backfill settlement is desired, a care should be taken in using this model.

Since the Mohr-Coulomb criterion gives appropriate solutions in practical works and the prediction of the excess porewater pressures were satisfactory, therefore the adopted model is suitable for stability analysis of the quay walls and cantilevered retaining walls.

6. CONCLUSION

Several constitutive models were recently developed by researchers that can simulate liquefaction behavior. They include UBCSAND model, PM4SAND model, Pastor-Zienkiewicz Mark III model, a multiple-yield surface plasticity model, the elastoplastic multimechanism Hujoux model, the modified Martin-Finn-Seed model, and a bounding surface plasticity model. In the present research, the capability of the Finn-Byrne model in liquefaction analysis of a quay wall model and a cantilevered retaining wall model conducted by centrifuge apparatus was evaluated.

In the quay wall model, the predicted horizontal displacement of the wall, the excess porewater pressure in the backfill, and the backfill and wall deformation pattern via the Finn-Byrne model were well. The predicted acceleration history of the quay wall was reasonable.

In the cantilevered retaining wall model, the residual deflection of the cantilevered retaining wall was reasonable. However, large oscillations observed in the deflection history during the seismic load. This was attributed to the linear elastic – perfectly plastic behavior and weakness of this model in simulating appropriate material damping. The results showed the reasonable prediction of the excess porewater pressures, acceleration histories, and lateral displacement using the Finn-Byrne model. The computed dynamic earth pressures behind the wall stem were not as reasonable as the formers. In addition, the predicted backfill settlement was not satisfactory.

The results showed that the use of the Finn-Byrne model may be recommended to do stability and displacement analyses of the quay walls and cantilevered retaining walls with similar conditions.

Since geotechnical engineers often prefer simple numerical models to simulate and design the ge-structures, therefore, the simplicity of the Finn-Byrne model and its reasonable results reveals its effectiveness in the practice. When there is a need to check the excess porewater pressures, accelerations, and lateral displacements of the walls, the application of the Finn-Byrne model will be useful in research works. However, a care should be taken in assessing the backfill settlements and dynamic earth pressures behind the wall stem. This weakness indicates that the adopted constitutive model with the Finn-Byrne formulation cannot predict volumetric strain and dynamic active pressures during and after seismic loads. The future developments can be focused on the modification of the used constitutive model to address these problems while maintaining its simplicity.

7. REFERENCES

- Rasti, A.R. and Marandi, S.M., "Parameters analysis of the covering soil of tunnels constructed in liquefiable soils", *International Journal of Engineering, Transactions A: Basics*, Vol. 25, No. 4, (2012), 333-346. doi: 10.5829/idosi.ije.2012.25.04a.05
- Marandi, S.M. and Goharriz, M., "Assessment of lateral displacements using neuro-fuzzy group method of data handling systems" *International Journal of Engineering, Transactions B: Applications*, Vol. 28, No. 5, (2015), 677-685. doi: 10.5829/idosi.ije.2015.28.05b.05
- Hussein, A. A., M. A. Al-Neami, and F. H. Rahil. "Effect of Hydrodynamic Pressure on Saturated Sand Supporting Liquid Storage Tank During the Earthquake." *International Journal of Engineering, Transactions B: Applications*, Vol. 34, No. 5 (2021), 1176-1183. doi:10.5829/ije.2021.34.05b.11
- Hamed Sangari, A. and Marandi, S.M., "Laboratory studies on the effect of vertical gravel column drains on liquefaction potential", *International Journal of Engineering, Transactions B: Applications*, Vol. 24, No. 3, (2011), 209-226. doi: 10.5829/idosi.ije.2011.24.03b.02
- Hossain, M. B., Roknuzzaman, M., and Rahman, M. M. "Liquefaction Potential Evaluation by Deterministic and Probabilistic Approaches." *Civil Engineering Journal*, (2022), Vol. 8, No. 07. doi: 10.28991/CEJ-2022-08-07-010
- Kalantary, F., and Kahani, M., "Optimization of the biological soil improvement procedure." *International Journal of Environmental Science and Technology*, (2019), No. 16, 4231-4240. doi: <https://doi.org/10.1007/s13762-018-1821-9>
- Byrne, P.M., "A cyclic shear-volume coupling and pore pressure model for sand" In Proceedings of the 2nd international conference on recent advances in geotechnical earthquake engineering and soil dynamics, Geotechnical Special Publication, Vol. 1, (1991), 47-55.
- National Research Council, Committee on Earthquake Engineering, Commission on Engineering and Technical Systems, "Liquefaction of Soils During Earthquakes", National Academy Press, Washington, D.C., (1985). <https://doi.org/10.17226/19275>
- De Alba, P.A., Chan, C.K. and Seed, H.B., "Sand liquefaction in large-scale simple shear tests", *Journal of the Geotechnical Engineering Division*, Vol. 102, No. 9, (1976), 909-927. <https://doi.org/10.1061/AJGEB6.0000322>
- Vargas, O., Ortiz, R. and Flores, F., "Liquefaction Analysis Using Pore Pressure Generation Models During Earthquakes", In from Fundamentals to Applications in Geotechnics, IOS Press, (2015), 1057-1064, doi: 10.3233/978-1-61499-603-3-1057
- Sudevan, P.B., Boominathan, A. and Banerjee, S., "Uplift analysis of an underground structure in a liquefiable soil subjected to dynamic loading", In Geotechnical Earthquake Engineering and Soil Dynamics V: Numerical Modeling and Soil Structure Interaction Reston, VA: American Society of Civil Engineers, (2018), 464-472. <https://doi.org/10.1061/9780784481479.048>
- Chian, S. C., Tokimatsu, K., and Madabhushi, S. P. G. "Soil Liquefaction-Induced Uplift of Underground Structures: Physical and Numerical Modeling." *Journal of Geotechnical and Geoenvironmental Engineering*, Vol. 140, No. 10, (2014), 1-18. [https://doi.org/10.1061/\(ASCE\)GT.19435606.0001159](https://doi.org/10.1061/(ASCE)GT.19435606.0001159)
- Masini, L. and Rampello, S., "Performance of large homogeneous earth dams during strong ground motions", In Proceedings of the 19th International Conference on Soil Mechanics and Geotechnical Engineering, Seoul, (2017).
- Chou, J.C., Yang, H.T. and Lin, D.G., "Calibration of Finn Model and UBSCAND Model for Simplified Liquefaction Analysis Procedures", *Applied Sciences*, Vol. 11, No. 11, (2021), 5283. <https://doi.org/10.3390/app11115283>
- Banerjee, R., Chattaraj, R., Parulekar, Y.M. and Sengupta, A., "Numerical prediction of undrained cyclic triaxial experiments on saturated Kasai River sand using two constitutive models of liquefaction", *Bulletin of Engineering Geology and the Environment*, Vol. 80, No. 11, (2021), 8565-8582. <https://doi.org/10.1007/s10064-021-02449-2>
- Singh, A.P. and Chatterjee, K., "Dynamic Analysis of Cantilever Sheet Pile Walls in Liquefiable Soil Using FLAC2D", In Proceedings of the 7th Indian Young Geotechnical Engineers Conference Springer, Singapore, (2022). 9-16. https://doi.org/10.1007/978-981-16-6456-4_2
- Zeng, X., "Seismic response of gravity quay walls. I: Centrifuge modelling", *Journal of Geotechnical and Geoenvironmental Engineering*, Vol. 124, No. 5, (1998), 406-417. [https://doi.org/10.1061/\(ASCE\)1090-0241\(1998\)124:5\(406\)](https://doi.org/10.1061/(ASCE)1090-0241(1998)124:5(406))
- Ghalandarzadeh, A., Orita, T., Towhata, I. and Yun, F., "Shaking table tests on seismic deformation of gravity quay walls", *Soils and Foundations*, Vol. 38(Special), (1998), 115-132. https://doi.org/10.3208/sandf.38.Special_115
- Miura, K., Kohama, E., Inoue, K., Ohtsuka, N., Sasajima, T. and Yoshida, N., "Behavior of gravity type quay wall during earthquake regarding dynamic interaction between caisson and backfill during liquefaction", In Proc. of 12th World Conference on Earthquake Engineering, Vol. 7, (2000), 1737.
- Kim, S.R., Jang, I.S., Chung, C.K. and Kim, M.M., "Evaluation of seismic displacements of quay walls", *Soil Dynamics and Earthquake Engineering*, Vol. 25, No. 6, (2005), 451-459. <https://doi.org/10.1016/j.soildyn.2005.03.002>
- Lee, C.J., "Centrifuge modeling of the behavior of caisson-type quay walls during earthquakes", *Soil Dynamics and Earthquake Engineering*, Vol. 25, No. 2, (2005), 117-131.
- Madabhushi, S.P.G. and Zeng, X., "Seismic response of gravity quay walls. II: Numerical modelling", *Journal of Geotechnical and Geoenvironmental Engineering*, Vol. 124, No. 5, (1998), 418-427. <https://doi.org/10.1016/j.soildyn.2004.10.011>
- Yang, Z., Elgamal, A., Abdoun, T. and Lee, C.J., "A numerical study of lateral spreading behind a caisson-type quay wall", In proceedings of the fourth international conference on recent advances in geotechnical earthquake engineering and soil

- dynamics and symposium in honor of Prof. WD Liam Finn, (2001).
24. Dakoulas, P. and Gazetas, G., "Insight into seismic earth and water pressures against caisson quay walls", *Geotechnique*, Vol. 58, No. 2, (2008), 95-111. <https://doi.org/10.1680/geot.2008.58.2.95>
 25. Abu Taiyab, M., Alam, M.J. and Abedin, M.Z., "Dynamic soil-structure interaction of a gravity quay wall and the effect of densification in liquefiable sites", *International Journal of Geomechanics*, Vol. 14, No. 1, (2014), 20-33 [https://doi.org/10.1061/\(ASCE\)GM.1943-5622.0000278](https://doi.org/10.1061/(ASCE)GM.1943-5622.0000278)
 26. Wu, G., "Earthquake-induced deformation analyses of the Upper San Fernando Dam under the 1971 San Fernando earthquake", *Canadian Geotechnical Journal*, Vol. 38, No. 1, (2001), 1-15. <https://doi.org/10.1139/t00-086>
 27. Wang, Z.L., Makdisi, F.I. and Egan, J., "Practical applications of a nonlinear approach to analysis of earthquake-induced liquefaction and deformation of earth structures", *Soil Dynamics and Earthquake Engineering*, Vol. 26, No. 2-4, (2006), 231-252. <https://doi.org/10.1016/j.soildyn.2004.11.032>
 28. Dewoolkar, M.M., Chan, A.H.C., Ko, H.Y. and Pak, R.Y., "Finite element simulations of seismic effects on retaining walls with liquefiable backfills", *International Journal for Numerical and Analytical Methods in Geomechanics*, Vol. 33, No. 6, (2009), 791-816. <https://doi.org/10.1002/nag.748>
 29. Pastor, M., Zienkiewicz, O.C. and Chan, A., "Generalized plasticity and the modelling of soil behaviour", *International Journal for Numerical and Analytical Methods in Geomechanics*, Vol. 14, No. 3, (1990), 151-190. <https://doi.org/10.1002/nag.1610140302>
 30. Chan, A.H.C., "User manual for diana-swandyne ii", School of Civil Engineering, University of Birmingham, Birmingham, (1993).
 31. Andrianopoulos, K.I., Papadimitriou, A.G. and Bouckovalas, G.D., "Bounding surface plasticity model for the seismic liquefaction analysis of geostructures" *Soil Dynamics and Earthquake Engineering*, Vol. 30, No. 10, (2010), 895-911. <https://doi.org/10.1016/j.soildyn.2010.04.001>
 32. Chakraborty, P. and Popescu, R., "Numerical simulation of centrifuge tests on homogeneous and heterogeneous soil models", *Computers and Geotechnics*, Vol. 41, (2012), 95-105. <https://doi.org/10.1016/j.compgeo.2011.11.008>
 33. Kamai, R. and Boulanger, R.W., "Simulations of a centrifuge test with lateral spreading and void redistribution effects", *Journal of Geotechnical and Geoenvironmental Engineering*, Vol. 139, No. 8, (2013), 1250-1261. [https://doi.org/10.1061/\(ASCE\)GT.1943-5606.0000845](https://doi.org/10.1061/(ASCE)GT.1943-5606.0000845)
 34. Arulmoli, K., Muraleetharan, K. K., Hossain, M. M., and Fruth, L. S., "VELACS: Verification of liquefaction analysis by centrifuge studies", Laboratory Testing Program, Soil Data Rep. No. 90, 562, (1992).
 35. Heidarzadeh, H., "Evaluation of modified Cam-Clay constitutive model in FLAC and its development by FISH programming.", *European Journal of Environmental and Civil Engineering*, Vol. 25, No. 2 (2021), 226-244. <https://doi.org/10.1080/19648189.2018.1521752>
 36. Heidarzadeh, H., and Kamgar, R. "Necessity of applying the concept of the steady state on the numerical analyses of excavation issues: laboratory, field and numerical investigations.", *Geomechanics and Geoengineering*, Vol. 17, No. 2, (2022), 413-425. <https://doi.org/10.1080/17486025.2020.1755466>
 37. Martin, G. R., Seed, H. B., and Finn, W. L., "Fundamentals of liquefaction under cyclic loading.", *Journal of the Geotechnical Engineering Division*, Vol. 101, No. 5, (1975), 423-438. <https://doi.org/10.1061/AJGEB6.0000164>
 38. Finn, W. L., and Byrne, P. M., "Estimating settlements in dry sands during earthquakes.", *Canadian Geotechnical Journal*, Vol. 13, No. 4, (1976), 355-363. <https://doi.org/10.1139/t76-037>
 39. Finn, W. L., Martin, G. R., and Byrne, P. M., "Seismic response and liquefaction of sands.", *Journal of the Geotechnical Engineering Division*, Vol. 102, No. 8, (1976), 841-856 <https://doi.org/10.1061/AJGEB6.00000310>
 40. Finn, W.D. Liam, Yogendrakumar, M., Yoshida, N. and Yoshida, H., "TARA-3: A program to compute the response of 2-D embankments and soil-structure interaction systems to seismic loadings. Dept. of Civil Eng., University of British Columbia. (1986).
 41. Dewoolkar, M.M., Ko, H.Y. and Pak, R.Y., "Seismic behavior of cantilever retaining walls with liquefiable backfills", *Journal of Geotechnical and Geoenvironmental Engineering*, Vol. 127, No. 5, (2001), 424-435. [https://doi.org/10.1061/\(ASCE\)1090-0241\(2001\)127:5\(424\)](https://doi.org/10.1061/(ASCE)1090-0241(2001)127:5(424))
 42. Iraj, A., Orang, F., and Seyedi Hosseinia, E., "A modification to dense sand dynamic simulation capability of Pastor-Zienkiewicz-Chan model.", *Acta Geotechnica*, No. 9, (2014), 343-353. <https://doi.org/10.1007/s11440-013-0291-y>
 43. Heidarzadeh, H., and Oliaei, M., "An efficient generalized plasticity constitutive model with minimal complexity and required parameters.", *KSCE Journal of Civil Engineering*, No. 22, (2018), 1109-1120. <https://doi.org/10.1007/s12205-017-1037-4>
 44. Iraj, A., "Reinforced soil wall analysis under working stress conditions using a two-phase model with the introduction of a new design parameter.", *International Journal of Engineering, Transactions C: Aspects*, Vol. 32, No. 12, (2019), 1762-1772. doi: 10.5829/ije.2019.32.12c.09

Persian Abstract

چکیده

دو آزمایش سانتریفیوژ بر روی یک دیوار وزنی حائل و یک دیوار طره‌ای حائل با خاک دانه‌ای و اشباع توسط مدل فین - بیرنه شبیه‌سازی شده است. توانایی مدل مذکور در آنالیز روانگرایی دیوارهای حائل وزنی و حائل طره‌ای ارزیابی شده است. دیوار حائل وزنی تحت یک رکورد زلزله افقی و دیوار حائل طره‌ای تحت همزمان دو رکورد زلزله افقی و قائم قرار گرفته است. مدل رفتاری استفاده شده برای خاک یک مدل با رفتار ارتجاعی خطی - پلاستیک کامل است. برای رفتار ارتجاعی از قانون هوک و برای سطح تسلیم از معیار موهر - کولمب استفاده شده است. پارامترهایی نظیر اضافه فشار آب حفره‌ای، شتاب دیوار و خاک، تغییر مکان افقی دیوارها، فشار جانبی لرزه‌ای ناشی از خاک در پشت دیوار، الگوی تغییر شکل خاک پشت دیوار و نشست در خاک پشت دیوار در مدل‌های عددی بررسی شده و با نتایج آزمایش‌های سانتریفیوژ مقایسه شدند. نتایج نشان دادند که مدل رفتاری به کار گرفته شده برای تحلیل پایداری و تغییر شکل لرزه‌ای دیوارهای حائل وزنی و حائل طره‌ای ابزاری مناسب است. با این حال به علت ضعف نسبی این مدل در ارزیابی نشست خاک پشت دیوار و فشار جانبی دینامیکی در پشت دیوار، بایستی احتیاط‌های لازم در خصوص استفاده از این دو پارامتر به عمل آید. نتایج نشان دادند که مدل عددی مذکور در خصوص پیش‌بینی سایر پارامترهای دیوار عملکرد رضایت‌بخشی دارد.



Human Disease Prediction using Machine Learning Techniques and Real-life Parameters

K. Gaurav, A. Kumar, P. Singh, A. Kumari, M. Kasar*, T. Suryawanshi

Department of Computer Science and Engineering, Bharati Vidyapeeth Deemed to be University College of Engineering, Pune, India

PAPER INFO

Paper history:

Received 26 February 2023

Received in revised form 26 March 2023

Accepted 31 March 2023

Keywords:

Random Forest

Support Vector Machine

Symptoms

Disease Prediction

Adaboost

Machine Learning

ABSTRACT

Disease prediction of a human means predicting the probability of a patient's disease after examining the combinations of the patient's symptoms. Monitoring a patient's condition and health information at the initial examination can help doctors to treat a patient's condition effectively. This analysis in the medical industry would lead to a streamlined and expedited treatment of patients. The previous researchers have primarily emphasized machine learning models mainly Support Vector Machine (SVM), K-nearest neighbors (KNN), and RUSboost for the detection of diseases with the symptoms as parameters. However, the data used by the prior researchers for training the model is not transformed and the model is completely dependent on the symptoms, while their accuracy is poor. Nevertheless, there is a need to design a modified model for better accuracy and early prediction of human disease. The proposed model has improved the efficacy and accuracy model, by resolving the issue of the earlier researcher's models. The proposed model is using the medical dataset from Kaggle and transforms the data by assigning the weights based on their rarity. This dataset is then trained using a combination of machine learning algorithms: Random Forest, Long Short-Term Memory (LSTM), and SVM. Parallel to this, the history of the patient can be analyzed using LSTM Algorithm. SVM is then used to conclude, the possible disease. The proposed model has achieved better accuracy and reliability as compared to state-of-the-art methods. The proposed model is useful to contribute towards development in the automation of the healthcare industries.

doi: 10.5829/ije.2023.36.06c.07

1. INTRODUCTION

Human disease predication is a crucial part of human life. Early disease prediction of a human is an important step in the treatment of disease. Since the very beginning, a doctor has handled it almost exclusively. Thus, the healthcare industry thrives on innovation to make logistics efficient [1]. Innovation is the heart of the medical industry. It is what drives new treatments, cures and therapies [2]. Innovation is also what keeps the medical industry current and relevant. The scope of development in the medical industry is vast [3, 4]. There are many areas where innovation is needed to make progress. Some of these include developing new treatments for diseases, finding ways to improve patient care, and making medical procedures more efficient. In the current digital age, innovation in the medical industry can be achieved through the digitalization of medical

processes [5]. One of the most pressing issues in the medical industry is the workload on the doctors [6] and the unaffordable consultation cost [7]. This issue is highlighted mainly in the disease prediction with the symptoms of the patients as input. The current methodology of the medical industry consists of the patient visiting a generalist doctor and explaining to the doctor the conditions, and symptoms faced by the patient upon which the doctor infers possible diseases and then channels them to a specialist doctor [8]. The logistics behind this methodology can be minimized with the help of a machine learning algorithm: Random Forest [9]. This algorithm is used for classifying multiple diseases based on symptoms and geographic locations. These locations help determine the results as the database assumes that for a particular location, there exist some symptoms that only occur at that location.

Thus, unlike other models, this model concentrates

*Corresponding Author Email: mmkasar@bvucoep.edu.in (M. Kasar)

more accurately on these results. The patient can simply enter the disease experienced by him/her, and then this data will be fed into the model, which in turn, provides the possible disease.

The generalized disease prediction architecture that is currently used as of now is not accurate and inconsiderate of the medical history of the patient. The present general model heavily depends on the presence of symptoms and human interaction [8]. All the other methodologies used the symptoms of the patients in the present scenario. For example, the SVM method intakes the symptoms of the patient that have occurred very recently [10]. The generalized disease prediction architecture consists of this methodology only. These methodologies do not intake the patient's medical history as input data. Due to this, the other generalized methodologies become less effective and have less human interaction. This also affects the accuracy of the model that is presented in the earlier studies. These locations help determine the results as the database assumes that for a particular location, there exist some symptoms that only occur at that location. Thus, unlike other models, this model concentrates more accurately on these results. The proposed model has the following major contributions:

1. The proposed model has improved Efficiency and accuracy to predict diseases
2. The proposed model is trained on the modified dataset (assigning the weights to the rare symptoms according to the geographical area)
3. The model is tested on real-life symptoms of patients.

The remaining section of this paper is structured as follows: section 2 discussed the earlier work done by the authors. Section 3 focussed on the proposed methodology with various methods used to increase the accuracy of the disease prediction model. In section 4 author discussed a comparative analysis of earlier methods and the proposed model. Section 5 concludes the work and is followed by the future scope in section 6.

2. LITERATURE REVIEW

As discussed in the introduction sections, some of the research papers include a plethora of models for predicting the disease that a patient may suffer, based on symptoms gathered from the patient. The models that are used often and have the best accuracy are as follows:

The Method proposed by Jianfang et al. [11] used Support Vector Machine (SVM) for the classification of diseases based on the symptoms. The SVM model is efficient for the prediction of diseases but requires more time to predict disease [12]. Also, a method is unable to increase the accuracy of the model. The approach has the drawback of classifying objects using a hyperplane, which is only partially effective [13, 14]. The hyperplane is accurate only for classifying sample data into 2 classes.

But in the current scenario, the medical industry requires more than 2 classes (diseases) for the identification of symptoms corresponding to the disease.

The K-Nearest Neighbors (KNN) algorithm used by Keniya et al. [15]. They used this method by assigning the data point to the class that most of the K data points belong to, while it is sensitive to noisy and missing data. They have considered certain factors such as age group, symptoms and gender of the person to predict the disease. While considering these parameters lower accuracy on machine learning models is getting [15]. The KNN method is also used by Kashvi et al. [16]. They also have proven high accuracy in several cases such as diabetics and heart risk prediction. There is the issue of considering a small data size for the classification of diseases [16].

The method proposed by Pingale et al. [17] using Naïve Bayes method they are predicting limited diseases such as Diabetes, Malaria, Jaundice, Dengue, and Tuberculosis. They have not worked on a large dataset to predict large numbers of diseases [17]. Also, Gomathy, and Rohith Naidu [18] used Naïve Bayes method for disease prediction. By using this method they have developed a web application for disease prediction that is accessible from anywhere. The accuracy of the model depends on the data provided to the system. The issue of the suggested model is to develop software for disease prediction with a more accurate dataset to enhance the accuracy [18]. The method proposed by Chhogyal and Nayak [19] used Naïve Bayes classifier. They have obtained poor accuracy in disease prediction also they are not using the standard dataset for training [19].

The method proposed by Kumar et al. [20] used Rustboost Algorithm. RUSBoost is developed to address the issue of class imbalance [20]. However, the RUSBoost algorithm employs random under-sampling as a resampling method which can lead to the loss of crucial information. Therefore, this algorithm was not taken into account when training the data.

The above-mentioned approaches have discussed various machine-learning techniques for disease prediction. However, the author has not employed some issues such as efficiency, accuracy, the limited size of the data set used to train the model and considered limited symptoms to diagnose the disease. To overcome all these issues there is a need to propose a modified and accurate model for predicting human diseases. The detailed proposed model is described below section.

3. PROPOSED METHODOLOGY

The proposed model is providing an enhanced and accurate model for predicting human diseases from the symptoms. The dataset from Kaggle is used, and the methods used to train the models are the Rainforest algorithm, LSTM algorithm and SVM algorithm to train

our data.

The working model will be as follows:

1. The human will enter his/her symptoms.
2. The symptoms will then be inputted into our model.
3. The model will then yield the possible disease.

The novelty of the proposed work is that tweaking the Radnom forest model by using hyperparameters, improves the efficacy of the model. Hence, it is providing more accuracy.

In this work standard dataset is used for training and testing the model, author has tested multiple models including the models discussed under the section “Literature Review”. With the conclusion to the experiment, the following combinations of methodologies are used in the proposed model:

3. 1. Random Forest Algorithm The random forest produces decision trees from multiple data using their average for regression and most of the voting for categorization [21]. The research reported by Paul et al. [22] used the Random Forest Algorithm as the main algorithm.

The random forest algorithm is used to train the model with the dataset which contains a combination of symptoms and the corresponding diseases [22]. The driving force behind using the random forest algorithm is that it has the capacity to handle data sets with continuous variables, as in regression, and categorical variables, as in classification [21, 23]. It produces superior results with regard to classification problems. The working method of the Random Forest is illustrated in Figure 1.

Step 1: Select arbitrary samples from a given data set or training set.

Step 2: This method will create a decision tree for every training data set.

Step 3: Using the decision tree's average, voting will be done.

Step 4: Lastly, select the predicted outcome that garnered the greatest support as the final prediction outcome.

The Random Forest Algorithm analyses the symptoms and geographical region in the provided database to make judgments about a disease. Then it analyzes the outcome with the labels supplied before

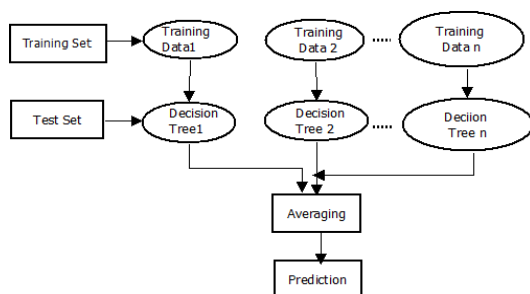


Figure 1. Methodology of Random Forest Algorithm

going back to assess the model's reliability. The formula for the random forest algorithm :

$$MSE = 1/N \sum_{i=1}^N (f_i - y_i)^2 \tag{1}$$

In Equation (1), N represents the total amount of data points, f_i denotes the model's output, and y_i denotes the real value for data point i. This is used for the calculation of the Mean Squared Error. This method calculates the distance between every node and the expected real value to identify which branch is the best option for your forest. f_i is the decision tree's output and y_i is the value of the data point that you are evaluating at a certain node. You should be aware that while running Random Forests with classification data, you typically use the Gini index, which is the method used to decide the order of nodes on a decision tree branch. Based on the class and likelihood, this method determines the Gini of each branch on a node, showing which branch is more probable. Thus, p_i denotes the class's proportional frequency throughout the dataset, while c is the overall number of classes present.

The architecture of Random Forest Algorithm:

Figure 2 represents the working architecture of the Random Forest Algorithm [24]. As evidently visible, the divided sample of the data is used for further calculation of decision trees at the final which combined serve as a result. The Random Forest algorithm consists of the following steps:

1. Dividing the entire dataset into test and training data
2. Dividing the datasets into multiple datasets
3. Generating Decision trees from each dataset
4. Evaluating these decision trees
5. Concluding the insights generated from the decisions trees
6. Generating the result as an output

3. 1. 1. Advantage of using Random Forest Algorithm In the database, the author has modified

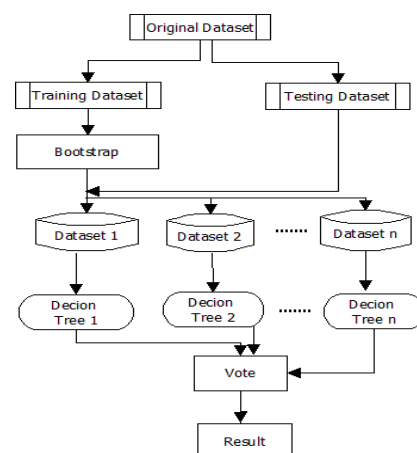


Figure 2. The architecture of the Random Forest Algorithm [24]

the symptoms (inputs) based on the following parameters:

1. **Rarity:** The rarer a symptom is, the more weight is given to it. Thus, the Random Forest Model predicts a disease more accurately according to the symptoms [1].
2. **Location:** Some diseases are only bound to happen in a particular geographic location.
3. Thus, the database is set in such a way that the algorithm discards all the diseases that are not present in the inputted location [24].

While training the model, the decision forests that are formed while concluding are pruned as soon as they encounter a weak symptom or a symptom that does not occur in a location. Thus, Random Forest Algorithm minimizes the cost whilst predicting a more realistic model [25].

3. 1. 2. Disadvantage of using Random Forest Algorithm

1. **Execution time:** It requires huge execution time and space for the compilation of the decision trees [24].
2. **Stability:** It works better in a stable environment where the dataset is less noisy and subjected to be less dynamic.
3. **Overfitting:** It may lead to an overfitted model when provided with noise.

3. 2. Long Short-Term Memory Long Short-Term Memory (LSTM) type recurrent neural networks are able to understand order dependency. The LSTM algorithm can be used to calculate and predict disease on the basis of the time-series data of the patient's history of symptoms. LSTM will be used for inculcating the new dataset with the involvement of the pre-trained dataset for increasing the accuracy of the model and discovering new possibilities and parameters [26].

The inclusion of LSTM will make the prediction of the model more accurate and stable. LSTM will be most accurate when provided a time-series data, which could be inculcated in the future. The input gate is described in the first equation, which also provides the new data that will be added to the cell state. The second is the forget gate, which tells the contents to be removed from the cell state. The final one serves as the output gate that is used to activate the LSTM block's final output at timestamp "t." [27].

$$i_t = \sigma(w_i[h_{t-1}, x_t] + b_i) \quad (2)$$

$$f_t = \sigma(w_f[h_{t-1}, x_t] + b_f) \quad (3)$$

$$o_t = \sigma(w_o[h_{t-1}, x_t] + b_o) \quad (4)$$

Equations (2), (3), and (4) are used for the calculation of the values that are of type-time series generally. Each term in the equations represents the following terms:

i_t : depicts the input gate. f_t : depicts forget gate.

o_t : depicts output gate. σ : depicts sigmoid function.

The LSTM model is shown in Figure 3. The above model explains the working of the LSTM algorithm.

3. 3. Support Vector Machine (SVM) After the result of the value from the LSTM model and the Random forest model, the SVM model will be used to predict whether the result is actually correlated or not. For example, if the LSTM model indicates "Hepatitis" and the Rainforest model also indicates "Hepatitis", we will check with SVM if the results of them are correlated and if it happens due to causation [28].

In short, SVM will be used to predict the outcome and categorization of the provided inputs depending on the parameters supplied. As a primary approach, the SVM is used in the research publications by Vijayarani, and Dhayanand [29] and Le et al. [30] to predict the outcome using symptoms as input. However, the SVM algorithm [31] used in our research is solely used for predicting the result between the two parameters. SVM is chosen as the model for the final prediction due to its ability to classify the dataset [11].

3. 4. Data Transformation About the dataset The dataset is imported from Kaggle¹. The dataset consists of 4500+ patients with the parameters as follows: Symptoms (133 columns), Disease (1 column), and Location (1 column).

3. 4. 1. Transformation Methodology This raw dataset from the Kaggle is then further processed and transformed into numerical values, according to the severity and the rarity of the symptoms. The dataset has been split in proportion for training and testing, 70% of the data consumed for training and 30% for testing, in a ratio of 70:30. The dataset can be further increased with the induction of new patients and new symptoms.

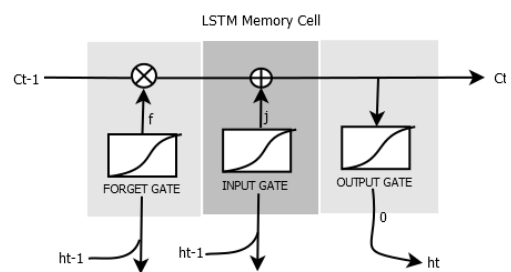


Figure 3. LSTM model [27]

¹

<https://www.kaggle.com/datasets/itachi9604/diseasesymptomdescripton-dataset?select=dataset.csv>

Additional to this data, the model would also required the dataset of the history of the patients. This data would be utilized for training another model for tracking the history of the disease that is and can be suffered by the patient. This dataset would then be trained with Random Forest for concluding. The combination of both these models would help in predicting the disease suffered by the patient. This patient history dataset is not required for prediction since without it, the model would operate on the obligatory model, which uses the disease's symptoms to detect it. As mentioned earlier, the various models have been tested on the modified dataset, finding the methodologies more efficient and accurate.

4. COMPARATIVE ANALYSIS

To get a glimpse of the difference between the models used by other research papers, Table 1 describes a comparative analysis of earlier methods and the proposed model.

Table 1 explains the comparative analysis of several state-of-the-art methods that are based on the derivation of the disease prediction of a patient using symptoms as input data. The first column represents the reference number, in other words, the serial number of the paper. The second column represents the methodology behind the derivation of the conclusion of the research paper. The basic methods used by the researchers are shown in this column. The research papers listed in the references and in the table have reached conclusions regarding the diagnosis of the disease based on input from symptoms. The third column represents the advantages of using the methodology mentioned in the second column. The advantages are determined on the basis of the analysis of the research paper. Some of these advantages are also unique factors in the research paper and are the factors

that differentiate them from other research papers. The fourth column in the table of the comparative analysis represents the disadvantages of the proposed research papers. These are the limitations that the research papers are not able to solve. However, By solving these limitations, It is analyzed that the proposed model has increased accuracy as compared to earlier state-of-the-art -methods. The fifth column represents the accuracy of the proposed methodology in the research papers. According to the comparison, the initial research paper's highest accuracy was close to 95% which is less than the modified proposed model. The Confusion Matrix for the Random Forest model of the proposed model is illustrated in Figure 4.

Figure 5 shows the comparative analysis of the accuracy of the training models. From the earlier necessities, Naive Bayes Algorithms [17] were best with a model accuracy of 94.8%. Following the Naive Bayes model [17] is a weighted KNN model [18] with an accuracy of 93.5%. The research papers using the SVM model [29, 30] were also very close. However, the suggested model, that is Random forest model, yields the most accurate result, 97% as compared to earlier methods.

5. CONCLUSION

The problems faced by the medical industry with the unaffordability of the patients to seek dictators and the unavailability of the medical staff can be diminished. This can happen by automating the channelization of the patients to a specialist instead of a generalist. This can happen via the use of a disease prediction system. This system will input the patient's symptoms and produce possible disease as an output with 97% accuracy as compare to earlier models. The proposed model can assist the healthcare industry by:

TABLE 1. Comparative Analysis

Ref.	Algorithm Used	Advantages	Limitation(s)	Accuracy
[17]	Naive Bayes Classifier	Highly Scalable	Only for independent features it works accurately	94.8%
[18]	Random forest, Decision tree, Naïve Bayes	Good accuracy for predicting disease	Model needs to be enhanced via ensemble model	90%
[15]	Weighted KNN	Smoother decision surface, less data dependency	Due the issue of over-fitting, model is not scalable	93.5%
[29]	SVM	Faster Execution, Less Space complexity	Not Suitable for Multi-parameter	76%
[30]	SVM	Faster Execution, Less Space complexity	Not Suitable for Multi-parameter	90%
[32]	Logistic Regression(LR)	It makes assumption about distribution	Over-Fitting issue is there. It requires less multi-collinearity	75%
Proposed Method	Random Forest	The dataset is suitable for Random Forest	Can be improved if time series dataset is provided	97%

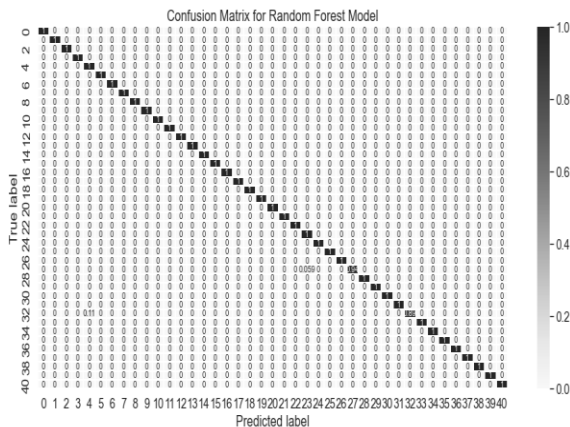


Figure 4. Confusion Matrix of the proposed model

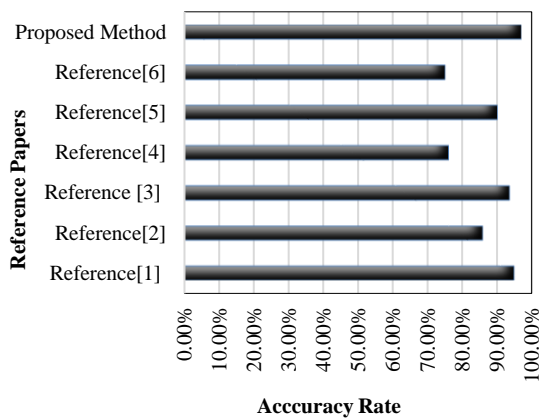


Figure 5. Accuracy of different models

1. Reduction in healthcare costs: By improving patient outcomes and reducing the need for unnecessary tests and treatments, disease prediction applications can help reduce healthcare costs and improve the overall efficiency of the healthcare system.
2. Improved patient outcomes: By providing healthcare providers with valuable insights into a patient's disease risk, disease prediction applications can help improve patient outcomes by allowing for earlier and more effective interventions.
3. Early diagnosis: By analyzing patient data and identifying risk factors for specific diseases, disease prediction applications can help healthcare providers make an early diagnosis, which is critical for improving patient outcomes. At last, we conclude that our model can provide increased accuracy and a reliable model for the prediction of the disease through symptoms.

6. FUTURE SCOPE

In the future, the model can be used in various sectors and can enhance efficiency by considering more

symptoms to predict disease. The model can be used for providing an enhanced, more accurate framework that would lead to a better human disease prediction model.

7. REFERENCES

1. Zhou, S.-M., Fernandez-Gutierrez, F., Kennedy, J., Cooksey, R., Atkinson, M., Denaxas, S., Siebert, S., Dixon, W.G., O'Neill, T.W. and Choy, E., "Defining disease phenotypes in primary care electronic health records by a machine learning approach: A case study in identifying rheumatoid arthritis", *PloS One*, Vol. 11, No. 5, (2016), e0154515. <https://doi.org/10.1371/journal.pone.0154515>
2. Littell, C.L., "Innovation in medical technology: Reading the indicators", *Health Affairs*, Vol. 13, No. 3, (1994), 226-235. <https://doi.org/10.1377/hlthaff.13.3.226>
3. Milella, F., Minelli, E.A., Strozzi, F. and Croce, D., "Change and innovation in healthcare: Findings from literature", *ClinicoEconomics and Outcomes Research*, (2021), 395-408. doi: 10.2147/CEOR.S301169.
4. Rathi, M. and Pareek, V., "Disease prediction tool: An integrated hybrid data mining approach for healthcare", *IRACST-International Journal of Computer Science and Information Technology & Security (IJCSITS)*, ISSN, (2016), 2249-9555.
5. Kelly, C.J. and Young, A.J., "Promoting innovation in healthcare", *Future Healthcare Journal*, Vol. 4, No. 2, (2017), 121. doi: 10.7861/futurehosp.4-2-121.
6. Mobeen, A., Shafiq, M., Aziz, M.H. and Mohsin, M.J., "Impact of workflow interruptions on baseline activities of the doctors working in the emergency department", *BMJ Open Quality*, Vol. 11, No. 3, (2022), e001813. doi: 10.1136/bmjopen-2022-001813.
7. Ahmed, S., Szabo, S. and Nilsen, K., "Catastrophic healthcare expenditure and impoverishment in tropical deltas: Evidence from the mekong delta region", *International Journal for Equity in Health*, Vol. 17, No. 1, (2018), 1-13. doi: 10.1186/s12939-018-0757-5.
8. Roberts, M.A. and Abery, B.H., "A person-centered approach to home and community-based services outcome measurement", *Frontiers in rehabilitation Sciences*, Vol. 4, (2023). doi: 10.3389/fresc.2023.1056530
9. Farooqui, M. and Ahmad, D., "Disease prediction system using support vector machine and multilinear regression", *International Journal of Innovative Research in Computer Science & Technology (IJIRCSIT) ISSN*, (2020), 2347-5552. <https://doi.org/10.21276/ijircsit.2020.8.4.15>
10. Olatunji, O.O., Adediji, P.A., Akinlabi, S., Madushele, N., Ishola, F. and Aworinde, A.K., "Improving classification performance of skewed biomass data", in IOP Conference Series: Materials Science and Engineering, IOP Publishing. Vol. 1107, (2021), 012191.
11. Cao, J., Wang, M., Li, Y. and Zhang, Q., "Improved support vector machine classification algorithm based on adaptive feature weight updating in the hadoop cluster environment", *PloS One*, Vol. 14, No. 4, (2019), e0215136. <https://doi.org/10.1371/journal.pone.0215136>
12. Hamidi, H. and Daraee, A., "Analysis of pre-processing and post-processing methods and using data mining to diagnose heart diseases", *International Journal of Engineering, Transactions B: Applications*, Vol. 29, No. 7, (2016), 921-930.
13. Pisner, D.A. and Schnyer, D.M., Support vector machine, in Machine learning, 2020, Elsevier.101-121.

14. Chen, J., Yu, J., Wen, J., Zhang, C., Yin, Z.e., Wu, J. and Yao, S., "Pre-evacuation time estimation based emergency evacuation simulation in urban residential communities", *International Journal of environmental Research and Public Health*, Vol. 16, No. 23, (2019), 4599. doi: 10.3390/ijerph16234599.
15. Keniya, R., Khakharia, A., Shah, V., Gada, V., Manjalkar, R., Thaker, T., Warang, M. and Mehendale, N., "Disease prediction from various symptoms using machine learning", *Available at SSRN 3661426*, (2020). <https://dx.doi.org/10.2139/ssrn.3661426>
16. Taunk, K., De, S., Verma, S. and Swetapadma, A., "A brief review of nearest neighbor algorithm for learning and classification", in 2019 International Conference on Intelligent Computing and Control Systems (ICCS), IEEE. (2019), 1255-1260.
17. Pingale, K., Surwase, S., Kulkarni, V., Sarage, S. and Karve, A., "Disease prediction using machine learning", *International Research Journal of Engineering and Technology (IRJET)*, Vol. 6, (2019), 831-833. doi: 10.1126/science.1065467.
18. Ibrahim, I. and Abdulazeez, A., "The role of machine learning algorithms for diagnosing diseases", *Journal of Applied Science and Technology Trends*, Vol. 2, No. 01, (2021), 10-19. doi: 10.38094/jastt20179.
19. Chhogyal, K. and Nayak, A., "An empirical study of a simple naive bayes classifier based on ranking functions", in AI 2016: Advances in Artificial Intelligence: 29th Australasian Joint Conference, Hobart, TAS, Australia, December 5-8, 2016, Proceedings 29, Springer., (2016), 324-331.
20. Kumar, A., Bharti, R., Gupta, D. and Saha, A.K., "Improvement in boosting method by using rustboost technique for class imbalanced data", in Recent Developments in Machine Learning and Data Analytics: IC3 2018, Springer., (2019), 51-66.
21. Biau, G. and Scornet, E., "A random forest guided tour", *Test*, Vol. 25, (2016), 197-227. doi: 10.1007/s11749-016-0481-7.
22. Paul, S., Ranjan, P., Kumar, S. and Kumar, A., "Disease predictor using random forest classifier", in 2022 International Conference for Advancement in Technology (ICONAT), IEEE., (2022), 1-4.
23. Negaresh, F., Kaedi, M. and Zojaji, Z., "Gender identification of mobile phone users based on internet usage pattern", *International Journal of Engineering, Transactions B: Applications*, Vol. 36, No. 2, (2023), 335-347. doi: 10.5829/IJE.2023.36.02B.13.
24. Ren, Q., Cheng, H. and Han, H., "Research on machine learning framework based on random forest algorithm", in AIP conference proceedings, AIP Publishing LLC. Vol. 1820, (2017), 080020.
25. Speiser, J.L., Miller, M.E., Tooze, J. and Ip, E., "A comparison of random forest variable selection methods for classification prediction modeling", *Expert Systems with Applications*, Vol. 134, (2019), 93-101. <https://doi.org/10.1016/j.eswa.2019.05.028>
26. Van Houdt, G., Mosquera, C. and Nápoles, G., "A review on the long short-term memory model", *Artificial Intelligence Review*, Vol. 53, (2020), 5929-5955. <https://doi.org/10.1007/s10462-020-09838-1>
27. Men, L., Ilk, N., Tang, X. and Liu, Y., "Multi-disease prediction using lstm recurrent neural networks", *Expert Systems with Applications*, Vol. 177, (2021), 114905. <https://doi.org/10.1016/j.eswa.2021.114905>
28. Christianini, N. and Shawe Taylor, J., *An introduction to support vector machines*, cambridge univ. 2000, Press.
29. Vijayarani, S. and Dhayanand, S., "Liver disease prediction using svm and naïve bayes algorithms", *International Journal of Science, Engineering and Technology Research (IJSETR)*, Vol. 4, No. 4, (2015), 816-820.
30. Le, H.M., Tran, T.D. and Van Tran, L., "Automatic heart disease prediction using feature selection and data mining technique", *Journal of Computer Science and Cybernetics*, Vol. 34, No. 1, (2018), 33-48. doi: 10.15625/1813-9663/34/1/12665.
31. Asghari Beirami, B. and Mokhtarzade, M., "Ensemble of log-euclidean kernel svm based on covariance descriptors of multiscale gabor features for face recognition", *International Journal of Engineering, Transactions B: Applications*, Vol. 35, No. 11, (2022), 2065-2071. doi: 10.5829/IJE.2022.35.11B.01
32. Rahman, A.S., Shamrat, F.J.M., Tasnim, Z., Roy, J. and Hossain, S.A., "A comparative study on liver disease prediction using supervised machine learning algorithms", *International Journal of Scientific & Technology Research*, Vol. 8, No. 11, (2019), 419-422.

Persian Abstract

چکیده

پیش‌بینی بیماری یک انسان به معنای پیش‌بینی احتمال بیماری‌ای است که بیمار ممکن است پس از بررسی ترکیبی از علائم بیمار داشته باشد. نظارت بر وضعیت و اطلاعات سلامتی بیمار در معاینه اولیه می‌تواند به پزشکان در درمان موثر وضعیت بیمار کمک کند. این تجزیه و تحلیل در صنعت پزشکی منجر به درمان ساده و سریع بیمار می‌شود. محققان قبلی عمدتاً بر مدل‌های یادگیری ماشینی عمدتاً از ماشین بردار پشتیبانی (SVM)، K-نزدیک‌ترین همسایگان (KNN) و RUSboost برای تشخیص بیماری‌ها با علائم به عنوان پارامتر تأکید کرده‌اند. با این حال، داده‌های مورد استفاده محققین قبلی برای آموزش مدل تغییر نکرده و مدل کاملاً به علائم وابسته است، در حالی که دقت آنها ضعیف است. با این وجود، نیاز به طراحی یک مدل اصلاح شده برای دقت بهتر و پیش‌بینی زودهنگام بیماری‌های انسانی وجود دارد. مدل پیشنهادی با حل مسئله مدل‌های محقق قبلی، مدل کارایی و دقت را بهبود بخشیده است. مدل پیشنهادی از مجموعه داده‌های پزشکی استفاده می‌کند و داده‌ها را با اختصاص وزن‌ها بر اساس نادر بودن آنها تبدیل می‌کند. سپس این مجموعه داده با استفاده از ترکیبی از الگوریتم‌های یادگیری ماشینی آموزش داده می‌شود: SVM، LSTM، Random Forest و SVM. به موازات این، تاریخچه بیمار را می‌توان با استفاده از الگوریتم LSTM تجزیه و تحلیل کرد. سپس از SVM برای نتیجه‌گیری از بیماری احتمالی استفاده می‌شود. مدل پیشنهادی در مقایسه با روش‌های پیشرفته، دقت و قابلیت اطمینان بهتری را به دست آورده است. مدل پیشنهادی برای کمک به توسعه در اتوماسیون صنایع بهداشت و درمان مفید است.



Irradiation and Temperature Estimation with a New Extended Kalman Particle Filter for Maximum Power Point Tracking in Photovoltaic Systems

M. Hooshmand, H. Yaghibi*, M. Jazaeri

Faculty of Electrical and Computer Engineering, Semnan University, Semnan, Iran

PAPER INFO

Paper history:

Received 14 February 2023

Received in revised form 29 March 2023

Accepted 30 March 2023

Keywords:

Photovoltaic Systems

Maximum Power Point Tracking Particle Filter

Extended Kalman Filter

Estimation

ABSTRACT

In this paper, a new method, based on the estimation of irradiation and temperature values, was proposed for Maximum Power Point Tracking (MPPT) in photovoltaic systems. The proposed estimation method is based on a new Extended Kalman Particle Filter (EKPF). Given that the basis of the proposed method is a particle filter, firstly, the estimation is performed with high accuracy, although the target system has severe nonlinearity; secondly, there is no limitation for the probability density functions of the measurement and process noise. This method works for Gaussian and non-Gaussian noises. To show the estimation accuracy, the proposed method will be compared with the common method based on extended Kalman filter (EKF) and both methods will be evaluated due to the root means square error criterion. Due to the accurate estimation, MPPT is performed with good performance. For validation, the proposed MPPT method was compared with the EKF method and the conventional incremental conductance (InC) method. The simulations show that the efficiency is improved from 0.1% to 1% compared to the EKF, and from 0.8% to 8.65% compared to the InC method, which shows the performance of the proposed MPPT method in noisy environments.

doi: 10.5829/ije.2023.36.06c.08

1. INTRODUCTION

Increasing demand for electricity and increasing attention paid to the environmental impacts of the conventional electricity generation, have led the world to focus on using renewable energy sources such as fuel cells, wind power, and photovoltaic systems. Due to the many advantages of photovoltaic (PV) systems, the demand for electricity generation by them, both on-grid and off-grid, is increasing [1, 2]. The power generated in a PV module depends on the amount of irradiation and its temperature. Therefore, with changing weather conditions, the output power changes [3]. The I-V characteristic of PV modules is nonlinear and has a specific point at which the power has its maximum value. This point is called the maximum power point (MPP). Therefore, an effective method for tracking the MPP is necessary to force the photovoltaic system to operate at this point in all weather conditions [4]. MPPT is one of the main components of photovoltaic

systems. In recent years, various techniques and methods have been proposed by researchers to track the MPP. Methods based on the relationship between MPP voltage and open-circuit voltage, or MPP current and short-circuit current are presented in literature [5, 6]. The drawback of this method is that some energy will be lost during the short-circuit and the open-circuit. Another common method is perturbation and observation (P&O). In P&O, first the current and voltage and consequently the power (P_1) are measured. By creating a perturbation in voltage or current in a certain direction, the power will be measured again (P_2). Then, P_2 is compared with P_1 ; if P_2 is more than P_1 , then the deviation is in the right direction; otherwise, it must be reversed. In this way, the maximum power point (P_{mpp}) and consequently the optimal point voltage (V_{mpp}) will be obtained [7-9]. P&O-based techniques have been widely acclaimed due to their simplicity and ease of implementation, although these techniques are limited to the inherent nature of oscillation

*Corresponding Author Institutional Email: yaghibi@semnan.ac.ir
(H. Yaghibi)

and noise in the system. Another common method is hill climbing (HC). The basic operation of this method is the same as P&O, but instead of perturbing the current or voltage, the duty cycle is perturbed to update the PV operating point. This algorithm can work based on fixed or variable step [10]. Due to the similarity, this method has the same advantages and drawbacks as P&O method does. Another common method that is widely used is InC. In this method, the slope of the P-V characteristic of the PV module is used to track the MPP. This method is based on the fact that the slope of the P-V characteristic is zero at the maximum power point, positive for output power less than MPP, and negative for output power greater than MPP. The MPP is obtained by deriving the output power function, with respect to the voltage, and setting it equal to zero. In fact, this method is performed by a stepwise comparison of the ratio of conductance derivative (dI/dV) with instantaneous conductance (I/V) [11, 12]. The InC method overcomes the inherent oscillation of the P&O method, although it is difficult to be implemented due to the presence of noise in the system. The aforementioned common methods are not accurate in rapid tracking of irradiation changes. Also, the presence of noise in real systems affects the performance of these methods. These methods are mainly used in combination with other methods [13, 14]. Also, different techniques are used to eliminate noise, which will result in the complexity of the system as well as the slowness of the tracker.

The attractiveness of the methods based on classical control theories and control concepts has prompted researchers to use some of these methods to track the maximum power point in PV systems. These methods are based on the mathematical model of the PV system and need the information of its parameters. The most common of these methods is the Kalman filter, which is widely used to estimate PV systems states. MPP tracking using the Kalman filter has been developed by Boutabba et al. [15], Motahhir et al. [16] and Farrokhi et al. [17]. Because of using Kalman filter, these methods are robust against noise. But due to linearization, the estimation error is significant. Owing to the severe nonlinearity of PV system equations, nonlinear versions of the Kalman filter (extended Kalman filter (EKF), Unscented Kalman Filter (UKF), etc.) have been developed for MPP tracking. Methods based on UKF stated by Abdelsalam et al. [18], EKF by Docimo et al. [19], and multiple model Kalman filter (MMKF) by Kumar et al. [20] have been proposed to estimate the states of PV systems for MPP tracking. In linear systems, the Kalman filter is the optimal estimator. Nonlinear versions of the Kalman filter can be used for nonlinear systems with Gaussian noise, but there is no reason for convergence and no proof that the resulting estimate is optimal. A method based on Bayesian inference is presented by Lefevre et al. [21] for MPP tracking, in this method there is no limitation on the

type of system (linear or nonlinear). Also, this method does not make any assumptions for the probability density function (PDF) of the process noise and measurement noises, and does not need to use temperature and irradiation sensors. This method has good performance, but since integration is done on probability distribution functions; it is very difficult to calculate them, so it requires a powerful computer processor. Using a hardware that can perform these calculations will greatly increase costs. Simon [22] has proposed particle filter to overcome the limitations of Kalman filter. This estimator has optimal estimation in linear and nonlinear models. It has more improved performance compared to nonlinear versions of the Kalman filter. It makes no assumptions for the PDF of the noise, and can perform well for both non-Gaussian and Gaussian noises. Considering the mentioned characteristics and the presence of non-Gaussian noise in the industry, it seems that the estimation of the states of PV systems (which have severe nonlinearity) based on particle filter is suitable for MPP tracking.

In this paper, a new MPP tracking method, which is based on irradiation and module temperature estimation, is proposed. The estimation is done with a new EKPF. Since the basis of the proposed estimation method is the particle filter, the target system can be nonlinear and there is no assumption for the PDF of the noise. Due to the use of the combination of Kalman and particle filters, the estimation accuracy has been greatly improved compared to the common methods based on the Kalman filter. This method tracks MPP quickly and has good performance in dynamic and static modes. In this method, expensive radiation and temperature sensors are not used. The structure of this paper is as follows: in section 2, the thermal and electrical models of the PV module are presented. The state space equations are explained in section 3. In section 4, the proposed MPPT method is presented. First, EKF and particle filter are introduced, then the proposed estimation method is described, and subsequently, the new $V_{m\text{pp\text{t}}}$ calculation method that uses the estimated values of temperature and irradiation is presented. In section 5, the simulation setup is explained. The simulations are done in MATLAB/SIMULINK. In section 6, the results are discussed, which confirm the effectiveness of the proposed method. Finally, in section 7, conclusions are presented.

2. THE CHARACTERISTICS OF PHOTOVOLTAIC MODULES

Photovoltaic cells use semiconductor materials to convert sunlight into electricity. The technology is very close to solid-state technology, which is used to make transistors and diodes. When a piece of p-type silicon, that is lightly

doped with boron, and n-type silicon, that is heavily doped with phosphorus, are brought together, a p-n junction is formed. When a photon is absorbed, an electron-hole pair is produced in the p-type region. Due to the built-in electric field, which points towards the p-type region, the electrons drift into the n-type region and the hole remains in place. By electrically connecting the two terminals of the p-n junction, almost all the electrons produced by the photon migrate to the n-type region through the connecting wire; thus, completing the circuit. Since each photovoltaic cell produces only about 0.5 volts, it is rarely used alone. By connecting the cells in series, a compact form called a module, which has more applications and is resistant to harsh weather conditions, is formed [23]. The output voltage and current of the module depend on such factors as the amount of irradiation and the module temperature. So, to analyze and study these effects, two electrical and thermal models for the module are required. These will be described in the next sections.

2. 1. Electrical Model Among the PV module models, the two models of single-diode and two-diode have been used in literature [24, 25]. Comparisons between single-diode and two-diode models show that both models have acceptable accuracy. Although the two-diode model is slightly more accurate, it has been used less frequently in research due to its high complexity. In contrast, due to the fact that the single-diode model requires fewer calculations and has a smaller number of parameters, it has been widely used in research articles [26, 27]. This paper uses a single-diode model that, while simple, is accurate enough. Figure 1 shows a single-diode equivalent circuit of a PV module. In general, the resistance of R_s series is very small and the parallel resistance of R_p is very large and it is often neglected [28]. Due to the presence of diodes in this equivalent circuit, current and voltage equations are nonlinear. The output current of the module is calculated according to Equations (1) to (4).

$$I = I_{pv} - I_d - I_p \quad (1)$$

$$I_{pv} = (I_{pv,n} + K_I(T - T_n))G/G_n \quad (2)$$

$$I_d = I_0 \left(\exp\left(q \frac{V + R_s I}{N_s k T a}\right) - 1 \right) \quad (3)$$

$$I_0 = \frac{I_{sc,n} + K_I(T - T_n)}{\exp\left(q \frac{V_{oc,n} + K_V(T - T_n)}{N_s k T a}\right) - 1} \quad (4)$$

where, I_{pv} , I_d , I_p , and I_0 are the photovoltaic current, diode current, parallel branch current, and diode saturation current, respectively. V and I are the voltage across the

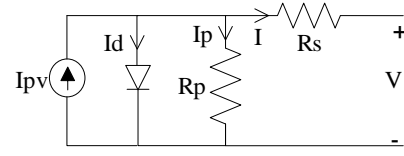


Figure 1. The equivalent circuit of the PV module

terminal and the module current, respectively.

T and G are the module temperature (in Kelvin) and the amount of irradiation (in kw/m^2), respectively. T_n and G_n are the nominal values of ambient temperature and irradiation, respectively. $V_{oc,n}$, $I_{sc,n}$, and $I_{pv,n}$ are the open-circuit voltage, short-circuit current, and photovoltaic current in standard irradiation and temperature, respectively. q is the charge of an electron, k is the Boltzmann constant, and parameter a is the diode ideality constant. The K_i and K_v constants indicate the relationship between the module temperature with the short-circuit current and the module temperature with the open-circuit voltage, respectively. Based on Equations (1) to (4), the I-V and P-V characteristic curves of the module are shown in Figure 2. In this figure, the effect of temperature and irradiation changes on the I-V and P-V curves as well as the MPP are specified.

2. 2. Thermal Model As shown in Figure 2 (c and d), the module temperature is one of the determining quantities of the MPP point in photovoltaic systems, so a suitable thermal model of photovoltaic modules is needed to determine MPP point. Different models are presented by Jones and Underwood [29], Mattei et al. [30] and Abdelhameed et al. [31] based on energy balance, multilayer model, and a model for hot spot conditions. In this work a thermal model, which is based on the simple method of energy balance, has been used. The photovoltaic module is approximated as a lumped capacity with a uniform temperature and the irradiation exchange between the module and its environment is neglected. After the sun radiates on the surface of the module, some of it is converted into electrical power by photovoltaic cells, and some of it changes the temperature of the module. Considering the amount of irradiation, the absorption coefficient, and heat exchange between the module and the surrounding environment, whether in the form of natural or forced convection, the final temperature of the module is determined. With these assumptions, the heat transfer equations of the PV module stated as follows:

$$\dot{x}_1 = (q_{sw} - q_{conv} - P_{out})/C_m \quad (5)$$

$$\begin{cases} q_{sw} = \alpha A_s w_1 \\ q_{conv} = A_s (h_{free} + h_{forced})(x_1 - w_2) \\ P_{out} = V_m I_m \end{cases} \quad (6)$$

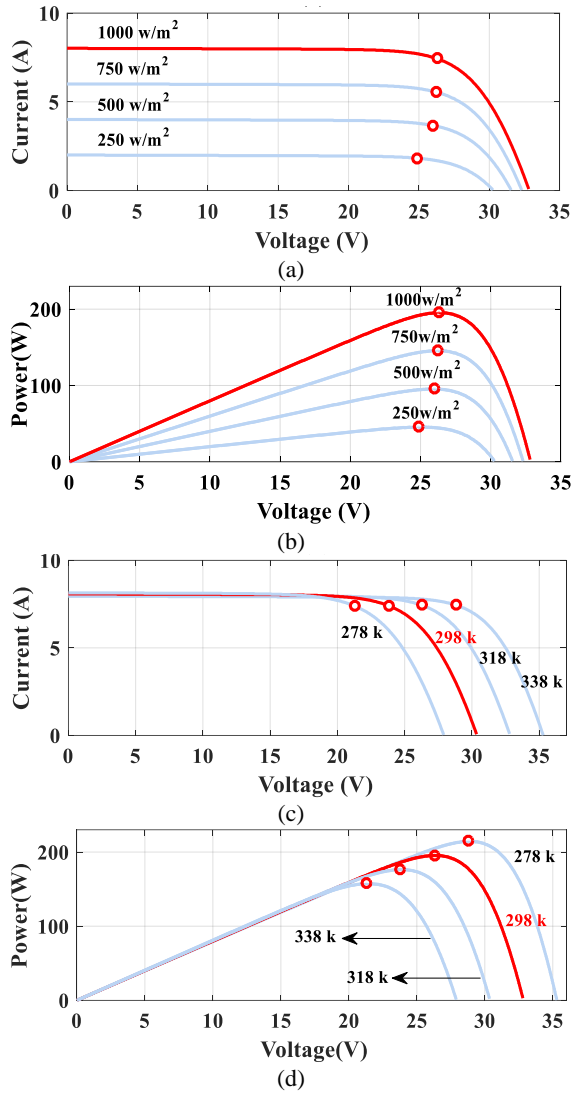


Figure 2. (a) and (b) I-V and P-V characteristic curves, respectively, for various irradiation and $T = 298$ k, (b) and (d) I-V and P-V characteristic curves for various temperature and $Irr = 1000$ w/m²

$$\begin{cases} h_{free} = 1.31(x_1 - w_2)^{1/3} \\ h_{forced} = 5.67 + 3.86w_3 \end{cases} \quad (7)$$

where, x_1 and w_2 are the module temperature and the ambient temperature, respectively. w_1 and w_3 are the irradiation value and wind speed in the area, V_m is the module voltage that is determined using MPP tracker, I_m is the output current of the module, which is multiplied by the voltage at which the output power (P_{out}) is obtained. Other parameters are described in Table 1. By combining Equations (5) to (7), the final equation of temperature changes will be calculated according to the climatic conditions of the region and the output power of the module as:

TABLE 1. Parameters of the Thermal Model of the PV Module

Parameter	Description
C_m	lumped thermal capacitance
q_{sw}	Short-wave radiation
q_{conv}	free and forced convection
A_s	module's surface area
A	Absorptivity
h_{free}	free convection coefficients
h_{forced}	forced convection coefficients

$$\begin{aligned} \dot{x}_1 = & \frac{1}{C_m} (\alpha A_s w_1 - A_s (1.31(x_1 - w_2))^{1/3} + 5.67 \\ & + 3.86w_3) \times (x_1 - w_2) - V_m I_m \end{aligned} \quad (8)$$

3. STATE SPACE EQUATIONS

The irradiance during a clear day follows a sinusoidal pattern. In this work, x_2 and x_3 states are used to model irradiation. Irradiation state equations are presented in Equation (9).

$$\begin{cases} \dot{x}_2 = x_3 + \Omega \\ \dot{x}_3 = -f^2 x_2 \\ x_2(0) = 0, x_3(0) = Af \end{cases} \quad (9)$$

where x_2 is irradiation value, f represents the frequency of the sine wave and depends on the number of sunny hours during the day, and A is the peak of irradiation during the day. Cloud cover changes affect the amount of solar irradiation on the photovoltaic module and it causes the irradiation to deviate from the sinusoidal shape. To consider these conditions, process noise Ω will be used in the equations, that is added to the irradiation state equation, as presented in this equation. By substituting Equation (2) to Equation (4) into Equation (1) and transferring all the factors to the left of the equation, the output current equation will be obtained. Voltage and current values are measured with sensors with measurement noises v_{u2} and v_y . In Equation (1), by substituting $G = w_1$, $T = x_1$, $I = y$ and $V = u$; in Equation (8), by substituting $w_1 = x_2$, $I_m = y$ and $V_m = u$, the variables are unified. In Equation (8), the voltage has the process noise v_{u1} because the voltage cannot be completely controlled, the wind speed and ambient temperatures are measured with the noise sensors v_{w2} and v_{w3} , respectively. In this way, the state space equations are expressed as follows:

$$\begin{cases} \dot{X} = f(X, U, \omega) \\ g(X, u, y, v) = 0 \end{cases} \quad (10)$$

where in these equations, the input vector, noise vectors, state vector, and the probability distribution function of process noise and measurement noise are presented in Equation (11).

$$\begin{cases} U = [u, w_2, w_3], \omega = [\Omega, v_{u1}, v_{w2}, v_{w3}] \\ \Omega = N(0, \sigma_\Omega), v_{u1} = N(0, \sigma_{u1}) \\ v_{w2} = N(0, \sigma_{w2}), v_{w3} = N(0, \sigma_{w3}) \\ v = [v_{u2}, v_y], v_{u2} = N(0, \sigma_{u2}), v_y = N(0, \sigma_y) \\ X = [x_1, x_2, x_3] \end{cases} \quad (11)$$

4. PROPOSED MPPT METHOD

In this section, the proposed maximum power point tracking method is presented. The module temperature and irradiation are required to track the MPP. These values are estimated by the proposed method which is very accurate; they are plugged into Equations (1) to (4), and then the V_{mpp} value is calculated through a new technique and applied to the converter. Highly accurate estimates lead to accurate V_{mpp} calculations which improve efficiency, thereby increasing the daily energy generation of the photovoltaic system. In this section, the conventional EKF, the standard particle filter, the proposed estimation method, and the proposed V_{mppt} calculation technique are presented, respectively.

4.1. Extended Kalman Filter The Kalman filter uses recursive least squares (RLS) to estimate the states of linear systems in noisy environments. This filter uses time and measurement updates and it works recursively and over time. The effect of noise on the system is reduced due to the recursive cycle and finally leads to the actual measurement value [22]. The EKF is a non-linear version of the Kalman filter and is suitable for nonlinear systems. The system is linearized around the point of the previous step, and after extracting the equations, the linear Kalman filter is applied to it. System equations are assumed as Equation (12).

$$\begin{cases} x_k = f_{k-1}(x_{k-1}, u_{k-1}, \omega_{k-1}) \\ y_k = h_k(x_k, u_k, v_k) \\ \omega_k \approx N(0, Q_k) \\ v_k \approx N(0, R_k) \end{cases} \quad (12)$$

where $x_k \in R_m$ is the state of the system, and $y_k \in R_m$ is the measured output of the system in step k . ω and v are process and measurement noise, respectively; which have Gaussian PDF, with zero mean value, and covariance matrices Q and R . u and y are the input and output of the system, respectively. $f(\cdot)$ and $h(\cdot)$ are the

nonlinear functions of the system and measurement, respectively. Assuming that the equations of the system are in the form of Equation (12), the state's estimation of the system is obtained through the following steps.

a. Initializing

$$\begin{cases} \hat{x}_0^+ = E(x_0) \\ P_0^+ = E[(x_0 - \hat{x}_0^+)(x_0 - \hat{x}_0^+)^T] \end{cases} \quad (13)$$

b. Time update stage

$$\begin{cases} F_{k-1} = \left. \frac{\partial f_{k-1}}{\partial x} \right|_{\hat{x}_{k-1}^+} \\ L_{k-1} = \left. \frac{\partial f_{k-1}}{\partial \omega} \right|_{\hat{x}_{k-1}^+} \\ P_k^- = F_{k-1} P_{k-1}^+ F_{k-1}^T + L_{k-1} Q_{k-1} L_{k-1}^T \\ \hat{x}_k^- = f_{k-1}(\hat{x}_{k-1}^+, u_{k-1}, 0) \end{cases} \quad (14)$$

c. Measurement update stage

$$\begin{cases} H_k = \left. \frac{\partial h_k}{\partial x} \right|_{\hat{x}_k^-} \\ M_k = \left. \frac{\partial h_k}{\partial v} \right|_{\hat{x}_k^-} \\ K_k = P_k^- H_k^T (H_k P_k^- H_k^T + M_k R_k M_k^T)^{-1} \\ \hat{x}_k^+ = \hat{x}_k^- + K_k [y_k - h_k(\hat{x}_k^-, u_k, 0)] \\ P_k^+ = (I - K_k H_k) P_k^- \end{cases} \quad (15)$$

where \hat{x}_k^- and \hat{x}_{k-1}^+ are the estimation of states in k and $k-1$, time step, respectively. The “+” and “-” superscripts indicate the posteriori and priori estimates, respectively. P_k is the error covariance matrix in the time step k , and K_k is Kalman gain.

4.2. Standard Particle Filter Particle filtering is a statistical method for estimating states. This filter is often used to estimate the states of systems with severe nonlinearity. The particle filter is based on the Bayesian state estimator. In fact, the purpose of this estimator is to find the PDF of the states assuming measurements y_1, y_2, \dots, y_k , and the initial conditions x_0 . The Bayesian state estimator has two steps: the calculation of the priori and posteriori PDF, respectively, and in accordance with Equations (16) and (17).

$$\begin{aligned} p(x_k | Y_{k-1}) &= \int p(x_k | x_{k-1}) p(x_{k-1} | Y_{k-1}) dx_{k-1} \\ Y_{k-1} &= y_1, y_2, \dots, y_{k-1} \end{aligned} \quad (16)$$

$$\begin{aligned} p(x_k | Y_k) &= \frac{p(y_k | x_k) p(x_k | Y_{k-1})}{\int p(y_k | x_k) p(x_k | Y_{k-1}) dx_k} \\ Y_k &= y_1, y_2, \dots, y_k \end{aligned} \quad (17)$$

In these equations, integration is performed on probability distribution functions. Normally, the

analytical response of these equations is very difficult due to the large dimensions of the state space and can only be calculated for very specific systems. The numerical calculation of these integrals is also a very tedious and time-consuming task. The particle filter solves this problem; in fact, the particle filter has been developed to numerically implement the Bayesian state estimator. This filter estimates signals by sampling, these samples are called particles [32-34]. The sampling process is performed on the system's dynamic equation, and the samples are weighted using the measurement equation, then based on these samples and their weights, the optimal estimate of the stochastic signal is obtained. System equations are assumed to be as Equation (10). The PDF of the process noise (ω) and the measurement noise (v) are not necessarily Gaussian, and just knowing the distribution is enough and the type of distribution is not important. With these assumptions, the particle filter algorithm estimates the states of the system as follows [33, 34]. In these steps, note that $p(\cdot)$ means the probability distribution function, not the probability value. The index i is the particle number, index k is the time step ($k = 0, 1, \dots$), and the superscripts “-” and “+” represent the priori and posteriori estimates, respectively.

1. Assuming that the initial PDF of the state $p(x_0)$ is known, first the N vector is generated randomly, and based on the initial PDF $p(x_0)$, these vectors are called particles and are denoted by $x_{0,i}^+$ ($i = 1, \dots, N$). The N parameter is a trade-off between the estimate accuracy and the amount of calculations and is determined by the designer.
2. In each time step $k = 1, 2, \dots$ the following steps will be performed.
 - a. Using the nonlinear equation of the system ($f(\cdot)$) and the known PDF of the process noise, the time propagation is performed to calculate the priori particles by Equation (18).

$$x_{k,i}^- = f_{k-1}(x_{k-1,i}^+, u_{k-1}, w_{k-1}^j) \quad (i = 1, \dots, N) \quad (18)$$

In this equation, each noise vector is generated randomly based on a known PDF of w_{k-1} .

- b. Once the measurement in step k is received, the relative likelihood q_i of each particle conditioned on the measurement y_k is calculated. This is done by evaluating the PDF ($p(y_k|x_{k,i})$) based on the nonlinear measurement equation ($h(\cdot)$) and the specified PDF of the measurement noise.
- c. The resulting likelihoods are normalized based on the following equation.

$$\bar{q}_i = \frac{q_i}{\sum_{j=1}^N q_j} \quad (19)$$

The sum of the total likelihood is now equal to one.

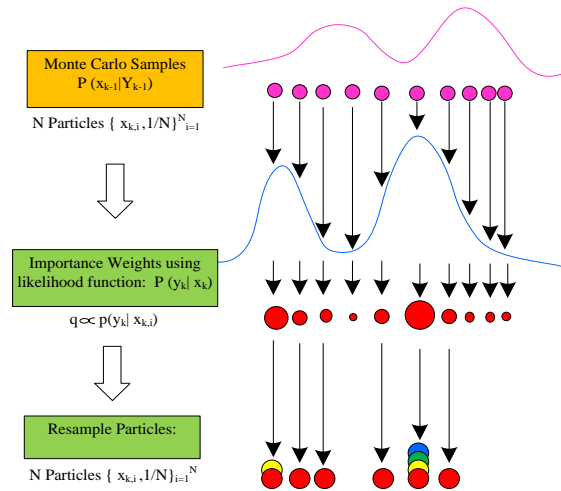


Figure 3. SIR method in solving particle impoverishment problem [33]

- d. Posteriori particles $x_{k,i}^+$ are produced based on q_i likelihoods. This step is called re-sampling. This is possible in several ways. The particle impoverishment is one of the problems that the process of sampling and signal estimation will face with if improper methods are used; however, the resampling algorithm is used to solve it. Figure 3 shows the most common SIR algorithm. In this method when $N_{eff} = 1 / \sum_{i=1}^N \bar{q}_i^2 < N_{thr}$ the resampling operation is performed in such a way that the weight of all the samples is converted to $1/N$ and then the re-weighting is performed. In this way, less valuable samples are automatically removed after a few steps.
- e. We now have a set of new particles $x_{k,i}^+$ distributed according to $p(x_k/y_k)$, so we can calculate any statistical criterion of this PDF. We are often only interested in calculating the mean and the covariance.

4. 3. Proposed Estimation Method To improve the performance of the particle filter, one of the proposed methods is to combine it with non-linear versions of the Kalman filter (EKF, UKF or CKF). In the proposed estimation method, the improved particle filter is combined with EKF. In the proposed method, particle classification is used in the resampling step. This makes the proposed combined filter very accurate in estimating system states, even if the system has severe nonlinearity. The proposed method in this paper is named EKPF in short. In this approach, each particle is updated by the EKF at the measurement time, and then resampling is performed using the measurement. In the proposed method, there is no assumption for the probability density functions. This method works correctly for Gaussian and

non-Gaussian noises. The steps of this method are as follows;

1. Equations of system and measurement are assumed according to Equation (10). Independent white noises ω_k and ν_k are considered with specific PDF. The covariance matrices of the noises are defined as Equation (20).

$$\begin{aligned} Q &= \text{diag}(\sigma_{\Omega}, \sigma_{u1}, \sigma_{w2}, \sigma_{w3}) \\ R &= \text{diag}(\sigma_{u2}, \sigma_y) \end{aligned} \quad (20)$$

2. It is assumed that the initial PDF of system states is $p(x_0)$. Based on this PDF, N number of primary particles are produced randomly. For $i = 1, \dots, N$, these particles are named $x_{0,i}^+$ and their covariance is named

$P_{0,i}^+ = P_0^+$. The number of particles is determined based on the trade-off between the calculations amount and the accuracy of the estimation.

3. The following steps are performed for $k = 1, 2, \dots$.
 - a. The time propagation step is performed using the known PDF of the process noise and the known process equation, to obtain a priori particles $x_{0,i}^+$ and covariances $P_{k,i}^-$.

$$\begin{cases} F_{k-1,i} = \left. \frac{\partial f_{k-1}}{\partial X} \right|_{x=x_{k-1,i}^+} \\ L_{k-1,i} = \left. \frac{\partial f_{k-1}}{\partial \omega} \right|_{x=x_{k-1,i}^+} \\ \hat{x}_{k,i}^- = f_{k-1}(\hat{x}_{k-1,i}^+, u_{k-1}, w_{2k-1,i}, w_{3k-1,i}, \omega_{k-1}^+) \\ P_{k,i}^- = F_{k-1,i} P_{k-1,i}^+ F_{k-1,i}^T + L_{k-1,i} Q L_{k-1,i}^T \end{cases} \quad (21)$$

where ω_{k-1}^+ noise vector is generated randomly based on the known PDF of ω_{k-1} , and L and F are Jacobin matrices.

- b. The priori particles and their covariance are updated and their posteriori values are obtained by Equation (22)

$$\begin{cases} H_{k,i} = - \left. \frac{\partial g_k}{\partial X} \left(\frac{\partial g_k}{\partial y} \right)^{-1} \right|_{x=\hat{x}_{k,i}^-} \\ M_{k,i} = - \left. \frac{\partial g_k}{\partial \nu} \left(\frac{\partial g_k}{\partial y} \right)^{-1} \right|_{x=\hat{x}_{k,i}^-} \\ K_{k,i} = P_{k,i}^- H_{k,i}^T (H_{k,i} P_{k,i}^- H_{k,i}^T + M_{k,i} R_k M_{k,i}^T)^{-1} \\ \hat{x}_{k,i}^+ = \hat{x}_{k,i}^- + K_{k,i} [y_{k,i} - \hat{y}_{k,i}] \\ P_{k,i}^+ = (I - K_{k,i} H_{k,i}) P_{k,i}^- \end{cases} \quad (22)$$

where H and M are Jacobian matrices, and K is the Kalman gain for i th particle. y_k is found at the reference point by solving the output Equation (10).

- c. The relative likelihood q_i of each posteriori particle $x_{k,i}^+$ is calculated under the condition of measurement y_k . This is done by evaluating the PDF $p(y_k | x_{k,i}^+)$, based on the nonlinear measurement equation g and the PDF of the measurement noises.
- d. The relative likelihoods obtained from the previous step are scaled by Equation (19). Now the sum of all of them equals to one.
- e. Based on the calculated likelihoods and the following resampling method, the posterior particles $x_{k,i}^+$ and the covariance $P_{k,i}^+$ will be refined.

The adopted resampling algorithm is that the particles are divided into three classes based on their weight. The values of the maximum and minimum thresholds (q_{trmax} and q_{trmin}), i. e. the boundary between the classes, are defined. The samples will be classified according to Equation (23).

$$\tilde{x}_{k+1} = \begin{cases} 0 & \tilde{q}_{k,i} < q_{thr\ min} \\ x_{k+1} & q_{thr\ min} < \tilde{q}_{k,i} < q_{thr\ max} \\ fission & \tilde{q}_{k,i} > q_{thr\ min} \end{cases} \quad (23)$$

And then, if $N_{eff} \leq N_{thr}$, the resampling step is done. It is assumed that the P particles are in the first class. K is the number of particles in the second class and the $N-P-K$ particles are in the third class. Class 1 particles are removed, class 2 particles remain unchanged, and class 3 particles are divided into several particles according to their weight and Equation (24)

$$m_i = [q_{k,i} (N - P - k)] \quad i = 1, 2, \dots, N - P - K \quad (24)$$

where m is the number of particles produced based on weight $q_{k,i}$ and $[..]$ is the integer function. In this algorithm, the breaking method is used, and to calculate the weight of the broken particles, relation (25) will be used.

$$q_{k,i'} = q_{k-1,i} \times p(y_k | x_{k,i'}) \quad (25)$$

Figure 4 shows the particle classification process.

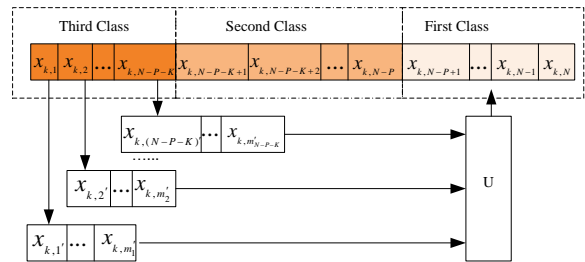


Figure 4. Particle weight classification process

f. We now have a set of new particles $x_{k,i}^+$ distributed according to $p(x_k/y_k)$, so we can calculate any statistical criterion of this PDF. Figure 5 shows the general algorithm of the proposed estimation method.

4. 4. Proposed V_{mpp} Calculation Method As shown in Figure 2, the PV module has different P-V characteristics for different amounts of irradiation and temperature, each with a different V_{mpp} value. Therefore, the irradiation and module temperature are two important quantities in determining the MPP. After each measurement, the proposed estimation method estimates the irradiation and module temperature. The tracker uses these values as input and determines the V_{mpp} based on the P-V equations. This is done by deriving the power equation, with respect to the voltage, and setting it to zero. By multiplying the two sides of Equation (1) by V , we have:

$$V \times I = V \times (I_{pv} - I_0 (\exp(q \frac{V + R_s I}{N_s k T a}) - 1) - \frac{V + R_s I}{R_p}) \quad (26)$$

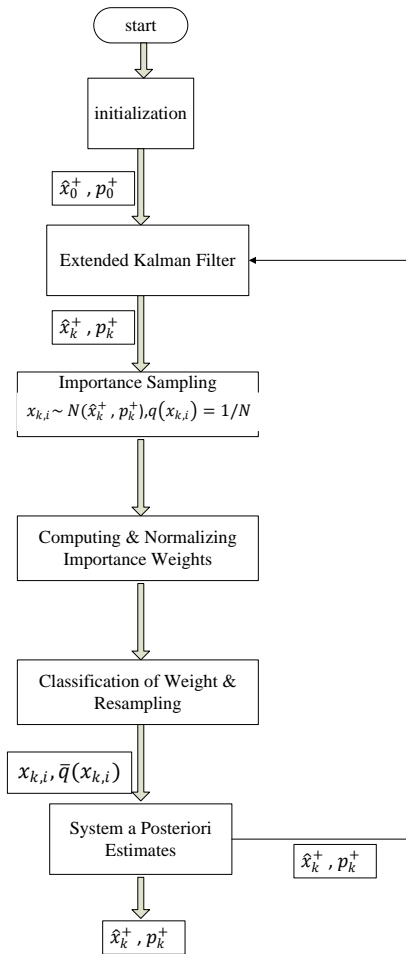


Figure 5. The proposed estimation algorithm

By replacing $I = P / V$ we have:

$$P - V(I_{pv} - I_0 (\exp(q \frac{V + R_s P / V}{N_s k T a}) - 1) - \frac{V + R_s P / V}{R_p}) = 0 \Rightarrow g(P, V) = 0 \quad (27)$$

By deriving P, with respect to V, we have:

$$\frac{dP}{dV} = - \frac{\partial g}{\partial V} (\frac{\partial g}{\partial P})^{-1} = 0 \quad (28)$$

where V and P are inseparable. This equation is solved by numerical methods in a certain voltage range. In this work, the Newton-Raphson method is used to solve the equation, because this method converges rapidly. The resulting voltage is immediately applied to the DC/DC converter to achieve maximum power. The voltage is kept constant until the next measurement is obtained. In this method, no data is stored, so no memory is required to store the data. Storing more data is a burden over any numerical solution. Therefore, this method is superior to the methods based on look-up table.

5. SIMULATION SETUP

The configuration of the simulation setup is shown in Figure 6. Climatic conditions (wind, sunlight, etc.) are applied to the module by the environment. The values of wind speed, ambient temperature, voltage and current are measured by sensors, then each of these quantities, which has an independent noise, are applied to the estimator. Estimation by the proposed method determines the amount of irradiation and module temperature. These values are applied as input to the MPP Tracker to determine the optimal point. No assumptions are made for noise distribution in the proposed method, but to be able to compare the proposed method with the EKF method, we assume that the noise is Gaussian. All variance values of noise, as well as initial values of

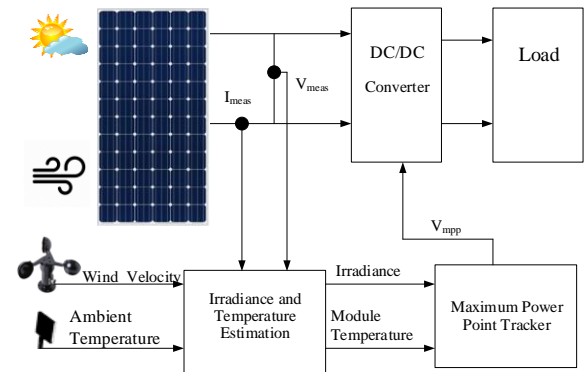


Figure 6. Simulation setup configuration

covariance and system states, are similar to the values reported in the literature [19].

It is assumed that all noises are uncorrelated and have zero mean value, although there is no need for this, and correlated noises with a non-zero mean value can be used with small changes in the equations. All values of noise variance are presented in Table 2. The initial values of the states and error covariances are presented in Equations (29) and (30), which are the expected values at the beginning of the PV module operation.

$$\hat{x}_{00} = [\tilde{w}_0(0), 0, (1000W/m^2)f]^T \tag{29}$$

$$P_{00} = \text{diag} \left((3k)^2, (50W/m^2)^2, (0.02 \frac{W \text{ rad}}{m^2 s})^2 \right) \tag{30}$$

A 250-watt module is used for simulation. All values of the parameters of the electric and thermal models are shown in Table 3. Environmental inputs for simulation, including irradiation, wind speed, and ambient temperature, have been obtained from the National Wind Technology Center (NWTC, 2016). Three sets of M2 tower data in Boulder, Colorado have been used. Dates are selected in a way that different weather conditions could be applied to the system. A day with a clear sky (May 28, 2014), a partly cloudy day (May 13, 2014), and a severely cloudy day (May 11, 2014) have been chosen. The values of irradiation, ambient temperature, and wind speed on the dates mentioned are shown in Figure 7. These values are used in Equations (2) and (8) to calculate the actual values of radiation and module temperature.

TABLE 2. Noise variance values

Variance	Value
\sum_{w2}	$(0.1 K)^2$
\sum_{w3}	$(1m/s)^2$
\sum_{u1}	$(0.1V)^2$
\sum_{u2}	$(0.01V)^2$
\sum_y	$(0.05A)^2$
\sum_Q	$(1W/m^2s)^2$

TABLE 3. System Parameters

Parameter	Value
A_s	0.8 (m^2)
C_m	4580 (J/K)
$I_{pv,n}$	8.02 (A)
K_i	0.0032 (A/K)
T_n	298 (k)
G_n	1000 ($W/m2$)
$I_{sc,n}$	8.21 (A)
q	$1.60217646 \cdot 10^{-19}$ (C)
$V_{oc,n}$	32.9 (V)
K_v	-0.1230 (V/K)
a	1.3
N_s	54
k	$1.3806503 \cdot 10^{-23}$ (J/K)
R_s	0.221 (Ω)
R_p	415.405 (Ω)
α	0.7

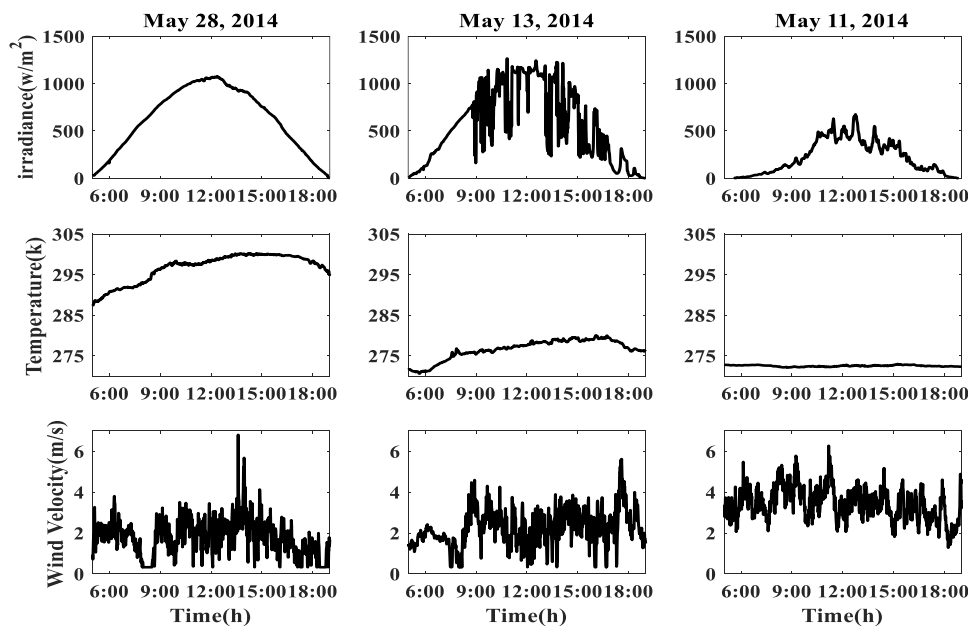


Figure7. Values of wind speed, irradiation, and ambient temperature on May 28, May 13, and May 11 2014

Given that the data is measured for every minute, the simulation step will be 60 seconds. The system's continuous equations are discretized by the Euler method with a time step of $T=60$ s. The number of particles in the simulation is considered to be $N=100$.

6. SIMULATION RESULTS

In order to confirm the accuracy of the estimated values, the proposed estimation method was compared with the common estimation method based on EKF. Both methods are simulated in similar atmospheric conditions. Gaussian noise with variance values presented in Table 2 was applied to both methods. The root means square error (RMSE) criterion will be used to compare the estimation error. Since the irradiation and module temperature are accurately estimated, the MPP is tracked with good accuracy in the proposed method. To verify this, the proposed method is compared with the EKF-based method and the common traditional method of InC in terms of the generated power. Also, these methods were compared in terms of efficiency, which can be calculated from Equation (31)

$$\eta_{mpp} = \frac{\sum_j i_{meas,j} v_{meas,j} \Delta t_j}{\sum_k i_{MPP,k} v_{MPP,k} \Delta t_k} \tag{31}$$

where i_{meas} and v_{meas} are the current and voltage of the PV

module during the j 'th time interval (Δt_j), respectively. i_{MPP} and v_{MPP} are the current and voltage of the MPP during the k 'th time interval (Δt_k), respectively. The methods were compared in different weather conditions, a day with a clear sky, a partly cloudy day, and a severely cloudy day.

6. 1. Clear Skies

The data for this condition is shown in Figure 7 for 28 May 2014. From top to bottom, the amount of radiation, ambient temperature and wind speed during the day are shown in this figure, respectively. As seen in the figure, the irradiation follows a sinusoidal trend. Figure 8 shows the performance of irradiation and temperature estimation with the proposed estimation method and EKF. As can be seen in Figures 8 (a and b), the temperature estimation error in the proposed method (except for the case of initial conditions) is less than 0.2K, while it is about 5K in EKF. The RMSE in the proposed method is 0.0053, which, compared to the number 0.04 for the EKF method, indicates the appropriate accuracy of the proposed method in estimating the temperature. In Figures 8 (c and d), the real value of irradiation is compared with its estimated value by the proposed and EKF methods. Estimation errors in Figure 8(d) indicate that the maximum estimation error in the proposed method was $5W/m^2$, while in the EKF method it is about $30 w/m^2$. The RMSE value in the proposed method is 0.089, which indicates the accuracy of the proposed estimator, compared to the 0.258.

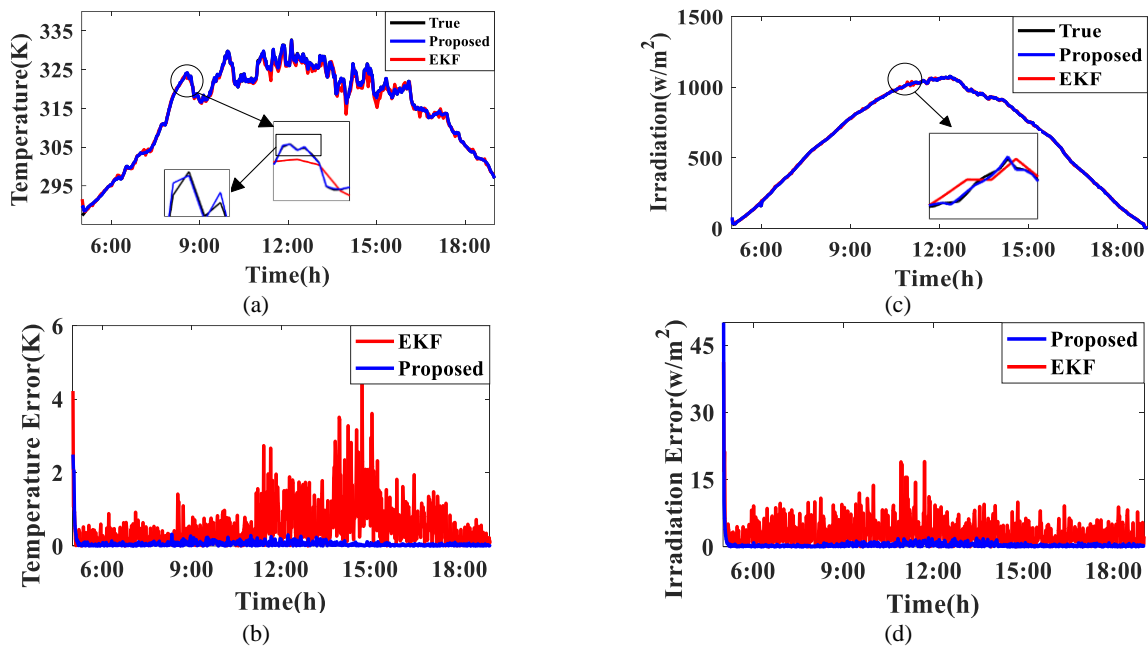


Figure 8. The comparison of actual and estimated values (Temperature and Irradiation) using the EKF and the proposed method in the first case (clear skies conditions- for May 28, 2014)

Figure 9 shows the generated maximum power of the PV module using the proposed method, the EKF-based method, and the InC method on a day with a clear sky in 2014. The results were compared with the real maximum power produced by the actual irradiation and module temperature. The error obtained from the three methods with the true power is also presented in this figure. The results show that in the proposed method, the maximum error is 0.1 watts, and for the EKF method, this value is increased to 1 watt and in the InC method it is about 6 watts. The proposed method has an efficiency of 99.99%, which is about 0.1% higher than the EKF method, and about 1% higher than the InC method. As a result, the proposed method produces 5.5 kJ more than the EKF method and about 50 kJ more than the InC method per day.

6. 2. The Partly Cloudy Sky Figure 7 shows the data for these conditions as of May 13, 2014. From top to bottom, the amount of radiation, ambient temperature and wind speed during the day are shown in this figure, respectively. Figure 10 shows a comparison of irradiation and temperature estimation performance using the proposed and EKF methods. The error in estimating the temperature in the proposed method (except for the case of initial conditions) in the semi-cloudy conditions is below 0.5 K, while it is about 4.5K in the EKF. The value of RMSE in the proposed method is 0.0027, which indicates the appropriate accuracy of the proposed estimator, compared to the number 0.029 for the EKF method. Figure 10 (c and d) shows the comparison of the

real and estimated values of irradiation by the proposed and the EKF methods. Errors indicate that the maximum estimate error in the proposed method is 2.5 w/m^2 , while it is about 28 w/m^2 in the EKF method. The value of RMSE in the proposed method is 0.065 and this value in EKF is 0.3.

Figure 11 shows the output power of the PV module using the proposed the EKF-based and the InC methods. The results were compared with the real maximum power generated by the actual irradiation and module temperature. The errors and their deviation from the true power are also presented in this figure. The results show that in the proposed method, the maximum output power error is less than 0.05 watts, and for the EKF method, this value is increased to 0.3 and in the InC method it is about 80 watts. The average efficiency of the proposed method is about 99.97, which is about 1.5% more than the EKF and about 7% more than the conventional InC method. This means that the proposed method generates about 33 kJ more than the EKF method and about 198 kJ more than the InC method daily.

6. 3. Severely Cloudy Skies The data for this condition is shown in Figure 7 for May 11, 2014. From top to bottom, the amount of radiation, ambient temperature and wind speed during the day are shown in this figure, respectively. Figure 12 shows a comparison of irradiation and temperature estimation performance with both the proposed and EKF methods. The maximum temperature estimation error in the proposed method (except for the case of initial conditions) is about 0.4 K,

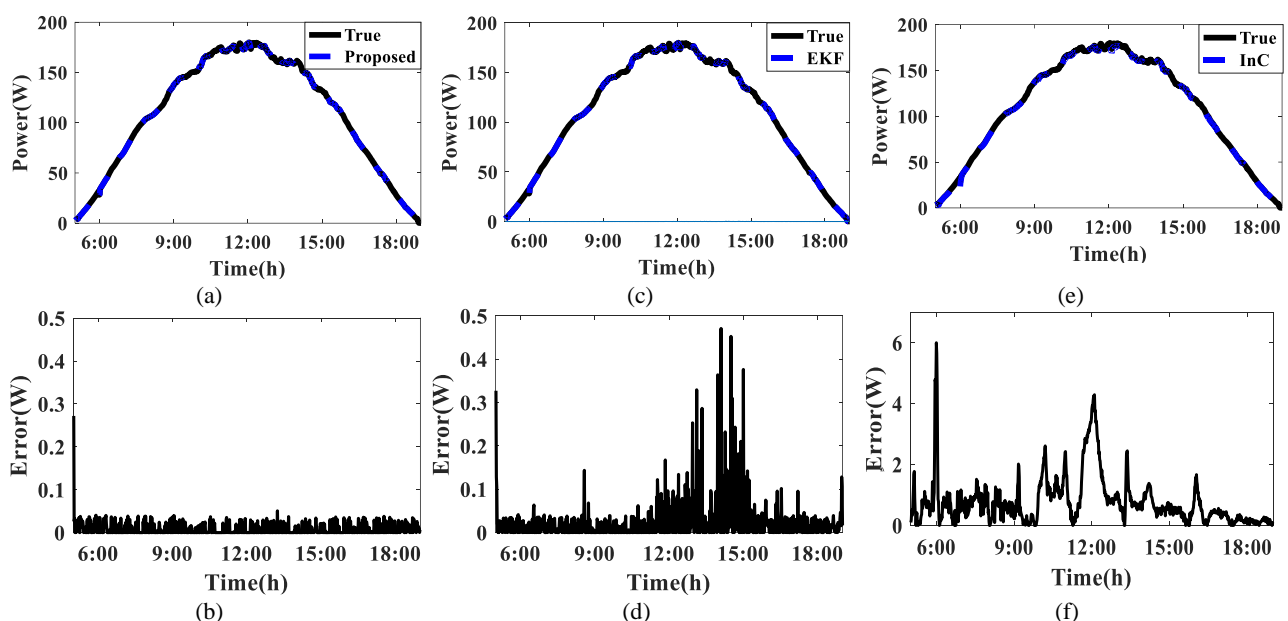


Figure 9. The comparison of the power generated by the PV module using the proposed method (a and b), EKF-based method (c and d), and InC method (e and f) in clear sky conditions

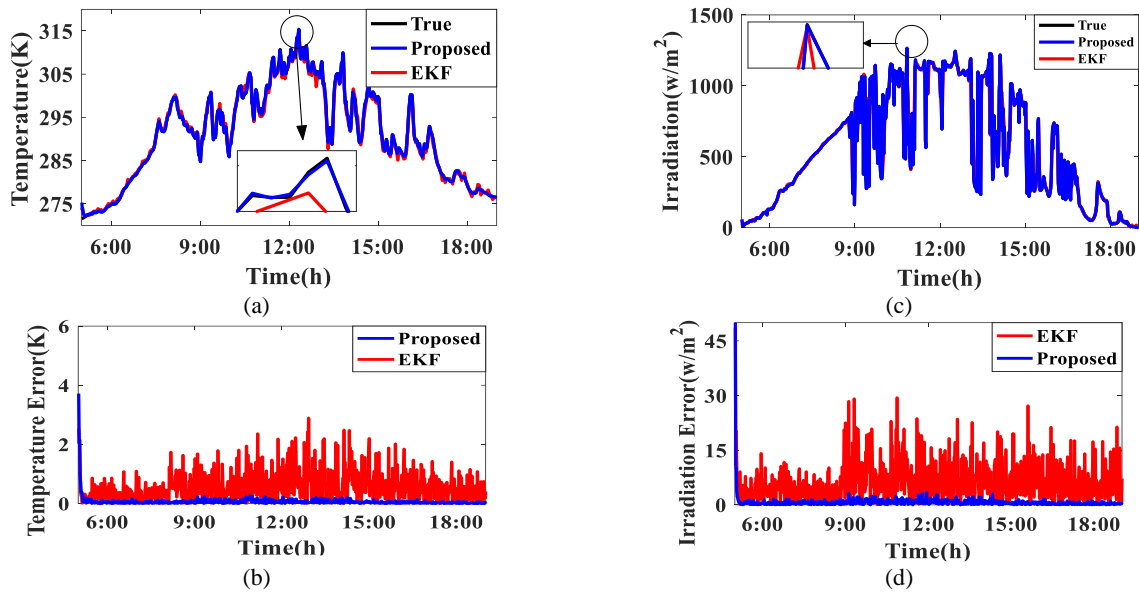


Figure 10. The comparison of actual and estimated values (Temperature and Irradiation) using the EKF and the proposed method in the second case (the partly cloudy sky conditions- for May 13, 2014)

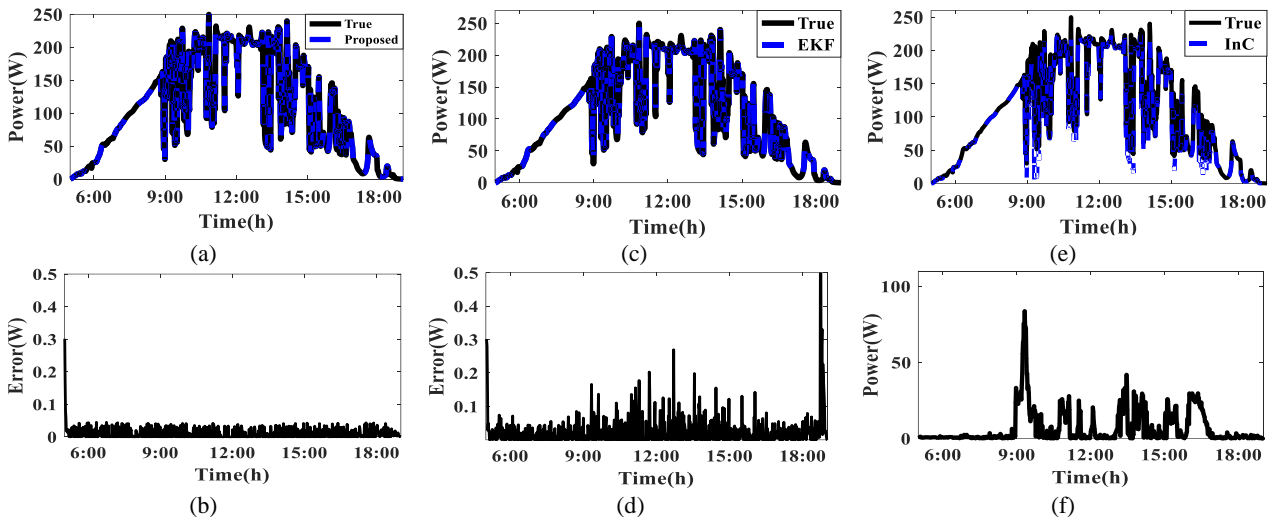


Figure 11. The comparison of the power generated by the PV module using the proposed method, InC method, and EKF-based method in partly cloudy conditions

while this value in the EKF method is about 3K. The RMSE in the proposed method is 0.006, which shows a very good accuracy of the proposed method in these weather conditions, compared to the 0.0179 for the EKF. Figure 12 (c and d) shows the comparison of the real and estimated values of irradiation by the proposed method and the EKF method. The maximum estimate error in the proposed method is 2w/m^2 and for EKF is about 40 w/m^2 approximately. The value of RMSE in both EKF and proposed estimation methods is 0.063 and 0.32, respectively, which indicates the appropriate accuracy of the proposed method. Figure 13 shows the output power of the PV module using the proposed method, the EKF-

based method and the InC method. The results were compared with the real maximum power generated by the actual irradiation and module temperature. The results show that the error is 0.05 watts for the proposed method, 22 watts for InC, and approximately 0.3 watts for EKF. The proposed method has an efficiency of 99.96%, which is 0.15% more than the EKF method and 8.65% more than the InC method. This means that the proposed method produces about 5.1 kJ more than EKF and about 294 kJ more than InC per day. Table 4 presents the RMSE values for the proposed method and EKF, and the efficiency and daily energy production values for all methods (Proposed, EKF-based and InC).

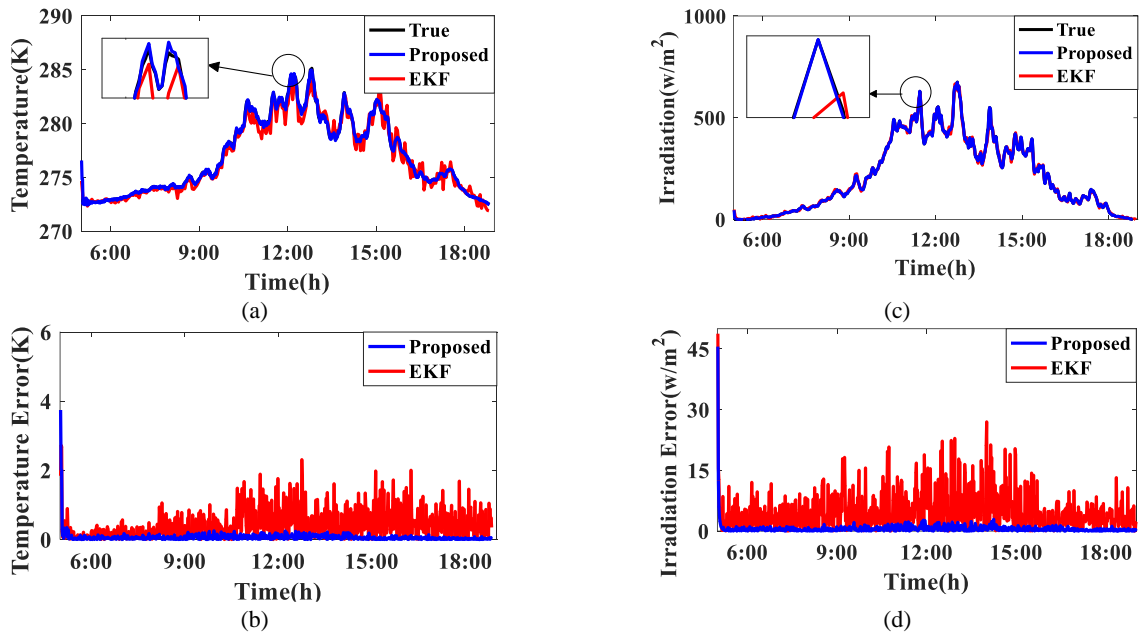


Figure 12. The comparison of actual and estimated values (Temperature and Irradiation) using the EKF method and the proposed method in the third case (the severely cloudy skies conditions- for May 11, 2014)

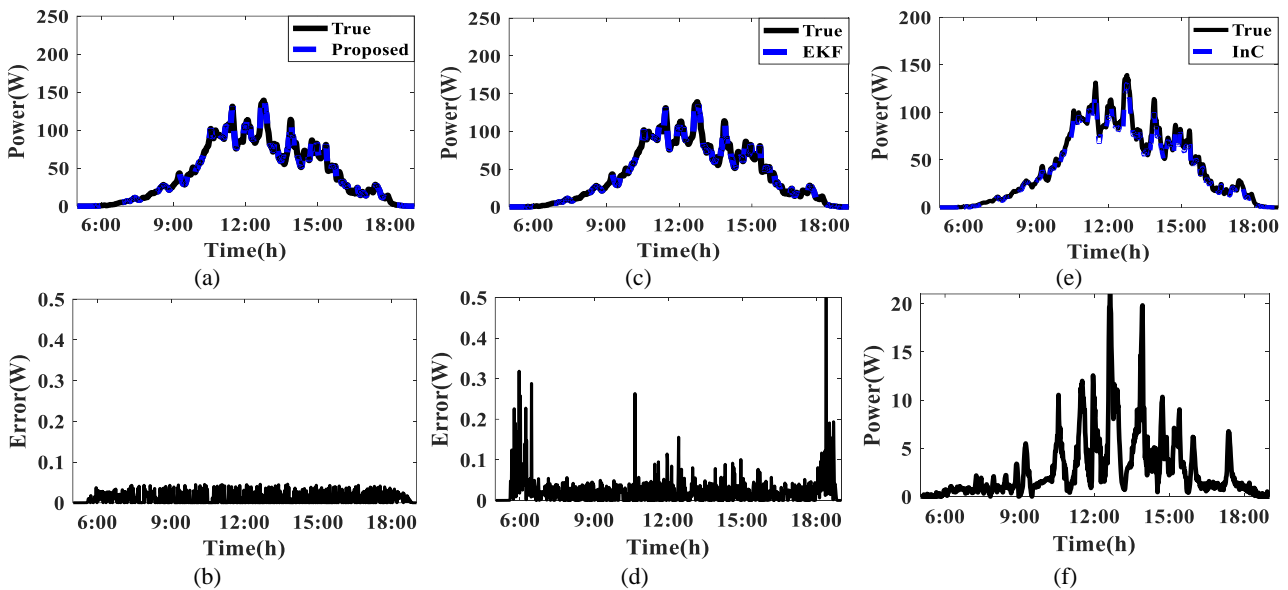


Figure 13. The comparison of the power generated by the PV module using the proposed method, InC method, and EKF-based method in severely cloudy conditions

TABLE 4. The Comparison of RMSE Value and Efficiency Value in the Proposed Method, EKF method and InC Method

Estimate Method	RMSE Value					
	Condition 1		Condition 2		Condition 3	
	<i>T</i>	<i>Irr</i>	<i>T</i>	<i>Irr</i>	<i>T</i>	<i>Irr</i>
EKF	0.04	0.258	0.029	0.3	0.0183	0.32
Proposed	0.0053	0.089	0.0027	0.065	0.0061	0.063

MPPT Method	Efficiency		
	Condition 1	Condition 2	Condition 3
InC	98.9	94	91.31
EKF	99.89	98.9	99.81
Proposed	99.99	99.97	99.96

7. CONCLUSIONS

In this paper, a new method was proposed using a combination of particle and Kalman filters to estimate the irradiation and temperature of a photovoltaic module. Using the estimated values, a new method was applied to the system to track the MPP, which used the power equation derivative, and due to the fact that this method does not require data storage, less memory is used. For evaluation, the proposed method was simulated in three different climatic conditions and compared with the EKF estimation method in terms of estimation accuracy. Also, in these three climatic conditions, the proposed method was compared with EKF and traditional and common InC methods in terms of accuracy and efficiency of MPPT and daily energy generation. The results showed that, firstly, the estimation accuracy of the proposed method is higher than EKF in all the three climatic conditions, and secondly, the proposed method is better than the other two methods in terms of tracking accuracy and efficiency. So, the proposed method is more efficient than EKF method with a rate of 0.1 to 1% and also more efficient than InC method with a rate of 0.8 to 8.65%. In general, it seems that due to the presence of noise in the environment and the measurement sensors, estimation-based methods for tracking perform better than traditional and tracker-based methods and can be a promising candidate for new PV systems.

8. REFERENCES

- Rupesh, M. and Vishwanath, T., "Intelligent controllers to extract maximum power for 10 kw photovoltaic system", *International Journal of Engineering, Transactions A: Basics*, Vol. 35, No. 4, (2022), 784-793. <https://doi.org/10.5829/ije.2022.35.04A.18>
- Feng, H. and Wang, Y., The application of adaptive algorithm in the maximum power tracking of power photovoltaic system, in Computational and experimental simulations in engineering: Proceedings of icces 2022. 2022, Springer.117-125.
- Rahimi Mirazizi, H. and Agha Shafiyi, M., "Evaluating technical requirements to achieve maximum power point in photovoltaic powered z-source inverter", *International Journal of Engineering, Transactions C: Aspects*, Vol. 31, No. 6, (2018), 921-931. <https://doi.org/10.5829/ije.2018.31.06c.09>
- Martynyuk, V., Voynarenko, M., Boiko, J. and Svistunov, O., "Simulation of photovoltaic system as a tool of a state's energy security", *International Journal of Engineering, Transactions B: Applications*, Vol. 34, No. 2, (2021), 487-492. <https://doi.org/10.5829/ije.2021.34.02b.21>
- Albatran, S. and Assad, O., "Online adaptive master maximum power point tracking algorithm and sensorless weather estimation", *Energy Systems*, Vol. 11, (2020), 73-93. <https://doi.org/10.1007/s12667-018-0313-9>
- Manna, S., Singh, D.K., Akella, A.K., Abdelaziz, A. and Prasad, M., "A novel robust model reference adaptive mppt controller for photovoltaic systems", *Scientia Iranica*, (2022). <https://doi.org/10.24200/sci.2022.59553.6312>
- Tan, C.W., Green, T.C. and Hernandez-Aramburo, C.A., "An improved maximum power point tracking algorithm with current-mode control for photovoltaic applications", in 2005 International Conference on Power Electronics and Drives Systems, IEEE. Vol. 1, (2005), 489-494.
- Swaminathan, N., Lakshminarasamma, N. and Cao, Y., "A fixed zone perturb and observe mppt technique for a standalone distributed pv system", *IEEE Journal of Emerging and Selected Topics in Power Electronics*, Vol. 10, No. 1, (2021), 361-374. <https://doi.org/10.1109/JESTPE.2021.3065916>
- Boutabba, T., Drid, S., Chrifi-Alaoui, L. and Benbouzid, M., "A new implementation of maximum power point tracking based on fuzzy logic algorithm for solar photovoltaic system", *International Journal of Engineering, Transactions A: Basics*, Vol. 31, No. 4, (2018), 580-587. <https://doi.org/10.5829/ije.2018.31.04a.09>
- Ishaque, K. and Salam, Z., "A review of maximum power point tracking techniques of pv system for uniform insolation and partial shading condition", *Renewable and Sustainable Energy Reviews*, Vol. 19, (2013), 475-488. <https://doi.org/10.1016/j.rser.2012.11.032>
- Reisi, A.R., Moradi, M.H. and Jamasb, S., "Classification and comparison of maximum power point tracking techniques for photovoltaic system: A review", *Renewable and Sustainable Energy Reviews*, Vol. 19, (2013), 433-443. <https://doi.org/10.1016/j.rser.2012.11.052>
- Motahhir, S., El Hammoumi, A. and El Ghzizal, A., "The most used mppt algorithms: Review and the suitable low-cost embedded board for each algorithm", *Journal of Cleaner Production*, Vol. 246, (2020), 118983. <https://doi.org/10.1016/j.jclepro.2019.118983>
- Lian, K., Jhang, J. and Tian, L., "A maximum power point tracking method based on perturb-and-observe combined with particle swarm optimization", *IEEE Journal of Photovoltaics*, Vol. 4, No. 2, (2014), 626-633. <https://doi.org/10.1109/JPHOTOV.2013.2297513>
- Ghassami, A.A., Sadeghzadeh, S.M. and Soleimani, A., "A high performance maximum power point tracker for pv systems", *International Journal of Electrical Power & Energy Systems*, Vol. 53, (2013), 237-243. <https://doi.org/10.1016/j.ijepes.2013.04.017>
- Boutabba, T., Fatah, A., Sahraoui, H., Khamari, D., Benlaloui, I., Drid, S. and Chrifi-Alaoui, L., "Dspace real-time implementation of maximum power point tracking based on kalman filter structure using photovoltaic system emulator", in 2021 International Conference on Control, Automation and Diagnosis (ICCAD), IEEE., (2021), 1-6.
- Motahhir, S., Aoune, A., El Ghzizal, A., Sebti, S. and Derouich, A., "Comparison between kalman filter and incremental conductance algorithm for optimizing photovoltaic energy", *Renewables: Wind, Water, and Solar*, Vol. 4, No. 1, (2017), 8. <https://doi.org/10.1186/s40807-017-0046-8>
- Farrokhi, E., Ghoreishy, H., Ahmadihangar, R. and Rosin, A., "Kalman-filter based maximum power point tracking for a single-stage grid-connected photovoltaic system", in IECON 2021-47th Annual Conference of the IEEE Industrial Electronics Society, IEEE. (2021), 1-6.
- Abdelsalam, A., Goh, S., Abdelkhalik, O., Ahmed, S. and Massoud, A., "Iterated unscented kalman filter-based maximum power point tracking for photovoltaic applications", in IECON 2013-39th Annual Conference of the IEEE Industrial Electronics Society, IEEE. (2013), 1685-1693.
- Docimo, D., Ghanaatpishe, M. and Mamun, A., "Extended kalman filtering to estimate temperature and irradiation for maximum power point tracking of a photovoltaic module", *Energy*, Vol. 120, (2017), 47-57. <https://doi.org/10.1016/j.energy.2016.12.089>

20. Kumar, N., Singh, B. and Panigrahi, B.K., "Integration of solar pv with low-voltage weak grid system: Using maximize-m kalman filter and self-tuned p&o algorithm", *IEEE Transactions on Industrial Electronics*, Vol. 66, No. 11, (2019), 9013-9022. <https://doi.org/10.1109/TIE.2018.2889617>
21. Lefevre, B., Herteleer, B., De Breucker, S. and Driesen, J., "Bayesian inference based mppt for dynamic irradiance conditions", *Solar Energy*, Vol. 174, (2018), 1153-1162. <https://doi.org/10.1016/j.solener.2018.08.090>
22. Simon, D., "Optimal state estimation: Kalman, h infinity, and nonlinear approaches, John Wiley & Sons, (2006).
23. Masters, G.M., "Renewable and efficient electric power systems, John Wiley & Sons, (2013).
24. Kayisli, K., "Super twisting sliding mode-type 2 fuzzy mppt control of solar pv system with parameter optimization under variable irradiance conditions", *Ain Shams Engineering Journal*, Vol. 14, No. 1, (2023), 101950. <https://doi.org/10.1016/j.asej.2022.101950>
25. Suckow, S., Pletzer, T.M. and Kurz, H., "Fast and reliable calculation of the two-diode model without simplifications", *Progress in Photovoltaics: Research and Applications*, Vol. 22, No. 4, (2014), 494-501. <https://doi.org/10.1002/pip.2301>
26. Shannan, N.M.A.A., Yahaya, N.Z. and Singh, B., "Single-diode model and two-diode model of pv modules: A comparison", in 2013 IEEE international conference on control system, computing and engineering, IEEE., (2013), 210-214.
27. Villalva, M.G., Gazoli, J.R. and Ruppert Filho, E., "Modeling and circuit-based simulation of photovoltaic arrays", in 2009 Brazilian Power Electronics Conference, IEEE., (2009), 1244-1254.
28. Jadli, U., Thakur, P. and Shukla, R.D., "A new parameter estimation method of solar photovoltaic", *IEEE Journal of Photovoltaics*, Vol. 8, No. 1, (2017), 239-247. doi: 10.1109/JPHOTOV.2017.2767602.
29. Jones, A. and Underwood, C., "A thermal model for photovoltaic systems", *Solar Energy*, Vol. 70, No. 4, (2001), 349-359. [https://doi.org/10.1016/S0038-092X\(00\)00149-3](https://doi.org/10.1016/S0038-092X(00)00149-3)
30. Mattei, M., Notton, G., Cristofari, C., Muselli, M. and Poggi, P., "Calculation of the polycrystalline pv module temperature using a simple method of energy balance", *Renewable Energy*, Vol. 31, No. 4, (2006), 553-567. <https://doi.org/10.1016/j.renene.2005.03.010>
31. Abdelhameed, M.M., Abdelaziz, M. and Bayoumi, A., "Enhancement of the output power generated from a hybrid solar thermal system", *International Journal of Research in Engineering and Technology*, Vol. 3, No. 1, (2014), 322-334.
32. Hartikainen, J., Solin, A. and Särkkä, S., "Optimal filtering with kalman filters and smoothers", Department of biomedical engineering and computational sciences, Aalto University School of Science, 16th August, (2011).
33. Sharifian, M.S., Rahimi, A. and Pariz, N., "Classifying the weights of particle filters in nonlinear systems", *Communications in Nonlinear Science and Numerical Simulation*, Vol. 31, No. 1-3, (2016), 69-75. <https://doi.org/10.1016/j.cnsns.2015.05.021>
34. Lee, D.-J., "Nonlinear bayesian filtering with applications to estimation and navigation, Texas A&M University, (2005).

Persian Abstract

چکیده

در این مقاله، روش جدیدی برای ردیابی نقطه حداکثر توان (MPPT) در سیستم‌های فتوولتائیک بر اساس تخمین مقادیر تابش و دما پیشنهاد شده است. روش تخمین پیشنهادی بر اساس ترکیب فیلترهای ذره‌ای و کالمن توسعه‌یافته (EKPF) است. با توجه به اینکه مبنای روش پیشنهادی فیلتر ذره‌ای است، اولاً تخمین با دقت بالایی انجام می‌شود، اگرچه سیستم هدف شدیداً غیر خطی است، ثانیاً محدودیتی برای توابع چگالی احتمال اندازه‌گیری و نویز فرآیند وجود ندارد. این روش برای نویزهای گاوسی و غیر گاوسی کار می‌کند. برای نشان دادن دقت تخمین، روش پیشنهادی با روش رایج مبتنی بر فیلتر کالمن توسعه‌یافته (EKF) مقایسه شده و هر دو روش با معیار ریشه میانگین مربعات خطا ارزیابی خواهند شد. با توجه به برآورد دقیق، MPPT با عملکرد خوبی انجام می‌شود. برای اعتبارسنجی، روش پیشنهادی با روش EKF و روش رایج InC مقایسه می‌شود. شبیه‌سازی‌ها نشان می‌دهد که راندمان از ۰.۱ تا ۱ درصد در مقایسه با EKF و از ۰.۸ تا ۸.۶۵ درصد در مقایسه با روش InC بهبود یافته است که عملکرد روش MPPT پیشنهادی را در محیط‌های با نویز بالا نشان می‌دهد.



Potential Use of Fly Ash for Developing Angular-shaped Aggregate

S. Singh*, S. Patel

Department of Civil Engineering, S. V. National Institute of Technology, Surat, Gujarat, India

PAPER INFO

Paper history:

Received 06 Marc 2023
Received in revised form 01 April 2023
Accepted 08 April 2023

Keywords:

Fly ash Aggregates
Hot Water Bath
Compressive Strength
Aggregate Impact Value
Water Absorption
ANOVA

ABSTRACT

The prices of aggregate are increasing in India due to the massive demand for natural aggregate for infrastructure development. An attempt has been made to check the feasibility of the past developed technique for developing angular-shaped light-weight fly ash coarse aggregate from three different types of fly ashes. In this study, the effects of binder content, water content and hot water bath curing temperature on the compressive strength of blocks, as well as the impact value of prepared aggregate for fly ash-binder mixes were investigated. A relationship between impact value and compressive strength has also been suggested to predict the impact value of fly ash aggregate based on the compressive strength of block. For making angular-shaped fly ash aggregate, it was found that the fly ash with CaO content of 0.71%-3.85% requires higher binder content and curing temperature than that required for fly ash with CaO content of 10.45%. The resulting lightweight aggregates from three fly ashes have a compacted structure and angular shape for good interlocking. The results of mechanical properties test showed that the aggregate also meets the criteria of Indian code specifications for structural concrete aggregate.

doi: 10.5829/ije.2023.36.06c.09

1. INTRODUCTION

Most of the electricity in India is generated in thermal power plants using coal. 232.56 million tons of fly ash was generated in 2020-21 after the consumption of 686.34 million tons of coal in 202 thermal power stations [1]. In 2016, Ministry of Environment, Forest and Climate Change (MoEF&CC) instructed all thermal power plants to achieve a target of 100% fly ash utilization within five years. However, the 100% fly ash utilization goal could not be achieved within the stipulated timeline. Still, 7.59% of fly ash has remained unutilized, which may harm the environment.

Conversely, the demand for stone aggregate is increasing daily for infrastructure development. Aggregate is the main component, covering more than 80% of raw materials for making concrete and pavements. On the basis of market survey, the nationwide aggregate demand for construction may be between 4,500 and 5,000 million tonnes. The cost of stone aggregates is Rs. 1300 to Rs. 1400 per cubic meter as per Delhi Schedule Rate, Central Public Works Department

[2]. This cost continues to rise as a result of rising demand. More aggregate is required for the fast infrastructure development of a country. Mining of natural aggregate leads to severe environmental impacts and consumption of natural resources [3].

The aggregate demand may be fulfilled by producing artificial aggregate from industrial fly ash and locally available resources that can replace mined stone aggregate for construction purposes using simple and appropriate technology. Production of aggregate from fly ash can also help thermal power plants in achieving the target of 100% fly ash utilization. Several advantages of producing fly ash artificial aggregate are natural resource conservation; reducing the amount of energy used in quarrying operations; transforming waste into high-value items; and producing lighter aggregate [4-7].

Raw material mixing, agglomeration and hardening are the main steps for producing fly ash aggregate. Several complicated, costly and time-consuming processes have been developed in the past, most of which are based on the agglomeration by pelletization and hardening by sintering process [8, 9]. Several other

*Corresponding Author Email: ssinghcivil1@gmail.com (S. Singh)

hardening processes, such as cold bonding and hydrothermal processes, have been developed in the past [5, 10, 11]. The shape of the aggregate is an important factor in governing the strength of concrete. [12]. The pelletization process produces spherical-shaped aggregates with smooth surfaces and the load bearing capacity of these aggregates is reduced due to their low interlocking properties [8].

Most of the literature is focused on developing granular fly ash aggregate by pelletization and sintering. Only a few studies on developing angular-shaped aggregate by water bath curing were reported in the literature, primarily dealing with different binders and hardening techniques. Shahane and Patel [8] developed a technique for producing angular-shaped fly ash aggregate (ASFA) using four simple steps: mixing, compaction, curing and crushing.

This study aims to increase the feasibility of the previously developed technique [8] for producing angular-shaped light-weight coarse aggregates from three types of fly ash using a commercially available binder. This will help in scaling up the utilization of fly ash. The current study is centered on the following novel objectives:

- i. To investigate the effects of water bath curing temperature, binder and water content on compressive strength of blocks and impact value of fly ash aggregate.
- ii. To provide suitable mix proportion and water bath curing temperature for developing fly ash aggregates from three fly ashes.
- iii. To compare the engineering properties of developed fly ash aggregates with the requirements of Indian standards.
- iv. To establish an empirical relation for predicting the aggregate impact value from the compressive strength value of blocks.

2. MATERIALS

The physical parameters and chemical constituents of fly ashes are presented in Table 1. Based on the chemical

constituents presented in Table 1, all three fly ashes are classified as Class F [13]. Fly ashes with CaO contents of 0.71%, 3.85%, and 10.45% are designated as F1, F2, and F3, respectively. In the present study, the CaO content of F3 fly ash was found higher than that of F1 and F2 fly ash. A combined percentage of 94.39%, 90.24%, and 75.34% of silica, alumina, and iron oxide were found in F1, F2 and F3 fly ashes, respectively. This indicates that a pozzolanic reaction may occur after adding a binder to the fly ashes [14].

The specific gravity of 1.83 to 2.15 and bulk density of 803 to 848 kg/m³ were found for the fly ashes. The specific gravities of fly ashes were determined as per IS 2720 (Part-III) [15]. The specific gravity of F3 fly ash was found to be less than that of F1 and F2 fly ashes. Commercially available hydrated lime was used as a binder in this study. The particle sizes present in fly ashes were determined using 2.00 mm, 0.425 mm, 0.075 mm and 0.045 mm Indian Standard (IS) sieves.

3. METHODOLOGY

3.1. Production Process and Experiments The following steps were followed for carrying out the experimental study-

Step 1. Determination of OMC and MDD of fly ash and fly ash-binder mixes.

Step 2. Preparation of blocks in brick pressing machine to achieve MDD.

Step 3. Curing in hot water bath for hardening of blocks.

Step 4. Determination of compressive strength of the cured blocks.

Step 5. Crushing of fractured blocks (fractured after compressive strength test) in laboratory-scale impact crusher to obtain aggregates.

Step 6. Sieving of aggregates to segregate different sizes of aggregates.

Step 7. Determination of AIV, i.e., aggregate impact value.

Step 8. Check whether AIV is less than 40%; if not, repeat steps from 2 to 7 after varying water bath curing

TABLE 1. Physical and chemical parameters of fly ashes

Physical	F1	F2	F3	Chemical (%)	F1	F2	F3
Color	Gray	Gray	Dark Gray	SiO ₂	61.91	60.32	44.54
Specific Gravity	2.11	2.15	1.83	Al ₂ O ₃	27.80	25.11	24.70
Bulk Density (kg/m ³)	818	848	803	Fe ₂ O ₃	4.68	4.81	6.10
Sieve size (mm)	Percentage Finer			SO ₃	0.11	0.35	4.53
2.000	100.0	100.0	100.0	MgO	0.56	1.27	0.62
0.425	99.5	99.4	99.7	CaO	0.71	3.85	10.45
0.075	81.5	77.3	87.7	Na ₂ O	0.10	0.15	0.55
0.045	61.0	46.7	63.9	P ₂ O ₅	0.35	0.17	0.40

temperature, binder content and water content, until AIV and crushing value become less than 40%. If yes, then move to step 9.

Step 9. Determination of typical physical properties of fly ash aggregate.

For developing angular-shaped fly ash aggregate (ASFA), the following parameters were adopted for all fly ashes to check the feasibility of the previously developed process [8]: (i) dry mixing of 96% fly ash and 4% lime and then thoroughly wet mixing after addition of water conforming to optimum moisture content; (ii) preparation of rectangular blocks of size 200 mm × 100 mm × 70 mm considering maximum dry density of fly ash-binder mixes and then samples were kept at a temperature of 50°C in oven for 6-7 hours; (iii) then kept for curing in water bath for 3 days under 75°C temperature; and (iv) crushing of cured blocks after keeping cured samples at ambient temperature for 1 day.

After performing compressive strength tests, the fractured blocks were crushed in a laboratory-scale impact crusher to obtain aggregates. The segregation of different sizes of aggregates was carried out by sieving aggregates through different Indian Standard sieves. For large-scale production, fly ash blocks can be crushed in an industrial crusher to obtain fly ash aggregates.

The binder content is mentioned in percentage by dry weight. Binder and water content percentages are with respect to the total dry weight of raw material. The blocks were pressed to their maximum density to obtain high-strength and densely-structured fly ash aggregate, which required determining the water content for molding the blocks. Optimum moisture content (OMC) and maximum dry density (MDD) of fly ash-binder mixes were determined by conducting a modified compaction test [16]. Then blocks were prepared in a brick-pressing machine by applying a pressing force of 350 kN. Green blocks were kept for accelerated curing in the water bath under specified temperature.

The compressive strength test was then performed on the cured blocks as per IS 3495 (Part-1) [17]. Three identical specimens were prepared for each study and compressive strength test was performed by applying axial load at a uniform rate of 14 N/mm² per minute till failure occurred. The mean value was taken as the strength value of the tests performed.

Different trials by varying water bath curing temperature and binder content were also carried out for the fly ashes, where the parameters adopted in the process failed to develop an aggregate impact value lower than 40%. Further improvement in strength was achieved by varying water content. The strength in aggregate may be due to formation of cementitious and binding gels [18].

Figure 1 shows the process for developing angular-shaped fly ash aggregate (ASFA) in the laboratory.

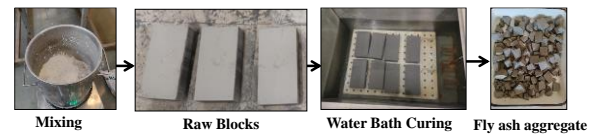


Figure 1. Process for developing angular-shaped fly ash aggregate

3. 2. Physical Tests on Fly Ash Aggregates

Different physical tests were conducted on aggregates developed by finalized mix, water content and curing temperature for three fly ashes. Loose bulk density, specific gravity and water absorption were determined for ASFA of size 6.3 mm to 20 mm as per IS 2386 (Part III) [15].

Aggregates must be tough and strong enough to withstand disintegration caused by sudden and gradually applied load. Aggregate impact value (AIV) and crushing value of aggregates were determined as per IS 2386 (Part IV) [19]. The durability test for ASFA was also carried out as per IS 2386 (Part V) [20] in sodium sulphate solution for five alternate wetting and drying cycles.

4. RESULTS AND DISCUSSION

4. 1. Compaction Test Results

A modified proctor test was conducted and OMC & MDD values of fly ash and fly ash-binder mixes were found. OMC & MDD values of F1, F2 and F3 fly ashes were 18.9%, 1.34 g/cm³; 19%, 1.35 g/cm³ and 25.6%, 1.38 g/cm³. OMC in the range of 18.5% to 19.0%, 18.0%-19.0% and 25.4%-25.5%, while MDD in the range of 1.38 g/cm³-1.41 g/cm³, 1.40 g/cm³-1.42 g/cm³ and 1.37 g/cm³-1.38 g/cm³ were found for F1, F2 and F3 fly ash-binder mixes, respectively. Blocks were prepared for different fly ash-binder mixes at their respective OMC and MDD.

4. 2. Results for Three Fly Ashes Following the Previous Mix and Curing Parameters

Initially, the mix proportions and water bath curing parameters following literature [8] were trialed to check the feasibility of the suggested parameters for three new fly ashes. Table 2 shows the compressive strength of blocks and AIV of aggregates prepared for 96% fly ash+4% lime (named F1+4L, F2+4L and F3+4L) for all three fly ashes.

TABLE 2. Compressive strength and AIV results of fly ashes following the previous mix and curing parameters

Mix	Compressive Strength (MPa)	AIV (%)	Target AIV (%)
F1+4L	6.2	51.0	
F2+4L	7.1	50.8	<40%
F3+4L	22.1	27.5	

The highest compressive strength of 22.1 MPa and AIV of 27.5% was found for F3+4L. The AIV for F3+4L was found below the permissible limit mentioned in IS 9142 [23] for aggregate to be used in structural concrete, while the AIVs of F1+4L and F2+4L were found above the permissible limit. This shows that the mix proportion and curing temperature mentioned in the literature [8] are unsuitable for F1 and F2 fly ashes. This may be due to the low percentage of CaO in F1 and F2 fly ashes. More trials were conducted to find the suitable mix proportion and curing temperature for making ASFA from F1 & F2 fly ashes.

4. 3. Influence of Temperature on AIV and Compressive Strength

Figure 2 shows the influence of water bath curing temperature on the compressive strength of blocks and AIV of aggregates prepared for F1+4L and F2+4L mixes. The compressive strength is increasing and AIV is decreasing with the temperature. The compressive strength was found to be decreased by 6%-8% on lowering the temperature from 75°C to 65°C, while the compressive strength was found to be increased by 53% on increasing the temperature from 75°C to 95°C in F1+4L & F2+4L mixes. The increase in compressive strength value may be due to an increase in the rate of pozzolanic reaction with the increase in temperature. Low curing temperatures are not favorable for early strength development because of the slower rate of pozzolanic reaction at low temperatures [21].

The lowest AIV of 47.6% and 46% were found for F1+4L and F2+4L at 95°C curing temperature. The impact values obtained were more than 40%. This proves that 4% binder is insufficient for developing high strength aggregate with F1 and F2 fly ashes, even at higher curing temperatures.

4. 4. Effect of Binder Content Due to the presence of low percentage of CaO in F1 and F2 fly ashes, the fly

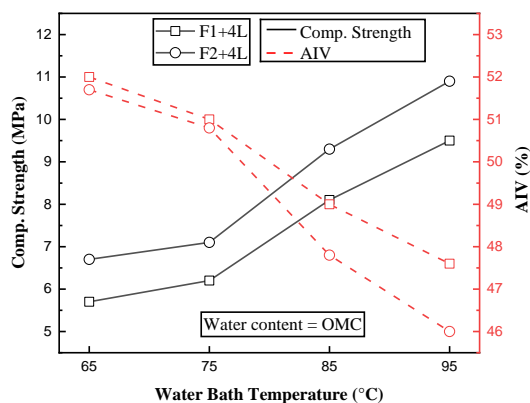


Figure 2. Influence of curing temperature on AIV and compressive strength AIV for F1+4L and F2+4L mixes

ashes have very low or no cementitious properties. A suitable amount of binder is required to improve the strength of aggregates. Figure 3 shows that as the binder content increases, so does the compressive strength of blocks of F1 and F2 fly ashes. More binders will provide more calcium for the reaction. Binder content of more than 14% was found suitable to make ASFA with AIV less than 40%.

Impact values of 35.6% and 34.8% were found to be highest for aggregates of F1+18%L and F2+18%L, respectively, prepared after curing at 95°C in the water bath for 3 days. Fly ash with low CaO content demanded a relatively higher binder content in the mix and accelerated curing to achieve sufficient strength [22]. As the AIV for 14% binder was found to be just touching the maximum permissible AIV limit, 16% -18% binder was chosen for further study.

4. 5. Effect of Water Content Further study was carried out by varying the water content as water content plays a vital role in gaining strength. Figure 4 shows the effect of water content on the compressive strength of blocks and AIV of aggregate prepared for OMC to OMC-8%. Lime of 16%-18% and curing temperature of 95°C were chosen for F1 and F2 fly ashes, while lime of 4% and curing temperature of 75°C was chosen for F3 fly ash.

It was found that on lowering the water content from OMC to OMC-4%, the compressive strength increases while AIV decreases for all mixes, which indicates that water content equal to OMC-4% is on the dry side of the OMC resulting in higher strength. Further decrease in water content was leading to decrease in strength of aggregate because the void space between fly ash particles increases as water content decreases, resulting in a loosely packed material and thus a decrease in aggregate strength.

Compressive strength was found to be improved by 4.1%-7.1%, while AIV was found to be lowered by

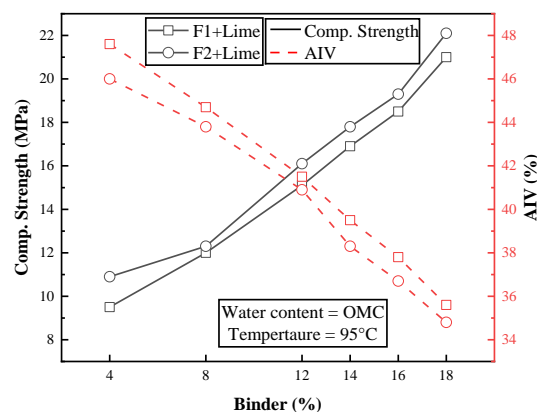


Figure 3. Variation in compressive strength and impact value with binder

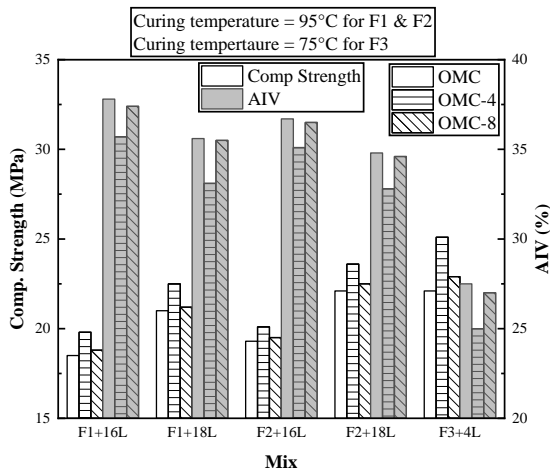


Figure 4. Effect of water content on compressive strength and impact value

4.3%-7.0% on lowering water content from OMC to OMC-4% for mentioned mixes of F1 and F2 fly ashes. An increment of 13.5% in compressive strength and a decrement of 9.1% in AIV was found for F3+4L mix.

4. 6. Abrasion Value Results

Los Angeles abrasion test was also carried out for ASFA prepared from F1+16L, F1+18L, F2+16L, F2+18L and F3+4L mixes by taking water content equal to OMC-4%. This test was carried out to check whether prepared ASFA at OMC-4% water content, fulfill the requirement of abrasion value as per IS codes [23, 25]. Table 3 shows the abrasion values for different mixes of F1, F2 and F3 fly ashes. Abrasion values for F1+18L, F2+18L and F3+4L were found below the maximum permissible limit of IS code [23]. This indicates that 18% lime is suitable for preparing ASFA from F1 and F2 fly ash and 4% lime is suitable for F3 fly ash.

4. 7. Empirical Relation between Compressive Strength and Aggregate Impact Value

Additionally, efforts have been made to establish empirical relations for predicting the aggregate impact value of ASFA from the compressive strength value of blocks of different mixes. The compressive strength (q)

TABLE 3. Comparison of abrasion value for different mix

Mix	AIV (%)	Abrasion Value (%)	Target Abrasion Value (%) [23]
F1+16L	35.7	42.8	
F1+18L	33.1	38.0	
F2+16L	35.1	42.1	<40%
F2+18L	32.8	38.2	
F3+4L	25.0	33.2	

of blocks and aggregate impact value (AIV) of ASFA depends on several critical leading parameters, like fly ash-binder mix proportion, binder type, curing temperature and water content. By multiple regression analysis, the empirical correlation for predicting AIV using compressive strength for 29 samples is presented as follows:

$$AIV = -12.1 q + 59.4 \tag{1}$$

where, AIV is impact value of aggregate in %, q is compressive strength of block in MPa, and R² is coefficient of correlation. The linear model is found to fit the experimental data best with R² value of 0.94, indicating that the fitness of the model is good.

Plot (Figure 5) of actual and predicted values indicates an excellent fit for AIV and compressive strength. The established empirical relation (Equation (1)) is a linear model that considers compressive strength as the independent variable. This independent variable can represent the cumulative influence of the parameters that control the aggregate impact value of ASFA. The analysis of variance (ANOVA) of the regression parameters of the predicted AIV by linear model is also summarized in Table 4 with the F-test. ANOVA shows that the selected linear model adequately represented the data obtained. The p-value less than 0.05 indicate that model terms are statistically significant at the 95% confidence level.

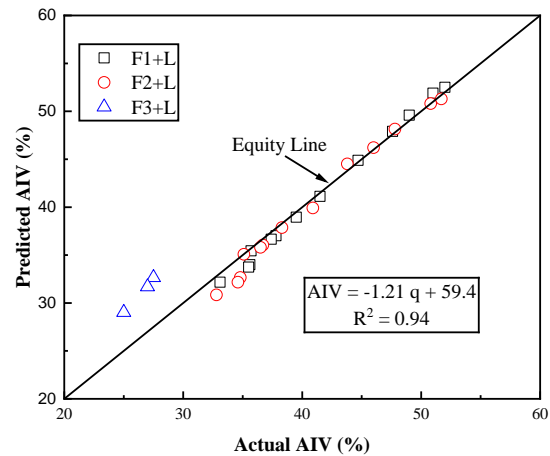


Figure 5. Comparison of predicted AIV with actual AIV

TABLE 4. ANOVA for AIV prediction by linear model

Source	df*	Sum of squares	Mean squares	F value	p-value
Regression	1	1524.2	1524.2	448.5	<0.05
Residual Error	27	91.7	3.4		
Total	28	1615.9			

*df = degree of freedom

4. 8. Comparison of Properties with Standards

Table 5 displays the results of laboratory tests on the physical and mechanical properties of fly ash aggregates. The dry loose bulk densities of fly ash aggregates are below the maximum value of IS 9142 (Part II) [23], which fulfills the requirement of dry loose bulk density of lightweight aggregate for structural concrete.

23.1%, 24.6% and 25.0% of water absorption were found for fly ash aggregates of F1+18L, F2+18L and F3+4L mixes, respectively. Due to the high water absorption of fly ash aggregates, more water will be absorbed by the aggregate in the early stages, enabling the concrete to withstand moisture loss in later stages. This absorbed water contributes to the internal curing of the concrete, making it more resistant to the lack of curing than natural aggregate concretes [24].

ALFC aggregates were found to have a satisfactory crushing value, meeting the requirement of IS 9142 (Part-II) [23] for structural concrete aggregates. The results of the soundness tests also revealed that the five-day dry weight of the fly ash aggregates of the finalised mixes was greater than 90% of the initial dry weight of the aggregates. This implies that weight loss during wetting and drying cycles preserves aggregate integrity regarding resistance to deterioration cycles. This is based on the assumption that stronger aggregate bonding is caused by the formation of binding gels, which results in high strength retention even after continuous wetting and drying cycles.

The wet aggregate impact values are reported in Table 5 because the water absorptions of ASFA of all three fly ashes were found higher than 2%. The impact, crushing, abrasion and soundness value of ASFA were found to be quite adequate, meeting the criteria of IS 383 [25] for application in non-wearing surfaces of concrete and IS 9142 (Part-II) [23] for application as lightweight aggregate in structural concrete. For using fly ash

aggregate in concrete, pre-soaking is essential before concrete mixing in order to compensate for its high water absorption value.

5. CONCLUSIONS

Engineering properties of angular-shaped aggregate developed from F1, F2 and F3 fly ashes under hot water bath curing were examined and compared. The following conclusions can be drawn:

1. It is found that high curing temperature and high binder content are required for developing angular-shaped fly ash aggregate from F1 and F2 fly ashes in comparison to F3 fly ash. 18% lime and 95°C water bath curing temperature for developing aggregate from F1 and F2 fly ashes, while 4% lime and 75°C water bath curing temperature for developing aggregate from F3 fly ash are found to be sufficient.
2. It is found that fly ash aggregates of F3 fly ash are quite stronger than fly ash aggregates of F1 and F2 fly ashes. Impact value of less than 40%, crushing value of less than 45%, abrasion value of less than 40% and soundness value of less than 12% were found for developed aggregates from all three fly ashes. These values are fulfilling the required specifications of IS 383 for aggregates to be used in non-wearing surfaces of concrete and specifications of IS 9142 (Part-II) for lightweight aggregates to be used in concrete.
3. Water absorptions of more than 20% are found for aggregates of three fly ashes. Pre-soaking is essential before mixing and using in order to compensate for its high water absorption value.
4. A linear correlation ($AIV = -1.21q + 59.4$) has been developed, which is found quite well for predicting the aggregate impact value (AIV) using compressive strength (q) of blocks.

TABLE 5. Typical properties of fly ash aggregates

Parameters	F1+18L	F2+18L	F3+4L	IS 383* [25]	IS 9142(II) [23]
Loose Bulk Density (kg/m ³)	872	880	755	-	≤ 950
Water absorption	23.1%	24.6%	25.0%	≤ 2%	≤ 18%
Impact value	33.1%	32.8%	25.0%	≤ 45%	≤ 40%
Crushing Value	42.5%	42.2%	31.1%	-	≤ 45%
Abrasion Value	38%	38%	33%	≤ 50%	≤ 40%
Soundness Value	8.2%	8.8%	9.2%	≤ 12%	≤ 12%

* Non-wearing surfaces

6. REFERENCES

1. Central Electricity Authority, "Report on fly ash generation at coal/lignite based thermal power stations and its utilization in the country for the year 2020-2021", Ministry of Power, Government of India, (2021), 1-78.
2. CPWD, Government of India, "Delhi Schedule of Rates", The Authority of Director General, CPWD, New Delhi, Vol. 1, (2021).
3. Turkane, S. D., and Chouksey, S. K., "Partial Replacement of Conventional Material with Stabilized Soil in Flexible Pavement Design", *International Journal of Engineering Transactions B: Applications*, Vol. 35, No. 05, (2022), 908-916. doi: 10.5829/IJE.2022.35.05B.07
4. Tajra, F., Elrahman, M. A., and Stephan, D., "The production and properties of cold-bonded aggregate and its applications in concrete: A review", *Construction and Building Materials*, Vol. 225, (2019), 29-43. <https://doi.org/10.1016/j.conbuildmat.2019.07.219>

5. Their, J. M., and Özakaça, M., "Developing geopolymers concrete by using cold-bonded fly ash aggregate, nano-silica, and steel fiber", *Construction and Building Materials*, Vol. 180, (2018), 12-22. <https://doi.org/10.1016/j.conbuildmat.2018.05.274>
6. Bakare, M. D., Pai, R. R., Patel, S., and Shahu, J. T., "Environmental Sustainability by Bulk Utilization of Fly Ash and GBFS as Road Subbase Materials", *Journal of Hazardous, Toxic, and Radioactive Waste*, Vol. 23, No. 4, (2019). [https://doi.org/10.1061/\(asce\)hz.2153-5515.0000450](https://doi.org/10.1061/(asce)hz.2153-5515.0000450)
7. Bakare, M. D., Shahu, J. T., and Patel, S., "Resources , Conservation & Recycling Complete substitution of natural aggregates with industrial wastes in road subbase : A field study", *Resources, Conservation & Recycling*, Vol. 190, No. August 2022, (2023), 106856. <https://doi.org/10.1016/j.resconrec.2022.106856>
8. Shahane, H. A., and Patel, S., "Influence of curing method on characteristics of environment-friendly angular shaped cold bonded fly ash aggregates", *Journal of Building Engineering*, Vol. 35, (2021), 101997. <https://doi.org/10.1016/j.jobe.2020.101997>
9. Sarabèr, A., Overhof, R., Green, T., and Pels, J., "Artificial lightweight aggregates as utilization for future ashes - A case study", *Waste Management*, Vol. 32, No. 1, (2012), 144-152. <https://doi.org/10.1016/j.wasman.2011.08.017>
10. Manikandan, R., and Ramamurthy, K., "Effect of curing method on characteristics of cold bonded fly ash aggregates", *Cement and Concrete Composites*, Vol. 30, No. 9, (2008), 848-853. <https://doi.org/10.1016/j.cemconcomp.2008.06.006>
11. Ramamurthy, K., and Harikrishnan, K. I., "Influence of binders on properties of sintered fly ash aggregate", *Cement and Concrete Composites*, Vol. 28, No. 1, (2006), 33-38. <https://doi.org/10.1016/j.cemconcomp.2005.06.005>
12. Darvishvand, H. R., Seiyed, S. A. H., and Ebrahimi, M., "Utilizing the Modified Popovics Model in Study of Effect of Water to Cement Ratio , Size and Shape of Aggregate in Concrete Behavior", *International Journal of Engineering Transactions B: Applications*, Vol. 34, No. 02, (2021), 393-402. doi: 10.5829/IJE.2021.34.02B.11
13. ASTM C618, "Standard Specification for Coal Fly Ash and Raw or Calcined Natural Pozzolan for Use", ASTM International, West Conshohocken, PA, (2022). <https://doi.org/10.1520/C0618-22>
14. Sai Giridhar Reddy, V., and Ranga Rao, V., "Eco-friendly blocks by Blended Materials", *International Journal of Engineering, Transactions B: Applications*, Vol. 30, No. 5, (2017), 636-642. doi: 10.5829/idosi.ije.2017.30.05b.02
15. IS 2386 (Part III), "Methods of Test for Aggregates for Concrete (Specific Gravity, Density, Voids, Absorption and Bulking)", Bureau of Indian Standards, New Delhi, (1963) (Reaffirmed 2002)
16. IS 2720 (Part VIII), "Determination of water content-dry density relation using heavy compaction", Bureau of Indian Standards, New Delhi, (1983) (Reaffirmed 2002).
17. IS 3495 (Parts 1-4), "Methods of Tests of Burnt Clay building brick", Bureau of Indian Standards, New Delhi, (1992).
18. Nguyen, D. T. and V. T. A. P., "Engineering Properties of Soil Stabilized with Cement and Fly Ash for Sustainable Road Construction", *International Journal of Engineering, Transactions C: Aspects*, Vol. 34, No. 12, (2021), 2665-2671. doi: 10.5829/IJE.2021.34.12C.12
19. IS 2386 (Part IV), "Methods of Test for Aggregates for Concrete (Mechanical properties)", Bureau of Indian Standards, New Delhi, (1963) (Reaffirmed 2002)
20. IS 2386 (Part V), "Methods of test for aggregates for concrete (Soundness)", Bureau of Indian Standards, New Delhi, (1963) (Reaffirmed 2002).
21. Samantasinghar, S., and Singh, S., "Effects of curing environment on strength and microstructure of alkali-activated fly ash-slag binder", *Construction and Building Materials*, Vol. 235, (2020), 117481. <https://doi.org/10.1016/j.conbuildmat.2019.117481>
22. Manikandan, R., and Ramamurthy, K., "Effect of curing method on characteristics of cold bonded fly ash aggregates", *Cement and Concrete Composites*, Vol. 30, No. 9, (2008), 848-853. <https://doi.org/10.1016/j.cemconcomp.2008.06.006>
23. IS 9142 (Part II), "Artificial Lightweight Aggregate for Concrete-Specification (Sintered Fly Ash Coarse Aggregate)", Bureau of Indian Standards, New Delhi, (2018).
24. Nadesan, M. S., and Dinakar, P., "Structural concrete using sintered flyash lightweight aggregate: A review", *Construction and Building Materials*, Vol. 154, (2017), 928-944. <https://doi.org/10.1016/j.conbuildmat.2017.08.005>
25. IS 383, "Coarse and Fine Aggregate for Concrete- Specification", Bureau of Indian Standards, New Delhi, (2016).

Persian Abstract

چکیده

توسعه زیرساخت ها. تلاشی برای بررسی امکان سنجی تکنیک توسعه یافته گذشته برای تولید دانه های درشت خاکستر بادی سبک وزن زاویه دار از سه نوع مختلف خاکستر بادی انجام شده است. در این مطالعه، تأثیر محتوای بایندر، محتوای آب و دمای پخت حمام آب داغ بر مقاومت فشاری بلوک ها و همچنین ارزش ضربه ای سنگدانه های آماده شده برای مخلوط های خاکستر بایندر مورد بررسی قرار گرفت. یک رابطه بین ارزش ضربه و مقاومت فشاری نیز برای پیش بینی ارزش ضربه خاکستر بادی بر اساس مقاومت فشاری بلوک پیشنهاد شده است. برای ساخت دانه های خاکستر بادی زاویه ای، مشخص شد که خاکستر بادی با محتوای $3.85\% - 0.71\% \text{ CaO}$ به محتوای چسب و دمای پخت بالاتری نسبت به خاکستر بادی با محتوای $10.45\% \text{ CaO}$ نیاز دارد. سنگدانه های سبک وزن حاصل از سه خاکستر بادی دارای ساختار فشرده و شکل زاویه ای برای در هم قفل شدن خوب هستند. نتایج آزمایش خواص مکانیکی نشان داد که سنگدانه با معیارهای آیین نامه هندی برای سنگدانه های بتن سازه ای نیز مطابقت دارد.



Evaluation of lightweight Concrete Core Test Including Steel Bars

H. A. Goaliz^a, H. A. Jabir^a, M. A. Abdulrehman^b, T. S. Al-Gasham^a

^a Department of Civil Engineering, Wasit University, Wasit, Iraq

^b Department of Materials Engineering, Mustansiriyah University, Baghdad, Iraq

PAPER INFO

Paper history:

Received 16 March 2023

Received in revised form 15 April 2023

Accepted 16 April 2023

Keywords:

Lightweight Concrete

Concrete Core Test

Steel Bars

ABSTRACT

In many steel reinforced concrete members, steel bars are not avoidable during concrete core drilling and the presence of these steel bars have a direct impact on the results of this test. This study aims to examine the effect of steel bars presence on the test results of recycled aggregate lightweight concrete (LWC) cores. For the purpose, one lightweight concrete mix was made with a total number of 48 concrete cores were taken from a slab having the dimensions of 1 m width, 1.5 m length and 0.15m thickness. Each core has the dimensions of 90 mm in diameter and 150 mm in height. Three different sizes of steel bars (12, 16 and 20 mm) were used in six different locations (25, 45 and 65 mm) from the base of the core and (15 and 30 mm) from the center line of the core. A recycled crashed clay brick (CCB) was used as an alternative to the coarse aggregate. Compare to the density of the normal concrete (2400 kg/m³), the LWC was able to achieve nearly 20% reduction of the total weight by fully replacing of normal aggregate with CCB. It has been found that the presence of the steel increases the compressive strength of the LWC cores. This effect is more noticeable when the location of the steel bar is near to the mid-height or the centerline of the concrete core. Also, the influence of the steel bar diameter has increased by increasing the size of the steel bar.

doi: 10.5829/ije.2023.36.06c.10

1. INTRODUCTION

Reducing the total self-weight of any structure is an important key in many structural designs. There are several advantages of this self-weight reduction including but not limited to improving the structural behaviour to seismic loads and reducing the total cost of the structure [1-3]. Decreasing the total weight of the structural elements can be achieved by different methods such as using thin concrete sections with high concrete strength or reducing the specific gravity of the concrete. Normally, concrete is produced with relatively high specific gravity of nearly 2400 kg/m³ and the main reason for that is the high content of the normal aggregate within the concrete mix (nearly 70% of the total weight of the mixture) [4]. The ACI C213 committee [5] mentioned that the specific gravity of the light weight concrete should not be exceeded the limit of 1850 kg/m³. Accordingly, several studies were conducted to partially or fully replacing the normal aggregate of the concrete

with other types of aggregates that having a lower specific gravity than the normal aggregate [6-9]. In general, by replacing normal aggregate with lightweight aggregate, the concrete strength is dramatically affected. The ACI requirements for compressive strength of light weight concrete should be kept more than 17 MPa for structural design [5]. Therefore, many researches were conducted on light weight concrete that aimed to achieve a reliable quality and strength in which could be suitable for structural applications [10-15].

It is well-known that the concrete quality is determined based on the test results of concrete samples at the age of 28 days. However, in some cases the test results do not fulfill the specified 28-day strength due to many reasons, such as; incorrect practice methods or improper testing procedures. In such cases, concrete coring could be one of the desired solutions to evaluate the in-situ quality of the placed concrete. Extracting concrete cores from existing concrete is preferable for some other reasons, especially when the placed concrete

*Corresponding Author Institutional Email: hussam@uowasit.edu.iq
(H. A. Goaliz)

is subjected to any type of deterioration, for instance; effect of fire, chemical attack, fatigue or other kinds of degradation effects. Concrete coring is considered as a semi-destructive test and can be performed on different types of structural members in horizontal or vertical directions. Normally, steel reinforcement is used along with concrete in the structural elements to resist the tensile stresses or to confine the concrete in which increases the loading carrying capacity of the structural members. The presence of the steel reinforcement is not desirable in the concrete coring and many international codes recommended testing concrete cores without steel bars, such as ASTM committee [16]. However, in some situations where heavy steel reinforcement is used, it would be very difficult to avoid steel bars during concrete core drilling. For this reason, some international codes [17, 18] suggested empirical equations to correct the compressive strength test results of the drilled concrete cores depending on many factors, such as the size, location and number of the steel bars within the core. These factors are also related to the geometry of the drilled core, for example the effect of the steel bar size is taken as a ratio of steel bar diameter to the core diameter.

Tuncan et al. [19] studied the reliability of testing small diameter drilled concrete cores and it has been found that the compressive strength of the smaller diameter drilled cores were more likely to be affected by the length of the core and the characteristics of the aggregate with in the concrete mixture. Also, by increasing the length to diameter ratio (l/d) of the concrete cores, the compressive strength tends to show lower values.

Momeni et al. [20] performed a study to investigate the reliability of steel bars correction factors for drilled cores. It has been stated that these factors are highly related to the size and the location of the steel bars. According to the experimental results, the inclusion of steel reinforcement led to an increment for the compressive strength and it was more noticeable for concrete cores with l/d ratio equal to one. Momeni et al. [20] also suggested a linear and nonlinear regression models to predict the cube compressive strength of an existing concrete from the test results of drilled concrete cores.

Lessly et al. [21] conducted an experimental study on the effect of steel reinforcement on the compressive strength of drilled concrete cores. This study was included different orientations and different sizes of the steel bars within the extracted cores. It had been found that the presence of steel bars led to a reduction up to 36% in the compressive strength of the concrete cores. The compressive strength reduction was explained as a result to the loss of bond strength between the steel bars and the concrete during the core cutting process. Accordingly, there are limited numbers of studies in the research field to obtain a fully understanding the effect of steel bars presence on the test results of drilled concrete cores.

The outcomes of this research could be helpful when steel reinforced lightweight concrete is used in real

structural applications and drilled cores are needed for quality control reasons. All the available researches were performed on normal concrete cores [22-24] and there is no single study dealt with drilled cores of light weight concrete. For this reason, the current study aimed to experimentally examine the effect of steel bars presence on the test results of light weight concrete cores made of locally crashed clay bricks.

2. EXPERIMENTAL PROGRAM

In order to attain the aim of this study, to examine the effect of steel reinforcement bars on the test results of compressive strength of light weight concrete (LWC) cores. The experimental work is executed at the Concrete laboratory of the civil engineering department in college of engineering/Wasit University. The testing program is organized to obtain information about the effect of steel bars on test results of concrete cores for light weight concrete. One concrete mix have been made with a total number of 48 concrete cores were taken from concrete slab having a dimensions of 1 m width, 1.5 m length and 0.15m thickness. Three different sizes of steel bars (12, 16 and 20 mm) have been used in three different locations (25, 45 and 65 mm) from the base of the core and (0, 15 and 30 mm) from the center line of the core. Table 1 shows the test matrix of this study. All concrete cores are tested for compressive strength at 28 days. Figure 1 shows the core samples before testing.

TABLE 1. Test matrix of core specimen

Core ID	Steel bars location [mm]		Steel bar diameter [mm]
	From the base of the core in Y direction	From the centerline of the core in X direction	
R	----	----	----
Steel bars in Y direction	S12-Y25	25	12
	S12-Y45	45	12
	S12-Y65	65	12
	S16-Y25	25	16
	S16-Y45	45	16
	S16-Y65	65	16
	S20-Y25	25	20
	S20-Y45	45	20
	S20-Y65	65	20
Steel bars in X direction	S12-X15	15	12
	S12-X30	30	12
	S16-X15	15	16
	S16-X30	30	16
	S20-X15	15	20
	S20-X30	30	20

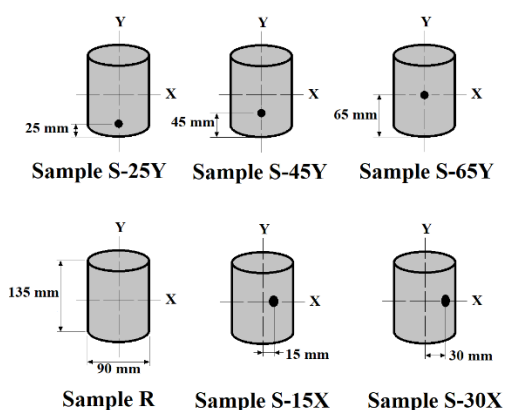


Figure 1. Steel bar location within the core samples

2. 1. Materials Effective production of LWC is achieved by several methods. One of these methods is to use light weight aggregate within the concrete mix. In this study, crashed clay brick (CCB) was used as an alternative to the coarse aggregate, see Figure 2. The CCB can be prepared locally as a recycled material from demolished brick buildings. The mix design of this study was planned to use the CCB as fully replacement to the normal coarse aggregate. As mentioned earlier, the CCB was prepared using local materials to comply with the Iraqi Standard 45: 1985 [25]. Tables 2 and 3 show the properties of the CCB that has been used to produce the LWC in this study. Along with the CCB aggregate, normal fine aggregate (sand) of Zone 2 grading (according to Iraqi Standard 45: 1985) [25] was used to form the filler ingredient within the LWC mixture.



Figure 2. Preparing the CCB for lightweight aggregate

TABLE 2. Grading of CCB aggregate of MAS (20 mm)

Sieve size (mm)	Passing by weight%	Limits of the Iraqi specification No. 45/1984 ^[23]
25	100	100
14	55	40-80
10	41	30-60
5	5	0-10

TABLE 3. Other properties of CCB aggregate

Physical properties	Test results	Limits of the Iraqi specification No. 45/1984 ^[23]
Specific gravity	1.67	--
Sulfate content	0.04%	≤ 0.1%
absorption	16 %	--

Also, ordinary Portland cement was mixed with the water to form the binder component that brings all the ingredients together. In addition to these materials, superplasticiser was also used to provide an acceptable compressive strength for the LWC due to the reduction of the water amount within the mix.

Three sizes of steel reinforcing bars are used in the present experimental work. These deformed steel bars of diameters 12, 16 and 20 mm were tested in a universal testing machine to determine the tensile properties before use. Properties of the steel bars are shown in Table 4.

2. 2. Molding The concrete cores were taken out from a concrete slab having the dimensions of 1500 mm length, 1000 mm width and 150 mm thickness. This concrete slab was designed to be reinforced in one direction parallel to the width of the slab as shown in Figure 3. Nine steel bars (3 Ø 12, 3 Ø 16 and 3 Ø 20 mm) were used and placed at a distance of 150 mm from each other in a wooden formwork as shown in Figure 3. Each group of steel bar diameter was placed in three different locations from the bottom of the mold (25, 45 and 65 mm). These steel bars were extended out of the formwork by 100 mm in length, so it can be easily located after concrete pouring.

2. 3. Lightweight Concrete Mix In order to achieve the target compressive strength of the LWC

TABLE 4. Tensile properties of steel bars

Nominal Diameter [mm]	Modulus of Elasticity [GPa]	Yield Stress [MPa]	Ultimate Stress [MPa]
12 deformed	200	400	676
16 deformed	200	485	719
20 deformed	200	517	635



Figure 3. Preparing the CCB for light weight aggregate

which is not less than 20 MPa, the following mix proportions shown in Table 5 were adopted. As mentioned above, the key to prepare a LWC mix in this study is to use crashed clay brick as a fully replacement to the normal coarse aggregate. Several trial mixes were made prior to the mixing day in order to obtain the target compressive strength. Mixing method is important to obtain the required workability and homogeneity of the concrete mix, especially when a superplasticiser is used. Concrete is mixed in drum laboratory mixer, with a capacity of (0.1 m³). Initially, CCB aggregate and fine aggregate are poured into the mixer, followed by (50%) of the mixing water to wet them. The cement is added at this stage, followed by (25%) of the mixing water, then the remaining (25%) of water is added gradually to the mix. The superplasticizer is added gradually after this stage. The total mixing time is in the range of 4-6 minutes. The slump test is the most well-known and widely used test method to characterize the workability of fresh concrete. According to ASTM C143/C143M [26], the slump test consists of a tamping rod and a truncated cone, (300 mm) height and (100 mm) diameter at the top, and (200 mm) diameter at the bottom. The cone is filled with concrete and then slowly lifted. The unsupported concrete cone slumps down by its own weight; and the decrease in the height of the slumped cone is called the slump of concrete. After casting, the steel reinforced LWC slab was covered with a nylon cover to prevent evaporation of water. After one day, the upper surface of the slab was covered with 15 mm layer of potable water for 28 days in a laboratory conditions.

2. 4. Concrete Core Drilling The American Standard ASTM C42/C42M-20 [5] recommended avoiding the presence of any steel bars within the concrete cores during the extraction process. This can be possibly achieved by means of cover meter or pachometer. However, in some cases when steel reinforcement cannot be avoided during the drilling, the concrete cores should be trimmed to eliminate any steel bars within the cores. On the other hand, other testing standard such as the British Standard 1881: Part 120 [17] suggested a correction factor to overcome the effect of the steel bar presence within the concrete cores. This correction factor takes into account the effects of the ratio of the diameter of the bar to the diameter of the core. Also the effect of the ratio between bar location from a nearest end to the length of the core was taken into account.

In this study, the surface of the concrete slab was dried out for one day before cores drilling were conducted. Also, the surface was lined up with a permanent marker to identify the locations of the steel bars accurately. The LWC cores were obtained according

to the standard test method of British Standard 1881: Part 120 [17]. A core drilling machine was used to take concrete cores out of the slab. The diameter of the cutting drill was 90 mm. The drilling machine was placed on the surface of the concrete slab. This machine was connected to a water source to cool down the drilling cylinder during cutting the concrete cores, see Figure 4.

2. 5. Test Setup and Procedure

2. 5. 1. Compression Test To determine the compressive strength of the LWC cores, a Matest compression testing machine with a loading capacity of 1500 kN was used. For each group, two cores were tested under a constant loading of 20 MPa/min according to BS EN 12390-3:2019 [27] at the age of 28 days, as shown in Figure 5.

3. RESULTS AND DISCUSSION

3. 1. Concrete Compressive Strength In this experimental work, compressive strength test is made on concrete cores of 90 mm × 135 mm (diameter × height).



Figure 4. Concrete core drilling of LWC slab



Figure 5. LWC cores under compression test

TABLE 5. Mix proportion of the light weight concrete

Mix	Cement [kg/m ³]	Fine aggregate [kg/m ³]	CCB [kg/m ³]	Water [kg/m ³]	SP [l/m ³]
LWC	360	760	1056	200	1.93

The steel bars of different sizes were placed in Y and X directions as can be seen in Figure 1 to investigate the effect of the steel bars on the compressive strength of the LWC drilled cores. Figure 6 and Table 6 show the experimental compressive test results of this study at the age of 28 days.

Initially, the test results of the LWC cores are represent concrete cores with length/diameter (l/d) ratio less than two, so they need two types of correction factors to invert their strength into the design cube strength (F_{cu}). The first one is due to the effect of l/d ratio (0.97) and the second correction factor is due to the shape effect (1.2) (from cylinder to cube), see Table 6. However, LWC is defined according to the ACI C213R-14 [5] is the concrete that has compressive strength more than 17 MPa and density equal or less than 1850 kg/m³. It can be seen that compressive strength of the LWC cores was increased by increasing the diameter of the steel bar that provide more lateral confinement for the concrete sample and delay the ultimate failure of the concrete as well as increasing the ultimate load capacity of the concrete cores.

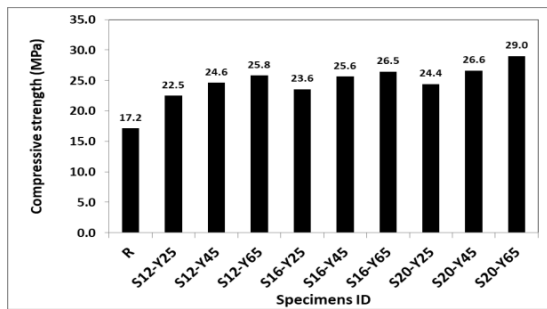
For LWC cores with steel bars in Y direction, the compressive strength was increased by nearly 30% to 68% for Specimens S12-Y25 and S20-Y45, respectively. This gain in the compressive strength is depending on the size and the location of the steel bar, as can be seen in Figure 6a. Also, it can be noticed the compressive strength of LWC cores was dramatically affected by the location of steel bar. The closer steel bar to the mid-height of the sample, the higher compressive strength is recorded. For LWC cores with steel bars in X direction, the compressive strength was increased by nearly 20% to

TABLE 6. The average compressive strength of LWC cores

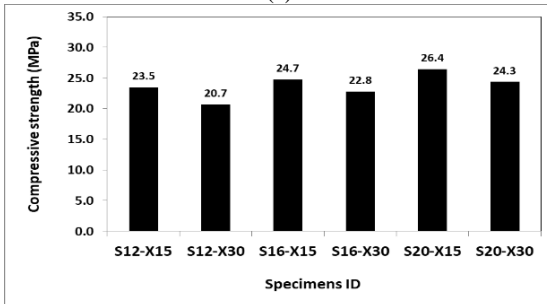
Specimen ID	Applied load (kN)	Core compressive strength (MPa)	Cube compressive strength (MPa)
R	109.2	17.2	20.0
S12-Y25	143.1	22.5	26.2
S12-Y45	156.5	24.6	28.6
S12-Y65	164.1	25.8	30.0
S16-Y25	149.9	23.6	27.4
S16-Y45	163.1	25.6	29.9
S16-Y65	168.3	26.5	30.8
S20-Y25	155.2	24.4	28.4
S20-Y45	169.3	26.6	31.0
S20-Y65	184.4	29.0	33.8
S12-X15	149.2	23.5	27.3
S12-X30	131.4	20.7	24.1
S16-X15	157.3	24.7	28.8
S16-X30	144.9	22.8	26.5
S20-X15	168.1	26.4	30.8
S20-X30	154.8	24.3	28.3

53% for Specimens S12-X30 and S20-X15, respectively. This increment was depending on the size and the location of the steel bar which has the same behavior of the steel bars in the Y direction, as shown in Figure 6b.

For concrete cores made with normal aggregate, it has been reported in previous studies that the presence of steel within the cores would dramatically reduce the strength of the cores [19]. However, in this study for concrete with LWC aggregate, the strength was increased slightly depending on the size and the location of the steel bars. This change in behaviour can be explained by the fact that more disturbance effect of core drilling is expected in normal concrete than LWC. This disturbance effect may causes weak bonding strength between aggregate and cement mortar and between concrete and steel bars during the drilling process. In contrast to normal aggregate concrete, LWC showed an excellent bonding microstructure between the light weight aggregate and the cement paste due to the high porosity of the light weight aggregate (crashed clay brick) as presented in Figure 7. This figure shows the microstructure of the LWC by the Scanning Electron Microscope (SEM) technique that shows the bonding between cement paste and the crashed clay brick aggregate after cores drilling.



(a)



(b)

Figure 6. Compressive strength results of LWC cores; (a) for steel bars in Y-direction and (b) for steel bars in X-direction

3. 2. Analytical Relationship between Steel Bars and Compressive Strength of LWC Cores

From the test results of concrete core samples, it can be found that the presence of steel bars has a noticeable effect on

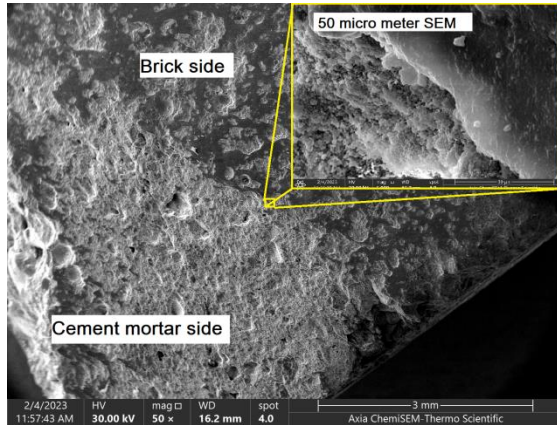


Figure 7. Scanning Electron Microscope (SEM) photo of the interfacial zone between the cement mortar and the CCB

the compressive strength test results of the LWC cores. In general, the experimental results showed that increasing steel bar diameter will increase the compressive strength of the LWC cores. Moreover; as the distance of steel bars from nearest core base increases, the compressive strength increases too. This can be explained by the effect of restraint degree, which is increase at the mid-distance of concrete core samples. The concrete cores samples that made of LWC are more affected by the presence of steel bars than those made of normal concrete.

As the steel reinforcement is unavoidable in many cases when concrete cores are taken out of the structural members, it was necessary to propose an equation that could take into account the effect of steel reinforcement. Although the current study has a limited number of concrete specimens (a total number of 48 samples) of LWC cores, but it can be the first step to suggest a new expression for LWC drilled cores to make the required correction for the compressive strength after the test. Also, there is a limited number of data in the literature that obtained from lightweight concrete which can be used to verify the proposed equation below.

The equation below takes into account the effect of steel bar diameter, the location of the steel bar from the nearest core base as well as the location of the steel bar from the centerline of the core. The general form of the equation shown in Equation 1, that showed a reliable correlation between the actual strength and the corrected strength with correlation coefficient of 0.97 as shown below:

$$f_{cc} = f_c \times [(1+1.51) \times (\frac{\phi}{D})^{0.136} \times (\frac{h}{L})^{0.185} \times (\frac{b}{D})^{0.04}] \quad (1)$$

where

f_{cc} : Corrected compressive strength

f_c : Actual compressive strength

ϕ : diameter of steel bar

D: diameter of concrete core

h: distance between steel bar and nearest core base

L: length of concrete core

b: distance between steel bar and centerline of the core
These expressions are obtained by using nonlinear estimation regression of Statistica program V7.1.

3. 3. Concrete Density The bulk density of the LWC in this study was to the LWC cores without steel bars. The density of these specimens can be compared to the density of normal concrete in order to indicate the reduction in the total weight of this type of concrete. By using recycled lightweight aggregate of CCB the average bulk density of the LWC was recorded to have 1899 kg/m³. Compare to the density of the normal concrete (nearly 2400 kg/m³), the LWC in this study was able to achieve about 20% reduction of the total weight by fully replacing of natural river aggregate with the CCB lightweight aggregate. Other specimens were recorded higher bulk density due to the presence of steel bars, as can be seen in Table 7.

3. 4. Failure Mode The failure mode was dramatically affected by the presence of the steel bars and their locations. It has been observed that the steel bar was confined the lateral strain of the specimens that is developed due to the effect of Poisons ratio while applying the axial load during the test. This type of confinement is due to the friction between the steel bar and the surrounding concrete. Accordingly, by the end of the compression test, the cracks were distributed and spread away from the steel bar location. Figure 8 shows the typical failure mode for both cases of LWC cores with and without steel bars.

TABLE 7. The average apparent density of LWC cores

Core ID	Height (m)	Weight (kg)	Volume (m ³)	Density (kg/m ³)
R	0.135	1.63	0.0008584	1899
S12-Y25	0.135	1.65	0.0008584	1922
S12-Y45	0.135	1.68	0.0008584	1957
S12-Y65	0.132	1.7	0.0008393	2025
S16-Y25	0.133	1.73	0.0008457	2046
S16-Y45	0.133	1.73	0.0008457	2046
S16-Y65	0.132	1.72	0.0008393	2049
S20-Y25	0.135	1.8	0.0008584	2097
S20-Y45	0.135	1.9	0.0008584	2213
S20-Y65	0.135	1.9	0.0008584	2213
S12-X15	0.133	1.68	0.0008457	1990
S12-X30	0.135	1.70	0.0008457	2010
S16-X15	0.135	1.75	0.0008584	2039
S16-X30	0.134	1.75	0.0008584	2039
S20-X15	0.135	1.84	0.0008393	2187
S20-X30	0.133	1.92	0.0008457	2270

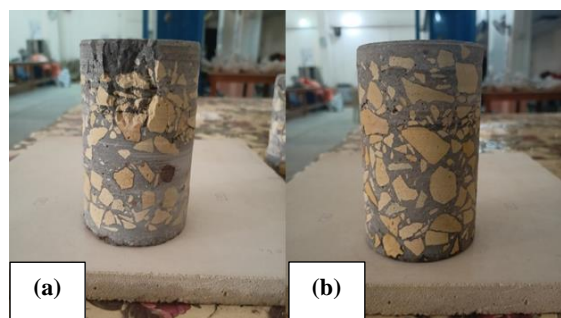


Figure 8. Typical failure mode of LWC cores (a) with steel bar and (b) without steel bar

4. CONCLUSIONS

On the basis of the experimental program presented above of the LWC mix described in the text, using two variables (steel bar diameter and steel bar location) the main conclusions can be summarized, as follows:

1. The experimental results showed that the presence of the steel bars within the LWC cores increases the compressive strength of the LWC cores. This behaviour is more noticeable when the location of the steel bar is near to the mid-height of the concrete core. Also, the influence of the steel bar diameter is increased by increasing the size of the steel bar which showed higher compressive strength.
2. An equation was suggested that can be used to determine the effect of the steel bar on the compressive strength of LWC drilled cores. However, this equation is limited to one steel bar within the core and compressive strength of with range of 17 to 27 MPa.
3. The apparent density of the LWC mix in this study was determined to have 1899 kg/m^3 which is very close to the requirement of the ACI C213 committee (1850 kg/m^3). This was achieved by full replacement of normal coarse aggregate with crushed clay brick aggregate.
4. The failure mode of the LWC cores was dramatically affected by the diameter and the location of the steel bar within the concrete cores.
5. The LWC was able to maintain excellent bond strength between the cement mortar and the crushed clay brick aggregate due to the high surface porosity of the aggregate that contained some of the hydrated cement products.

5. REFERENCES

1. Weigler, H. and Karl, S., "Structural lightweight aggregate concrete with reduced density—lightweight aggregate foamed concrete", *International Journal of Cement Composites and Lightweight Concrete*, Vol. 2, No. 2, (1980), 101-104. doi: 10.1016/0262-5075(80)90029-9.
2. Amran, Y.M., Farzadnia, N. and Ali, A.A., "Properties and applications of foamed concrete; a review", *Construction and*

Building Materials, Vol. 101, (2015), 990-1005. doi: 10.1016/j.conbuildmat.2015.10.1112.

3. Lu, Y., Hu, X., Yang, X. and Xiao, Y., "Comprehensive tests and quasi-brittle fracture modeling of light-weight foam concrete with expanded clay aggregates", *Cement and Concrete Composites*, Vol. 115, (2021), 103822. doi: 10.1016/j.cemconcomp.2020.103822.
4. Neville, A., "Properties of concrete, John Wiley & Sons Inc., New York, 1996", Vol., No. doi.
5. Akers, D.J., Gruber, R.D., Ramme, B.W., Boyle, M.J., Grygar, J.G., Rowe, S.K., Bremner, T.W., Kluckowski, E.S., Sheetz, S.R. and Burg, R.G., "Guide for structural lightweight-aggregate concrete", ACI 213R-03. American Concrete Institute (ACI), Michigan, (2003).
6. Cui, H., Lo, T.Y., Memon, S.A. and Xu, W., "Effect of lightweight aggregates on the mechanical properties and brittleness of lightweight aggregate concrete", *Construction and Building Materials*, Vol. 35, (2012), 149-158.
7. Del Rey Castillo, E., Almesfer, N., Saggi, O. and Ingham, J.M., "Light-weight concrete with artificial aggregate manufactured from plastic waste", *Construction and Building Materials*, Vol. 265, (2020), 120199. doi: 10.1016/j.conbuildmat.2020.120199.
8. Vakhshouri, B. and Nejadi, S., "Mix design of light-weight self-compacting concrete", *Case Studies in Construction Materials*, Vol. 4, (2016), 1-14.
9. Wei, H., Wu, T., Liu, X. and Zhang, R., "Investigation of stress-strain relationship for confined lightweight aggregate concrete", *Construction and Building Materials*, Vol. 256, (2020), 119432. doi: 10.1016/j.conbuildmat.2020.119432.
10. Yang, Y., Ge, Z., Li, Y., Xiong, Y. and Yuan, Q., "Study on impact resistance of precast light-weight concrete sandwich panels", in *Structures*, Elsevier. Vol. 47, (2023), 966-975.
11. Aarthi, K., Jeyshankaran, E. and Aranganathan, N., "Comparative study on longitudinal shear resistance of light weight concrete composite slabs with profiled sheets", *Engineering Structures*, Vol. 200, (2019), 109738. doi: 10.1016/j.engstruct.2019.109738.
12. Martins, R., Carmo, R., Costa, H., Júlio, E., Cordeiro, T. and Almeida, V., "Interface role in composite rc beams with a light-weight concrete core and an ultra high-durability concrete skin", *Engineering Structures*, Vol. 228, (2021), 111524. doi: 10.1016/j.engstruct.2020.111524.
13. Ghanbari, M., Kohnehpooshi, O. and Tohidi, M., "Experimental study of the combined use of fiber and nano silica particles on the properties of lightweight self compacting concrete", *International Journal of Engineering, Transactions B: Applications*, Vol. 33, No. 8, (2020), 1499-1511. doi: 10.5829/IJE.2020.33.08B.08.
14. Kulkarni, P. and Muthadhi, A., "Improving thermal and mechanical property of lightweight concrete using n-butyl stearate/expanded clay aggregate with alcofine1203", *International Journal of Engineering, Transactions A: Basics*, Vol. 33, No. 10, (2020), 1842-1851. doi: 10.5829/ije.2020.33.10a.03.
15. Mohammed, T. and Kadhim, H., "Static and dynamic behavior of high-strength lightweight reinforced concrete one-way ribbed slabs", *International Journal of Engineering, Transactions A: Basics*, Vol. 35, No. 4, (2022), 732-739. doi: 10.5829/ije.2022.35.04a.13.
16. International, A., *Astm c42/c42m—16 standard test method for obtaining and testing drilled cores and sawed beams of concrete*. 2016, ASTM International West Conshohocken, PA, USA.
17. BSI, B., "Testing concrete: Part 120—method for determination of compressive strength of concrete cores", British Standards Institution, London, (1983).
18. 11, C.S.T.R., *Concrete core testing for strength*, in *Technical Report No.11*, The Concrete Society, London. 1976.
19. Tuncan, M., Arioz, O., Ramyar, K. and Karasu, B., "Assessing concrete strength by means of small diameter cores",

- Construction and Building Materials*, Vol. 22, No. 5, (2008), 981-988. doi: 10.1016/j.conbuildmat.2006.11.020.
20. Momeni, K., Madandoust, R. and Ranjbar, M.M., "Evaluating the application of reinforcement correction factor for concrete core testing", *Journal of Rehabilitation in Civil Engineering*, Vol. 7, No. 3, (2019), 166-182. doi: 10.22075/JRCE.2018.14724.1269.
 21. Lessly, S.H., Senthil, R. and Krishnakumar, B., "A study on the effect of reinforcement on the strength of concrete core", *Materials Today: Proceedings*, Vol. 45, (2021), 6476-6481. doi: 10.1016/j.matpr.2020.11.367.
 22. Reddy, B. and Wanjari, S., "A partially destructive method for testing in-situ strength of concrete", in IOP Conference Series: Materials Science and Engineering, IOP Publishing. Vol. 431, (2018), 052012.
 23. Haavisto, J., Husso, A. and Laaksonen, A., "Compressive strength of core specimens drilled from concrete test cylinders", *Structural Concrete*, Vol. 22, (2021), E683-E695. doi: 10.1002/suco.202000428.
 24. Reddy, B.S.K. and Wanjari, S., "Core strength of concrete using newly developed in situ compressive testing machine", *Magazine of Concrete Research*, Vol. 70, No. 22, (2018), 1149-1156. doi: 10.1088/1757-899X/431/5/052012.
 25. No, I.S., "For aggregates of natural resources used for concrete and construction", Baghdad, Iraq, (1984).
 26. ASTM, American standard for testing materials. C143-03, standard test method for slump of hydraulic cement concrete in ASTM International. 2003.
 27. BSI, "Bs en 12390-3: 2019: Testing hardened concrete. Part 3: Compressive strength of test specimens, BSI British Standards Institution, (2022).

Persian Abstract

چکیده

در بسیاری از بخش‌های بتنی مسلح، میلگردهای فولادی در حین حفاری هسته بتن قابل اجتناب نیستند و وجود این میلگردهای فولادی تأثیر مستقیمی بر نتایج این آزمایش دارد. هدف این مطالعه بررسی اثر حضور میله‌های فولادی بر نتایج آزمایش هسته‌های بتن سبک وزن دانه‌های باز یافتی (LWC) است. برای این منظور، یک مخلوط بتن سبک با تعداد کل ۴۸ هسته بتنی از دالی به ابعاد ۱ متر عرض، ۱.۵ متر طول و ۰.۱۵ متر ضخامت تهیه شد. هر هسته دارای ابعاد ۹۰ میلی متر قطر و ۱۵۰ میلی متر ارتفاع است. سه اندازه مختلف میله فولادی (۱۲، ۱۶ و ۲۰ میلی متر) در شش مکان مختلف (۲۵، ۴۵ و ۶۵ میلی متر) از پایه هسته و (۱۵ و ۳۰ میلی متر) از خط مرکزی هسته استفاده شد. یک آجر رسی شکسته باز یافت شده (CCB) به عنوان جایگزینی برای سنگدانه درشت استفاده شد. در مقایسه با چگالی بتن معمولی (۲۴۰۰ کیلوگرم بر متر مکعب)، LWC توانست با جایگزینی کامل سنگدانه معمولی با CCB، نزدیک به ۲۰ درصد کاهش وزن کل را به دست آورد. مشخص شده است که وجود فولاد استحکام فشاری هسته های LWC را افزایش می دهد. این اثر زمانی که محل میلگرد فولادی نزدیک به ارتفاع وسط یا خط مرکزی هسته بتنی باشد بیشتر قابل توجه است. همچنین تأثیر قطر میلگرد فولادی با افزایش اندازه میله فولادی افزایش یافته است.



Design and Qualitative Analysis of Hetero Dielectric Tunnel Field Effect Transistor Device

S. Howldar, B. Balaji*, K. Srinivasa Rao

Department of Electronics and Communication Engineering, Koneru Lakshmaiah Education Foundation, Green Fields, Vaddeswaram, Guntur, Andhra Pradesh, India

PAPER INFO

Paper history:

Received 25 March 2023

Received in revised form 05 April 2023

Accepted 09 April 2023

Keywords:

High K Dielectric Materials

Tunnel Field Effect Transistor

Hafnium Oxide

Drain Current

Technology Computer Aided Desisn

ABSTRACT

A Hetero Dielectric Tunnel field effect transistor with the spacer on both sides of the gate is proposed in this paper. The performance and characteristics of Hetero Dielectric Tunnel field effect transistor using the ATLAS Technology Computer-Aided Design in 5nm regime were analyzed. The band-to-band tunneling leakage current will be reduced by introducing heterojunction and hetero dielectric spacer material in the proposed structure. In Hetero Dielectric Tunnel field effect transistor, double metal gate and high-k dielectric spacer improves high on the current and subthreshold swing. The high-k dielectric Hafnium oxide spacer is placed on both sides of the source and drains to import the tunneling mechanism. The proposed device in the 5nm node has improved DC characteristics such as a High ON-state current of 1.68×10^{-5} Amp & OFF-state Current reduced from 7.83×10^{-11} Amp to 5.13×10^{-12} Amp and ION / IOFF ratio has increased from 3.22×10^5 to 3.27×10^6 compared to conventional dual gate Tunnel field effect transistor. Therefore, this device is suitable for low power applications

doi: 10.5829/ije.2023.36.06c.11

1. INTRODUCTION

As the Semiconductor industry leads into nanoscale technology and the device dimensions are continuously downscaling, The Hetero Dielectric Tunnel field effect transistor is the alternative because of its tunneling mechanism, lower leakage current and reduced short channel effect. Several attempts have been made to improve the electrical properties and drain current characteristics of Tunnel Field Effect transistors [1]. Due to its band to band tunneling and wide variety of methods and strategies are developed in the Tunnel Field Effect transistors devices The gate-oxide semiconductor materials being low-k dielectric material such as Silicon Dioxide, high-k dielectric materials as Hafnium oxide and gate-electrodes play vital role in the improvement of electrical and drain current characteristics [2]. The source-side oxide regions of Tunnel Field Effect transistors device will improve on-current, and the drain-side oxide region reduces the off-current. Therefore, the tunneling mechanism occurs in the source-channel region

during the on-state condition and same tunneling process will determine the ambipolar off-current [3].

The Nanoscale Tunnel Field Effect transistors is an advanced transistor suitable for digital circuit applications and Radio Frequency applications based on improved drain current characteristics [4]. In Tunnel Field Effect transistors the tunnel width is narrow, therefore electrons can tunnel from the p+ source to the channel for conduction and higher band to band tunneling generation rate. As a result, the channel has more carriers accessible for current conduction. Due to their lower power dissipation, tunnel field-effect transistors are widely used in nanoscale semiconductor devices and can operate at reduced bias voltages [5].

In the reverse bias structure, Tunnel Field Effect Transistor exhibits a miniaturized short channel effect, reduced leakage current, and decreased temperature dependency and has major issues correlated to lower drain current, and lacking in high-frequency applications. To overcome these issues, several techniques were introduced by the researchers as gate overlap and

*Corresponding Author Email: vahividi@gmail.com (B. Balaji)

underlap engineering on the drain side, source extension engineering, drain extension engineering, gate work function engineering, pocket layer, and hetero dielectric materials to increase the on-current (I_{on}) [6]. To increase the drain current characteristics all the approaches depend on tunneling narrow width and a large electric field (E). In addition, different heterostructures come up for low band gap semiconductor materials Gallium arsenide, and Indium phosphide to achieve improved current. But due to the complexity of these structures hard to achieve a good on-state current. Due to the large band gap and effective mass, all the Tunnel Field Effect transistors devices provide a lower band-to-band tunneling rate. Therefore, heterostructure Tunneling Field Effect Transistor with low band gap material is preferable to enhance on-state performance characteristics [7].

We proposed a hetero dielectric Tunnel Field Effect transistors device made of Nanomaterial oxide with a spacer to combine all the low-k dielectric material such as Silicon Dioxide and high-k dielectric semiconductor materials such as Hafnium Oxide to achieve good tunneling mechanism and reduce leakage. The high-k dielectric material hafnium oxide and Titanium Dioxide are used as spacer material on both sides of dual metal gate to improve device drain current (I_d) [8]. The lower bandgap should increase the device drain current characteristics whereas the higher band gap should reduce the ambipolar current in the device. Due to lower operating voltage, the I_{on}/I_{off} ratio decreases. Therefore, we applied spacer material as high-k dielectric material being hafnium oxide on both sides of the dual metal gate and having smaller tunneling bandgap has been introduced in the proposed device [9].

In this paper, we have considered spacer engineering on both sides of a dual gate with a high-k dielectric material as hafnium oxide along with hetero dielectric and hetero junction engineering techniques and Nanomaterial oxide materials to improve I_{on} current and lower the ambipolar current. Due to the spacer engineering technique, the drain-channel interface could be suppressed because of increased depletion width. In the proposed device hetero dielectric material is used to modulate the tunneling barrier at source-channel and drain channel interfaces. High-k dielectric material Hafnium oxide is chosen for improved results. The drain current characteristics of the device have been carried out and compared with other models such as Conventional - Tunnel Field Effect Transistor, Dual Gate- Tunnel Field Effect, and Hetero junction Dual Gate - Tunnel Field Effect. The simulations have been performed and extracted using the Silvaco Technology Computer Aided Design simulator [10].

The organization of the paper is as follows: The proposed Nanoscale device, its models, methods, and device parameters are presented in second section. The third section presented results and discussion of drain

current characteristics such as I_{on} current, I_{off} current, and I_{on}/I_{off} ratio. The final section is presented as conclusion.

2. STRUCTURE

Figure 1 shows 2-Dimensional view of conventional Tunnel Field Effect transistor with Hafnium Oxide, Silicon Dioxide, and Nanomaterial oxide materials are utilized for the design. The device dimension (W_d) is 60 nanometers long and gate length (L_g) of 5 nanometers, a source length (L_s) of 27.5 nanometers, a drain length of 27.5 nanometers, and a channel length of 5 nanometers. The symmetric dual metal gate is connected on top and bottom with oxide material with Silicon Dioxide. 5nm channel length is connected equally from source and drain terminals [11].

Figure 2 shows the 2-Dimensional view of Dual Material Gate Tunnel Field Effect transistor where the materials such as Hafnium Oxide, Silicon Dioxide, and Nanomaterial oxide materials are used. An asymmetric dual metal gate is connected on top and bottom with oxide material with Silicon Dioxide. 5nm channel length is connected equally from source and drain terminals [12].

Figure 3 shows the 2-Dimensional view of view of High-k Dielectric material with Hafnium Oxide Spacer. The material utilized for the spacer in this Spacer Tunnel Field Effect Transistor is Hafnium Oxide [11, 12]. Spacers are used at the top and bottom gates of the source side and drain side. The spacers are 7nm long and 2nm wide, with a length of 7nm and a width of 2nm are utilized in Silvaco TCAD tool along with Nanomaterial oxides [13].

Figure 4 depicts the 2-Dimensional view of structure of the Hetero-Dielectric Tunnel Field Effect Transistor

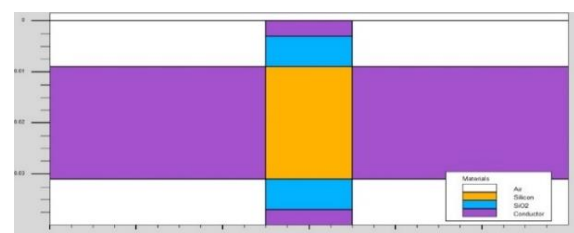


Figure 1. Structure of Conventional device

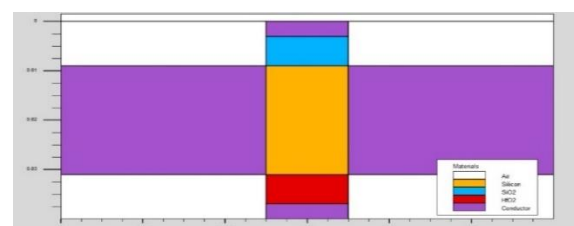


Figure 2. Structure of Dual Material Gate Tunnel Device

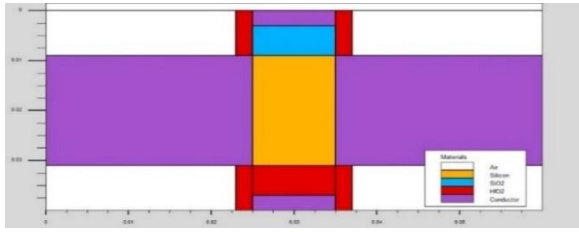


Figure 3. Structure of Spacer Tunnel Device

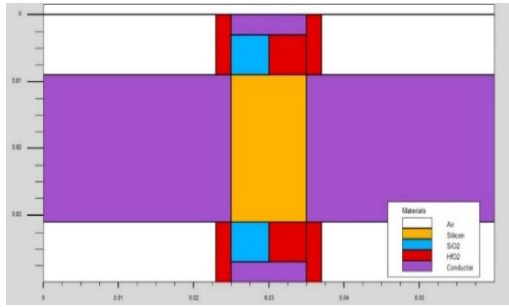


Figure 4. Proposed device

in this structure interface layer improves contact between the semiconductors [14]. The device dimension (W_d) is 60 nanometers long, with a gate length (L_g) of 5 nanometers, source length (L_s) of 27.5 nanometers, and drain length of 27.5 nanometers. The material utilized for the Spacer is Hafnium Oxide. Spacers are used at both sides of the source and the drain. The spacers are 7nm long and 2nm wide, with a length of 7nm and a width of 2nm [15].

In the above architectures, a lightly doped channel is employed with a $1 \times 10^{16} \text{ cm}^{-3}$ doping concentration, and an increased doping concentration of $5 \times 10^{19} \text{ cm}^{-3}$ is employed in the channel to introduce spacer at the end of the source side with the implantation method in the fabrication process for adopting channel engineering.

Table 1 shows the effective parameters used to simulate the Hetero Dielectric- Dual Material Gate Spacer Tunnel Field Effect Transistor device using the Silvaco tool. The on-state current and off-state current of various architectures and variations of channel length are shown in Tables 2, 3 and 4.

In Symmetrical Dual-k Hetero- Dielectric Tunnel Field Effect Transistor, the length ratio of Hafnium oxide and Low-k is varied from 1:14 to 14:1 over the total spacer length of 10nm. The spacer length of Hafnium oxide and Low-k plays a significant role in describing the electrostatics of a gate-S/D underlap in the device. For underlap architecture, high-permittivity (k) spacer material modulates the charge transport dynamics inside the channel and the underlap region.

The technical report of the proposed device is analyzed with a 2D simulation tool SILVACO for striving design. To obtain the optimum structure of the device, enhanced meshing is used to design the device.

TABLE 1. Used Parameters for the proposed structure

Parameter	Proposed Values
Device Length(W_L)	60nm
Gate Length(L_G)	10nm
Source Length(L_S)	25nm
Drain Length(L_D)	25nm
Channel Length(L_C)	10nm
Doping of Source(D_S)	$1 \times 10^{17} \text{ cm}^{-3}$
Doping of Drain(D_D)	$1 \times 10^{18} \text{ cm}^{-3}$
Doping of Channel(D_C)	$1 \times 10^{20} \text{ cm}^{-3}$
Metal Gate Work Function(W_F)	4.8eV
Thickness of SiO_2	2nm
Thickness of HfO_2	3nm

The Two-Dimensional graphical representation of the proposed dielectric material Spacer Tunnel Field Effect Transistor is extensively used for low power digital applications due to its improved performance parameters.

The originality of the proposed structure is designed from one to one i.e conventional Tunnel Field Effect Transistor, dual material gate, symmetrical spacer material and hetero dielectric Tunnel Field Effect Transistor with length of dual gate is 5nm and thickness of each oxide layer 2nm, 3nm using Silvaco tool.

The future prospect of the proposed device could be designed with Low-k source side Asymmetric Spacer Halo doped Tunnel Field Effect Transistor, then there is a 74% reduction in gate capacitance and 31% reduction in intrinsic Delay

The proposed dual material hetero dielectric spacer Tunnel device is invented using Silvaco tool with gate length of 5nm. In this model both high-k and low-k materials are symmetrical. Therefore, the drain current characteristics of proposed model is higher than the existed models.

3. RESULTS AND DISCUSSION

3. 1. Drain Current

The following equation is used to drain current of any conventional device:

$$I_{\text{drain-sat}} = z b(x) q n(x) v(x)$$

where z is channel width, $b(x)$ is effective depth of the channel, q is electron charge, $n(x)$ is electron density, and $v(x)$ is electron velocity.

The drain current and gate voltage characteristics of the proposed device Hetero- Dielectric -Dual Material Gate Tunnel Field Effect Transistor for varied Gate lengths of 5nm, 7nm, 10nm, and 15nm are shown in Figure 5. The drain current of the proposed device increased as the length of gate is reduced [16-18]. Figure

6 shows that the proposed device drain current Vs gate voltage, where the drain current of the device is higher than the conventional device and it has high drain current characteristics [19].

In Figure 7, the Hetero- Dielectric -Dual Material Gate -Tunnel Field Effect Transistor device's I_{ON} to I_{off} ratio rises with increasing high-k dielectric length up to 5 nm. Because of a significant increase in ON-state current, the current ratio has increased exponentially. However, as I_{off} and saturated I_{on} increase above 5 nm, the ratio decreases significantly. As a result, the lengths of Hafnium dioxide and Silicon dioxide dielectric materials are 5 and 10 nanometers, respectively.

Figure 8 depicts the effect of Hafnium dioxide Spacer length variation on the suggested structure's transfer properties. As the Spacer length of Hafnium dioxide is increased, on current (I_{on}) increases to 5 nm, and then drain current (I_d) increases at lengths of 7nm and 10 nm. Because the tunneling barrier width at the channel-drain interface is reduced, the ambipolar current steadily increases. We chose 10 nm and 20 nm for the Hafnium dioxide and Silicon dioxide layers, respectively, to retain a greater I_{on}/I_{off} ratio without impairing the Hetero-Dielectric -Dual Material Gate-Tunnel Field Effect Transistor structure's OFF current. The adjusted 5nm gate length is proposed for this structure, because of improved performance characteristics [20].

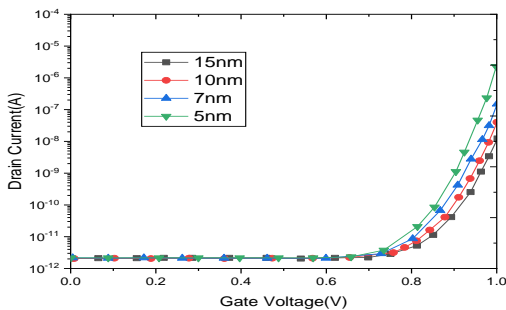


Figure 5. Drain current versus Gate voltage with different Gate length

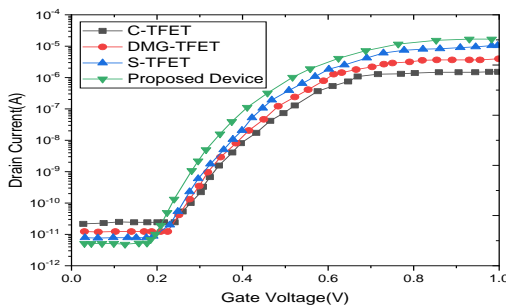


Figure 6. Drain current versus Gate voltage for different structures

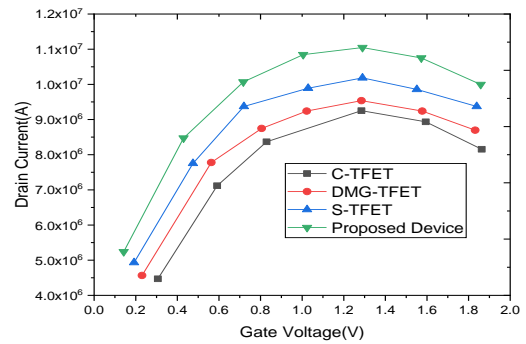


Figure 7. Variation of on current for different structures

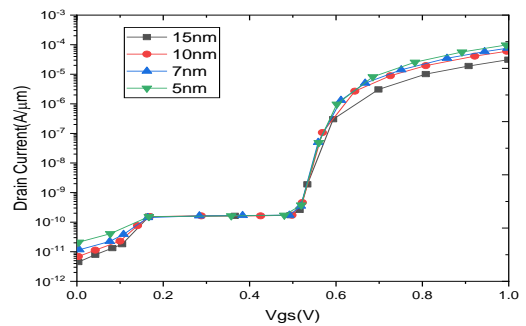


Figure 8. Drain current versus Gate voltage with Spacer material

Due to the applied narrow band gap material as silicon dioxide on the source side, the heterojunction Tunnel Field Effect Transistor demonstrates improved band bending is shown in Figure 9. Based on high-k dielectric materials such as Hafnium oxide at the tunneling side, the width of Hetero Dielectric-Dual Material Gate- Tunnel Field Effect Transistor is reduced when compared to other structures [21, 22]. As a result, a large number of carriers can tunnel from the source to the channel region, resulting in a greater on-state current. Because of an increase in depletion width in the drain area, both Dual Material Gate- Tunnel Field Effect Transistor and Spacer-Tunnel filed effect transistor exhibit reduced band bending. On the drain side of the Hetero- Dielectric -Dual Material Gate -Tunnel Field Effect Transistor, Silicon dioxide also reduced.

3. 2. Electric Field

Figure 10 shows the electric field distribution of proposed device with device length in state condition ($V_{gs} = 1.5V$) and ambipolar voltage ($V_{gs} = 1.5V$) states. Due to the electric field crowding effect, the breakdown should be happening at the gate nearer the drain. Hence the electric field concentration has increased compared to conventional devices. Based proposed structure, the electric field concentration is more compared to the electric field distribution of other

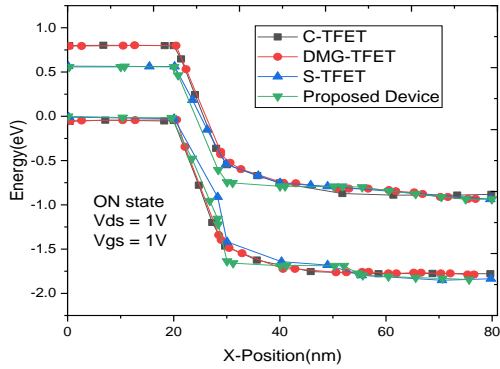


Figure 9. Energy band diagram of the proposed device

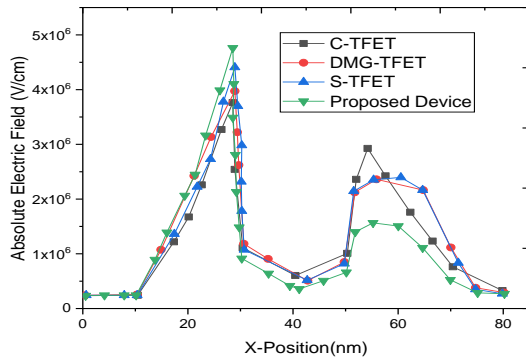


Figure 10. Absolute electric field of proposed device

devices [23]. The reduction in the tunneling barrier width in heterojunction Tunnel Field Effect Transistor s results in a greater electric field along the source-channel interfaces, as shown in the figure. The use of Hafnium oxide as a dielectric in the source channel when compared to previous simulated structures, the suggested Hetero– Dielectric –Dual Material Gate –Tunnel Field Effect Transistor has less ambipolar behavior [24, 25].

3. 3. Transconductance The Trans conductance versus Gate voltage for different structures are shown in Figure 11. The proposed device attains the highest packing density due to better current flow in the device. Hence this structure provides more improvement in transconductance. To achieve proper gain of device high transconductance is needed and calculated. Using the Silvaco tool transistor characteristics simulations are performed dielectric is used, resulting in less band-to-band tunneling process will exist [26].

The higher drain current driving power of charge carriers, gm increases exponentially with an increase in gate bias. Because of higher drain current (Id), heterojunction Tunnel Field Effect Transistor has a higher gm value than Dual Material Gate-TFET and

Spacer-Tunnel Field Effect Transistor. However, due to mobility degradation, it decreases with a bigger magnitude of gate bias. Another essential measure for estimating device efficiency is the transconductance generation factor [27, 28]. Transconductance generation factor demonstrates the efficiency with which current can be converted into transconductance (speed).

$$\text{Transconductance } (G_m) = \frac{\partial I_{ds}}{\partial V_{gs}} \quad (1)$$

The performance Improvements of proposed hetero dielectric structure compared with on current, leakage current and its ratio for three different devices are shown in Table 2. Based on comparison on current is increases, leakage current reduces and its ratio is increases. Therefore, the proposed device performance parameters are improved compared to previous devices (Tables 3 and 4) [29, 30].

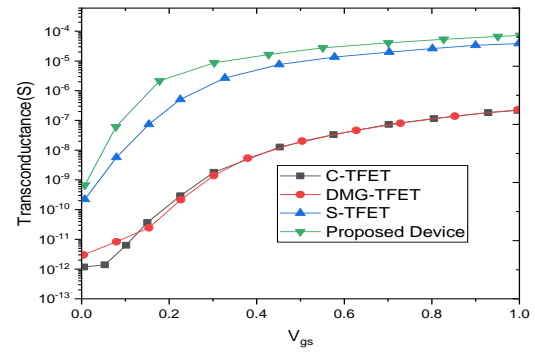


Figure 11. Comparison of Transconductance for the proposed device

TABLE 1. On current and off current for different Structures

Architecture	IOFF	ION	ION/IOFF
C-TFET	2.17E-11	1.51E-6	6.95E+4
DMG-TFET	1.23E-11	3.97E-6	3.22E+5
S-TFET	7.83E-12	1.03E-5	1.31E+6
Proposed Device	5.13E-12	1.68E-5	3.27E+6

TABLE 2. Comparison of on current and off current for the hetero structure

Architecture	IOFF	ION	ION/IOFF
C-TFET	1.00E-9	7.44E-8	7.44E+1
DMG-TFET	6.25E-11	7.65E-8	1.22E+3
S-TFET	1.23E-11	1.90E-5	1.54E+6
Proposed Device	7.03E-12	3.52E-5	5.00E+6

TABLE 4. On current and off current for the proposed device with the variation of Gate Length

Gate Length	IOFF	ION	ION/IOFF
15nm	2.05E-12	1.23E-8	6.00E+3
10nm	2.05E-12	4.02E-8	1.96E+4
7nm	2.15E-12	1.49E-7	6.93E+4
5nm	2.15E-12	2.27E-6	1.03E+6

4. CONCLUSION

In this paper, we have designed and analyzed the DC performance analysis of Hetero– Dielectric Tunnel Field Effect Transistor (Hetero Dielectric -Nanowire-Tunnel Field Effect Transistor) with spacer using Silvaco tool in sub 5nm node. The high-k dielectric material hafnium oxide as spacer material is placed on both sides of the dual metal gates. The impact of the proposed device is to reduce the ambipolar current and significantly increase the drain current compared to dual gate Tunnel Field Effect Transistor. The proposed structure with potential high-k dielectric material being hafnium oxide, as a spacer on both sides of the gate has improved better performance over conventional Dual gate Tunnel Field Effect Transistor. Due to maximum drain currents (I_d), less sub-threshold swing (SS), lower leakage current (I_{off}), greater trans conductance (gm), and larger drain conductance (\bar{G}) the proposed Hetero Dielectric-Nanowire –Tunnel Field Effect Transistor is useful in low power applications

5. REFERENCES

- Cui, N., Liu, L., Xie, Q., Tan, Z., Liang, R., Wang, J. and Xu, J., "A two-dimensional analytical model for tunnel field effect transistor and its applications", *Japanese Journal of Applied Physics*, Vol. 52, No. 4R, (2013), 044303. doi: 10.7567/JJAP.52.044303.
- Bardon, M.G., Neves, H.P., Puers, R. and Van Hoof, C., "Pseudo-two-dimensional model for double-gate tunnel fets considering the junctions depletion regions", *IEEE Transactions on Electron Devices*, Vol. 57, No. 4, (2010), 827-834. doi: 10.1109/TED.2010.2040661.
- Gholizadeh, M. and Hosseini, S.E., "A 2-d analytical model for double-gate tunnel fets", *IEEE Transactions on Electron Devices*, Vol. 61, No. 5, (2014), 1494-1500. doi: 10.1109/TED.2014.2313037.
- Yadav, M., Bulusu, A. and Dasgupta, S., "Two dimensional analytical modeling for asymmetric 3t and 4t double gate tunnel fet in sub-threshold region: Potential and electric field", *Microelectronics Journal*, Vol. 44, No. 12, (2013), 1251-1259. doi: 10.1007/s12633-021-01509-2.
- Liao, X., Tsui, K., Liu, H., Chen, K. and Sin, J., "A step-gate-oxide soi mosfet for rf power amplifiers in short-and medium-range wireless applications", in 2003 Topical Meeting on Silicon Monolithic Integrated Circuits in RF Systems, 2003. Digest of Papers., IEEE., (2003), 33-36.
- Boucart, K. and Ionescu, A.M., "Double-gate tunnel fet with high- κ gate dielectric", *IEEE Transactions on Electron Devices*, Vol. 54, No. 7, (2007), 1725-1733. doi: 10.1109/TED.2007.899389.
- Luong, G.V., Narimani, K., Tiedemann, A., Bernardy, P., Trelenkamp, S., Zhao, Q. and Mantl, S., "Complementary strained si gaa nanowire tfet inverter with suppressed ambipolarity", *IEEE Electron Device Letters*, Vol. 37, No. 8, (2016), 950-953. doi: 10.1109/LED.2016.2582041.
- Hu, V.P.-H., Chiu, P.-C. and Lu, Y.-C., "Impact of work function variation, line-edge roughness, and ferroelectric properties variation on negative capacitance fets", *IEEE Journal of the Electron Devices Society*, Vol. 7, (2019), 295-302. doi: 10.1109/JEDS.2019.2897286.
- Asthana, P.K., Ghosh, B., Goswami, Y. and Tripathi, B.M.M., "High-speed and low-power ultradeep-submicrometer iii-v heterojunctionless tunnel field-effect transistor", *IEEE Transactions on Electron Devices*, Vol. 61, No. 2, (2014), 479-486. doi: 10.1039/C4RA00538D.
- Balaji, B., Srinivasa Rao, K., Girija Sravani, K., Bindu Madhav, N., Chandras, K. and Jaswanth, B., "Improved drain current characteristics of $\text{HfO}_2/\text{SiO}_2$ dual material dual gate extension on drain side-tfet", *Silicon*, (2022), 1-6. doi: 10.1007/s12633-022-01955-6.
- Wadhwa, G. and Raj, B., "Design, simulation and performance analysis of jltfet biosensor for high sensitivity", *IEEE Transactions on Nanotechnology*, Vol. 18, (2019), 567-574. doi: 10.1109/TNANO.2019.2918192.
- Kumar, P.K., Balaji, B. and Rao, K.S., "Performance analysis of sub 10 nm regime source halo symmetric and asymmetric nanowire mosfet with underlap engineering", *Silicon*, Vol. 14, No. 16, (2022), 10423-10436. doi: 10.1007/s12633-022-01747-y.
- Balaji, B., Rao, K.S., Sravani, K.G. and Aditya, M., "Design, performance analysis of gaas/6h-sic/algan metal semiconductor fet in submicron technology", *Silicon*, (2022), 1-5. doi: 10.1007/s12633-021-01545-y.
- Narang, R., Reddy, K.S., Saxena, M., Gupta, R. and Gupta, M., "A dielectric-modulated tunnel-fet-based biosensor for label-free detection: Analytical modeling study and sensitivity analysis", *IEEE Transactions on Electron Devices*, Vol. 59, No. 10, (2012), 2809-2817. doi: 10.1109/LED.2011.2174024.
- Kumar, N. and Raman, A., "Design and investigation of charge-plasma-based work function engineered dual-metal-heterogeneous gate si-si 0.55 ge 0.45 gaa-cylindrical nwtfet for ambipolar analysis", *IEEE Transactions on Electron Devices*, Vol. 66, No. 3, (2019), 1468-1474. doi: 10.1109/TED.2019.2893224.
- Morifuji, E., Yoshida, T., Kanda, M., Matsuda, S., Yamada, S. and Matsuoka, F., "Supply and threshold-voltage trends for scaled logic and sram mosfets", *IEEE Transactions on Electron Devices*, Vol. 53, No. 6, (2006), 1427-1432. doi: 10.1109/TED.2006.874752.
- Musalganekar, G., Sahay, S., Saxena, R.S. and Kumar, M.J., "Nanotube tunneling fet with a core source for ultrastep subthreshold swing: A simulation study", *IEEE Transactions on Electron Devices*, Vol. 66, No. 10, (2019), 4425-4432. doi: 10.1109/TED.2019.2933756.
- Guin, S., Chattopadhyay, A., Karmakar, A. and Mallik, A., "Impact of a pocket doping on the device performance of a schottky tunneling field-effect transistor", *IEEE Transactions on Electron Devices*, Vol. 61, No. 7, (2014), 2515-2522. doi: 10.1109/TED.2014.2325068.
- Lee, J.W. and Choi, W.Y., "Design guidelines for gate-normal hetero-gate-dielectric (GHG) tunnel field-effect transistors (tfets)", *IEEE Access*, Vol. 8, (2020), 67617-67624. doi: 10.1109/ACCESS.2020.2985125.

20. Naraiah, R., Balaji, B., Radhamma, E. and Udutha, R., "Delay approximation model for prime speed interconnects in current mode", *IJITEE*, ISSN, (2019), 2278-3075. doi: 10.35940/ijitee.I8019.078919.
21. Singh, N., Buddharaju, K.D., Manhas, S.K., Agarwal, A., Rustagi, S.C., Lo, G., Balasubramanian, N. and Kwong, D.-L., "Si, sige nanowire devices by top-down technology and their applications", *IEEE Transactions on Electron Devices*, Vol. 55, No. 11, (2008), 3107-3118. doi: 10.1109/TED.2008.2005154.
22. Han, K., Zhang, Y. and Deng, Z., "A simulation study of gate-all-around nanowire transistor with a core-substrate", *IEEE Access*, Vol. 8, (2020), 62181-62190. doi: 10.1109/ACCESS.2020.2983724.
23. Zou, B., Sun, H., Guo, H., Dai, B. and Zhu, J., "Thermal characteristics of gan-on-diamond hemts: Impact of anisotropic and inhomogeneous thermal conductivity of polycrystalline diamond", *Diamond and Related Materials*, Vol. 95, (2019), 28-35. doi: 10.1088/1361-6641/ac1c4f.
24. Dipalo, M., Gao, Z., Scharpf, J., Pietzka, C., Alomari, M., Medjdoub, F., Carlin, J.-F., Grandjean, N., Delage, S. and Kohn, E., "Combining diamond electrodes with gan heterostructures for harsh environment isfets", *Diamond and Related Materials*, Vol. 18, No. 5-8, (2009), 884-889. doi: 10.1016/j.diamond.2009.01.011.
25. Sachid, A.B., Manoj, C., Sharma, D.K. and Rao, V.R., "Gate fringe-induced barrier lowering in underlap finfet structures and its optimization", *IEEE Electron Device Letters*, Vol. 29, No. 1, (2007), 128-130. doi: 10.1109/LED.2007.911974.
26. Sahay, S. and Kumar, M.J., "A novel gate-stack-engineered nanowire fet for scaling to the sub-10-nm regime", *IEEE Transactions on Electron Devices*, Vol. 63, No. 12, (2016), 5055-5059. doi: 10.1109/TED.2016.2617383.
27. Sachid, A.B., Chen, M.-C. and Hu, C., "Finfet with high- κ spacers for improved drive current", *IEEE Electron Device Letters*, Vol. 37, No. 7, (2016), 835-838. doi: 10.1109/LED.2016.2572664.
28. Francis, D., Faily, F., Babić, D., Ejeckam, F., Nurmikko, A. and Maris, H., "Formation and characterization of 4-inch gan-on-diamond substrates", *Diamond and Related Materials*, Vol. 19, No. 2-3, (2010), 229-233. doi: 10.1016/j.diamond.2009.08.017.
29. Pal, P.K., Kaushik, B.K. and Dasgupta, S., "Investigation of symmetric dual-k spacer trigate finfets from delay perspective", *IEEE Transactions on Electron Devices*, Vol. 61, No. 11, (2014), 3579-3585. doi: 10.1109/TED.2014.2351616.
30. Sachid, A.B., Lin, H.-Y. and Hu, C., "Nanowire fet with corner spacer for high-performance, energy-efficient applications", *IEEE Transactions on Electron Devices*, Vol. 64, No. 12, (2017), 5181-5187. doi: 10.1109/TED.2017.2764511.

Persian Abstract

چکیده

در این مقاله یک ترانزیستور اثر تونل دی تریک هترو با اسپیزر در دو طرف دروازه پیشنهاد شده و ویژگی های عملکرد آن را با استفاده از طراحی به کمک کامپیوتر فناوری اطلس در رژیم 5nm مورد تجزیه و تحلیل قرار داده است. جریان نشست تونل زنی باند به باند با معرفی مواد هتروجرکشن و اسپیزر دی هترو دی تریک در ساختار پیشنهادی کاهش خواهد یافت. در ترانزیستور اثر میدان تونل دی هترو دی تریک، دروازه فلزی مضاعف و اسپیزر دی لوکتریک با k بالا بر روی نوسان جریان و زیرمدارندگی بهبود می یابد. اسپیزر اکسید دی تریک بالا K هافنیوم (IV) در دو طرف منبع قرار می گیرد و تخلیه می شود تا مکانیسم تونل زنی وارد شود. دستگاه پیشنهادی در گره 5nm ویژگی های DC مانند جریان حالت ON با 1.68×10^{-5} Amp & OFF-state Current را از 7 کاهش داده است 83×10^{-11} آمپر به 5.13×10^{-12} آمپر و ION نسبت از 3.22×10^5 به 3.27×10^6 نسبت به ترانزیستور میدان تونل دروازه دوگانه معمولی افزایش یافته است. بنابراین این دستگاه برای کاربردهای کم توان مناسب است.



Application of Ultra-sensitive Pillar-enhanced Quartz Crystal Resonators for Airborne Detection of Nanoparticles: A Theoretical Study

X. Xie^{*a}, B. Zheng^b

^a Nanjing University, Gulou, Nanjing, Jiangsu, China

^b Lanzhou University, Lanzhou, Gansu, China

PAPER INFO

Paper history:

Received 04 April 2023

Received in revised form 25 April 2023

Accepted 26 April 2023

Keywords:

Quartz Crystal Resonator

Micropillar

Nanoparticle

Bandwidth

Ultra-sensitive Actuator

ABSTRACT

Although quartz crystal resonators (QCR) have been used for airborne detection of particles and viruses, they suffer from various limitations, such as low sensitivity compared to other devices. Therefore, it is necessary to develop a new device capable of achieving high sensitivity, which can be used for practical airborne detections. The current study reports a comprehensive parametric theoretical model for analyzing the response of ultra-sensitive pillar-enhanced QCR (QCR-P) for airborne detection of nanoparticles. The electromechanical model comprised an equivalent circuit integrated with pillars containing nanoparticles. It was shown that pillar height and particle radius play a critical role in the response of QCR-P devices. The study revealed that selecting the optimal pillar height can lead to a significant frequency shift depending on the nanoparticle radius and pillar height, while it is independent of particle mass density. These results underscore the potential of utilizing pillars to substantially enhance the sensitivity of conventional QCR up to 140 times in the airborne detection of nanoparticles. These findings can be utilized to design optimum pillar heights to achieve maximum sensitivity in the airborne detection of nanoparticles and proteins, thereby enabling the adoption of ultra-sensitive pillar-enhanced quartz crystal resonators for practical airborne applications.

doi: 10.5829/ije.2023.36.06c.12

1. INTRODUCTION

Detection of proteins and nanoparticles has gained increasing attention in various applications, such as immunosensors and breath analyzers [1, 2]. For indication, Farsaeivahid et al. [3] developed an electrochemical device to detect the COVID-19 virus. In another study, they utilized X-Fe₂O₄-buckypaper nanocomposites for nonenzymatic electrochemical glucose biosensing [4, 5]. Compared to other devices, AT-cut quartz crystal resonator (QCR) devices have shown great potential as airborne detecting sensors [6]. The adhered mass on the QCR substrate can be calculated by using the observed frequency of the QCR in the Sauerbrey theory [7]. Generally, a thin film of polymer or fiber [8] is fabricated on the substrate, enabling the device to detection of particles, organic compounds, bacteria, colloidal particles, and cells [9, 10]. Pato et al. [11] analyzed the physicochemical properties of cellulose

in order to evaluate the efficacy of the hydrogel. Budianto et al. [12] developed a QCR coated with graphene oxide for measuring fungal spore mass. The developed system exhibited strong performance with sensitivities ranging from 27×10^{-2} to 29×10^{-2} Hz/ng. In another study, Lee et al. [13] aimed at airborne detection of vaccinia viruses using highly sensitive QCR. They concluded that the QCR has great potential for the quantitative detection of airborne viruses. QCR devices coated with monoclonal antibodies have also been utilized as immunosensor for airborne cat allergens [14]. It was shown that the QCR is capable of achieving a low limit of detection due to high sensitivity and selectivity. Although QCR-based devices have been used for airborne detection of particles and viruses, they suffer from various limitations, such as low sensitivity compared to other immunosensors. Therefore, it is necessary to develop a new device capable of achieving high sensitivity, which can be used for real-time airborne detections.

*Corresponding Author Email: xuanxie263@gmail.com (X. Xie)

Microbeams have recently been printed on QCR surfaces to characterize their geometric/physical features and develop a coupled sensor [15, 16]. As the pillar height approaches critical values, the frequency jump is generated by resonance between the pillars and QCR [17]. By selecting proper pillar characteristics, such as height, one can increase mass sensitivity by lowering the frequency shift produced by even a nanoscale change in the size of the pillars at this moment [18]. For single monolayer films, the mass sensitivity and reaction time of coupled sensors were also studied [19]. The effect of the contact area of the SU-8 pillar on the QCR was studied by Kashan et al. [20].

Numerical and analytical models have been widely used to analyze the fundamental behavior of mechanical systems [21-23]. For example, Abdollahi et al. [24] developed a finite element model (FEM) to analyze the impact of hybrid nanofluid on the flow field and heat transfer in parallel surfaces. In the case of coupled QCR-pillar devices, numerical models have been widely applied. Kashan et al. [25] developed a finite element model (FEM) to analyze the resonance frequency of coupled QCR-pillars (QCR-P). Wang et al. [26] utilized coupled QCR with polymer pillars to numerically analyze the liquid penetration from the Cassie state to the Wenzel state. Esfahani and Sun [27] developed a droplet-based QCR-P device to study the viscosity of sample solutions. Liquid loading on the QCR was calculated using COMSOL simulation, and Kerr-lens mode-locked (KLM) equivalent circuit was used to calculate the resonance frequency of QCR. They observed that the QCR-micropillar can produce up to 20 times sensitivity enhancement compared to conventional QCR devices [27]. While these studies are largely concerned with surface wetting and viscosity measurements, they do not address the impact of solid particle detection, such as colloidal particles and bacteria on the response of coupled QCR-P devices.

Despite extensive research into the influence of pillars on the resonance frequency of QCR, there is a significant research gap pertaining to the application of QCR-P devices for the airborne detection of particles. The use of QCR-P devices has the potential to enhance the sensitivity of conventional QCR devices in detecting airborne particles in real time, thereby enabling their widespread adoption in real-world applications. In view of this, it becomes imperative to undertake an in-depth study of the response of QCR-P devices containing nanoparticles. The current investigation presents a groundbreaking electromechanical model that facilitates the analysis of the response of QCR-P devices with adhered nanoparticles on the tip of the pillars. Specifically, this study explores the correlation between the response of the QCR-P device and the characteristics of adherent nanoparticles, thereby providing invaluable insights into the design of optimum pillars to achieve

maximum sensitivity in detecting nanoparticles. The findings of this study have significant implications for future research on the development and optimization of QCR-P devices for diverse airborne applications.

In section 2, we discussed the methodology for the analytical model. In section 3, we presented the result in detail and discussed the key points of QCR-P for airborne detection of nanoparticles. A comparison of our model with existing experimental measurements is also shown in section 3. Finally, in section 4, the results are analyzed, and the conclusions are made for this study.

2. THEORETICAL ANALYSIS

2.1. Load Impedance Calculation It is assumed that the main displacement of pillars is in the y -direction, and the displacement in other directions is negligible. Also, pillars have the same characteristics and vibrational states for simplicity of the calculations. The equation of pillar motion for an element with a thickness of dz is shown in Figure 1(a) [28]:

$$F + \frac{\partial F}{\partial z} dz - F = (\rho A dz) \frac{\partial^2 u}{\partial t^2} \quad (1)$$

where u is the displacement, A is the cross-sectional area, ρ is the density, and t is the time. The shear force (F) can be calculated as:

$$F = \kappa A G \frac{\partial u}{\partial z} \quad (2)$$

where G is the complex shear modulus, and κ is the shear coefficient of pillars. Using Equation (2) in Equation (1), the equation of pillar motion can be represented as follows:

$$\frac{\partial^2 u}{\partial z^2} + \lambda^2 u = 0 \quad (3)$$

where:

$$\lambda^2 = \frac{\omega^2 \rho}{\kappa G} \quad (4)$$

It is assumed that the nanoparticles are rigidly attached to the tip of pillars. A shear force is applied to the top surface of pillars due to the vibration of nanoparticles which is represented in Figure 1(b):

$$F(H) = -m_p \omega^2 u(H) \quad (5)$$

where H is the height of the pillar, m_p is the mass of an attached particle, and ω is the angular frequency. The displacement at the bottom of the pillars can be represented as:

$$u(0) = u_0 \quad (6)$$

where u_0 is the displacement of the top surface of QCR. Using boundary conditions (Equations (5) and (6)) in Equation (3), the displacement of pillars with rigidly attached nanoparticles can be calculated as:

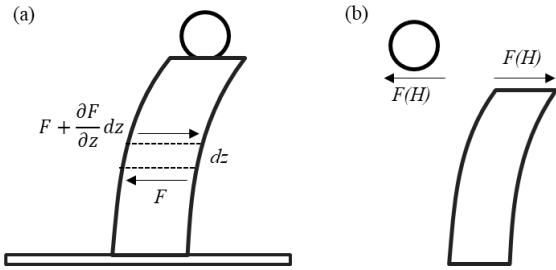


Figure 1. (a) shear vibration of a pillar in air medium (b) shear force acting on the pillar-particle interface

$$u = C_1 \cos \lambda z + C_2 \sin \lambda z \tag{7}$$

where:

$$C_1 = u_0 \tag{8}$$

$$C_2 = \frac{\kappa A G \lambda \sin \lambda H - m_p \omega^2 \cos \lambda H}{\kappa A G \lambda \cos \lambda H + m_p \omega^2 \sin \lambda H} u_0 \tag{9}$$

Based on Equation (7), the load impedance (Z_L) applied to a top surface of QCR can be evaluated as [28]:

$$Z_L = -\frac{\kappa A G \lambda C_2}{i \omega u_0} \tag{10}$$

2. 2. QCR-pillar Coupling In the current study, it is assumed that the obtained shift is significantly lower compared to the quartz resonance frequency. Thus, a small load approximation technique is used to couple the QCR resonator with pillars [29, 30]. The response of QCR with load impedance on the surface can be calculated as:

$$\frac{\Delta f + i \Delta \Gamma}{f_0} = \frac{i Z_L}{\pi Z_q} \tag{11}$$

where Δf is the frequency shift, $\Delta \Gamma$ is the bandwidth shift, f_0 is the quartz resonance frequency, and Z_q is the quartz characteristic impedance. According to Equation (11), the frequency shift and bandwidth shift of coupled QCR-pillar can be evaluated as:

$$\frac{\Delta f}{f_0} = \text{Re} \left(\frac{i Z_L}{\pi Z_q} \right) \tag{12}$$

$$\frac{\Delta \Gamma}{f_0} = \text{Im} \left(\frac{i Z_L}{\pi Z_q} \right) \tag{13}$$

For theoretical example, we considered 10 MHz AT-cut quartz resonators with $f_0 = 10$ MHz and $Z_q = 8.8 \times 10^6 \text{ kgm}^{-2}\text{s}^{-1}$. The materials of pillars are SU-8 with a shear modulus of $G = 1.66 \times 10^9 + 1i (6 \times 10^7)$, a density of $\rho = 1200 \text{ kgm}^{-3}$, a cross-sectional radius of $R = 0.25 \mu\text{m}$, and a shear coefficient of $\kappa = 0.9$. Figure 2 summarizes the flow chart of the developed methodology for predicting the response of QCR carrying an array of pillars with nanoparticles.

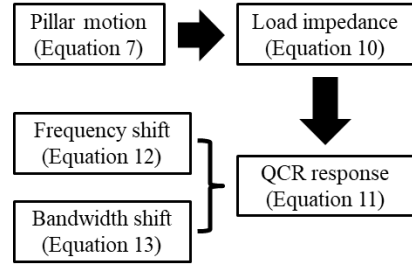


Figure 2. Flow chart of the developed model

3. RESULTS AND DISCUSSION

3. 1. Special Case: No Particles

In order to validate the model, we consider a special case where no particles are attached to the pillars. In this case, it is assumed that the attached particles have a mass of $m_p = 0$. The model prediction was compared with the previous experimental measurement using PMMA pillars in the air [27]. It should be noted that the size and detail of the pillars can be found in literature [27]. The results are shown in Figure 3. The prediction of the model is in good agreement with experimental measurements. As the height increased, the frequency of the QCR-P decreased. When the pillar height approached a specific height, known as "resonance height", a sudden drop-jump was observed in the response of the device. This is related to the elastic loading of the pillar on the QCR substrate. When the height is much smaller than the resonance height, the pillar acts as inertial loading on the QCR substrate, consistent with the Saurebrey theory. However, the pillar coupled with QCR acts as an elastic loading on the QCR substrate at the resonance height, resulting in a phase-veering behavior in the pillar vibration. When the pillar is smaller than the resonance height, the pillar's displacements are in the same phase as the QCR. A phase shift occurs when the pillar is larger

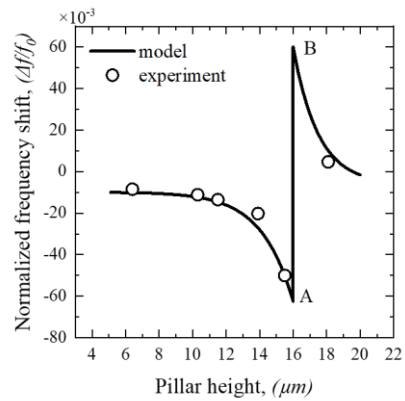


Figure 3. Model prediction of the frequency shift of QCR-P at various pillar heights vs. experimental measurements [27]

than the resonance height, leading to the out-phase vibration of pillars and QCR. This phase-veering phenomenon results in a sudden drop-and-jump in the device's response. It is believed that the discrepancies between the experimental measurements and the model are due to the thickness of the residual layer in experimental measurements.

The sensitivity of the QCR-P with respect to pillar height is shown in Figure 4. It should be noted that the sensitivity of QCR-P is normalized with respect to the sensitivity of conventional QCR. As can be seen, the sensitivity of the QCR-P is close to conventional QCR when the pillar height is small. As the pillar height increases, the sensitivity of the QCR-P increases. The maximum sensitivity is achieved at the resonance height, which is consistent with previous experimental measurements. It is also noticed that a small shift in the height of the QCR-P can result in a significant shift in the sensitivity of the device when the pillar height is at resonance height. Therefore, it is necessary to consider the accuracy of the fabrication procedure of pillars on the QCR when the height is close to the resonance point.

Figure 5 shows the displacement of pillars at points A and B. As can be seen, a phase shift is observed in the displacements. Pillars vibrate in phase with the QCR when the height is lower than the resonance height, resulting in inertial loading on the device. However, an out-phase vibration of pillars is obtained when the height is higher than the resonance height, indicating elastic loading on the device.

3. 2. Impact of Adhered Particles on Microbeams

To rigorously study the response of coupled QCR-pillar, it is necessary to model the impact of nanoparticles on the QCR-P. Figure 6(a) represents the effect of particle radius with a density of 1200 kg/m^3 on the resonance frequency shift of QCR-P devices. The behavior of QCR-P can be divided into two categories: below resonance height (A), and above resonance height (B). When the

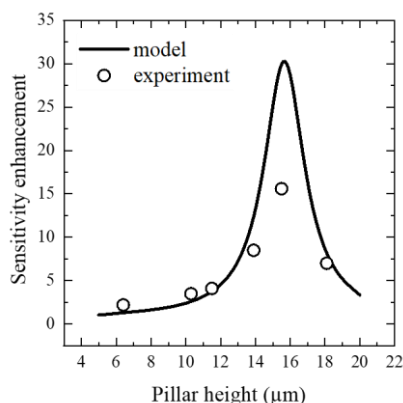


Figure 4. Model prediction of the sensitivity of QCR-P with respect to pillar height vs. experimental measurements [27]

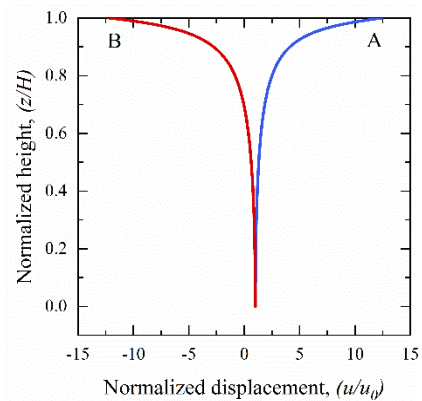


Figure 5. Displacement of pillars at points A and B

height is lower than resonance height (A), as the radius increases, a positive frequency shift is obtained, which is inconsistent with the Sauerbrey theory. This is related to the couple resonance phenomena between pillars and QCR. With an increase in the radius, the hydrodynamic loading on the tip of the pillar increases, resulting in decreasing the equivalent height of the QCR-P device. However, a different trend is observed when the pillar height is higher than the resonance height (B). In these cases, as the radius increases, the frequency shift increases. A sudden jump and drop behavior is observed at the critical particle radius due to decreasing the equivalent pillar height. Figure 6(b) indicates the effect of particle radius with a density of 1200 kg/m^3 on the bandwidth shift of QCR-P devices. The QCR-P behavior is consistent with the resonance frequency shift and the equivalent height analysis. When the height of the pillar is above resonance height (B), as the radius increases, the bandwidth increases. It reaches its maximum at the critical radius and decreases afterward. However, when the pillar height is lower than the resonance height, a constant decrease in the bandwidth is observed.

Figure 7 represents the sensitivity enhancement of QCR-P devices for airborne detection of nanoparticles compared to conventional QCR-based devices. It should be noted that the sensitivity of QCR-P was normalized to that of a conventional QCR device. As can be seen, as the

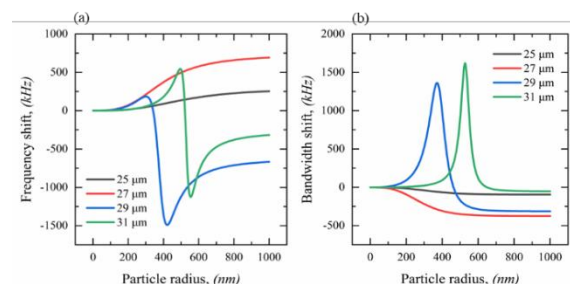


Figure 6. Frequency shift (a) and bandwidth shift (b) of QCR-P with nanoparticles with respect to particle radius

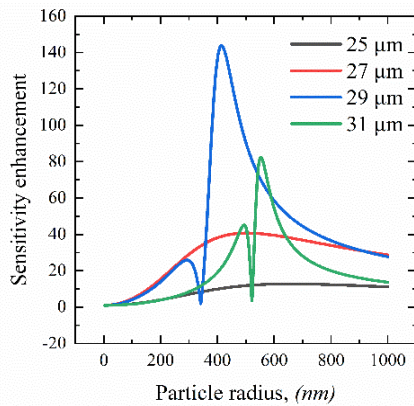


Figure 7. Sensitivity enhancement of QCR-P with respect to particle radius at different pillar heights

particle radius increases, the sensitivity of QCR-P devices increases. For pillar height lower than resonance height, the sensitivity enhancement of QCR-P devices tends to become stable at higher radiuses of nanoparticles. However, the QCR-P devices with pillar height higher than resonance height follow a different trend. In these cases, the sensitivity enhancement increases as the particle radius increases. Then, it starts to decrease and suddenly increases until reaching maximum enhancement. With a further increase in particle radius, the sensitivity enhancement decreases. These results highlight that the pillar height higher than the resonance height has superior performance compared to pillar heights lower than the resonance height. Furthermore, QCR-P devices have the potential to achieve 140-times sensitivity enhancement for airborne detection of nanoparticles compared to conventional QCR, which makes them a suitable candidate for the practical application of QCR-P devices.

Figure 8 represents the effect of particle density with a radius of 100 nm on the resonance frequency and bandwidth shifts of QCR-P devices. Except for no jump existing because of no resonance, similar trends, and characteristics can be found in these two figures. As the density increases, the mass on the device increases, resulting in a negative frequency shift and positive bandwidth shift of QCR-P devices.

At last, the effect of particle density on the sensitivity of QCR-P devices is plotted in Figure 9. As can be seen, with increasing particle density, the sensitivity of QCR-P devices remains unchanged, indicating that the density of the particle has a negligible impact on the sensitivity. In addition, the results indicated that the micropillars near the resonance height show higher sensitivity than others. For indication, the pillars with a height of 25 μm have a sensitivity enhancement of 7.4, while it increases substantially to 35.6 as the pillar height approaches 27 μm .

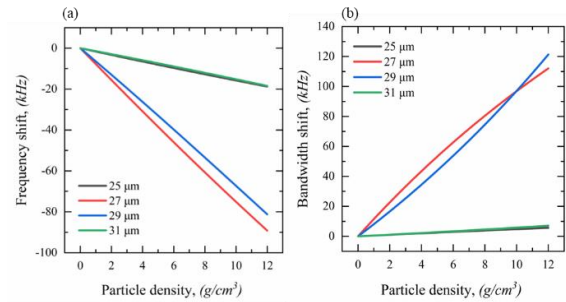


Figure 8. Frequency shift (a) and bandwidth shift (b) of QCR-P with nanoparticle with respect to particle radius

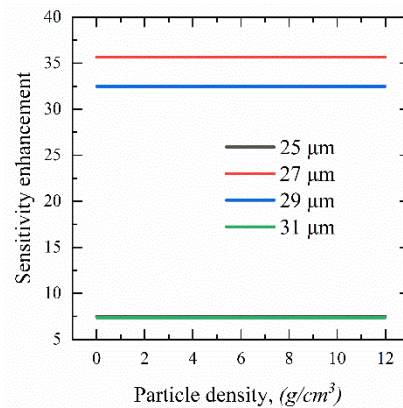


Figure 9. Sensitivity enhancement of QCR-P with respect to particle density at various pillar heights

4. CONCLUSION

In this study, the application of ultra-sensitive pillar-enhanced quartz crystal resonator (QCR-P) devices for the airborne detection of nanoparticles was theoretically investigated. An analytical model was developed by calculating the induced load impedance on the QCR substrate due to the array of pillars carrying nanoparticles on the tip. Then, a small load approximation technique was applied to predict the frequency and bandwidth shifts of the QCR. The developed model was validated by comparing the prediction results with previous experimental measurements for QCR-P in air. The study revealed that the sensitivity enhancement of QCR-P devices significantly depends on the particle radius and the pillar height, while it is independent of the particle mass density. It was obtained that selecting the optimal pillar height can substantially enhance the sensitivity of conventional QCR up to 140 times for the airborne detection of nanoparticles. Furthermore, we observed that as the pillar height approaches the resonance height, the sensitivity of QCR-P increases, indicating that fabricating pillars close to resonance height can lead to ultra-sensitivity of the device. The obtained results can help the researchers in designing optimum pillar height

in order to achieve maximum sensitivity for airborne detection of the nanoparticles, paving the way for adopting pillar-enhanced quartz crystal resonators for real-world applications such as breath analyzers. For future work, an experimental setup for measuring the response of QCR-P for airborne detection of nanoparticles or proteins will be initiated, with the goal of achieving ultra-high sensitive QCR by fabricating pillars at optimum pillar height.

5. REFERENCES

- Kadam, V., Deshmukh, A. and Bhosale, S., "Hybrid beamforming for dual functioning multi-input multi-output radar using dimension reduced-baseband piecewise successive approximation", *International Journal of Engineering, Transactions A: Basics*, Vol. 36, No. 1, (2023), 182-190. doi: 10.5829/IJE.2023.36.01A.20.
- Nistratov, A.V., Klimenko, N.N., Pustynnikov, I.V. and Vu, L.K., "Thermal regeneration and reuse of carbon and glass fibers from waste composites", *Emerging Science Journal*, Vol. 6, (2022), 967-984. doi: 10.28991/ESJ-2022-06-05-04.
- Farsaeivahid, N., Grenier, C., Nazarian, S. and Wang, M.L., "A rapid label-free disposable electrochemical salivary point-of-care sensor for sars-cov-2 detection and quantification", *Sensors*, Vol. 23, No. 1, (2022), 433. doi: 10.3390/s23010433.
- Vahid, N.F., Marvi, M.R., Naimi-Jamal, M.R., Naghib, S.M. and Ghaffarinejad, A., "X-fe2o4-buckypaper-chitosan nanocomposites for nonenzymatic electrochemical glucose biosensing", *Anal. Bioanal. Electrochem*, Vol. 11, No., (2019), 930-942.
- Farsaei Vahid, N., Marvi, M.R., Naimi-Jamal, M.R., Naghib, S.M. and Ghaffarinejad, A., "Effect of surfactant type on buckypaper electrochemical performance", *Micro & Nano Letters*, Vol. 13, No. 7, (2018), 927-930. doi: 10.1049/mnl.2017.0691.
- Ji, S., Chiniforooshan Esfahani, I., Sun, H. and Wan, K.-t., "Particle deposition on a filtration bed using a quartz crystal microbalance embedded in a microfluidic channel", *SSRN Electronic Journal*, doi: 10.2139/ssrn.4265353.
- Ji, S., Ran, R., Chiniforooshan Esfahani, I., Wan, K.-t. and Sun, H., "A new microfluidic device integrated with quartz crystal microbalance to measure colloidal particle adhesion", in ASME International Mechanical Engineering Congress and Exposition, American Society of Mechanical Engineers. Vol. 85598, (2021), V005T005A075.
- Hashim, A.M. and Kadhum, M.M., "Compressive strength and elastic modulus of slurry infiltrated fiber concrete (SIFCON) at high temperature", *Civil Engineering Journal*, Vol. 6, No. 2, (2020), 265-275. doi: 10.28991/cej-2020-03091469.
- Marchione, F., "Investigation of vibration modes of double-lap adhesive joints: Effect of slot", *International Journal of Engineering, Transactions A: Basics*, Vol. 33, No. 10, (2020), 1917-1923. doi: 10.5829/ije.2020.33.10a.10.
- Karevan, M., Motalleb, M., Jannesari, A. and Zeinali, M., "High energy release-high retraction smart polymer fibers used in artificial muscle fabrication", *International Journal of Engineering, Engineering, Transactions A: Basics*, Vol. 36, No. 4, (2023), 788-796. doi: 10.5829/IJE.2023.34.04A.15
- Pato, U., Ayu, D.F., Riftyan, E., Restuhadi, F., Pawenang, W.T., Firdaus, R., Rahma, A. and Jaswir, I., "Cellulose microfiber encapsulated probiotic: Viability, acid and bile tolerance during storage at different temperature", *Emerging Science Journal*, Vol. 6, (2022), 106-117. doi: 10.28991/ESJ-2022-06-01-08.
- Budianto, A., Wardoyo, A.Y.P., Masruroh, H.A.D. and Dharmawan, H., "An airborne fungal spore mass measurement system based on graphene oxide coated qcm", *Polish Journal of Environmental Studies*, Vol. 31, No. 4, (2022), 1-7. doi: 10.15244/pjoes/147057.
- Lee, J., Jang, J., Akin, D., Savran, C.A. and Bashir, R., "Real-time detection of airborne viruses on a mass-sensitive device", *Applied Physics Letters*, Vol. 93, No. 1, (2008), 013901. doi: 10.1063/1.2956679.
- Morris, D.R., Fatissou, J., Olsson, A.L., Tufenkji, N. and Ferro, A.R., "Real-time monitoring of airborne cat allergen using a qcm-based immunosensor", *Sensors and Actuators B: Chemical*, Vol. 190, (2014), 851-857. doi: 10.1016/j.snb.2013.09.061.
- Wang, P., Su, J., Dai, W., Cernigliaro, G. and Sun, H., "Ultrasensitive quartz crystal microbalance enabled by micropillar structure", *Applied Physics Letters*, Vol. 104, No. 4, (2014), 043504. doi: 10.1063/1.4862258.
- Zaza, G., Hammou, A., Benchatti, A. and Saiah, H., "Fault detection method on a compressor rotor using the phase variation of the vibration signal", *International Journal of Engineering, Transactions B: Applications*, Vol. 30, No. 8, (2017), 1176-1181. doi: 10.5829/ije.2017.30.08b.09.
- Wang, P., Su, J., Su, C.-F., Dai, W., Cernigliaro, G. and Sun, H., "An ultrasensitive quartz crystal microbalance-micropillars based sensor for humidity detection", *Journal of Applied Physics*, Vol. 115, No. 22, (2014), 224501. doi: 10.1063/1.4880316.
- Su, J., Esmailzadeh, H., Zhang, F., Yu, Q., Cernigliaro, G., Xu, J. and Sun, H., "An ultrasensitive micropillar-based quartz crystal microbalance device for real-time measurement of protein immobilization and protein-protein interaction", *Biosensors and Bioelectronics*, Vol. 99, (2018), 325-331. doi: 10.1016/j.bios.2017.07.074.
- Kashan, M., Kalavally, V., Lee, H. and Ramakrishnan, N., "Resonant characteristics and sensitivity dependency on the contact surface in qcm-micropillar-based system of coupled resonator sensors", *Journal of Physics D: Applied Physics*, Vol. 49, No. 19, (2016), 195303. doi: 10.1088/0022-3727/49/19/195303.
- Kashan, M.A.M., Kalavally, V. and Ramakrishnan, N., "Sensing film-coated qcm coupled resonator sensors: Approach, fabrication, and demonstration", *Sensors and Actuators A: Physical*, Vol. 274, (2018), 64-72. doi: 10.1016/j.sna.2018.03.006.
- Mulyawati, I.B., Riza, M., Dermawan, H. and Pratiwi, V., "Numerical simulation of embankment settlement in vacuum preloading systems", *International Journal of Engineering, Transactions A: Basics*, Vol. 36, No. 4, (2023), 817-823. doi: 10.5829/IJE.2023.36.04A.18
- Thepade, S., Dindorkar, M., Chaudhari, P. and Bang, S., "Enhanced face presentation attack prevention employing feature fusion of pre-trained deep convolutional neural network model and thepade's sorted block truncation coding", *International Journal of Engineering, Transactions A: Basics*, Vol. 36, No. 4, (2023), 807-816. doi: 10.5829/IJE.2023.36.04A.17
- Marchione, F., "Shear stress distribution in double-lap adhesive joints reinforced with nylon fabric: Numerical investigation", *International Journal of Engineering, Transactions A: Basics*, Vol. 36, No. 1, (2023), 35-40. doi: 10.5829/IJE.2023.36.01A.05
- Abdollahi, S.A., Alizadeh, A.a., Chiniforooshan Esfahani, i., Zarinfar, M. and Pasha, P., "Investigating heat transfer and fluid flow betwixt parallel surfaces under the influence of hybrid nanofluid suction and injection with numerical analytical technique", *Alexandria Engineering Journal*, Vol. 70, (2023), 423-439. doi: 10.1016/j.aej.2023.02.040.

25. Kashan, M.A.M., Kalavally, V., Mazumdar, P., Lee, H.W. and Ramakrishnan, N., "Qcm coupled resonating systems under vacuum: Sensitivity and characteristics", *IEEE Sensors Journal*, Vol. 17, No. 16, (2017), 5044-5049. doi: 10.1109/JSEN.2017.2719104.
26. Wang, P., Su, J., Shen, M., Ruths, M. and Sun, H., "Detection of liquid penetration of a micropillar surface using the quartz crystal microbalance", *Langmuir*, Vol. 33, No. 2, (2017), 638-644. doi: 10.1021/acs.langmuir.6b03640.
27. Esfahani, I.C. and Sun, H., "A droplet-based micropillar-enhanced acoustic wave (μ paw) device for viscosity measurement", *Sensors and Actuators A: Physical*, Vol. 350, (2023), 114121. doi: 10.1016/j.sna.2022.114121.
28. Xie, X., Xie, J., Luo, W. and Wu, Z., "Electromechanical coupling and frequency characteristics of a quartz crystal resonator covered with micropillars", *Journal of Vibration and Acoustics*, Vol. 141, No. 4, (2019). doi: 10.1115/1.4042936.
29. Kanazawa, K.K. and Gordon, J.G., "Frequency of a quartz microbalance in contact with liquid", *Analytical Chemistry*, Vol. 57, No. 8, (1985), 1770-1771. doi: 10.1021/ac00285a062.
30. Mason, W., "Viscosity and shear elasticity measurements of liquids by means of shear vibrating crystals", *Journal of Colloid Science*, Vol. 3, No. 2, (1948), 147-162. doi: 10.1016/0095-8522(48)90065-8.

Persian Abstract

چکیده

اگرچه تشدید کننده های کریستال کوآرتز (QCR) برای تشخیص ذرات و ویروس ها در هوا استفاده شده است، اما از محدودیت های مختلفی مانند حساسیت کم در مقایسه با سایر دستگاه ها رنج می برند. بنابراین، توسعه دستگاه جدیدی با قابلیت دستیابی به حساسیت بالا ضروری است که بتوان از آن برای تشخیص عملی هوا برد استفاده کرد. مطالعه حاضر یک مدل نظری پارامتریک جامع را برای تجزیه و تحلیل پاسخ QCR تقویت شده با ستون فوق حساس (QCR-P) برای تشخیص نانوذرات در هوا گزارش می کند. مدل الکترومکانیکی شامل یک مدار معادل یکپارچه با ستون های حاوی نانوذرات است. نشان داده شد که ارتفاع ستون و شعاع ذرات نقش مهمی در پاسخ دستگاه های QCR-P دارند. این مطالعه نشان داد که انتخاب ارتفاع بهینه ستون می تواند منجر به تغییر فرکانس قابل توجه بسته به شعاع نانوذرات و ارتفاع ستون شود، در حالی که مستقل از چگالی جرم ذرات است. این نتایج بر پتانسیل استفاده از ستون ها برای افزایش قابل ملاحظه حساسیت QCR معمولی تا ۱۴۰ برابر در تشخیص نانوذرات در هوا تأکید می کند. این یافته ها را می توان برای طراحی ارتفاع ستون های بهینه برای دستیابی به حداکثر حساسیت در تشخیص نانوذرات و پروتئین ها در هوا مورد استفاده قرار داد، در نتیجه استفاده از تشدید کننده های کریستال کوآرتز با ستون های فوق حساس برای کاربردهای عملی در هوا را ممکن می سازد.



A Dynamic Model for Laminated Piezoelectric Microbeam

Z. Zhang^{*a}, G. Fu^b, D. Xu^c^a School of Mechanical Engineering and Automation, University of Science and Technology Liaoning, Anshan City, Liaoning, China^b School of Mechanical Engineering, Shandong University of Technology, Zibo, Shandong, China^c Jilin Province Construction Engineering Quality Test center, Jilin Research and Design Institute of Building Science, Changchun, Jilin, China

P A P E R I N F O

Paper history:

Received 14 February 2023

Received in Revised form 26 April 2023

Accepted 28 April 2023

Keywords:

Size Effect

Laminated Piezoelectric Microbeams

Dynamic Model

Natural Frequencies

A B S T R A C T

Piezoelectric beams are widely used in micro-electromechanical systems. At the microscale, the influence of the size effect on a piezoelectric beam cannot be ignored. In this paper, higher-order elasticity theories are considered to predict the behaviors of piezoelectric micro-structures and a size-dependent dynamic model of a laminated piezoelectric microbeam is established. The governing equations for the laminated piezoelectric microbeam are derived using the variational principle. The natural frequencies of piezoelectric microbeams are obtained by size-dependent dynamic models. The results reveal that the size effect can enhance the structural stiffness at the microscale. The natural frequency obtained by using the classical model is smaller than that obtained using the size-dependent model. Compared with the modified couple stress model, the modified couple stress model underestimates the size-dependent response. Thus, the modified couple stress model is a simplification of the modified strain gradient model. The influence of beam thickness on the natural frequency is also discussed. With increasing the thickness, the natural frequency of the size-dependent models gradually approaches the result of the classical model. If the value of h/l is greater than 15, the influence of the size effect can be neglected. Additionally, the relative thickness can influence the natural frequency, and if the relative thickness is greater than 5 or less than -5 , the bilayer beam can be simplified to a single-layer beam.

doi: 10.5829/ije.2023.36.06c.13

NOMENCLATURE

L	Beam length (m)	D_i	Vector of electrical displacement
h	Thickness(mm)	e_{31}	Piezoelectric coefficient N/ (V m)
M	Bending moment (N·m)	l_n	Material length-scale parameters
b	Width (m)	Greek Symbols	
w	Deflection(m)	ρ	Density (kg/m ³)
$q(x)$	Uniformly distributed load(N/mm)	ω	Natural frequency (Hz)
F	Shear force (N)	κ	Dielectric constant
G	Material elastic modulus (GPa)	σ	Stress tensor (Pa)
$A=bh$	Cross-sectional area of the beam(m ²)	ε	Strain tensor
$S=bh^2/2$	Static moment(m ³)	γ	Dilatation gradient tensor
$I=bh^3/3$	Second moment of cross-sectional area(m ⁴)	χ	Rotation gradient tensor
$w(x, t)$	Amplitude (m)	η	Strain gradient tensor
E_i	Electric field	τ	Higher stress
t	Relative thickness	λ	Lame constants
H	Electric enthalpy density(J)	μ	Lame constants
U	Strain energy (J)	ε_0	The permittivity of vacuum
P	The polarization vector (C/m ²)	φ	Electric potential(V)
W	Work done by the external forces(J)	θ	Rotation vectors
T	Kinetic energy(J)	Subscripts	
u_i	Displacement vector	1	Piezoelectric layer
d	Distance from the neutral layer to the bottom layer(mm)	2	Elastic layer

*Corresponding Author Email: zzj512682701@126.com (Z. Zhang)

1. INTRODUCTION

Several piezoelectric structures are used in MEMS, such as micro-actuators [1] and micro-sensors [2]. Recently, people have been concerned about the energy crisis [3]. Thus, micro-energy harvesters [4], which are related to energy recovery, have attracted great research attention. The performance of the MEMS depends on the electromechanical control system [5] and the piezoelectric component's mechanical properties [6]. However, on the microscale, the performance of piezoelectric structures is size-dependent. Multani et al. [7] experimentally found that the piezoelectric effect of piezoelectric structures is proportional to the thickness. Bühlmann et al. [8] observed that the bending deflection of the PZT thin film decreases with decreasing thin film thickness at the microscale. Additionally, Shaw et al. [9] reported that the responses of a piezoelectric beam decrease when the thickness approaches to nanometer.

According to experiment reports, the size effect can influence the mechanical properties of piezoelectric microstructures. However, the classical piezoelectric theory [10] neglects the size effect phenomenon. Thus, the theoretical results obtained by this theory will have deviation from the experimental results. Because of the economic downturn caused by the COVID-19 pandemic [11], scholars want to establish more accurate theoretical calculation models to reduce the cost of trial and error. At micro scale, the constitutive relation of a microbeam model not only contains the classical material parameters, but also contains the material scale parameters l_n [1, 2]. However, the simple beam model doesn't consider the material scale parameters l_n , it ignores the influence of size effect. Therefore, higher-order elasticity effects have been introduced into the classical piezoelectric theory to establish a modified piezoelectric theory. Higher-order elasticity effects comprising two branches have been proposed. They are the couple stress effects [12] and the strain gradient effects [13].

Yang et al. [14] used the modified couple stress (MCS) theory [15] to establish the laminated piezoelectric microcantilever model. Subsequently, Noori and Jomehzadeh [16] derived a functionally graded plate model. Bakhshi Khaniki and Hosseini Hashemi [17] found that the size effect can increase the natural frequency of a microbeam under free vibration. Additionally, based on the strain gradient elasticity theory [18], Nikpourian et al. [19] derived a size-dependent model for a piezoelectric microbeam. They found that considering the size effect, the amplitude of the microbeam is reduced, but the natural frequency has increased. Radgolchin and Moenfarid [20] applied the modified strain gradient (MSG) theory [21] to derive a mathematical model for a micro-bridge energy harvester.

To provide a theoretical basis for the researching of a micro beam piezoelectric energy harvester. This paper established a size-dependent dynamic model of a laminated piezoelectric microbeam. This piezoelectric microbeam model is able to reflect size effects more appropriately. And it has higher precision and wider universality than other types of microbeams. Furthermore, this piezoelectric microbeam model can provide the theoretical basis for designing of a micro beam piezoelectric energy harvester.

The structure of this paper is as follows: In section 2, higher-order elasticity effects are discussed to establish the modified piezoelectric theory. In section 3, a size-dependent dynamic model of a laminated piezoelectric microbeam is derived. Further, the natural frequency of piezoelectric microbeams is analyzed in section 4. Finally, section 5 gives the conclusion of this article.

2. THE MODIFIED PIEZOELECTRIC THEORY

Based on the MSG effect [21], the modified piezoelectric theory can be given as:

$$H = \frac{1}{2} \left(\sigma_{ij} \varepsilon_{ij} + p_i \gamma_i + \tau_{ijk}^{(1)} \eta_{jk}^{(1)} + m_{ij}^s \chi_{ij}^s - D_i E_i \right) \quad (1)$$

where, D_i denotes the vector of electrical displacement, it is shown in Equation (2). E_i denotes the electric field, as shown in Equation (3).

$$D_i = -\varepsilon_0 E_i + P_i \quad (2)$$

$$E_i = -\varphi_{,i} \quad (3)$$

ε_{ij} is strain tensor, γ_i is dilatation gradient tensor, χ_{ij}^s is rotation gradient tensor, η_{ijk} represent strain gradient tensor, as shown:

$$\varepsilon_{ij} = \frac{1}{2} (u_{i,j} + u_{j,i}) \quad (4)$$

$$\gamma_i = \varepsilon_{mm,i} \quad (5)$$

$$\eta_{ijk}^{(1)} = \frac{1}{3} (\varepsilon_{jk,i} + \varepsilon_{ki,j} + \varepsilon_{ij,k}) - \frac{1}{15} \left[\delta_{ij} (\varepsilon_{mm,k} + 2\varepsilon_{mk,m}) + \delta_{jk} (\varepsilon_{mm,i} + 2\varepsilon_{mi,m}) + \delta_{ki} (\varepsilon_{mm,j} + 2\varepsilon_{mj,m}) \right] \quad (6)$$

$$\chi_{ij}^s = \frac{1}{2} (\theta_{i,j} + \theta_{j,i}) \quad (7)$$

where, θ is the rotation vector defined as:

$$\theta_i = \frac{1}{2} (\text{curl}(u))_{,i} \quad (8)$$

The Cauchy stress σ_{ij} , higher stress p_i , $\tau_{ijk}^{(1)}$ and m_{ij}^s can be written as:

$$\begin{aligned} \sigma_{ij} &= \frac{\partial H}{\partial \varepsilon_{ij}} = c_{ijkl} \varepsilon_{kl} - e_{ijk} E_k \\ p_i &= \frac{\partial H}{\partial \gamma_i} = 2\mu l_0^2 \\ \tau_{ijk}^{(1)} &= \frac{\partial H}{\partial \eta_{ijk}^{(1)}} = 2\mu l_1^2 \eta_{lmn}^{(1)} \\ m_{ij}^s &= \frac{\partial H}{\partial \chi_{ij}^s} = 2\mu l_2^2 \chi_{ij}^s \\ D_i &= \frac{\partial H}{\partial E_i} = e_{ikl} \varepsilon_{kl} + \kappa_i E_k \end{aligned} \quad (9)$$

where λ and μ are the Lamé constants, l_n ($n=0, 1, 2$) are three material length-scale parameters.

3. MODELLING OF A PIEZOELECTRIC MICROBEAM

The laminated piezoelectric beam is shown in Figure 1.

If a beam length is much larger than beam width i.e., $L \gg h$, the Euler-Bernoulli beam hypothesis model can be taken. The hypothesis model neglects the shear deformation of the beam. The electric field direction is assumed in the normal direction Z-axis. The displacement components are defined as follows [22]:

$$u = -(d+z) \frac{dw(x)}{dx} \quad v = 0 \quad w = w(x) \quad (10)$$

Substituting the Equation (10) into Equations (4) - (7), and ignored the strain gradient η_{xxx} [23]. the non-zero terms can be written as follows:

$$\varepsilon_{xx} = -(d+z) \frac{d^2 w}{dx^2} \quad (11)$$

$$\gamma_z = -\frac{d^2 w}{dx^2} \quad (12)$$

$$\begin{aligned} \eta_{xxz}^{(1)} = \eta_{xxz}^{(1)} = \eta_{xxz}^{(1)} &= -\frac{4}{15} \frac{d^2 w}{dx^2} \\ \eta_{yyz}^{(1)} = \eta_{yyz}^{(1)} = \eta_{yyz}^{(1)} &= -\frac{1}{15} \frac{d^2 w}{dx^2} \\ \eta_{zzz}^{(1)} &= \frac{1}{5} \frac{d^2 w}{dx^2} \end{aligned} \quad (13)$$

Substituting Equations (11-13) into Equation (1), the electric enthalpy density is given as follows:

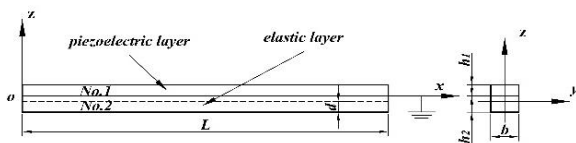


Figure 1. Schematic diagram of a laminated piezoelectric beam

$$\begin{aligned} H_1 &= \frac{1}{2} \left[E_1 \varepsilon_{xx}^2 + 2e_{31} \varphi_{,z} \varepsilon_{xx} + 2\mu_1 l_{0(1)}^2 \gamma_z^2 + 6\mu_1 l_{1(1)}^2 \left(\eta_{xxz}^{(1)} \right)^2 \right. \\ &\quad \left. + 6\mu_1 l_{1(1)}^2 \left(\eta_{yyz}^{(1)} \right)^2 + 2\mu_1 l_{1(1)}^2 \left(\eta_{zzz}^{(1)} \right)^2 + 4\mu_1 l_{2(1)}^2 \left(\chi_{xy}^s \right)^2 - \kappa_2 \varphi_{,z}^2 \right] \end{aligned} \quad (14)$$

The strain energy density of the elastic layer is given as follows:

$$\begin{aligned} U_2 &= \frac{1}{2} \left[E_2 \varepsilon_{xx}^2 + 2\mu_2 l_{0(2)}^2 \gamma_z^2 + 6\mu_2 l_{1(2)}^2 \left(\eta_{xxz}^{(1)} \right)^2 \right. \\ &\quad \left. + 6\mu_2 l_{1(2)}^2 \left(\eta_{yyz}^{(1)} \right)^2 + 2\mu_2 l_{1(2)}^2 \left(\eta_{zzz}^{(1)} \right)^2 + 4\mu_2 l_{2(2)}^2 \left(\chi_{xy}^s \right)^2 \right] \end{aligned} \quad (15)$$

The summation of the electric enthalpy is shown as follows:

$$\Theta = b \int_0^L \int_{h_2}^{h_1} H_{total} dz dx = b \int_0^L \int_0^{h_1} H_1 dz dx + b \int_0^L \int_{-h_2}^0 U_2 dz dx \quad (16)$$

The virtual work done can be defined as follows:

$$W_{ext} = \int_0^L q(x) w dx + [Fw]_0^L + [Mw']_0^L + [M^h w'']_0^L \quad (17)$$

3. 1. Modelling for a Microbeam

The schematic diagram of the piezoelectric cantilever is shown in Figure 2.

The Hamilton's principle is shown as follows:

$$\delta \int_{t_1}^{t_2} (T - \Theta + W_{ext}) dt = 0 \quad (18)$$

Under the free vibration, $W_{ext}=0$. The kinetic energy T is defined as follows:

$$T = \frac{1}{2} \int_0^L \rho_e A_e \left(\frac{\partial w}{\partial t} \right)^2 dx \quad (19)$$

Inserting Equations (16-17) and Equation (19) into Equation (18), yields:

$$\begin{aligned} &\delta \int_{t_1}^{t_2} (T - \Theta + W_{ext}) dt \\ &= \int_0^L \left[-(a_1 + a_3) w^{(4)} + e_{31} a_2 \varphi_{,zz} + q(x) \right] \delta w dx \\ &\quad - \int_0^L \int_{h_2}^{h_1} b \left(e_{31} w'' + \kappa_2 \varphi_{,z} \right) \delta \varphi dz dx \\ &\quad - \left[-(a_1 + a_3) w^{(3)} + e_{31} a_2 \varphi_{,zx} - F \right] \delta w \Big|_0^L \\ &\quad - \left[-b \int_0^L e_{31} (d+z) w'' + \kappa_2 \varphi_{,z} dx \delta \varphi \Big|_0^h \right] \\ &\quad - \left[(a_1 + a_3) w'' - e_{31} a_2 \varphi_{,z} - M \right] \delta w' \Big|_0^L = 0 \end{aligned} \quad (20)$$

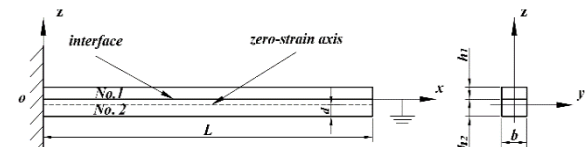


Figure 2. Schematic diagram of a piezoelectric cantilever microbeam under free vibration

where,

$$\begin{aligned} a_1 &= E_1(A_1d^2 + 2dS_1 + I_1) + E_2(A_2d^2 + 2dS_2 + I_2) \\ a_2 &= A_1d + S_1 \\ a_3 &= A_1\left(2\mu_1l_{0(1)}^2 + \frac{8}{15}\mu_1l_{1(1)}^2 + \mu_1l_{2(1)}^2\right) \\ &+ A_2\left(2\mu_2l_{0(2)}^2 + \frac{8}{15}\mu_2l_{1(2)}^2 + \mu_2l_{2(1)}^2\right) \end{aligned} \quad (21)$$

Solving Equation (20), the mechanical and electrical governing equations can be expressed as Equations (22) and (23), respectively.

$$(\rho_1A_1 + \rho_2A_2)\frac{\partial^2 w(x,t)}{\partial t^2} + (a_1 + a_3)w^{(4)} - a_2e_{31}\varphi_{,zz} = 0 \quad (22)$$

$$\kappa_2\varphi_{,zz} + e_{31}w''(x,t) = 0 \quad (23)$$

Inserting Equation (23) into electrical boundary conditions Equation (24), the electrical potential φ can be derived as Equation (25).

$$(d+z)e_{31}w'' + \kappa_2\varphi_{,z}|_{z=h} = 0 \quad \varphi|_{z=0} = 0 \quad (24)$$

$$\varphi = -\frac{e_{31}}{2\kappa_2}z^2w'' - \frac{e_{31}d}{\kappa_2}zw''', \quad \varphi_{,zz} = -\frac{e_{31}(z+d)}{\kappa_2}w^{(4)} \quad (25)$$

Taking Equation (25) into Equation (22), leads to:

$$(\rho_1A_1 + \rho_2A_2)\frac{\partial^2 w}{\partial t^2} + \left(a_1 + a_3 + a_2\frac{e_{31}^2(z+d)}{\kappa_2}\right)w^{(4)} = 0 \quad (26)$$

where the $w(x, t)$ can be assumed as:

$$w(x,t) = W_0(x)e^{i\omega t} \quad (27)$$

Then substituting Equation (27) into Equation (26) gives:

$$JW_0^{(4)}e^{i\omega t} - (\rho A)_e W_0\omega^2 e^{i\omega t} = 0 \quad (28)$$

where,

$$J = a_1 + a_3 + a_2\frac{e_{31}^2(z+d)}{\kappa_2}, \quad (\rho A)_e = \rho_1A_1 + \rho_2A_2 \quad (29)$$

Solving Equation (28) then gives amplitude equation:

$$\begin{aligned} W(x) &= C_1 \sin(\beta x) + C_2 \cos(\beta x) \\ &+ C_3 \sinh(\beta x) + C_4 \cosh(\beta x) \end{aligned} \quad (30)$$

where,

$$\beta = \left(\frac{(\rho A)_e \omega^2}{J}\right)^{(1/4)} \quad (31)$$

The first order natural frequency can be written as Equation (32):

$$\omega_1 = 1.875^2 \sqrt{\frac{J}{(\rho A)_e L^4}} \quad (32)$$

3. 2. Analytical Flowchart

The size-dependent dynamic model is solved using MATLAB. The design of the analytical flowchart is presented in Figure 3. First, the modified piezoelectric theory is established, and a size-dependent model of the microbeam based on this theory is developed. Second, the governing Equation (22) is solved using Hamilton's principle. Taking the amplitude, Equation (30), into the boundary condition, the natural frequency, Equation (32), can be obtained.

4. RESULTS AND DISCUSSION

The natural frequencies obtained using different size-dependent models are discussed in this section. The material parameters are shown in Table 1 [24]. The length scale parameters of the material can be assumed as $l_{01} = l_{11} = l_{21} = l_1$ and $l_{02} = l_{12} = l_{22} = l_2$, where $l_2 = 2 \times l_1 = 2 \times l$.

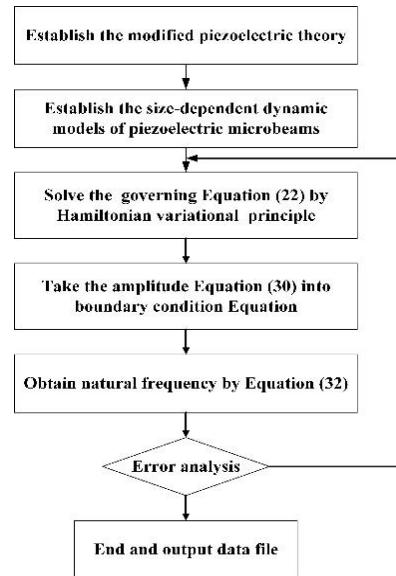


Figure 3. Analytical flowchart of the dynamic model

TABLE 1. Material parameters

Parameters	Value	Parameters	Value
G_1	126 GPa	h	1.2 μm
G_2	160 GPa	h_1	0.2 μm
ρ_1	$7.5 \times 10^3 \text{ kg/m}^3$	h_2	1 μm
ρ_2	$2.7 \times 10^3 \text{ kg/m}^3$	L	20 μm
ε_0	$8.85 \times 10^{-12} \text{ C/V}\cdot\text{m}$	b	1 μm
κ_2	$13 \times 10^{-9} \text{ C/V}\cdot\text{m}$	e_{31}	-6.5N/ (V m)

4. 1. Model Validation To validate the accuracy of the present model, the natural frequencies were compared with those reported data in previous research [25]; results are shown in Figure 4. The obtained results proved the accuracy of the model.

4. 2. Mechanical-electrical Coupling Responses under Free Vibration

Figure 5 compares the dimensionless natural frequency of a piezoelectric microbeam predicted using the present and MCS models. ω is the natural frequency obtained using the size-dependent model, and ω_0 is the natural frequency that obtained using the classical model. ω is larger than ω_0 , it means that the size effect can enhance the structural stiffness when h/l is smaller than 15. The results obtained using the MCS model are less than those obtained using the present model. This difference is due to the fact that the MCS model is a simplification of the present model. Furthermore, with an increase in the thickness, the influence of the size effect gradually decreases. When h/l is much greater than 15, the size effect can be neglected.

Figure 6 shows the effect of the relative thickness t on the natural frequency ω under free vibration. The t can be calculated using Equation (33). When t is greater than 5

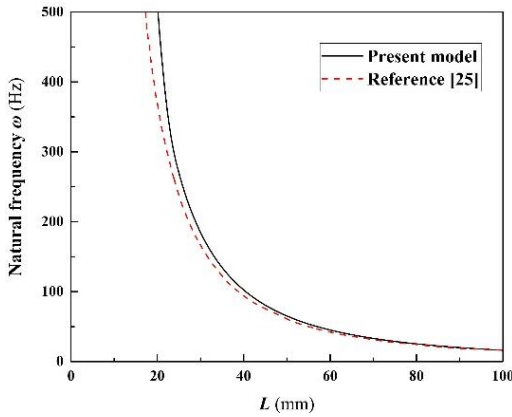


Figure 4. Model validation

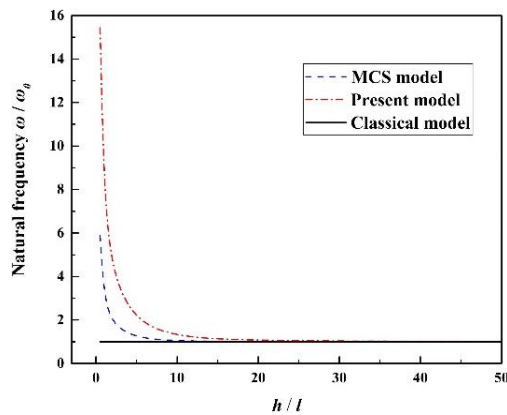


Figure 5. Influence of the h/l value on the natural frequency

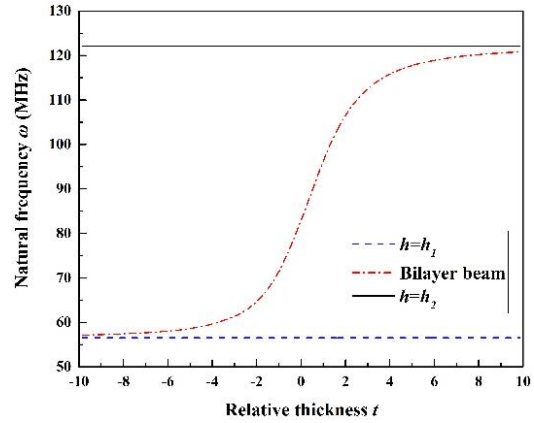


Figure 6. Influence of relative thickness t on the natural frequency

(the thickness of h_2 is 27 times greater than that of h_1), the ω is approximately equal to the ω of the single elastic layer no. 2 beam (122.06 MHz). When t is less than -5 (h_1 is 27 times greater than h_2), the ω of the piezoelectric microbeam is approximately equal to that of the single piezoelectric layer no. 1 beam (56.54 MHz).

$$t = \frac{h_2 - h_1}{\sqrt{h_1 h_2}} \tag{33}$$

5. CONCLUSIONS

In this article, a size-dependent dynamic model of a laminated piezoelectric microbeam is presented to predict the behaviour of a piezoelectric microbeam. The natural frequencies of microbeams are obtained under free vibration. Numerical results reveal that when the size effect is considered, the natural frequency of the piezoelectric microbeam increases, meaning that the size effect can strengthen the beam’s structural stiffness. When h/l is larger than 15, the size effect can be neglected. Compared with the present model, the MCS model underestimates the size-dependent response. Thus, the MCS theory is a simplification of the MSG theory. In addition, the relative thickness can obviously influence the natural frequency. When the relative thickness is greater than 5 or less than -5 , the laminated beam can be simplified to a single-layer beam. The influence of working conditions on the natural frequency will be considered in future research to study the design method of the MEMS.

6. ACKNOWLEDGEMENT

This work is supported by the Shandong Youth Science Foundation of China, (grant nos. ZR2021QA078).

7. REFERENCES

- Huang, G. L., and Sun, C. T., "The Dynamic Behaviour of a Piezoelectric Actuator Bonded to An Anisotropic Elastic Medium", *International Journal of Solids and Structures*, Vol. 43, No. 5, (2006): 1291-1307. doi: 10.1016/j.ijsolstr.2005.03.010
- Xie, X. D., Liao, H., Zhang, J. F., Du, G. F., Wang, Q., and Hao, Y., "An Investigation on a Cylinder Harvester Made of Piezoelectric Coupled Torsional Beams", *Energy Conversion and Management*, Vol. 251, (2022), 114857.
- Shahsavari, M.M., Akrami, M., Gheibi, M., Kavianpour, B., Fathollahi-Fard, A.M., and Behzadian, K., "Constructing a Smart Framework for Supplying the Biogas Energy in Green Buildings Using an Integration of Response Surface Methodology, Artificial Intelligence and Petri Net Modelling", *Energy Conversion and Management*, Vol. 248, (2021), 114794. doi: DOI: 10.1016/j.enconman.2021.114794
- Soheila, E., Zahra, E., and Manouchehr, B., "Numerical Simulation for Sensitivity and Accuracy Enhancement of Micro Cantilever-Based Biosensor Employing Truss Structure", *Microsystem Technologies*, Vol. 25, No. 6, (2019), 2205-2214. doi: 10.1007/s00542-018-4092-y
- Gholizadeh, H., Fathollahi-Fard, A.M., Fazlollahtabar, H., and Charles, V., "Fuzzy Data-Driven Scenario-Based Robust Data Envelopment Analysis for Prediction and Optimisation of an Electrical Discharge Machine's Parameters", *Expert Systems with Applications*, Vol. 193, (2022), 116419. doi: 10.1016/j.eswa.2021.116419
- El khouddar, Y., Adri, A., Outassafat, O., Rifai, S., and Benamar, R., "Non-linear Forced Vibration Analysis of Piezoelectric Functionally Graded Beams in Thermal Environment", *International Journal of Engineering, Transactions B: Applications*, Vol. 34, No. 11, (2021), 2387-2397. doi: 10.5829/IJE.2021.34.11B.02
- Multani, M. S., Gokarn, S. G., Palkar, V. R., and Vijayaraghavan, R., "Morphotropic Phase Boundary in the System Pb (ZrxTi1-x)O3", *Materials Research Bulletin*, Vol. 17, No. 1, (1982), 101-104. doi: 10.1016/0025-5408(82)90189-1
- Bühlmann, S., Dwir, B., Baborowski, J., and Murali, P., "Size Effect in Mesoscopic Epitaxial Ferroelectric Structures: Increase of Piezoelectric Response with Decreasing Feature Size", *Applied Physics Letters*, Vol. 80, No. 17, (2002), 3195-3197. doi: 10.1063/1.1475369
- Shaw, T. M., Trolrier-McKinstry, S., and McIntyre, P. C., "The Properties of Ferroelectric Films at Small Dimensions", *Annual Review of Materials Science*, Vol. 30, No. 1, (2000), 263-298. doi: 10.1146/annurev.matsci.30.1.263
- Chun, D., Sato, M., and Kanno, I., "Precise Measurement of The Transverse Piezoelectric Coefficient for Thin Films on Anisotropic Substrate", *Journal of Applied Physics*, Vol. 113, No. 4, (2013), 044111. doi: 10.1063/1.4789347
- Moosavi, J., Fathollahi-Fard, A.M., and Dulebenets, M.A., "Supply Chain Disruption During the COVID-19 Pandemic: Recognizing Potential Disruption Management Strategies", *International Journal of Disaster Risk Reduction*, Vol. 75, (2022), 102983. doi: 10.1016/j.ijdrr.2022.102983
- Mindlin, R. D., and Tiersten, H. F., "Effects of Couple-Stresses in Linear Elasticity," *Archive for Rational Mechanics and Analysis*, Vol. 11, No. 1, (1962), 415-448. doi: 10.1007/bf00253946
- Mindlin, R. D., "Micro-Structure in Linear Elasticity", *Archive for Rational Mechanics and Analysis*, Vol. 16, No. 1, (1964), 51-78. doi: 10.1007/bf00248490
- Yang, F., Chong, A. C. M., Lam, D. C. C., Tong, P., "Couple Stress Based Strain Gradient Theory for Elasticity", *International Journal of Solids and Structures*, Vol. 39, No. 10, (2002), 2731-2743. doi: 10.1016/s0020-7683(02)00152-x
- Korayem, M. H., Hashemi, A., and Korayem, A. H., "Multilayered Non-Uniform Atomic Force Microscope Piezoelectric Microcantilever Control and Vibration Analysis Considering Different Excitation Based on the Modified Couple Stress Theory", *Microscopy Research and Technique*, Vol. 84, No. 5, (2020), 943-954. doi: 10.1002/jemt.23655
- Noori, H. R., and Jomehzadeh, E., "Length Scale Effect on Vibration Analysis of Functionally Graded Kirchhoff and Mindlin Micro-plates", *International Journal of Engineering Transactions C: Aspects*, Vol. 27, No. 3, (2014), 431-440. doi: 10.5829/idosi.ije.2014.27.03c.11
- Bakhshi Khaniki, H., and Hosseini Hashemi, S., "Free Vibration Analysis of Nonuniform Microbeams Based on Modified Couple Stress Theory: An Analytical Solution", *International Journal of Engineering, Transactions B: Applications*, Vol. 30, No. 2, (2017) 311-320. doi: 10.5829/idosi.ije.2017.30.02b.19
- Aifantis, E. C., "On the Role of Gradients in the Localization of Deformation and Fracture", *International Journal of Engineering Science*, Vol. 30, No. 10, (1992), 1279-1299. doi: 10.1016/0020-7225(92)90141-3
- Nikpourian, A., Ghazavi, M. R., and Azizi, S., "Size-Dependent Secondary Resonance of a Piezoelectrically Laminated Bistable MEMS Arch Resonator", *Composites Part B Engineering*, Vol. 173, (2019), 106850. doi: 10.1016/j.compositesb.2019.05.061
- Radgolchin, M., and Moeenfarid, H., "Size-Dependent Piezoelectric Energy Harvesting Analysis of Micro/Nano Bridges Subjected to Random Ambient Excitations", *Smart materials and structures*, Vol. 27, No. 2, (2018), 25015. doi: 10.1088/1361-665x/aaa1a9
- Lam, D. C. C., Yang, F., Chong, A. C. M., Wang, J., and Tong, P., "Experiments and Theory in Strain Gradient Elasticity", *Journal of the Mechanics and Physics of Solids*, Vol. 51, No. 8, (2003), 1477-1508. doi: 10.1016/S0022-5096(03)00053-X
- Fu, G., and Zhou, S., "On the Size Dependency of a Dielectric Partially Covered Laminated Microbeam", *Thin-Walled Structures*, Vol. 161, (2021), 107489. doi: 10.1016/j.tws.2021.107489
- Yan, Z., and Jiang, L. Y., "Flexoelectric Effect on The Electroelastic Responses of Bending Piezoelectric Nanobeams", *Journal of Applied Physics*, Vol. 113, No. 19, (2013), 04102. doi: 10.1063/1.4804949
- Mcmeeeking, R. M., "The Energy Release Rate for A Griffith Crack in A Piezoelectric Material", *Engineering Fracture Mechanics*, Vol. 71, No. 7-8, (2004), 1149-1163. doi: 10.1016/S0013-7944(03)00135-8
- Thomas, J. J., David, C., William, W. C., Michael, B., and George, K., "Energy harvesting from mechanical vibrations using piezoelectric cantilever beams," *Smart Structures and Materials 2006: Damping and Isolation*, Vol. 6169 (2006) 61690D. doi: 10.1117/12.659466

Persian Abstract

چکیده

پرتوهای پیزوالکتریک به طور گسترده در سیستم های میکرو الکترومکانیک استفاده می شود. در مقیاس میکرو، تأثیر اثر اندازه بر یک پرتو پیزوالکتریک را نمی توان نادیده گرفت. در این مقاله، تئوری های الاستیسیته مرتبه بالاتر برای پیش بینی رفتار ریزساختارهای پیزوالکتریک در نظر گرفته می شوند و یک مدل دینامیکی وابسته به اندازه یک ریزپرتو پیزوالکتریک چند لایه ایجاد می شود. معادلات حاکم برای ریزپرتوهای پیزوالکتریک چند لایه با استفاده از اصل تغییرات به دست می آیند. فرکانس های طبیعی ریزپرتوهای پیزوالکتریک توسط مدل های دینامیکی وابسته به اندازه به دست می آیند. نتایج نشان می دهد که اثر اندازه می تواند سفتی ساختاری را در مقیاس میکرو افزایش دهد. فرکانس طبیعی به دست آمده با استفاده از مدل کلاسیک کوچکتر از فرکانس بدست آمده با استفاده از مدل وابسته به اندازه است. در مقایسه با مدل استرس زوج اصلاح شده، مدل استرس زوجی اصلاح شده پاسخ وابسته به اندازه را دست کم می گیرد. بنابراین، مدل تنش زوجی اصلاح شده، ساده سازی مدل گرادیان کرنش اصلاح شده است. تأثیر ضخامت پرتو بر فرکانس طبیعی نیز مورد بحث قرار گرفته است. با افزایش ضخامت، فرکانس طبیعی مدل های وابسته به اندازه به تدریج به نتیجه مدل کلاسیک نزدیک می شود. اگر مقدار h/l بیشتر از ۱۵ باشد، می توان از تأثیر اندازه چشم پوشی کرد. علاوه بر این، ضخامت نسبی می تواند فرکانس طبیعی را تحت تأثیر قرار دهد و اگر ضخامت نسبی بزرگتر از ۵ یا کمتر از ۰-۵ باشد، پرتو دولایه را می توان به یک پرتو تک لایه ساده کرد.



The Equipment Scheduling and Assignment Problem in the Overhaul Industry

M. Torkashvand^a, N. Shamami*^b, H. Bigdeli^c

^a Department of Industrial Engineering, University of Kurdistan, Sanandaj, Iran

^b Department of Industrial Engineering, Faculty of Industrial and Mechanical Engineering, Qazvin Branch, Islamic Azad University, Qazvin, Iran

^c Department of Mathematics, University of Birjand, Birjand, Iran

PAPER INFO

Paper history:

Received 06 March 2023

Received in revised form 28 March 2023

Accepted 30 March 2023

Keywords:

Genetic Algorithm

Flow Shop

Shortest Processing Time

Particle Swarm Optimization

ABSTRACT

In this article, equipment overhaul is considered in a multi-stage flow shop scheduling problem. In this problem, the equipments are disassembled in the first stage, overhaul and repairs are done on the equipment in parallel workshops in the second stage, and the assembly operation is done in parallel workshops in the third stage. Considering a three-stage overhaul with parallel machines in the second and third stages is new in the overhaul industry. The sequence of equipment processing is determined in the first stage, as well as the allocation and sequence of equipment in the second and third stages should be done in such a way that the total completion time of jobs is minimized. Unlike most articles, the sequence of processing jobs is not the same in all stages and changes with the use of decoding. For the next innovation: in order to solve the problem, a new mathematical model is presented. Two new improved algorithms, Genetic Algorithms (GA) and Particle Swarm Optimization (PSO) are presented to solve the problem in large dimensions. By using the shortest processing time (SPT) heuristic, these two algorithm have been improved and Hybrid GA (HGA) and Hybrid PSO (HPSO) algorithms have been presented. In order to achieve better results with the current conditions, the parameters setting is done by one-way analysis of variance (ANOVA). Finally, it is possible to improve the performance of the equipment by applying the discussed issues.

doi: 10.5829/ije.2023.36.06c.14

1. INTRODUCTION

The equipment and physical assets of the organization undergo depreciation during their life cycle, and this puts the organizations in intermittent periods of time in front of the decision to decommission or refurbish the equipment. In many cases, the renovation and overhaul of industrial equipment, if implemented correctly, is a decision that can help the organization in creating the most value from physical assets.

Luh et al. [1] investigated the effect of overhaul, they considered three cases. Based on the results, after using the equipment overhaul, the average cost of delay is significantly reduced from 53.81 in case 1 to 13.66 in case 2, which leads to the reduction of the average possible cost from 59.84 to 27.38. The standard deviation of the feasible cost is also significantly reduced from 27.53 to 3.03, implying a more predictable asset delivery.

As a result, asset delivery becomes more reliable and the standard deviation of the feasible cost is further reduced from 3.03 to 0.88.

As another example, an Maintenance, Repair, and Overhaul (MRO) activity in the aviation industry is typically a scheduled periodic check to determine the condition of an aircraft or its components, including service, repair, modification, overhaul, and inspection. The MRO industry can be described as a strong supporter in the aviation industry for the provision of aircraft parts and services. For airlines, MRO costs cover 12% of total annual operating costs, the third hidden cost after fuel and operations. As the number and age of aircraft worldwide increases, the annual growth rate of the MRO market is now 4.2%, and the MRO market is forecast to reach \$87.8 billion by 2024. With incumbent MRO companies competing for markets and new entrants entering, intense competition puts them under great pressure to increase

*Corresponding Author Institutional Email: n.shamami@casu.ac.ir
(N. Shamami)

profit margins and optimize business operations. Therefore, effective management technologies and tools are needed for MRO companies to improve operation efficiency and reduce operation cost [2].

According to a general definition, it can be said that overhaul is the comprehensive and complete restoration of an asset to bring it to an acceptable condition through reconstruction or replacement of its parts and subassemblies. The purpose of the overhaul is actually to restore the optimal performance of the equipment while ensuring its reliability. The overhaul process of industrial equipment generally includes the following steps [3]:

- Segregation
- Disassembly
- Cleaning
- Inspection
- Repair (or replace)
- Assembly and testing

In “segregation”, the equipment is separated for overhaul. In “disassembly”, the components of each equipment are separated. In “cleaning”, the operation of cleaning separated parts is performed. After cleaning, each part is inspected to determine the need for repair (“inspection”). In the “repair (or replace)” stage, the repair or replacement operation is performed on the parts that have been specified from the previous stage. Finally, after the repair, the repaired or replaced or cleaned parts are put together and then tested and the “assembly and testing” operation is performed. In this article, all the above steps are done in three steps, so that the steps of segregation, disassembly, cleaning and inspection are known as disassembly, and two steps with the same title are mentioned in this article.

The overhaul word is usually used for mechanical equipment and this process is generally implemented in the middle of the useful life of the equipment. Sometimes, instead of the word "overhaul", the term "major repairs" is used. In order to overhaul some equipment, it is necessary to remove them from the site and move them to a suitable place for the implementation of the reconstruction process, although many equipment must also be overhauled at their location. In the overhaul process of industrial equipment, sometimes there is a need to rebuild some parts and sub-category equipment. For the parts that cannot be repaired, they must be replaced.

Overhaul operation can be done as an emergency and after an unexpected failure or form of a predetermined program and when the equipment is out of operation. In general, the implementation of the overhaul process imposes two types of costs on the organization, one is the direct costs of the overhaul process and the other is the costs associated with the equipment being unavailable during the overhaul. Correct planning and based on the health status of the equipment during its life cycle can

adjust the scheduling of the overhaul operations in such a way that both types of costs are minimized.

In this century, organizations are operating in a very unstable and dynamic environment, and they are always facing risks and threats, which will undoubtedly face very important challenges if they are not responded to in a timely and quick manner. Considering that the use duration of military equipment is longer than that of commercial equipment, and changes in it usually take longer, one of these key factors in using equipment is overhaul and optimization, which has been the focus of most managers and organizations in recent years. according to these conditions, the scheduling of overhaul and repairs of devices and equipment can show a significant role in the field of defense in military industries, whenever any of the devices and equipment needs major repairs and optimization, sent to the overhaul and optimization centers, the readiness and combat power of that unit will decrease in the same proportion, and with this description, any speed and agility will help to strengthen the power and readiness of that unit. The level of readiness can be a standard for allocating funds, purchasing equipment and support items, as well as carrying out military actions in peacetime or wartime. The readiness of equipment is one of the basic components in the operational readiness of organizations, which is the main goal of the maintenance and repair system and its existential philosophy in the process of supporting organizations.

In this plan, a flow shop scheduling problem is proposed in order to reduce the cost and time of equipment overhaul. Also, in order to prevent additional repairs, it is used to diagnose and predict defects before failure and reduce waste. One of the most important defense factors of any country is its equipment. One of the necessities of presenting this research is keeping the equipment ready and having the maximum ability when needed. Its importance is related to the time that the protection of the country and people's lives are involved. It is used in times of peace to maintain security and in times of war to speed up the preparation of equipment. In order to increase the defense power, the preparation and availability of equipment for use in emergency situations, repairs and overhaul of the equipment are carried out. In case of possible threats, it will be possible to use the equipment when needed. Also, proper, accurate, high-reliability and high-quality overhaul and optimization scheduling can increase the trust of employees and the organization in the internal overhaul and repair system, and as a result, increase the morale and self-confidence of technical personnel, which causes a kind of lack of dependence on external factors. Also, the scheduling of repairs, overhaul and optimization with high quality and reliability will prevent rework and return of refurbished equipment and tools to the centers, which can be effective

in reducing the cost and time of the organization's personnel.

The following sections are presented below. In the second part, a literature review is presented, which examines the articles presented in this field. The third part of the mathematical model is defined along with the limitations. In the fourth section, classical solution methods for large-scale problems are presented. In the fifth section, improved problem solving methods for large sizes are shown. Calculation results for small and large problem sizes as well as sensitivity analysis are analyzed in the sixth section. Finally, the conclusion is made in the seventh section.

2. LITERATURE REVIEW

Reményi and Staudacher. [3] investigated the maintenance, repair and overhaul operations of aircraft engines. Since it is difficult to control maintenance planning and maintenance operations, the focus of research has been on improving maintenance operations by finding appropriate scheduling for job shop operations in maintenance operations. They emphasized that scheduling can improve maintenance operations. According to the needs of different researches, they presented a simulation model. The maintenance and repair process is defined in 3 separate stages: disassembly, repair and assembly. Qin et al. [4] proposed an integrated aircraft maintenance scheduling and hangar layout planning problem. They developed a mathematical model incorporating the variation of parking capacity and blocking during aircraft movements. To obtain good quality feasible solutions for large scale instances, presented a rolling horizon approach incorporating the enhanced mathematical model. Pinhão et al. [5] studied integration of line balancing and scheduling problems in aircraft engines assembly and presented integer programming models define a standard work for multi-skilled operators. Models were implemented in the system and hierarchically solved by the CPLEX on data of two different assembly lines from a Brazilian MRO company.

Dinis et al. [6] proposed a framework for the qualitative and quantitative characterization of maintenance work to support MRO organizations in performing capacity planning and scheduling. They proposed a framework, entitled Framework for Aircraft Maintenance Estimation (FRAME), is intended to allow MROs in managing this uncertainty throughout the maintenance planning process and comprises for that end a set of requirements for data treatment and a method for data analysis.

Sharma and Rai [7] proposed arithmetic reduction of age based virtual age model to estimate reliability parameters by considering the complete MRO as

imperfect and provides the likelihood and log-likelihood functions for parameter estimation of the proposed model and also presents the various extensions of the proposed model.

Huang et al. [8] presented a simulation optimization for maintenance, repair and overhaul scheduling problem based on multi credit models. A simulation model with a high degree of credibility, which is probable and time-consuming. The solution space was divided into several parts. They also divided the process into three parts: disassembly workshop, repair workshop and assembly workshop. The repair workshop consists of one or more multifunctional machines with one or more parallel machines. Mayto et al. [9] presented a research with the aim of improving the scheduling of machines so that the maximum completion time of job is minimized in the scheduling of job shop using genetic algorithm. They created a new plan to carry out the repair process of the CT7 engine cold section module at PT XYZ. Chang and Abdullah [10] presented an operations management model that creates the concept of soft production and sustainable development in the maintenance process and the management process for factory maintenance, repairs and overhaul. Aircraft maintenance, repairs and overhaul are very important for air operations. MRO company should focus on delivery, quality, cost and flexibility in order to increase customer satisfaction. Luh et al. [1] presented a new formulation for repair and overhaul services so that key characteristics such as asset arrival and non-deterministic processing times of parts are presented in the model including an overhaul center and several repair shop centers. They developed a solution method including a combination of the Lagrange method and probabilistic dynamic planning in order to schedule operations so that the total tardiness and inventory maintenance costs are minimized. Liu et al. [2] presented a scheduling problem in the class of maintenance, repair and overhaul systems. Considering all the key characteristics such as disassembly, non-deterministic material recovery, material matching requirements, possible routing and possible processing times, they formulated a scheduling problem as a simulation problem. In order to solve the problem, they presented two combined algorithms. For a set of jobs, the problem is to determine the sequence of jobs for disassembly in the disassembly shop, the sequence of components for repair in the repair shop, and the sequence of jobs for assembly operations in the assembly stage, so that the weighted sum of tardiness times is minimized. Li et al. [11] presented a scheduling optimization method for maintenance, repairs, and operation of service resources in complex products, which improves customer satisfaction, increases product value, and increases competitive advantage. First, they analyzed the scheduling problem in service resources, presented a mathematical model for the service scheduling problem,

and presented three objective functions including minimizing the waiting time of customers, reducing excess resources, and maximizing the resource performance cost index. Then each of the three objective functions have been analyzed based on three methods including improved genetics, combined weight coefficient optimization method and non-dominant sorted genetic method. Tran et al. [12] proposed Swarm Intelligence Algorithm, Ant Colony Optimization in order to solve the scheduling problem of MRO processes with two objective functions of minimizing the maximum completion time and the total tardiness times of all jobs. They considered three stages for the MRO process: all components are inspected in the inspection stage (first stage), the repair operations are performed based on the defined sequence (scheduling is done in this stage) in the second stage, the release operation is done in the third stage.

Yuan et al. [13] proposes a capacitated fuzzy disassembly scheduling model with cycle time and environmental cost as parameters, which has broad applications in remanufacturing and many other production systems. A mixed-integer mathematical programming model proposed to minimize the cycle time and environmental cost, whilst a metaheuristic approach based on a fruit fly optimization algorithm (FOA) is developed to find a fuzzy disassembly scheduling scheme.

Guo et al. [14] due to the heavy problems of accompanying support jobs, high timely requirements and the mismatch between the types and number of repair units and support activities in wartime, together with the scheduling of equipment maintenance activities, they considered the problem of flexible flow shop scheduling and presented a scheduling model for equipment maintenance activities based on the accompanying maintenance group. Based on the limited ability of repairs and the repair time of the repair team, the proposed model was considered to schedule the activities of the repair team with the aim of minimizing the time spent on repairs. Rahman et al. [15] believe that the MRO process is an action to control, identify and ensure the life of a defense equipment. Indonesia should have MRO concept in defense industry. The relevant issue is how to prioritize the weighting and develop strategic planning for the maintenance and overhaul of warships implemented by Fasharkan Surabaya to support the readiness of naval operations. The aim of the presented research is to create a strategic planning in the development of MRO of Fasharkan Surabaya warships in support of maritime operations readiness. Considering that the problem investigated in this article is a special type of flow shop, some articles have been presented in this field. Fathollahi-Fard et al. [16] proposed a sustainable Distributed Permutation Flow Shop Scheduling Problem (DPFSP). The study total energy

consumption related to production, and the social factors linked to job opportunities and lost working days. In order to solve the problem they presented a novel multi-objective learning-based heuristic is established, as an extension of the Social Engineering Optimizer (SEO). Gholizadeh et al.[17] addressed this challenge more broadly, this paper presents an optimization model for the problem of flexible flowshop scheduling in a series-parallel waste-to-energy (WTE) system. A preventive maintenance (PM) policy is proposed to find an optimal sequence for processing tasks and minimize the delays.

Amirian and Sahraeian [18] proposed an effective multi-objective differential evolution algorithm (MDES) to solve a permutation flow shop scheduling problem (PFSSP) with the modified Dejong's learning effect. The proposed algorithm combines the basic differential evolution (DE) with local search and borrows the selection operator from NSGA-II to improve the general performance. Naseri et al. [19] consider the production environment of no-wait reentrant flow shop with the objective of minimizing makespan of the jobs. They constructed simulated annealing (SA), genetic algorithm (GA) and a bottleneck based heuristic (BB) algorithms to solve the problem. A summary of the subject literature is shown in Table 1. According to Table 1, two of the articles are job shop. In four articles, the second stage is the job shop, and in three articles, a three-stage flow shop is presented. In order to complete the presented problems and fill the gaps in the literature, in this article, parallel machines are considered in the second and third stages of the flow shop.

According to the reviewed literature, in this research, a combined flow shop scheduling problem will be presented in order to maintain, repair and overhaul military equipment in the army. In this problem, the equipment considered for the scheduling of repairs and overhaul are placed in a multi-stage flow shop where the first stage is equipment disassembly, the second stage is repairs and overhaul, and the third stage is assembly. The innovations of the problem are:

TABLE 1. Summary of the subject literature

Row	Author	Problem
1	Tran et al. [19]	Job shop
2	Guo et al. [14]	Flexible job shop
3	Reményi and Staudacher [18]	Job shop in the second stage
4	Huang et al. [8]	Job shop in the second stage
5	Mayto et al. [9]	Job shop in the second stage
6	Liu et al. [2]	Job shop in the second stage
7	Chang and Abdullah [10]	Three-stage flow shop
8	Luh et al. [1]	Three-stage flow shop
9	Rahman et al. [15]	Three-stage flow shop

- Providing improved meta-heuristic algorithms to solve large-scale problems
- Considering parallel machines in the second and third stages
- Regarding the three-stage flow shop for equipment overhaul
- Presenting a new model to accurately solve the problem in small dimensions

3. MATHEMATICAL MODEL

The problem investigated in this article is a three-stage flow shop problem for equipment repairs and overhaul. In this problem, there are n number of machines to perform overhaul operations in a three-stage flow shop, where the first stage has a single machine, the second stage has m_2 machines, and the third stage has m_3 parallel machines. If the equipment is considered as job and each stage is considered as a machine, the problem under investigation is a three-stage flow shop problem where there is one machine in the first stage and identical parallel machines in the second and third stages. The problem model is presented by considering the following assumptions [20]:

- The number of steps is fixed and equal to 3.
- Each machine processes only one job at a time in each step.
- Storage space between stages is considered free.
- Each job is processed on only one machine at a time.
- The operation of a job in each step starts when its operation in the previous step is completed.

Parameters and Indices	
n	The number of jobs
m_2	The number of machines in the second stage
m_3	The number of machines in the third stage
s	Position indexes, $\{1,2,\dots, n\}$
i, j, r	The jobs indexes $\{1,2,\dots, n\}$
e	The machines index in the second stage $\{1,2, \dots, m_2\}$
l	The machines index in the third stage $\{1,2, \dots, m_3\}$
tf_j	the processing time of job j at the first stage
ts_j	the processing time of job j at the second stage
tt_j	the processing time of job j at the third stage
A	A large positive number

Decision variables	
$Q_{i,s}$	1 If job i is processed in position s in the disassembly stage otherwise 0.
$Z_{i,s,e}$	1 If job i is processed in position s on machine e in the overhaul stage otherwise 0.

$W_{i,s,l}$	1 If job i is processed in position s on machine l in the assembly stage otherwise 0.
COF_s	Completion time of job in position s at disassembly stage
$COS_{s,e}$	Completion time of the job in position s on the machine e in the overhaul stage
$COT_{s,e}$	Completion time of the job in position s on the machine l in the third stage

$$\text{Minimize } \sum_{s=1}^n \sum_{l=1}^{m_3} COT_{s,l} \tag{1}$$

$$\sum_{s=1}^n Q_{i,s} = 1 \quad \forall i = 1,2, \dots, n \tag{2}$$

$$\sum_{i=1}^n Q_{i,s} = 1 \quad \forall s = 1, \dots, n \tag{3}$$

$$\sum_{i=1}^n Q_{i,s-1} \geq \sum_{j=1}^n Q_{j,s} \quad \forall s = 2, \dots, n \tag{4}$$

$$\sum_{s=1}^n \sum_{e=1}^{m_2} Z_{i,s,e} = 1 \quad \forall i = 1,2, \dots, n \tag{5}$$

$$\sum_{i=1}^n Z_{i,s,e} \leq 1 \quad \forall s = 1, \dots, n; e = 1,2, \dots, m_2 \tag{6}$$

$$\sum_{i=1}^n Z_{i,s-1,e} \geq \sum_{j=1}^n Z_{j,s,e} \quad \forall s = 2, \dots, n; e = 1,2, \dots, m_2 \tag{7}$$

$$\sum_{s=1}^n \sum_{l=1}^{m_3} W_{i,s,l} = 1 \quad \forall i = 1,2, \dots, n \tag{8}$$

$$\sum_{i=1}^n W_{i,s,l} \leq 1 \quad \forall s = 1, \dots, n; l = 1,2, \dots, m_3 \tag{9}$$

$$\sum_{i=1}^n W_{i,s-1,l} \geq \sum_{j=1}^n W_{j,s,l} \quad \forall s = 2, \dots, n; l = 1,2, \dots, m_3 \tag{10}$$

$$COF_s \geq COF_{s-1} + \sum_{i=1}^n tf_i * Q_{i,s} \quad \forall s = 2, \dots, n, \tag{11}$$

$$COF_1 \geq \sum_{i=1}^n tf_i * Q_{i,1} \tag{12}$$

$$COS_{s,e} \geq COS_{s-1,e} + \sum_{i=1}^n tt_i * Z_{i,s,e} - A * (1 - \sum_{i=1}^n Z_{i,s,e}) \tag{13}$$

$$\forall e = 1,2, \dots, m_2; s = 2, \dots, n$$

$$COS_{s,e} \geq COF_r + ts_i * Z_{i,s,e} - A * (2 - Z_{i,s,e} - Q_{i,r}) \tag{14}$$

$$\forall i = 1,2, \dots, n; s, r = 1,2, \dots, n; e = 1,2, \dots, m_2$$

$$\forall l = 1,2, \dots, m_3; s = 2, \dots, n \tag{15}$$

$$COT_{s,l} \geq COS_{r,e} + tt_i * W_{i,s,l} - A * (2 - W_{i,s,l} - Z_{i,r,e}) \tag{16}$$

$$\forall i = 1,2, \dots, n; s, r = 1,2, \dots, n; e = 1,2, \dots, m_2; l = 1,2, \dots, m_3$$

$$Q_{i,s} \in \{0,1\}, Z_{i,s,e}, W_{i,s,l} \in \{0,1\} \tag{17}$$

$$\forall i = 1, \dots, n; e = 1,2, \dots, m_2; s = 1, \dots, n; l = 1, \dots, m_3$$

Equation (1) shows the objective function of the problem, which is to minimize the total time to complete the jobs. Constraint 2 indicates that each job is assigned to only one position in the first stage. Constraint 3 specifies that each position must be assigned a job in the first stage. Constraint 4 determines that a position in the first stage is completed when its previous position is occupied by a job. Constraint 5 shows that every job in the second stage must be assigned to a position of one of the machines. Constraint 6 specifies that a position of a machine is occupied by at most one job. Constraint 7 shows that a position of a machine is occupied in the second stage when its previous position is occupied. Constraint 8 specifies that every job in the third stage must be processed by one machine and it is not possible to stop processing and move between machines. Constraint 9 shows that at most one job is assigned to each position of each machine in the third stage. Constraint 10 specifies that in the third stage, a position of a machine is completed when its previous position is occupied by a job. Constraint 11 specifies the time to complete the job in the first stage. Constraint 12 specifies the completion time of the job that is in the first position of the first stage. Constraints 13 and 14 specify the time to complete the jobs in the second stage. Constraints 15 and 16 specify the time to complete the job in the third stage. Constraint 17 specifies binary variables. Constraint 18 determines the range of continuous variables.

4. SOLUTION METHOD

It is possible to solve the problem in small dimensions using the model. For the two-stage scheduling problem with parallel machines in one stage and the objective function of maximum completion time, Chen [21] showed that the problem is NP-hard. Considering that the problem investigated in this article is a three-stage flow shop with parallel machines in the third stage, it is more complicated than the problem addressed in the literature [21], so it is NP-hard.

Considering that the problem is NP-hard, it is possible to solve it in small dimensions in reasonable time using the exact solution approach, and the solution time is long for larger dimensions. Therefore, two meta-heuristic algorithms GA and PSO have been used to solve the problem in large dimensions. In the following, the common parts of two algorithms and each of the algorithms are presented separately.

4. 1. Genetic Algorithm Genetic algorithm is one of the most well-known metaheuristic algorithms that was first presented by Holland [22]. This algorithm is population based and inspired by nature. Each solution to the problem is known as a chromosome, which is created from the combination of genes. By making changes in

each chromosome, a new solution is created. Genetic algorithm includes mutation and crossover operators to create a new population. Genetic algorithm in many articles including Yazdani et al. [23], Tavakkoli-Moghaddam [24], Ghafari [25] has been used.

The presented algorithm consists of several parts, which are: 1. Presenting the solution representation in order the problem coding 2. Decoding the problem from the way it is displayed in the second and third stages 3. Creating the initial population in the amount of N_{POP} 4. Randomly selecting the solution from the existing population in order to performing crossover operations with the probability of P_{cross} 5. Random selection of solution in order to perform mutation operations with the probability of P_{mut} 6. Performing local search in order to improve the solutions. In this paper, an improved genetic algorithm is presented. According to the objective function of the problem, the algorithm presented in this problem is a combination of the genetic algorithm with the shortest processing time (SPT) heuristic method [26], which is called HGA. In the following, the steps of the algorithm are described until generating a new solution.

4. 1. 1. Solution Representation Each chromosome in the genetic algorithm is specified by using a representation in coding. Assuming that there are 10 jobs, the solution representation in the genetic algorithm presented in this article is according to Figure 1 and based on the sequence of job processing [27]. In this representation, the solution to the sequence of jobs processing in the first stage is determined. In the second and third stages, considering that there are parallel machines, the processing sequence on each machine is determined by decoding.

4. 1. 2. Decoding After determining the sequence of jobs in the first stage, considering that the second and third stages include parallel machines, the sequence of processing jobs will be different. For this purpose, after finishing the processing of a job in the first stage, in the second stage, the job is processed on a machine that is free or free earlier than other machines. It is the same for the third stage.

4. 1. 3. Initial Population In order to implement the genetic algorithm, an initial population of solution with the size of N_{POP} should be created and by applying changes to each solution, a new population is generated. According to the representation of the solution that presented in the previous section, the initial population is randomly generated and after making the necessary changes, it is updated in each iteration.

4 7 8 2 5 10 6 3 9 1

Figure 1. Solution representation

4. 1. 4. Crossover Operator In order to create a new population and improve the solutions, the crossover operator in the genetic algorithm is applied to two randomly selected solution. In order to perform the crossover in this section, the partially mapped crossover (PMX) crossover operator has been used [28]. In this operator, two points are randomly selected on the parents. The numbers between these two points are transferred from the first parent to the second child and from the second parent to the first child. We used the first parent to fill the rest of the positions in the first child.

If the selected number is not between two points, the position is filled and if there is, the opposite number is selected in the opposite child. An example of this type of crossover is shown in Figure 2. The crossover operator in the presented algorithm is performed with the probability of P_{Cross} on a solution.

Parent 1	1	2	3	4	5	6	7	8	9	10
Parent 2	2	7	8	5	4	9	6	3	10	1
Child 1	*	7	8	5	*	*	*	*	*	*
Child 2	*	2	3	4	*	*	*	*	*	*
Child 1	1	7	8	5	*	6	*	*	9	10
Child 2	*	2	3	4	*	9	6	*	10	1
Child 1	1	7	8	5	4	6	2	3	9	10
Child 2	7	2	3	4	5	9	6	8	10	1

Figure 2. Crossover operation

4. 1. 5. Mutation Operator In order to make small changes in each solution, the genetic algorithm uses the mutation operator. This operator in the genetic algorithm produces a new solution by applying changes to each solution. If the new solution is better than the previous solution, it will be replaced, otherwise the previous solution will remain unchanged. Different modes for performing mutation are presented by different authors. In this article, insert mutation is used for mutation [20], which is shown in Figure 3.

In this type of mutation, two genes are randomly selected. The second gene is transferred after the first gene. Numbers between two genes of a cell move to the right. For example, according to Figure 3, the genes in cells 4 and 8 are randomly selected. The 8th gene has been moved to the side of the 4th gene, and the numbers between the two genes have been moved one cell to the right. As a result, a new solution has been obtained. The mutation operator in the presented algorithm is performed with the probability P_{mut} on a solution.

Parent	4	7	8	2	5	10	6	3	9	1
child	4	7	8	2	3	5	10	6	9	1

Figure 3. Mutation operation

4. 1. 6. Updating The Solutions After performing crossover and mutation operations, the value of the objective function is calculated. If the obtained solutions are better than the current solution, the new solution will replace the current solution, otherwise the solution will remain unchanged.

4. 2. Particle Swarm Optimization The particle swarm optimization algorithm was proposed by Kennedy, and Eberhart [29] and has been successfully used in many fields of science. The PSO algorithm has been used by Daliri et al. [30] and Rabbani et al. [31].

This algorithm is one of evolutionary computing techniques and was invented by imitating the flight of birds or the movements of fishes and the exchange of information between them. In this algorithm, each solution is only one particle in the search space. All

particles have a fitness value that is evaluated by the fitness function that must be optimized. In addition, each particle i has a position in the d -dimensional space of the problem, which is represented by the vector (19) in the t iteration.

$$X_i^t = (X_{i1}^t, X_{i2}^t, \dots, X_{id}^t) \tag{19}$$

Also, this particle has a speed that guides its movement and is represented by the vector (20) in the t th repetition:

$$V_i^t = (V_{i1}^t, V_{i2}^t, \dots, V_{id}^t) \tag{20}$$

In each iteration of the search, each particle is updated considering the two best values. The first value is related to the best solution that the particle has experienced so far. This value is called the best P. The second best followed by the particle swarm optimization algorithm is the best position obtained so far in the population. This value is the general optimum, which is called the best g.

$$V_i(t + 1) = WV_i(t) + C_1 r_{1,i}(t)(p_i(t) - X_i(t)) + C_2 r_{2,i}(t)(p_g(t) - X_i(t)) \tag{21}$$

$$X_i(t + 1) = X_i(t) + V_i(t + 1) \tag{22}$$

After these two best values are found, the position and velocity of each particle is updated by relations (21) and (22). In the above relationships, t represents the repetition number, and variables C_1 and C_2 are learning factors. Usually, $C_1 = C_2 = 2$, which controls the amount of displacement of a particle in one repetition. r_1 and r_2 are two uniform random numbers in the interval $[0,1]$, the parameter w represents the inertia weight, which takes an initial value in the interval $[0,1]$.

4. 2. 1. Discrete PSO Algorithm The discrete mode of PSO algorithm was presented by Pan et al. [32]. In this article, the discrete mode of the PSO algorithm is used to solve the problem. The way to solution representation and decode each particle is the same as the genetic algorithm presented in section 4-1. The equation of the algorithm for the discrete state is according to Equation (23) in which the mutation and crossover operators are used.

$$X_i^t = c_2 \otimes F_3(c_1 \otimes F_2(\omega \otimes F_1(X_i^{t-1}), P_i^{t-1}), G^{t-1}) \quad (23)$$

In relation 24, X_i^t is the position of the particle, P_i^t is the best solution of the particle and G^t is the best global solution. $\gamma = \omega \otimes F_1(X_i^{t-1})$ is the speed of the particle and F_1 is the mutation operator with probability ω . The expression $\beta = c_1 \otimes F_2(\gamma, P_i^{t-1})$ is part of the particle and F_2 is the crossover operator with probability c_1 . The expression $\alpha = c_2 \otimes F_3(\beta, G^{t-1})$ shows the general part and F_3 performs the crossover operator with probability c_2 . In each iteration of the algorithm, each particle is updated based on Equation (23) and a new solution is created.

4. 2. 2. Mutation Operator In order to create diversity in the solutions of the problem, the mutation operator has been used. The mutation operator used here is swap, an example of which is shown in Figure 4 [33]. For this purpose, two genes are randomly selected from the chromosome and the jobs in them are moved. According to Figure 4, two jobs 2 and 3 are randomly selected and moved with each other.

4. 2. 3. Crossover Operator In order to create a new solution, the crossover operator has been used in the equation of the problem. There are different modes of this operator, the order crossover (OX) mode is used here [28]. In this case, two points are randomly selected on two parents. The sequence between two points is directly transferred from the first parent to the first child and from the second parent to the second child. The sequence of jobs is transferred from the second point of the second parent to the first child. An example of this mode is shown in Figure 5. Two points are randomly selected on the parents. The numbers 5, 6 and 7 are directly transferred from the first parent to the first child. In the same way, the sequence of jobs is transferred to the first child after the second point of the second parent. It is done in the same way for the second child.

4. 3. Stop Condition After performing operations on the solution and creating a new population, the

Parent	4	7	8	2	5	10	6	3	9	1
Child	4	7	8	3	5	10	6	2	9	1

Figure 4. Swap Mutation operation

Parent 1	1	2	3	4	5	6	7	8	9	10
Parent 2	2	7	8	5	4	9	6	3	10	1
Child 1	*	*	*	*	5	6	7	*	*	*
Child 2	*	*	*	*	4	9	6	*	*	*
Child 1	2	8	4	9	5	6	7	3	10	1
Child 2	*	*	*	*	4	9	6	*	*	*
Child 1	2	8	4	9	5	6	7	3	10	1
Child 2	2	3	5	7	4	9	6	8	10	1

Figure 5. OX crossover operation

condition for stopping the algorithm execution is checked. In this article, the stop condition is 600 seconds. It means that after reaching the stopping condition, the execution of the algorithm is stopped and the best solution obtained is selected as the solution of the algorithm.

5. IMPROVEMENT OF GA AND PSO ALGORITHM

The In order to improve the results and performance of the GA and PSO algorithm, the shortest processing time (SPT) method is used in this section. The problem investigated in this article consists of three stages. Therefore, each job has three processing times. In order to use the SPT method, different modes of combining processing times can be considered [34]:

1. Considering the processing times of the first stage for each job
2. Considering the processing times of the second stage for each job
3. Considering the processing times of the third stage for each job
4. Considering the total processing times of the first and second steps for each job
5. Considering the sum of the second and third processing times for each job
6. Considering the total processing times of the first, second and third steps for each first

In this method, in order to create a new population, one of the solutions is created using SPT. Each of the 6 states mentioned is calculated for an initial solution. The value of the objective function is calculated for each state and the best state is selected and considered as a solution.

For example, suppose we have 3 jobs. Their processing times are shown in Table 2. In the first case, the jobs are sorted in ascending order of the processing time of the first stage. Therefore, job 2 is processed first, then job 1 and finally job 3. In the second case, the jobs

TABLE 2. An example of local search

Job	Processing time		
	Stage 1	Stage 2	Stage 3
1	12	31	57
2	2	87	23
3	91	76	14

are sorted in ascending order of the processing time of the second stage. Therefore, job 1 is processed first, then job 3 and finally job 2. In the third mode, the jobs are arranged in ascending order of the processing time of the third stage. Therefore, job 3 is processed first, then job 2 and finally job 1. In the fourth mode, the jobs are arranged in ascending order of the total processing time of the first and second stages. Therefore, job 1 (31+12) is processed first, then job 2 (87+2) and finally job 3 (76+91) is processed. In the fifth mode, the jobs are arranged in ascending order of the total processing time of the second and third stages. Therefore, job 1 (57+31) is processed first, then job 3 (14+76) and finally job 2 (23+87). In the sixth mode, the jobs are sorted in ascending order of the total processing time of the first, second and third stages. Therefore, job 1 (57+31+12) is processed first, then job 2 (23+87+2) and finally job 3 (14+76+91) is processed. It is created from the combination of GA and PSO algorithms with the local search of the combined Hybrid Genetic Algorithm (HGA) and Hybrid Particle Swarm Optimization (HPSO) algorithms. In HGA and HPSO algorithms, the steps of the algorithm are the same as GA and PSO respectively, with the difference that one of the initial solutions is checked using the mentioned 6 states and the sequence with the best value of the objective function is considered as an initial solution.

6. CALCULATION RESULTS

In this section, the calculation results are presented in two sizes, small and large. For the small size of the presented model, it has been solved in GAMS software and by using Cplex solver, and for the large size, it has been implemented in Java software. The different values of the parameters for creating different samples in small and large sizes are shown in Table 3. Due to the time limit applied to the presented algorithms, the maximum number of jobs for the large size is 100 in order to achieve the appropriate solutions in a reasonable number of repetitions. For the flow shop problem, based on the reported data of Xiong et al. [34], processing times are set in the range of 0 to 100. Also, the number of cars of the second and third stages according to the article. Jolai et al. [35] is considered equal to 2, 3 and 4.

According to the model's ability to solve problems accurately, the sizes of 3 to 10 jobs are considered as small size problems and the problems with size 15 to 100 are considered as large size problems.

6. 1. Parameter Setting Different parameter values of GA and PSO algorithms have been used to solve the problem using one-way analysis of variance (ANOVA). For GA algorithm parameters, three different levels are considered according to Table 4.

For sample, with the values of $n = 9$, $m_2 = 4$ and $m_3 = 4$ from the combination of different levels of parameters using the orthogonal matrix according to Table 5, number of 9 different combinations of parameters are shown.

Each combination has been implemented 5 times and the average deviation from the best solution has been calculated using Equation (24).

$$ARE = \frac{obj - bestobj}{bestobj} \quad (24)$$

In relation 24, Average Relative Error (ARE) shows the amount of relative deviation. *obj* specifies the value of the objective function in each execution of the algorithm and *bestobj* determines the best value obtained by all algorithms for each instance.

TABLE 3. Parameter values to create problem examples

Parameter	Range of parameters values	
	Small size	Large size
n	{3,4,5,6,7,8,10}	{15,20,25,35,45,50,70,90,100}
m_2	{2,3,4}	{2,4,6,8}
m_3	{2,3,4}	{2,4,6,8}
tf	U(1,100)	U(1,100)
ts	U(1,100)	U(1,100)
tt	U(1,100)	U(1,100)

TABLE 4. GA algorithm parameter levels

Factor	Level	Value
PS	1	30
	2	50
	3	70
P_{Cross}	4	0.7
	5	0.8
	6	0.9
P_{mut}	1	0.1
	2	0.2
	3	0.3

TABLE 5. Relative deviation mean values for ANOVA samples for GA algorithm

Experiment number	Parameters level			Ave
	PS	P_{Cross}	P_{mut}	
1	1	1	1	0.0303
2	1	2	2	0.0357
3	1	3	3	0.0638
4	2	1	2	0.0328
5	2	2	3	0.0491
6	2	3	1	0.0203
7	3	1	3	0.0682
8	3	2	1	0.0442
9	3	3	2	0.0679

Average and scatter diagrams were drawn for each of the parameters. For PS parameter, as the population increases, the average value first decreases and then increases. Therefore, the best value of this parameter is at level 2 and is equal to PS=50.

For P_{Cross} parameter, as the rate of crossover parameter increases, the average value first decreases and then increases. Therefore, the best value of this parameter is at level 2 and is equal to $P_{Cross} = 0.8$.

For P_{mut} parameter, by the increasing of the rate of mutation parameter, the average value increases in levels 2 and 3, but the dispersion value first increases and then decreases. In level one, the average values are lower than the other two levels. Therefore, level one is selected with the value of $P_{mut} = 0.1$.

According to the results, the values of PS = 50, $P_{Cross} = 0.8$ and $P_{mut} = 0.1$ are considered. For the parameters of PSO algorithm, three different levels are considered according to Table 6.

For example, with the values of $n = 10$, $m_2 = 2$ and $m_3 = 2$ from the combination of different levels of

TABLE 6. PSO algorithm parameter levels

Factor	Level	Value
PS	1	70
	2	80
	3	90
C_1, C_2	4	0.7
	5	0.8
	6	0.9
ω	1	0.1
	2	0.2
	3	0.3

parameters using the orthogonal matrix according to Table 7, 9 different combinations of parameters are shown.

Each combination has been executed 5 times and the average deviation from the best solution has been calculated using Equation (22). For the PSO algorithm, average and scatter diagrams were drawn for each of the parameters. For PS parameter, as the population increases, the mean value increases. Therefore, the best value of this parameter is at level 1 and equal to PS = 70.

For C_1 and C_2 parameters, as the parameter rate increases, the average value increases. Therefore, the best value of this parameter is at level 1 and equal to $C_1 = C_2 = 0.7$.

For parameter ω , as the mutation rate increases, the average value decreases. Therefore, the best value of this parameter is at level 3 and is equal to $\omega = 0.3$.

Therefore, the values of PS = 70, $C_1 = C_2 = 0.7$ and $\omega = 0.3$ were specified. We have considered the values. Experiments have been carried out for two sizes, small and large, which are shown in the following calculation results.

6. 2. The Results of Small Size Calculations

In order to check the performance of the presented algorithms, the results of calculations in small-sized problems have been compared with the results of GAMS to solve the problem accurately. GAMS calculations have been done with a time limit of 3600 seconds and for other algorithms with a time limit of n seconds. In order to check the performance of GAMS to solve the problem, different sizes have been considered. As the number of jobs increases, the solution time increases and it becomes difficult to find the solution. Therefore, up to 20 jobs have been produced for a small sample size and 44 samples of the combination of different amounts of jobs, second-stage machines and third-stage machines have

TABLE 7. Relative deviation mean values for ANOVA samples for PSO algorithm

Experiment number	Parameters level			Ave
	PS	C_1, C_2	ω	
1	1	1	1	0.0442
2	1	2	2	0.0581
3	1	3	3	0.0514
4	2	1	2	0.0544
5	2	2	3	0.0501
6	2	3	1	0.0789
7	3	1	3	0.0673
8	3	2	1	0.0702
9	3	3	2	0.0807

been created. Each algorithm has been executed 5 times in each sample. In order to compare the results of the algorithms, the deviation from the best solution has been calculated from Equation (25).

The calculation results are shown in Table 8. In this table, the percentage deviation of the CPLEX solution from the best solution of the algorithms is calculated from Equation (25).

$$RD = \frac{CplexObj - bestobj}{bestobj} \quad (25)$$

In the above equation, *CplexObj* is the value of the objective function obtained from solving the model and *bestobj* is the best obtained solution from solving the model and algorithms.

The value of the objective function (obj), the time it takes the model to reach the optimal solution or stop the solution (Time), the minimum (Min), maximum (Max) and average (Ave) values of the relative deviation (ARE) have been calculated. The average values obtained for all samples are shown at the end of Table 8. The average deviation of the total samples for Cplex, GA, HGA, PSO,

HPSO methods is 0.197, 0.055, 0.038, 0.068 and 0.046, respectively. The lowest amount of deviation is related to the HGA algorithm. The obtained results of HGA algorithm are better than Cplex, which indicates the effectiveness of the algorithm. Also, due to the fact that the solution has been reached in less time, the efficiency of the algorithm is also high.

The average solving time is 10 seconds for the algorithms and 3102 seconds for Cplex. In 6 sizes, The model will be able to solve the problem in large dimensions, but according to the specifications of the processor system, with the increase in the problem size, the processor may not be able to process the model. Therefore, due to the inability of the processor to solve the model, an "out of memory" error occurs. the model is not able to reach the optimal solution (NA) and has a memory error, which is shown in the table with Out of Memory (OM). Also, considering the time limit of 3600 seconds, no solution has been received by Cplex. Therefore, it is possible to use algorithms to solve large size problems.

TABLE 8. Comparison of different algorithms with exact solution results in small size

Instance	n	m ₂	m ₃	CPLEX			GA			HGA			PSO			HPSO			Time (s)	
				RD	Obj	Time (s)	Min	Ave	Max											
1	3	2	2	0.000	704	1.7	0.000	0.000	0.000	0.000	0.000	0.000	0.000	0.000	0.000	0.000	0.000	0.000	0.000	3
2	4	2	2	0.000	973	22.5	0.000	0.000	0.000	0.000	0.000	0.000	0.000	0.000	0.000	0.000	0.000	0.000	0.000	4
3	4	3	2	0.000	973	14.8	0.000	0.002	0.011	0.000	0.000	0.000	0.000	0.004	0.018	0.000	0.000	0.000	0.000	4
4	5	2	2	0.000	1087	980	0.000	0.000	0.000	0.000	0.000	0.000	0.000	0.016	0.068	0.000	0.000	0.000	0.000	5
5	5	3	3	0.000	1087	3600	0.000	0.000	0.000	0.000	0.000	0.000	0.000	0.013	0.022	0.000	0.026	0.064	0.064	5
6	5	4	3	0.000	1087	1865	0.000	0.000	0.000	0.000	0.000	0.000	0.000	0.018	0.044	0.000	0.009	0.022	0.022	5
7	6	2	2	0.000	1524	3600	0.000	0.000	0.000	0.000	0.000	0.000	0.000	0.000	0.000	0.000	0.000	0.000	0.000	6
8	6	3	3	0.000	1524	3600	0.000	0.000	0.000	0.000	0.000	0.000	0.000	0.000	0.000	0.000	0.000	0.000	0.000	6
9	6	4	3	0.000	1524	3600	0.000	0.000	0.000	0.000	0.000	0.000	0.000	0.004	0.014	0.000	0.004	0.018	0.018	6
10	6	4	4	0.000	1524	3600	0.000	0.000	0.000	0.000	0.000	0.000	0.000	0.010	0.019	0.000	0.003	0.010	0.010	6.0
11	7	2	2	0.012	1640	3600	0.000	0.023	0.038	0.020	0.024	0.038	0.020	0.024	0.038	0.020	0.072	0.111	0.111	7.0
12	7	3	2	0.000	1635	3600	0.000	0.007	0.036	0.000	0.000	0.000	0.000	0.001	0.006	0.000	0.000	0.000	0.000	7
13	7	3	3	0.000	1621	3600	0.000	0.000	0.000	0.000	0.000	0.000	0.000	0.016	0.082	0.000	0.008	0.022	0.022	7
14	7	4	2	0.003	1640	3600	0.000	0.007	0.024	0.000	0.000	0.000	0.000	0.003	0.007	0.000	0.011	0.047	0.047	7
15	7	4	3	0.000	1621	3600	0.000	0.004	0.013	0.000	0.001	0.006	0.000	0.004	0.018	0.000	0.000	0.000	0.000	7
16	8	2	2	0.058	2202	3600	0.000	0.010	0.020	0.006	0.006	0.008	0.006	0.020	0.042	0.022	0.063	0.096	0.096	8
17	8	3	2	0.002	2052	3600	0.000	0.002	0.006	0.000	0.001	0.003	0.000	0.004	0.022	0.030	0.032	0.041	0.041	8
18	8	4	2	0.014	2052	3600	0.006	0.012	0.031	0.008	0.008	0.008	0.000	0.013	0.061	0.000	0.010	0.029	0.029	8.0
19	8	4	4	0.002	2009	3600	0.000	0.002	0.002	0.000	0.001	0.002	0.002	0.011	0.041	0.002	0.015	0.068	0.068	8
20	9	2	2	0.043	2770	3600	0.019	0.066	0.087	0.000	0.034	0.075	0.015	0.038	0.061	0.009	0.083	0.131	0.131	9

21	9	3	2	0.021	2679	3600	0.005	0.016	0.029	0.000	0.020	0.051	0.006	0.039	0.099	0.032	0.053	0.080	9
22	9	3	3	0.000	2613	3600	0.000	0.016	0.030	0.000	0.024	0.050	0.004	0.032	0.064	0.033	0.037	0.051	9
23	9	4	2	0.019	2644	3600	0.000	0.009	0.025	0.002	0.020	0.046	0.040	0.057	0.078	0.000	0.028	0.069	9
24	9	4	3	0.000	2581 (OM)	2608	0.006	0.025	0.046	0.002	0.028	0.060	0.039	0.061	0.081	0.000	0.021	0.064	9
25	9	4	4	0.047	2581	3600	0.049	0.051	0.053	0.050	0.073	0.096	0.000	0.072	0.125	0.047	0.077	0.097	9
26	10	2	2	0.002	2947	3600	0.000	0.029	0.057	0.029	0.065	0.101	0.005	0.058	0.168	0.038	0.074	0.117	10
27	10	2	3	0.000	2836	3600	0.012	0.039	0.067	0.000	0.024	0.038	0.029	0.057	0.109	0.027	0.068	0.122	10
28	10	2	4	0.000	2730	3600	0.032	0.061	0.101	0.017	0.041	0.086	0.000	0.022	0.039	0.000	0.050	0.121	10
29	10	3	2	0.086	2990 (OM)	773	0.035	0.075	0.094	0.000	0.027	0.073	0.058	0.069	0.084	0.010	0.045	0.089	10
30	10	3	3	0.032	2863 (OM)	2633	0.004	0.017	0.044	0.005	0.023	0.044	0.000	0.034	0.108	0.005	0.023	0.037	10
31	10	4	4	0.025	2764	3600	0.001	0.028	0.066	0.018	0.036	0.053	0.003	0.020	0.035	0.000	0.018	0.083	10
32	15	2	2	0.231	7650	3600	0.195	0.274	0.360	0.178	0.202	0.237	0.100	0.301	0.518	0.000	0.040	0.105	15
33	15	2	3	0.208	7640	3600	0.144	0.195	0.256	0.059	0.142	0.202	0.095	0.203	0.291	0.000	0.048	0.087	15
34	15	3	2	-0.097	5920	3600	0.058	0.150	0.235	0.000	0.041	0.087	0.114	0.252	0.345	0.128	0.154	0.180	15
35	15	3	3	0.292	7589	3600	0.065	0.103	0.185	0.077	0.120	0.167	0.082	0.139	0.216	0.000	0.029	0.075	15
36	15	4	2	0.058	6184 (OM)	1603	0.029	0.055	0.080	0.055	0.059	0.070	0.069	0.116	0.186	0.000	0.027	0.069	15
37	15	4	3	0.100	6247	3600	0.016	0.056	0.114	0.000	0.020	0.054	0.040	0.125	0.211	0.025	0.079	0.210	15
38	15	4	4	0.138	6343	3600	0.045	0.083	0.123	0.029	0.048	0.066	0.000	0.093	0.162	0.003	0.036	0.074	15
39	20	2	2	0.813	20359	3600	0.257	0.345	0.473	0.030	0.065	0.111	0.120	0.180	0.269	0.000	0.072	0.240	20
40	20	3	2	0.806	19893	3600	0.020	0.066	0.122	0.060	0.133	0.175	0.069	0.128	0.246	0.000	0.163	0.265	20
41	20	3	3	NA	NA	3600	0.099	0.198	0.426	0.000	0.111	0.210	0.007	0.165	0.331	0.090	0.190	0.315	20
42	20	3	4	0.696	17735	3600	0.072	0.191	0.370	0.000	0.071	0.096	0.174	0.265	0.341	0.030	0.196	0.318	20
43	20	4	3	2.579	34663 (OM)	3600	0.059	0.095	0.140	0.000	0.112	0.180	0.058	0.151	0.250	0.035	0.110	0.182	20
44	20	4	4	2.180	30558 (OM)	3600	0.001	0.112	0.201	0.000	0.072	0.166	0.056	0.150	0.227	0.034	0.069	0.104	20
Average				0.197	-	3,102	0.028	0.055	0.090	0.015	0.038	0.060	0.028	0.068	0.117	0.014	0.046	0.087	10

6. 3. Large Size Calculation Results After checking the performance of the presented algorithms in small sizes, the calculation results of large sizes are presented in Table 9. As the size of the problem increases, the number of iterations of the algorithm decreases. Due to the time limit considered in order to solve the problems in large size, the number of jobs is considered up to 100 and calculations have been done in

35 different samples. Each sample has been run 5 times and the deviation from the best solution has been obtained. The average deviation of all samples for GA, HGA, PSO, HPSO methods is 0.277, 0.0677, 0.038, 0.2665 and 0.1215, respectively. The lowest amount of deviation is related to the algorithm, which is equal to 0.038.

TABLE 9. Comparison of different algorithms in order to solve the problem in large size

Instance	n	m ₂	m ₃	GA			HGA			PSO			HPSO		
				Min	Ave	Max									
1	25	2	2	0.0524	0.1427	0.2157	0.0000	0.0200	0.0355	0.0869	0.2189	0.3889	0.0110	0.0308	0.0550
2	25	2	4	0.0270	0.2539	0.5199	0.0026	0.0139	0.0423	0.0737	0.1411	0.3046	0.0000	0.0211	0.0287

3	25	4	2	0.0577	0.0899	0.1636	0.0112	0.0802	0.1893	0.0000	0.0598	0.1386	0.0192	0.1191	0.2138
4	25	4	4	0.0080	0.0864	0.1340	0.0000	0.1121	0.1891	0.0377	0.1124	0.2088	0.1479	0.1878	0.2407
5	35	2	2	0.3270	0.4234	0.5283	0.0000	0.0061	0.0225	0.2675	0.3449	0.4579	0.0000	0.2392	0.4796
6	35	2	4	0.3637	0.4388	0.5376	0.0552	0.0894	0.1409	0.2104	0.3699	0.5489	0.0000	0.0669	0.1409
7	35	4	2	0.0113	0.1861	0.2962	0.0024	0.0158	0.0372	0.1346	0.2703	0.3474	0.0000	0.0423	0.1063
8	35	4	4	0.0000	0.0522	0.1727	0.0241	0.0464	0.0594	0.0607	0.1244	0.2546	0.0210	0.0411	0.0683
9	45	2	2	0.4757	0.5287	0.5635	0.0133	0.0637	0.1141	0.4651	0.5218	0.6352	0.0000	0.0363	0.0952
10	45	4	2	0.2182	0.3000	0.3854	0.0000	0.0077	0.0264	0.2451	0.3012	0.3345	0.0047	0.1090	0.4196
11	45	4	4	0.4019	0.4333	0.4705	0.0000	0.0565	0.1257	0.3786	0.4204	0.4692	0.0364	0.1440	0.3757
12	45	6	2	0.1678	0.2074	0.2628	0.1164	0.1592	0.2039	0.1731	0.2040	0.2630	0.0000	0.1375	0.3407
13	45	6	4	0.1290	0.1542	0.1753	0.0000	0.0855	0.1801	0.0761	0.1464	0.1969	0.0036	0.1019	0.2176
14	65	2	2	0.4325	0.4463	0.4562	0.0000	0.0537	0.1148	0.4165	0.4385	0.4671	0.0440	0.3425	0.5060
15	65	4	2	0.2484	0.2664	0.2906	0.0000	0.0794	0.1481	0.2354	0.2707	0.3129	0.0233	0.1169	0.2810
16	65	4	4	0.5721	0.6049	0.6542	0.1055	0.2954	0.5532	0.2455	0.3966	0.6357	0.0000	0.2648	0.7134
17	65	6	2	0.1170	0.1666	0.1867	0.0089	0.0768	0.1139	0.1544	0.1915	0.2073	0.0000	0.0665	0.1861
18	65	8	6	0.1235	0.1462	0.1645	0.0253	0.0527	0.0845	0.1129	0.1621	0.1883	0.0000	0.0299	0.0532
19	75	2	2	0.3290	0.3689	0.3948	0.0000	0.1270	0.3680	0.3286	0.3700	0.4136	0.0021	0.0945	0.2987
20	75	4	2	0.2997	0.3818	0.4140	0.0026	0.0099	0.0201	0.3320	0.3707	0.4107	0.0000	0.1063	0.3513
21	75	4	4	0.3660	0.3847	0.3945	0.0000	0.0330	0.0879	0.3784	0.4187	0.4559	0.0136	0.1894	0.3098
22	75	6	2	0.2486	0.2647	0.2912	0.0539	0.1616	0.2738	0.2747	0.3073	0.3295	0.0000	0.1211	0.2883
23	75	6	6	0.3339	0.3519	0.3781	0.0824	0.1370	0.2038	0.3324	0.3621	0.3819	0.0000	0.2007	0.3475
24	85	2	4	0.3293	0.3877	0.4161	0.0000	0.0152	0.0272	0.4087	0.4357	0.4789	0.0122	0.1263	0.4459
25	85	4	2	0.2292	0.2549	0.2933	0.0000	0.0646	0.2304	0.2511	0.2739	0.2906	0.0282	0.1399	0.3079
26	85	6	4	0.1963	0.2062	0.2139	0.0000	0.0134	0.0410	0.1984	0.2150	0.2310	0.0033	0.0435	0.1953
27	85	8	4	0.1361	0.1477	0.1586	0.0000	0.0648	0.1677	0.1485	0.1743	0.1888	0.0016	0.1075	0.1867
28	95	2	4	0.3610	0.4201	0.4715	0.0000	0.0204	0.0689	0.2069	0.2224	0.2359	0.0245	0.2009	0.4296
29	95	4	2	0.2363	0.2448	0.2646	0.0272	0.0807	0.1544	0.2349	0.2665	0.2987	0.0000	0.0937	0.2724
30	95	6	4	0.1181	0.1312	0.1452	0.0325	0.0568	0.0929	0.1130	0.1411	0.1569	0.0000	0.0717	0.1525
31	95	8	4	0.0913	0.1039	0.1134	0.0700	0.0953	0.1253	0.1051	0.1145	0.1271	0.0000	0.0708	0.1284
32	100	2	4	0.4646	0.4891	0.5038	0.0000	0.0544	0.2084	0.2599	0.2861	0.2937	0.0090	0.2009	0.5093
33	100	4	2	0.2648	0.2804	0.3009	0.0000	0.0115	0.0179	0.2906	0.2999	0.3242	0.0394	0.1539	0.3056
34	100	6	4	0.2264	0.2361	0.2519	0.0413	0.0803	0.1087	0.2510	0.2616	0.2754	0.0000	0.1435	0.2736
35	100	8	4	0.0988	0.1136	0.1232	0.0000	0.0276	0.0753	0.0830	0.1137	0.1395	0.0386	0.0901	0.1345
Average				0.2304	0.2770	0.3230	0.0193	0.0677	0.1329	0.2163	0.2665	0.3255	0.0138	0.1215	0.2703

6. 4. Sensitivity Analysis In order to analyze and investigate the effect of each of the parameters of the problem, in this section, the comparative diagrams of the algorithms are presented. According to Figure 6, deviation values for 4 algorithms are shown. The average values of all samples corresponding to the minimum, average and maximum for all algorithms have been calculated.

As can be seen, the HGA algorithm has the lowest values for Ave and Max and it has the best performance compared to other algorithms.

According to Figure 7, the average values of deviations have been calculated and plotted for different standards of work.

By increasing of jobs number, the amount of deviation increases on average, and the slope of the graph

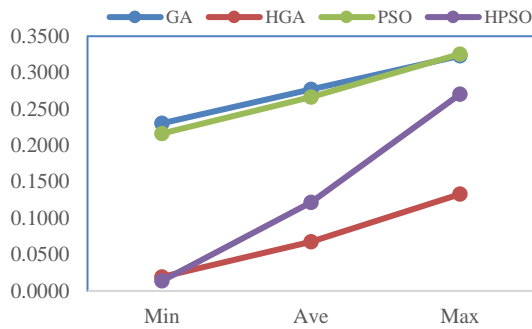


Figure 6. Comparison of mean of Min, Ave and Max deviation values from the best solution of different algorithms

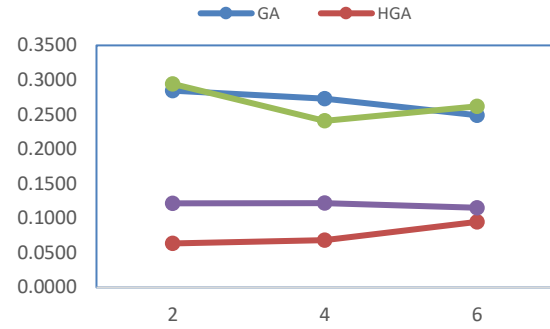


Figure 9. Comparison of the mean values of the average deviation of the machines number in the third stage.

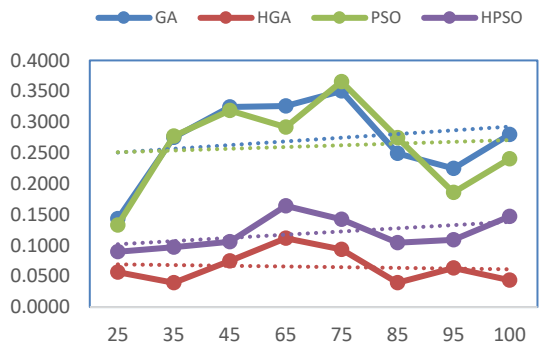


Figure 7. Comparison of the average values of the average deviation based on the number of jobs

is upward for all algorithms. For the HGA algorithm, the slope of the graph is less. Therefore, it performs better than other algorithms.

According to Figures 8 and 9, the average values of deviation for different values of the machines in the second and third stages have been calculated and plotted.

An increase in the number of machines in the second stage, the amount of deviation decreases for all

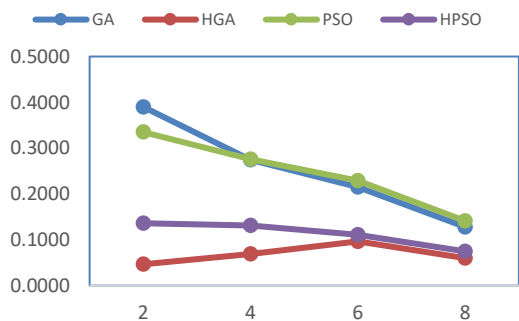


Figure 8. Comparison of the mean values of the average deviation of the machines number in the second stage

algorithms. Therefore, the more the number of machines increases, the better, but the number of machines should be increased according to the available capital. The values related to the HGA algorithm are lower than the another algorithms.

According to learning-based algorithm [36], the Adaptive Polyploid Memetic Algorithm (APMA) [37, 38] alternative method of solutions were presented. Finally, the universal island-based metaheuristic algorithm (UIMA) [39], the nature-inspired evolutionary algorithm [40], the discrete gravitational search algorithm [41], multi-objective scheduling were discussed and compared.

7. CONCLUSION

Equipment overhaul is a fundamental issue in improving the performance of any system. In this article, we investigated the equipment overhaul by a three-stage flow shop system. The works done and the articles presented in this field were reviewed.

A number of equipments are available for repairs and overhaul. A new mathematical model was presented. The planning and scheduling of the overhaul of this equipment in a flow shop system with parallel machines in the second and third stages should be done in such a way that the total time of the equipment overhaul is minimized. In order to schedule, for small sizes with few equipment, a new mathematical model is presented. Considering that the problem is NP-hard, it is not possible to solve it in large dimensions by the model. Therefore, approximate methods are provided to solve the problem in large size. Genetic algorithms (GA) and Particle Swarm Optimization (PSO) were used for this purpose. These algorithms were improved using local search. In the small size, the results were compared with the Cplex method, and the efficiency and effectiveness of the presented algorithms were determined. Then the problem was solved in large sizes. According to the obtained results, the improved genetic algorithm has

better results than other algorithms and is the best algorithm that can be used for the relevant problem.

Some cases can be mentioned as future suggestions:

1. Using other functions such as earliness and tardiness
2. Other solution methods can be used and the results can be compared.
3. Parallel machines can also be considered for the first stage.

8. REFERENCES

1. Luh, P.B., Yu, D., Soorapanth, S., Khibnik, A.I. and Rajamani, R., "A lagrangian relaxation based approach to schedule asset overhaul and repair services", *IEEE Transactions on Automation Science and Engineering*, Vol. 2, No. 2, (2005), 145-157. <https://doi.org/10.1109/TASE.2005.844221>
2. Liu, P., Zhang, X., Shi, Z. and Huang, Z., "Simulation optimization for mro systems operations", *Asia-Pacific Journal of Operational Research*, Vol. 34, No. 02, (2017), 1750003. <https://doi.org/10.1142/S0217595917500038>
3. Reményi, C. and Staudacher, S., "Systematic simulation based approach for the identification and implementation of a scheduling rule in the aircraft engine maintenance", *International Journal of Production Economics*, Vol. 147, (2014), 94-107. <https://doi.org/10.1016/j.ijpe.2012.10.022>
4. Qin, Y., Wang, Z., Chan, F.T., Chung, S. and Qu, T., "A mathematical model and algorithms for the aircraft hangar maintenance scheduling problem", *Applied Mathematical Modelling*, Vol. 67, (2019), 491-509. <https://doi.org/10.1016/j.apm.2018.11.008>
5. Pinhão, J.d.M.O.B., Ignacio, A.A.V. and Coelho, O., "An integer programming mathematical model with line balancing and scheduling for standard work optimization: A realistic application to aircraft engines assembly lines", *Computers & Industrial Engineering*, Vol. 173, (2022), 108652. <https://doi.org/10.1016/j.cie.2022.108652>
6. Dinis, D., Barbosa-Póvoa, A. and Teixeira, Â.P., "A supporting framework for maintenance capacity planning and scheduling: Development and application in the aircraft mro industry", *International Journal of Production Economics*, Vol. 218, (2019), 1-15. <https://doi.org/10.1016/j.ijpe.2019.04.029>
7. Sharma, G. and Rai, R.N., "Reliability parameter estimation of repairable systems with imperfect maintenance, repair and overhaul", *International Journal of Quality & Reliability Management*, Vol. 38, No. 4, (2021), 892-907. <https://doi.org/10.1108/IJQRM-05-2019-0139>
8. Huang, Z., Ding, J., Song, J., Shi, L. and Chen, C.-H., "Simulation optimization for the mro scheduling problem based on multi-fidelity models", in 2016 IEEE International Conference on Industrial Technology (ICIT), IEEE. (2016), 1556-1561.
9. Mayto, M.W., Suryadhini, P.P. and Astuti, M.D., "Job shop scheduling at in-house repair department in cold section module ct7 engine to minimize makespan using genetic algorithm at pt xyz".
10. Chang, H.-M. and Abdullah, K., "The operation management model of aircraft maintenance, repair and overhaul (mro) business", *International Journal of Trends in Economics Management & Technology (IJTEMT)*, Vol. 3, No. 3, (2014), 21-28.
11. Li, H., Mi, S., Li, Q., Wen, X., Qiao, D. and Luo, G., "A scheduling optimization method for maintenance, repair and operations service resources of complex products", *Journal of Intelligent Manufacturing*, Vol. 31, (2020), 1673-1691. <https://doi.org/10.1007/s10845-018-1400-4>
12. Tran, L.V., Huynh, B.H. and Akhtar, H., "Ant colony optimization algorithm for maintenance, repair and overhaul scheduling optimization in the context of industrie 4.0", *Applied Sciences*, Vol. 9, No. 22, (2019), 4815. <https://doi.org/10.3390/app9224815>
13. Yuan, G., Yang, Y., Tian, G. and Fathollahi-Fard, A.M., "Capacitated multi-objective disassembly scheduling with fuzzy processing time via a fruit fly optimization algorithm", *Environmental Science and Pollution Research*, (2022), 1-18. <https://doi.org/10.1007/s11356-022-18883-y>
14. Guo, Y., Cao, J., Chen, C. and Zhang, C., "Research on task scheduling of emergency repair team in wartime based on improved genetic algorithm", in 6th International Technical Conference on Advances in Computing, Control and Industrial Engineering (CCIE 2021), Springer. (2022), 897-906.
15. Rahman, A., Kuswoyo, A., Prabowo, A.R. and Suharyo, O.S., "Developing strategy of maintenance, repair and overhaul of warships in support of navy operations readiness", *JOURNAL ASRO*, Vol. 11, No. 2, (2020), 146-151. <https://doi.org/10.37875/asro.v11i2.277>
16. Fathollahi-Fard, A.M., Woodward, L. and Akhrif, O., "Sustainable distributed permutation flow-shop scheduling model based on a triple bottom line concept", *Journal of Industrial Information Integration*, Vol. 24, (2021), 100233. <https://doi.org/10.1016/j.jii.2021.100233>
17. Gholizadeh, H., Fazlollahi-Fard, H., Fathollahi-Fard, A.M. and Dulebenets, M.A., "Preventive maintenance for the flexible flowshop scheduling under uncertainty: A waste-to-energy system", *Environmental Science and Pollution Research*, (2021), 1-20. <https://doi.org/10.1007/s11356-021-16234-x>
18. Amirian, H. and Sahraeian, R., "Multi-objective differential evolution for the flow shop scheduling problem with a modified learning effect", *International Journal of Engineering Transactions B: Applications*, Vol. 27, No. 9, (2014). doi: 10.5829/idosi.ije.2014.27.09c.09.
19. Amin Naseri, M., Tasouji Hassanpour, S. and Nahavandi, N., "Solving re-entrant no-wait flow shop scheduling problem", *International Journal of Engineering*, Vol. 28, No. 6, (2015), 903-912. https://www.ije.ir/article_72531.html
20. Branda, A., Castellano, D., Guizzi, G. and Popolo, V., "Metaheuristics for the flow shop scheduling problem with maintenance activities integrated", *Computers & Industrial Engineering*, Vol. 151, (2021), 106989. <https://doi.org/10.1016/j.jii.2021.100233>
21. Chen, B., "Analysis of classes of heuristics for scheduling a two-stage flow shop with parallel machines at one stage", *Journal of the Operational Research Society*, Vol. 46, No. 2, (1995), 234-244. <https://doi.org/10.1057/jors.1995.28>
22. Holland, J.H., "Adaptation in natural and artificial systems: An introductory analysis with applications to biology, control, and artificial intelligence, MIT press. (1992).
23. Yazdani, M., Kabirifar, K., Fathollahi-Fard, A.M. and Mojtahedi, M., "Production scheduling of off-site prefabricated construction components considering sequence dependent due dates", *Environmental Science and Pollution Research*, Vol., No., (2021), 1-17. <https://doi.org/10.1007/s11356-021-16285-0>
24. Tavakkoli-Moghaddam, R., "A hybrid genetic algorithm for a bi-objective scheduling problem in a flexible manufacturing cell", *International Journal of Engineering, Transactions A: Basics*, Vol. 23, No. 3, (2010), 235-252. https://www.ije.ir/article_71865_bd75ddfdb3cf9f40fb09539fc3513250.pdf
25. Ghafari, E., "Appling metaheuristic algorithms on a two stage hybrid flowshop scheduling problem with serial batching

- (research note)", *International Journal of Engineering, Transactions C: Aspects*, Vol. 27, No. 6, (2014), 899-910. doi: 10.5829/idosi.ije.2014.27.06c.08.
26. Baker, K.R. and Trietsch, D., "Principles of sequencing and scheduling, a John Wiley & Sons", *Inc. Publication*, (2009). <https://doi.org/10.1016/j.jii.2021.100233>
 27. Etiler, O., Toklu, B., Atak, M. and Wilson, J., "A genetic algorithm for flow shop scheduling problems", *Journal of the Operational Research Society*, Vol. 55, (2004), 830-835. <https://doi.org/10.1057/palgrave.jors.2601766>
 28. Hussain, A., Muhammad, Y.S., Nauman Sajid, M., Hussain, I., Mohamd Shoukry, A. and Gani, S., "Genetic algorithm for traveling salesman problem with modified cycle crossover operator", *Computational Intelligence and Neuroscience*, Vol. 2017, (2017). <https://doi.org/10.1155/2017/7430125>
 29. Kennedy, J. and Eberhart, R., "Particle swarm optimization", in Proceedings of ICNN'95-international conference on neural networks, IEEE. Vol. 4, (1995), 1942-1948.
 30. Daliri, H., Mokhtari, H. and Nakhai, I., "A particle swarm optimization approach to joint location and scheduling decisions in a flexible job shop environment", *International Journal of Engineering, Transactions C: Aspects*, Vol. 28, No. 12, (2015), 1756-1764. doi: 10.5829/idosi.ije.2015.28.12c.08.
 31. Rabbani, M., Oladzad-Abbasabady, N. and Akbarian-Saravi, N., "Ambulance routing in disaster response considering variable patient condition: Nsga-ii and mopso algorithms", *Journal of Industrial and Management Optimization*, Vol. 18, No. 2, (2022), 1035-1062. <https://doi.org/10.3934/jimo.2021007>
 32. Pan, Q.-K., Tasgetiren, M.F. and Liang, Y.-C., "A discrete particle swarm optimization algorithm for the no-wait flowshop scheduling problem", *Computers & Operations Research*, Vol. 35, No. 9, (2008), 2807-2839.
 33. Deng, J., Wang, L., Wang, S.-y. and Zheng, X.-l., "A competitive memetic algorithm for the distributed two-stage assembly flowshop scheduling problem", *International Journal of Production Research*, Vol. 54, No. 12, (2016), 3561-3577. <https://doi.org/10.1080/00207543.2015.1084063>
 34. Xiong, F., Xing, K. and Wang, F., "Scheduling a hybrid assembly-differentiation flowshop to minimize total flow time", *European Journal of Operational Research*, Vol. 240, No. 2, (2015), 338-354. <https://doi.org/10.1016/j.ejor.2014.07.004>
 35. Jolai, F., Asefi, H., Rabiee, M. and Ramezani, P., "Bi-objective simulated annealing approaches for no-wait two-stage flexible flow shop scheduling problem", *Scientia Iranica*, Vol. 20, No. 3, (2013), 861-872. <https://doi.org/10.1016/j.scient.2012.10.044>
 36. Zhao, H. and Zhang, C., "An online-learning-based evolutionary many-objective algorithm", *Information Sciences*, Vol. 509, (2020), 1-21. <https://doi.org/10.1016/j.ins.2019.08.069>
 37. Dulebenets, M.A., "An adaptive polyploid memetic algorithm for scheduling trucks at a cross-docking terminal", *Information Sciences*, Vol. 565, (2021), 390-421. <https://doi.org/10.1016/j.ins.2021.02.039>
 38. Dulebenets, M.A., "A novel memetic algorithm with a deterministic parameter control for efficient berth scheduling at marine container terminals", *Maritime Business Review*, (2017). <https://doi.org/10.1108/MABR-04-2017-0012>
 39. Kavooosi, M., Dulebenets, M.A., Abioye, O., Pasha, J., Theophilus, O., Wang, H., Kampmann, R. and Mikijeljević, M., "Berth scheduling at marine container terminals: A universal island-based metaheuristic approach", *Maritime Business Review*, Vol. 5, No. 1, (2019), 30-66. <https://doi.org/10.1108/MABR-08-2019-0032>
 40. Pasha, J., Nwodu, A.L., Fathollahi-Fard, A.M., Tian, G., Li, Z., Wang, H. and Dulebenets, M.A., "Exact and metaheuristic algorithms for the vehicle routing problem with a factory-in-a-box in multi-objective settings", *Advanced Engineering Informatics*, Vol. 52, (2022), 101623. <https://doi.org/10.1016/j.aei.2022.101623>
 41. Tian, G., Fathollahi-Fard, A.M., Ren, Y., Li, Z. and Jiang, X., "Multi-objective scheduling of priority-based rescue vehicles to extinguish forest fires using a multi-objective discrete gravitational search algorithm", *Information Sciences*, Vol. 608, (2022), 578-596. <https://doi.org/10.1016/j.ins.2022.06.052>

Persian Abstract

چکیده

در این مقاله، تعمیرات اساسی تجهیزات در یک مسئله زمان‌بندی جریان کارگاهی چند مرحله‌ای در نظر گرفته شده است. در این مسئله در مرحله اول تجهیزات دمونتاژ شده و در مرحله دوم توسط کارگاه‌های موازی تعمیرات اساسی روی تجهیزات انجام می‌شود و در مرحله سوم عملیات مونتاژ در کارگاه‌های موازی صورت می‌گیرد. در نظر گرفتن اورهال سه مرحله‌ای با ماشین‌های موازی در مراحل دوم و سوم در صنعت اورهال جدید است. توالی پردازش تجهیزات در مرحله اول تعیین می‌شود و همچنین تخصیص و توالی تجهیزات در مرحله دوم و سوم باید به گونه‌ای انجام شود که کل زمان اتمام کارها به حداقل برسد. برخلاف اغلب مقالات توالی پردازش کارها در تمام مراحل یکسان نیست و با استفاده از رمزگشایی تغییر می‌کند. برای نوآوری بعدی: به منظور حل مسئله، یک مدل ریاضی جدید ارائه شده است. دو الگوریتم بهبودیافته جدید به منظور حل مسئله در ابعاد بزرگ ارائه شده است. با توجه به اینکه مسئله NP-hard است و حل مسئله در ابعاد بزرگ توسط مدل زمان بر است، دو الگوریتم فراابتکاری الگوریتم ژنتیک و بهینه‌سازی ازدحام ذرات همراه با بهبودهای لازم برای حل ابعاد بزرگ ارائه شده است. با استفاده از روش ابتکاری کوتاه‌ترین زمان پردازش (SPT)، این دو الگوریتم بهبود یافته و الگوریتم‌های ژنتیک ترکیبی و بهینه‌سازی ازدحام ذرات ترکیبی ارائه شده‌اند. به منظور دستیابی به نتایج بهتر با شرایط فعلی تنظیم پارامترها توسط آنالیز واریانس یک طرفه (ANOVA) انجام شده است. نهایتاً بهبود عملکرد تجهیزات با بکارگیری مسئله ارائه شده میسر می‌گردد.



A Novel Hybrid Model for Technology Strategy Formulating in High-tech Industries under Uncertainty: A Case Study

N. Kazemifard^a, L. Bashir^{a,b}, D. Rahmani^{*c}

^a Technical Affairs and Network Development Department, Mobile Telecommunication Company of Iran, Tehran, Iran

^b Department of Management, University of Tehran, Tehran, Iran

^c Department of Industrial Engineering, K. N. Toosi University of Technology, Tehran, Iran

PAPER INFO

Paper history:

Received 16 January 2023

Received in revised form 28 March 2023

Accepted 01 April 2023

Keywords:

Technology Strategy

Attractiveness-capability Matrix

Fuzzy TOPSIS

Uncertainty

ABSTRACT

Globalization and increased virtual communication have posed many challenges to high-tech companies; hence, such companies are sparing efforts to detect the best technologies in this field to solve new and emerging challenges addressing traffic load, communication system security, and infrastructure optimization. Telecommunications companies deal with a highly dynamic and uncertain environment, where their relevant technologies are changing and developing at an increasing speed. Regarding such an environment in telecommunications companies, the present study aimed to present an efficient model for formulating technology strategies for these companies. The proposed model is a hybrid method of attractiveness-capability matrix and, multi-criteria decision-making approaches in an uncertain and dynamic environment. The model provides the attractiveness-capability evaluation factors and criteria regarding the requirements of dynamic and uncertain environments in these companies. This approach provides a more accurate picture of the rapidly changing technologies in formulating technology strategy. The model also used the fuzzy TOPSIS to control the uncertainty aroused by widespread emerging technologies in such organizations. The proposed model is implemented concerning the requirements of the Mobile Communications Company of Iran (MCI), and its results are discussed in detail.

doi: 10.5829/ije.2023.36.06c.15

1. INTRODUCTION

Nowadays, enhanced traffic load, exacerbated by the COVID-19 pandemic, has imposed much more pressure on public, cloud infrastructures, edges and access points serving residential areas. As such traffic load is also incurred on the edges and access points of service provider networks, some innovative solutions are mandatory to match bandwidth and traffic control demands. New technologies and digital ecosystems' multi-layered structure, encompassing network, software, and services, determine how new values are defined, thereby setting the grounds for communication service providers to offer practical and novel solutions [1].

Managers of large and high-tech industries are constantly faced with the question of which decisions

should be selected and which should be left to company-level managers. Technology planning is one of those cases that its process of making decisions and the degree of attention is unclear, especially at the level of a large-scale industry [2]. These reasons have caused it essential and, so difficult to attain challenging technologies.

Accordingly, telecommunications companies are sparing efforts to detect the best technologies in this field and develop Technology Strategy Formulating (TSF) models to solve new and emerging challenges addressing traffic load, communication system security, and infrastructure optimization. In this regard, technology development and acquisition projects are the main components affecting enterprises' modernization, sustainability, and competitiveness [3]. In a similar vein, the technology portfolio is introduced to determine decisions about technology combination and Technology Strategy (TS), achieve investment goals,

*Corresponding Author Email: drahmani@knru.ac.ir (D. Rahmani)

and establish a balance between risk/performance and asset allocation. Framing TS mainly aims to limit some technologies balancing risks, benefits and matching with organizational strategies.

This paper is outlined as follows: Section 2 considers the related literature. Section 3 presents a framework based on the attractiveness- competitiveness evaluation matrix. In section 4, the proposed TSF model is described, and section 5 analyses the proposed methodology using the fuzzy TOPSIS for MCI. The last section contains the results and suggestions for future research.

2. LITERATURE REVIEW

In this section, the relevant literature is reviewed in separate parts, as follows:

2. 1. Technology Strategy Formulation Models

Researchers have proposed many approaches and models to TSF, the most appropriate of which is compatible with the industry's features and flexible in the face of changes. A literature review revealed two main approaches to TSF [4] in the past years. The first approach is concerned with organizations or companies' position includes Poret's model, Hax and Mahluf's model and Little's model. The second one is a resource-oriented approach regarding key organizational capabilities and includes Kieza, Prahalad, and Hamel's Core Competency model and D'Oney's Super Competition model, and others [5]. Little's model deals with the market and its determinants and focuses on competition and success in the market. In this model, technologies associated with critical determinants should be specified to formulate TSs to detect future investments by recognizing the company's technology-related priorities. Poret's model considers decisive attitudes toward technology development and exploitation as a critical factor in promoting competitiveness. According to Poret's model, there are six steps to formulate TS. Hax and Mahluf developed their model based on Poret's conceptual TSF model. In their proposed model, the key inputs of the TSF process are considered the organization's macro strategies. According to this model, the strategy of the selected technologies is formulated when the attractiveness of the selected technologies affecting TSF is determined, and the organization's capabilities regarding the concerned technologies are assessed. Arasti et al. [6] presented an integrated TSF model using the positioning approach. Ebrahimi et al. [7] presented a new TSF model for Iran's petrochemical industry. Nezhad et al. [5] also proposed a seven-stage TSF model underpinned by Hax and Mahluf's and Little's model using the positioning approach for the Auto Parts Manufacturing

Industry. Alvarado et al. [8] developed a comprehensive and economic Technology Selection and Operation (TSO) model, which allowed decision makers to optimally select technology from the existing options and simultaneously optimize technology selection and usage. Mohammadzadeh et al. [9] used attractiveness-capability matrix of Technology to strategic technologies selection for oil production.

Besides the aforementioned classical models in the literature, some quantitative technology portfolio selection (TPS) methods have also been proposed to the model selection. Heidenberger and Stummer [4] classified quantitative TPS methods into six categories. Schuh et al. [10] tried to conceptualizing a turbulence-induced initiation phase for technology strategy development. Ghazinoory et al. [2] presented cascade roadmaps as a tool for technology strategy formulation in Oil Industry .

2. 2. Technology Portfolio under Uncertainty and Conflict Criteria

Evidently, in line with developing a technology portfolio, the selected technologies need to be evaluated using different criteria; however, their evaluation is challenging. As some of emerging technologies are new and vague for decision makers to evaluate, it seems that applying techniques based on the uncertainty and ambiguity of the input information is essential. Such techniques greatly reduce the evaluation error and increase the validity of the results rather than using traditional qualitative methods. In the evaluation of recognized technologies, experts often should provide assessments based on intangible and conflicting criteria. For example, in analyzing the strategic nature of new technology, it is possible to be better in some criteria and be weaker in others, and the analysis of such a contrast in the traditional approaches caused a higher averaging error. The conflict between various criteria is managed using Multi-Criteria Decision Making (MCDM) methods to address such issues.

Shen et al. [11] adopted an MCDM approach developing a technology selection model regarding organizations' economic and industrial perspectives. Since the preferences of experts regarding these criteria are frequently descriptive and qualitative rather than quantitative; therefore, such issues frequently lead to mental uncertainty especially because these technologies are essentially new and have a lot of uncertainties for the expert. Fuzzy set theory is one of the most effective methods for addressing the uncertainty caused by the complexity of the features of options and the decision-making behaviour of experts. In this project, the high uncertainty of technology analysis and the inherent conflict between criteria are managed using a fuzzy multi-criteria decision-making approach. Fuzzy TOPSIS technique is one of the

famous and reliable methods of fuzzy multi-criteria decision-making, which is used in this project to rank options under uncertainty.

Moazenzadeh and Hamidi [12] developed a model for mobile banking; they proposed the TOPSIS (Technique for Order Preference by Similarities to Ideal Solution) method, the underlying concept of which is that the selected alternative should have the smallest and the largest distance from the positive and negative ideal solutions, respectively. A positive ideal solution maximizes profit and minimizes cost; however, a negative ideal solution maximizes cost and minimizes profit [12]. In the classic TOPSIS method, the weights of the criteria and the ratings of the alternatives are precisely specified. This is, while exact data are insufficient to model real decision-making problems in some other cases. Accordingly, the fuzzy TOPSIS method is proposed where the weights of criteria and the ratings of alternatives are evaluated by linguistic variables represented by fuzzy numbers to deal with the deficiency in the traditional TOPSIS [13, 14].

Cil et al. [15] proposed an integrated evaluation model using fuzzy AHP and fuzzy TOPSIS to select the positioning technology offering advanced services in the SEDEF shipyard. Aliakbari et al. [16] also developed a hybrid model using Fuzzy TOPSIS to evaluate and rate technologies appropriately in a company.

2. 3. Research Gap and Novelty There has been an increase in environmental dynamism and uncertainty in technology-oriented companies over the past years. A TS mandates maintaining and expanding sustainable competitive advantage by establishing technological capabilities. However, the established methods for this purpose are highly time-consuming and rarely adapt to the situation because of their discrete sequential approach combined with extensive analyses [17]. Organizations have been increasingly experiencing volatility, uncertainty, complexity, and ambiguity in their environment, which were posed by various factors, including globalization, digitalization, and industry convergence [18]. Telecommunications industry organizations operate in highly dynamic and uncertain environments, and technologies associated with their operations (e.g., Emerging Technologies (ETs)) are remarkably changing and developing for such organizations worldwide. Valinejad et al. [19] developed a hybrid model for telecommunication industry to assess the supply chain risk management based on five-dimensional sustainability approach.

ETs have become one of the main fields of global competition, and their complicated features challenge managers to formulate TSs encompassing both systematic theories and methods. According to Zhao et al. [20], the core content of ETs is technology selection and formulation. Accordingly, TSF is more complicated

in telecommunications organizations; hence, more precise approaches are required to develop their TSF model and determine benchmarks and technology evaluation techniques.

A review of the literature reveals no efficient TSF model compatible with the dynamic and uncertain environment of such companies. In fact, by examining the case study, it was observed that there are three requirements for telecommunications companies to formulate :

1. Since the technologies in this field are extremely diverse and rapidly changing, they need a model that not only conceptually, but also determines the exact characteristics and criteria for evaluating the technologies. To the best of our knowledge, there is no comprehensive research in the telecommunications industry that has comprehensively and accurately determined criteria and sub-criteria for evaluating emerging technologies .
2. Since many of these technologies are emerging and there is no complete information about all of them by experts, so the uncertainty in the evaluation is quite evident. Therefore, the proposed model should have the power to manage uncertainty.
3. The existence of many operational, social and political restrictions such as transaction means that the evaluation of technologies should not be based solely on their capabilities and attractiveness, therefore, a model is needed that, in addition, measures the ability of the organization to use each technology.

The proposed model of this study, to cover the above requirements, proposes a hybrid model that, to cover the first requirement, determines the analysis steps in detail and especially the evaluation criteria and sub-criteria. For the second requirement, it uses the fuzzy approach to control the uncertainty, and to cover the third requirement, it uses the attractiveness-capability matrix.

Accordingly, the present study aimed to provide a new analytical framework compatible with the uncertain environment of such organizations to illustrate telecommunications technologies clearly. This new analytical model mixes the existing quantitative models and uses the fuzzy approach for non-deterministic technology analysis and evaluation.

3. ATTRACTIVENESS-COMPETITIVE CAPABILITY MATRIX

The attractiveness-competitive capability matrix (ACM) is used to detect technological priorities and their appropriate strategies. This matrix is developed based on Porter's conceptual model. When allocating resources, including capital resources, human resources, equipment, and physical facilities, to strategic plans,

some internal competition exists to overcome resource limitations [21]. The results of this matrix facilitate specifying the strategic position of technologies and the key technologies [22]. Using this matrix, however, mandates the definition and development of factors and criteria facilitating a multi-dimensional and comprehensive evaluation [23].

Technology assessment models are underpinned by a two-dimensional framework. In these models, one-dimension deals with internal factors, which are mainly controlled by companies and are intertwined with their behaviour and decisions. Such factors are known as technological competitiveness [24, 25]. On the other hand, external factors, including the behaviour of customers, competitors, governments, and other stakeholders, are beyond the organization's control. They explain the status of technology outside the organization; hence, they are called technological attractiveness [23]. To detect appropriate TSs, both the attractiveness of each technology and the organization's competitive capability should be addressed. To this end, the attractiveness-competitive capability matrix is drawn for technologies, according to which a decision can be made to determine the appropriate strategy for the concerned technology. The ACM has four distinct districts, as presented in Figure 1. A strategic approach can be adopted for each of the technologies existing in these four districts:

District (1): The attractiveness of the technologies in this district is not high, and the organization's competitive strength is also low. Accordingly, these technologies are not necessary, and the organization's appropriate strategy is to hand them over to other companies or not focus on them.

District (2): The attractiveness of the technologies in this district is high; hence, they are necessary. However, the organization's competitive strength is low. Accordingly, two different TSs can be adopted: (a) The organization can use the services of successful organizations, or (b) The organization reinforces its competitive capability for these technologies.

District (3): The attractiveness of the technologies in this district is low; however, the organization's competitive strength is high. Due to the organization's mastery of these technologies, the appropriate TS is either to transfer them to other organizations or to use them in other products.

District (4): The technologies of this district are of paramount importance since they are highly attractive, and the organization's competitive strength is also high in this district. Accordingly, the appropriate TS is to be prioritized in the acquisition list. Moreover, regarding the organization's highly competitive strength, these technologies should be acquired as internal or collaborative research and development.

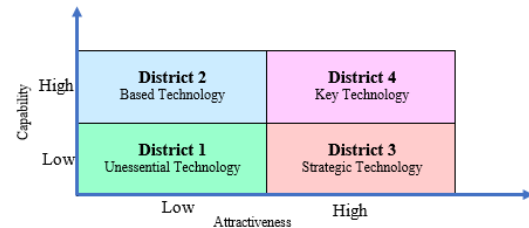


Figure 1. Attractiveness-Competitive Capability Matrix

4. METHODOLOGY: A MODEL FOR TECHNOLOGY STRATEGY FORMULATION IN THE TELECOMMUNICATIONS INDUSTRY

Organizations have been increasingly experiencing volatility, uncertainty, complexity, and ambiguity in their environment, which were posed by various factors, including globalization, digitalization, and industry convergence [18, 19]. Such organizations require a TSF model tailored to their dynamic and uncertain conditions. In this section, according to Figure 2, the hybrid TSF model for telecommunications companies is proposed. To this end, after detecting the technologies, the following steps were taken:

- (1) Designing decision matrices for competitive strength and attractiveness separately;
- (2) Prioritizing technologies using the fuzzy TOPSIS technique for competitive strength and attractiveness separately;
- (3) Designing the attractiveness-competitive matrix and positioning each technology;
- (4) Analysis and Strategy formulation.

In Step 2, the fuzzy TOPSIS technique was used to control the uncertainty aroused by evaluating technologies. This is briefly explained below:

- Fuzzy TOPSIS

The steps of fuzzy TOPSIS used for ranking the technologies are as follows [26]:

First Step:

Firstly, k experts are defined as $D_k = \{1, 2, \dots, K\}$. Then, each team is asked to evaluate m technologies based on each n criteria, which is defined (for each attractiveness and competitive capability index, separately) based on fuzzy linguistic variables according to the following Table 1. Each linguistic variable has an equivalent triangular fuzzy number in the form of $\tilde{A}_{ijk} = (a_{ijk}, b_{ijk}, c_{ijk})$ in which, after replacement based on verbal variables, a primary decision matrix will be formed.

After creating the decision matrices for each expert team, the matrices should be normalized. The following equations are used for matrices normalization. The normal matrix of each expert team is defined as $\tilde{R}_k = [\tilde{r}_{ijk}]_{m \times n}$: in which:

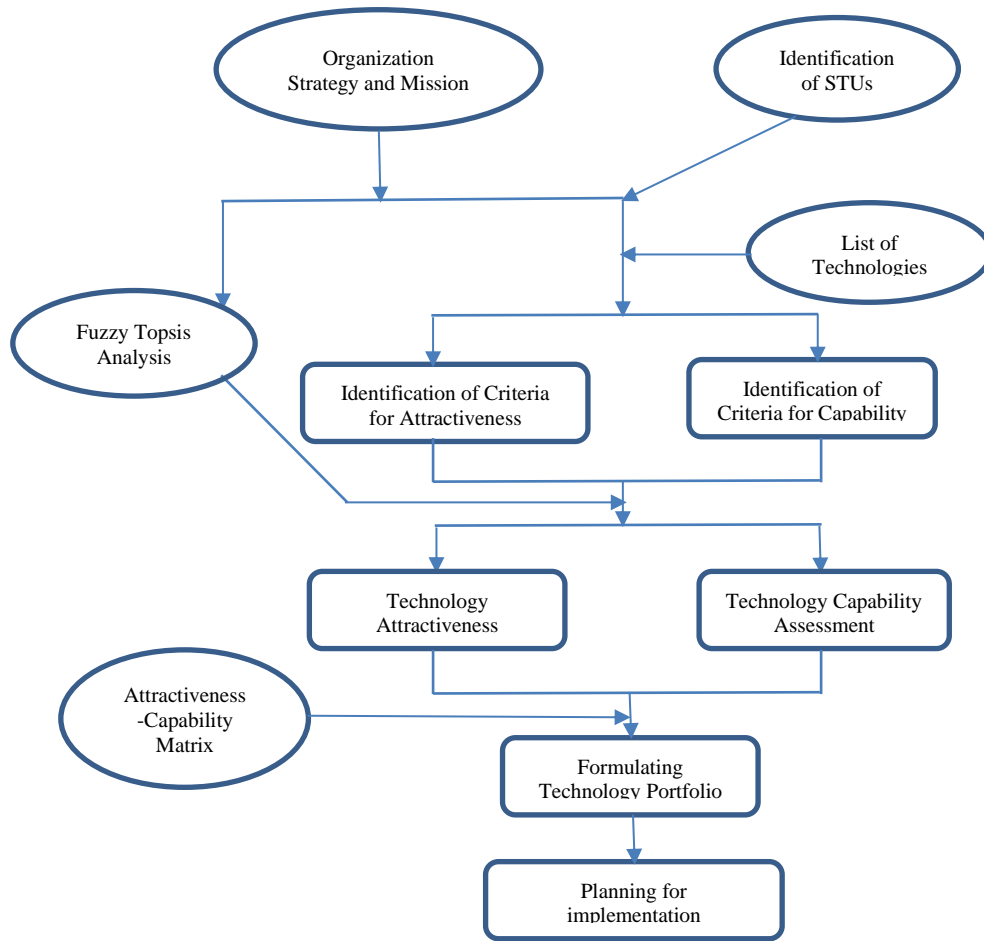


Figure 2. Proposed model for technology strategy formulation

TABLE 1. Linguistic variables for ratings

Linguistic Variables	Triangular Fuzzy Numbers
Very Poor	(0,1,2)
Poor	(1,2,3)
Medium Poor	(2,3.5,5)
Fair	(4,5,6)
Medium Good	(5,6.5,8)
Good	(7,8,9)
Very Good	(8,10,10)

$$\tilde{r}_{ijk} = \left(\frac{a_{ijk}}{c_{jk}^*}, \frac{b_{ijk}}{c_{jk}^*}, \frac{c_{ijk}}{c_{jk}^*} \right) \quad (1)$$

where:

$$c_{jk}^* = \text{Max}_k \{c_{ijk}\} \quad (2)$$

Second Step:

Since different criteria have different importance for each expert group, each team is asked to determine the importance of each criterion based on the fuzzy linguistic variables in Table 2.

Based on the fuzzy numbers in Table 2, the weight of the criteria is defined as a fuzzy number $\tilde{W}_{jk} = (w_{jk1}, w_{jk2}, w_{jk3})$. Then, the following equations

TABLE 2. Linguistic variables for importance weight of each criterion

Linguistic Variables	Triangular Fuzzy Numbers
Very Low	(0,0,0.2)
Low	(0.1,0.2,0.3)
Medium Low	(0.2,0.35,0.5)
Medium	(0.4,0.5,0.6)
Medium High	(0.5,0.65,0.8)
High	(0.7,0.8,0.9)
Very High	(0.8,1,1)

are used to the union the weights, which are determined by the expert to define them as $\tilde{W}_j = (w_{j1}, w_{j2}, w_{j3})$ according to the following equations:

$$w_{j1} = \text{Min}_k \{w_{jk1}\} \tag{3}$$

$$w_{j2} = \frac{1}{K} \sum_k w_{jk2} \tag{4}$$

$$w_{j3} = \text{Max}_k \{w_{jk3}\} \tag{5}$$

Since this problem is a group decision problem, it is necessary to integrate the matrix of all k experts. The following equation are used to create the final integrated matrix is defined as $\tilde{R} = [\tilde{r}_{ij}]_{m \times n}$ in which

$$\tilde{r}_{ij} = (a_{ij}, b_{ij}, c_{ij}) .$$

where:

$$a_{ij} = \text{Min}_k \{a_{ijk}\} \tag{6}$$

$$w_{ij} = \frac{1}{K} \sum_k w_{ijk} \tag{7}$$

$$c_{ij} = \text{Max}_k \{c_{ijk}\} \tag{8}$$

Third Step:

The weight of each criterion should be multiplied in the normalized matrix to get the final normalized weighted matrix as $\tilde{V} = [\tilde{v}_{ij}]_{m \times n}$ in which $\tilde{v}_{ij} = \tilde{r}_{ij} * \tilde{W}_j$.

Fourth step:

In this step, the positive (FNIS, A^*) and negative (FNIS, A^-) ideals for each criterion are calculated by the following equations and known as the "calculation of ideals".

$$A^* = (\tilde{v}_1^*, \tilde{v}_2^*, \dots, \tilde{v}_n^*) \tag{9}$$

$$A^- = (\tilde{v}_1^-, \tilde{v}_2^-, \dots, \tilde{v}_n^-) \tag{10}$$

where:

$$\tilde{v}_j^* = \text{Max}_i \{v_{ij3}\} \tag{11}$$

$$\tilde{v}_j^- = \text{Max}_i \{v_{ij1}\}, \quad i=1,2,\dots,m \quad j=1,2,\dots,n \tag{12}$$

Fifth step:

At this step, the distance of each technology from the positive and negative ideals is calculated through the following equations, which are known as "calculation of the distance to the negative ideal" and "calculation of the distance to the positive ideal", respectively.

$$d_i^* = \sum_j d(\tilde{v}_{ij} - \tilde{v}_j^*) \quad i=1,2,\dots,m \tag{13}$$

$$d_i^- = \sum_j d(\tilde{v}_{ij} - \tilde{v}_j^-) \quad i=1,2,\dots,m \tag{14}$$

D is the distance between two fuzzy numbers, (a_1, b_1, c_1) and (a_2, b_2, c_2) are two fuzzy numbers. The distance is calculated as:

$$d_v(\tilde{M}_1, \tilde{M}_2) = \sqrt{1/3((a_1 - a_2)^2 + (b_1 - b_2)^2 + (c_1 - c_2)^2)} \tag{15}$$

Sixth step:

The following equation is used to compute the relative closeness to the ideal solution, and the results are presented on a sheet, Index of Similarity calculation.

$$CC_i = \frac{d_i^-}{d_i^* + d_i^-} \tag{16}$$

Seventh step:

The calculated CC_i score for each technology in the previous step should now be scaled between 0 and 1, as these scores will be used to create the attractiveness matrix. Then the final scores are used in the analysis and provision of decision matrices.

5. TECHNOLOGY STRATEGY FORMULATION FOR MCI

The first step of this model is to detect telecommunications technologies and their position in the hype cycle. To this end, the telecommunications technologies were first examined according to the world's most prestigious institutions. As result, 191 technologies were selected according to international reports and approved by specialized experts. Moreover, seven main fields of the STU (App, Device, Smart Network, Service Support, Security, Management, People and Process) technology were detected by and the opinions of experts and specialists in the field. During meetings with them, the extracted 191 technologies were classified into the seven fields regarding their applications.

5. 1. Designing a Decision Matrix for Attractiveness Index (A)

Evaluation indicators should first be specified to analyze technology attractiveness. Hax and Mahluf attributed technology attractiveness to the effect of technology outside the organization and introduced factors facilitating the external analysis of each technology. Some of those criteria are as follows: the potential to reinforce competitive advantage in the product and the process, the technological change rate, the added value potential, the long-term effect of technology on costs, performance, and quality, and the effect on industry standards. Jolly [23] classified attractiveness indicators

into four categories, namely market potential, technical potential, competitive capability, and socio-political situation.

The present study considered four main criteria to evaluate attractiveness. Given the significance of the accuracy and specialization for each of these four criteria, some sub-criteria were also introduced.

5. 1. 1. Strategic Attractiveness Index (A1)

The extent the technologies affect the realization of the organization's strategic goals determines the strategic attractiveness (A1) of technologies. As shown in Table 3, 10 sub-criteria are specified for A1. Moreover, the expert uses linguistic variables in Table 1 to evaluate the technologies in each sub-criterion.

5. 1. 2. Market/economic Attractiveness Index (A2)

The market/economic attractiveness (A2) is the second evaluation criterion measured by the amount and significance of technology use in the company's current and future services/products. To this end, we need a service-technology matrix to detect the most attractive technologies using the intersection of services and technologies.

5. 1. 3. Technical Attractiveness Index (A3)

This criterion assesses the technical features of technology. It is determined by some sub-indices, including the level and the potential effect of technology on business regarding positioning indices on the HYPE cycle, benefit rating (extent of the effect on industry), penetration in the market, acceptance time, and life cycle maturity. Table 4 presents the decision matrix regarding this index and its sub-criteria.

5. 1. 4. Environmental Attractiveness Index (A4)

This criterion determined the extent of access to technologies regarding the following issues: sanctions on access to suppliers, legal and regulatory requirements, the effect of technology on the organization, and environmental requirements. Table 5 shows the matrix for A4 and its sub-criteria.

5. 2. Developing a Decision Matrix for Competitive Capability Index (B)

The following four criteria are suggested to evaluate an organization's competitive capability strength for a given technology: Competitive strength of HR, competitive strength of equipment (existing hardware and infrastructure), competitive strength of technical knowledge, and competitive strength of orgaware (Table 6).

TABLE 3. Decision matrix for Environmental attractiveness criterion according to four sub-criteria

	Sub-criteria for strategic attractiveness									
Technology	Maintaining and reinforcing a unique architecture consistent with the future of information technology;	Promoting customer experience at all contact points;	Offering a customer-oriented product portfolio	Acquiring and developing technologies of priority	Having effects on regulatory organizations' telecom programs	Ensuring the provision of efficient information technology services	Institutionalizing security in organizations from the first steps of design	Ensuring network efficiency and reliability	Establishing a future-oriented network	Ensuring income growth and diversification

TABLE 4. Decision matrix for technical attractiveness criterion according to five sub-criteria

	Sub-criteria for technical attractiveness																							
Technology	Position on the HYPE cycle					Benefit Ratings				Penetration in the market					Acceptance time				Maturity in the life cycle					
	1	2	3	4	5	1	2	3	4	1	2	3	4	5	1	2	3	4	1	2	3	4	5	6

TABLE 5. Decision matrix for environmental attractiveness criterion according to four sub-criteria

	Sub-Criteria for Environmental attractiveness			
Technology	Access to suppliers regarding some issues (e.g., sanctions)	Effect of technology on organization	Environmental effects, with higher values indicating being more destructive	Legal/regulatory requirements and obligations

TABLE 6. Decision matrix for competitive capability criterion according to four sub-criteria

Technology	Sub-Criteria for Environmental attractiveness			
	The competitive strength of HR (B1)	The competitive strength of equipment (hardware and infrastructure) (B2)	The competitive strength of technical knowledge (B3)	The competitive strength of orgaware (B4)

5. 3. Step 2: Prioritizing Technologies

Considering the designed matrices, 191 technologies were completed by six expert teams using fuzzy numbers. In the following, the matrices are aggregated to evaluate the technologies in terms of attractiveness and competitive capability.

5. 3. 1. Prioritizing Technologies by Attractiveness Index

Adopting the Fuzzy TOPSIS technique, the matrices completed by six expert groups were aggregated regarding attractiveness. Due to space limitations, the aggregate matrix results are reported only for the first 10 technologies (out of 191 technologies) in Tables 7-11.

Following aggregation, the technologies were rated in terms of attractiveness using the fuzzy TOPSIS technique (Table 8).

5. 3. 2 .Prioritizing Technologies by Competitive Capability Index

In the next step, the matrices should be aggregated in terms of competitive capability. In Table 9, the aggregate matrix results are reported concerning competitive capability only for the first 10 technologies.

Following aggregation, the technologies were rated in terms of competitive capability using the fuzzy TOPSIS technique (Table 10).

TABLE 7. Fuzzy aggregate matrix of experts' opinions on attractiveness for the first 10 detected technologies

Code	Technology	STU	A1	A2	A3	A4								
T1	DigitalOps	Service support/ Apps	0.08	0.57	0.85	0.00	0.29	0.88	0.44	0.46	0.48	0.51	0.76	1.00
T2	Total Experience for CSPs	People & process	0.11	0.57	0.81	0.00	0.54	1.00	0.02	0.13	0.52	0.14	0.59	1.00
T3	CSP Data Monetization	Management	0.26	0.62	0.94	0.04	0.30	0.70	0.33	0.34	0.35	0.40	0.75	1.00
T4	Converged Cloud Management	Infrastructure	0.17	0.68	0.98	0.00	0.18	0.50	0.41	0.43	0.44	0.50	0.71	0.88
T5	Intercarrier Service Automation	Infrastructure/ service support	0.18	0.59	0.96	0.00	0.14	0.37	0.25	0.26	0.27	0.45	0.70	0.93
T6	B2B Service Platform	Service support/ Apps	0.54	0.76	0.95	0.07	0.32	0.44	0.40	0.41	0.43	0.47	0.78	0.98
T7	5G Charging	Service support	0.52	0.81	1.00	0.09	0.37	1.00	0.48	0.50	0.52	0.45	0.73	0.97
T8	Data Literacy	People & process	0.00	0.56	0.90	0.00	0.39	0.86	0.51	0.53	0.55	0.50	0.80	1.00
T9	Service and Resource Orchestration	Service support	0.51	0.73	0.96	0.02	0.14	0.48	0.53	0.56	0.58	0.55	0.78	1.00
T10	Platform Operating Models	Apps	0.03	0.60	0.93	0.00	0.46	0.92	0.06	0.09	0.19	0.51	0.72	0.94

TABLE 8. Final rating of technologies in terms of attractiveness index using fuzzy TOPSIS technique for the first 10 detected technologies

Code	Technologies	STUs	d_i^-	d_i^*	Score	
T1	DigitalOps	service support/ Apps	2.37	2.16	0.523648	0.577359
T2	Total Experience for CSPs	People & process	2.21	2.57	0.462445	0.398191
T3	CSP Data Monetization	Management	2.20	2.23	0.496796	0.498752
T4	Converged Cloud Management	Infrastructure	2.14	2.23	0.489049	0.476073
T5	Intercarrier Service Automation	Infrastructure/ service support	1.86	2.48	0.428713	0.299441
T6	B2B Service Platform	service support/ Apps	2.27	1.95	0.537576	0.618134
T7	5G Charging	Service support	2.66	1.79	0.597352	0.793125
T8	Data Literacy	people & process	2.48	2.09	0.542652	0.632994
T9	Service and Resource Orchestration	service support	2.40	1.87	0.561735	0.688857
T10	Platform Operating Models	Apps	2.10	2.48	0.459269	0.388893

TABLE 9. Fuzzy aggregate matrix of experts' opinions on competitive capability for the first 10 detected technologies

Code	Technology	STU	B1		B2		B3		B4					
T1	DigitalOps	Service support/ Apps	0.00	0.38	0.67	0.00	0.35	0.67	0.00	0.26	0.75	0.00	0.31	0.63
T2	Total Experience for CSPs	People & process	0.00	0.43	0.89	0.00	0.48	0.89	0.00	0.39	1.00	0.00	0.41	0.80
T3	CSP Data Monetization	Management	0.10	0.36	0.67	0.10	0.39	0.89	0.00	0.34	0.75	0.10	0.45	0.80
T4	Converged Cloud Management	Infrastructure	0.10	0.51	0.89	0.10	0.51	1.00	0.10	0.48	1.00	0.10	0.57	0.90
T5	Intercarrier Service Automation	Infrastructure/ service support	0.00	0.40	0.89	0.00	0.38	1.00	0.00	0.34	0.75	0.00	0.33	0.80
T6	B2B Service Platform	Service support/ Apps	0.00	0.43	0.89	0.00	0.35	0.89	0.00	0.34	0.75	0.00	0.28	0.80
T7	5G Charging	Service support	0.00	0.45	0.89	0.00	0.43	0.89	0.00	0.47	1.00	0.00	0.30	0.80
T8	Data Literacy	people & process	0.00	0.40	0.89	0.00	0.38	0.89	0.00	0.34	1.00	0.00	0.28	0.63
T9	Service and Resource Orchestration	Service support	0.00	0.38	0.67	0.00	0.35	0.67	0.00	0.26	0.75	0.00	0.31	0.63
T10	Platform Operating Models	Apps	0.00	0.43	0.89	0.00	0.48	0.89	0.00	0.39	1.00	0.00	0.41	0.80

TABLE 10. Final rating of technologies in terms of competitive capability index using fuzzy TOPSIS technique for the first 10 detected technologies

Code	Technology	STU	d_i^-	d_i^+	CC_i	Score
T1	DigitalOps	Service support/ Apps	1.74	2.89	0.375575	0.213178
T2	Total Experience for CSPs	People & process	2.29	2.68	0.461053	0.373605
T3	CSP Data Monetization	Management	2.01	2.63	0.433598	0.322077
T4	Converged Cloud Management	Infrastructure	2.51	2.36	0.514723	0.474334
T5	Intercarrier Service Automation	Infrastructure/ service support	2.16	2.76	0.438141	0.330604
T6	B2B Service Platform	Service support/ Apps	2.08	2.79	0.427922	0.311425
T7	5G Charging	Service support	2.28	2.70	0.457707	0.367326
T8	Data Literacy	People & process	2.13	2.79	0.43254	0.320091
T9	Service and Resource Orchestration	Service support	2.16	2.71	0.44294	0.33961
	Platform Operating Models	Apps	1.95	2.78	0.412197	0.281911

5. 4. Designing ACM ACM was finally developed after obtaining the final ratings of attractiveness and competitive capability for each technology (Table 11). Accordingly, Figure 3 illustrates ACM.

In the company's technology portfolio encompassing existing technologies or some technologies partially affecting existing/future services and products, 20 technologies were placed in District 4 of ACM, considered priority technologies. Attractive technologies consisted of 28 technologies in District 3 of ACM, and mature and essential technologies consisted of 41 technologies in District 2 of ACM.

5. 5. Result Analyses and Technology Acquisition Solutions The final step in TSF is to propose solutions to develop and acquire TSs regarding technological fields and technologies under investigation. To provide appropriate TSF for each technology, its technical features, along with the company's existing competitive strength in a

concerned district, should be considered. For example, the company's existing competitive strength, along with the position of technology in the life cycle or its maturity extent, should be considered. In this regard, one should not ignore technological dimensions, which were also examined in evaluating the technical attractiveness of these technologies.

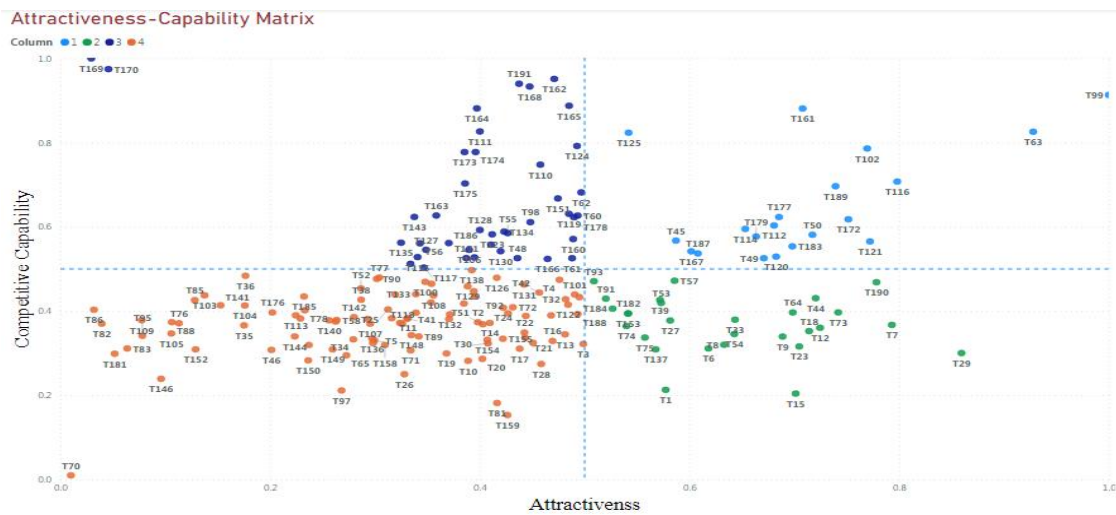
In this updating phase of the TSF project, a questionnaire addressing technologies identified in Districts 3 and 4 of ACM (priorities 1 and 2) and technology acquisition techniques was prepared and completed by the experts.

- **Suggestions to promote technological competitiveness and technology acquisition with priorities 1 and 2**

Tables A1 and A2 in the appendix present the attractiveness and competitive capability scores for some technologies as samples. As shown in this Table

TABLE 11. Final attractiveness and competitive capability scores and the district of the first 10 detected technologies

District	Competitiveness score	Attractiveness score	STU	Technology	Code
3	0.2132	0.5774	service support/ Apps	DigitalOps	T1
1	0.3736	0.3982	People & process	Total Experience for CSPs	T2
1	0.3221	0.4988	Management	CSP Data Monetization	T3
1	0.4743	0.4761	Infrastructure	Converged Cloud Management	T4
1	0.3306	0.2994	Infrastructure/ service support	Intercarrier Service Automation	T5
3	0.3114	0.6181	service support/ Apps	B2B Service Platform	T6
3	0.3673	0.7931	service support	5G Charging	T7
3	0.3201	0.6330	People & process	Data Literacy	T8
3	0.3396	0.6889	service support	Service and Resource Orchestration	T9
1	0.2819	0.3889	Apps	Platform Operating Models	T10



A1, the selected 5 technologies, a majority of which are infrastructure technologies. In this district, the technologies are of paramount importance since both their attractiveness and the company's competitive strength are high. Accordingly, the most appropriate strategy for these technologies is prioritized in the acquisition, maintenance, and promotion list. Moreover, regarding the company's high competitiveness, these technologies should be acquired as internal or collaborative research and development.

Table A2 lists some technologies with high attractiveness for which the company's competitive strength is low (technologies in district 3). They are the second priority of technology development or acquisition.

Although the company's general competitiveness is high for these technologies, some techniques to promote competitiveness are as follows:

- Cooperation in research and supporting technology companies, universities, and research centers;
- Employment and development of specialized HR;
- Promoting organizational knowledge by granting scholarships, holding specialized training courses, and others;
- Concluding consultation and educational contracts with natural and legal persons;
- Establishing or supporting centers for technological growth, acceleration, and development in affiliated companies;
- Developing existing hardware infrastructure in companies, equipment purchase, technical knowledge, infrastructure, and others;
- Possessing or purchasing some shares of small-sized enterprises /start-ups; and
- Maintaining and promoting existing competitiveness

• Managerial insights

When managers of a single and large industry such as telecommunications face the emergence of new and diverse technologies in a fast and dynamic manner, choosing among them and investing in them is a very complicated matter. Basically, choosing between them causes complexity and disagreement between managers. The presented hybrid model can be a conceptual and technical guide for tech industry managers to determine their technology portfolio. The design of this new model helps managers to identify technologies first at certain times. Then, step by step, it allows the analyst to finally assign the necessary points to each technology based on the opinion of the managers and in an uncertain environment and choose the best set of technologies for the organization.

According to the literature, advanced industries, while having the ability to use new technologies, see their future as dependent on handling fast changes in technology [27].

6. CONCLUSION AND RECOMMENDATION FOR FUTURE RESEARCH

Nowadays, technology plays a critical role in promoting organizational competitiveness; hence, it should be considered an essential organizational resource from a strategic perspective. In fact, appropriate TSF helps organizations reach a technological advantage. Regarding the research novelty, the present study, for the first time, addressed a complicated issue, i.e., determining some attractiveness-competitiveness evaluation indices and their weights in technology-oriented industries, including MCI. We consider the methodology of the present study to be unique and as such, it makes a significant contribution to the literature on national innovation systems.

The present study sought to combine the models existing in the technology management literature to develop a novel model more compatible with the telecom industry's uncertain environment. In this regard, a TSF model underpinned by ACM was proposed. Given the inherent uncertainty in this industry, the fuzzy TOPSIS method was used to evaluate the company's attractiveness and competitiveness. After analysing the position of each technology in ACM, an appropriate strategy was introduced for each technology. If the proposed model is to be used in technology-oriented industries, ETs and existing technologies are recommended to be detected in detail, and their positioning, including their position in the hype cycle, should be specified.

When ACM was used to evaluate technologies, many technologies in this matrix were in District 3, indicating their high attractiveness and low competitive

strength. Accordingly, since the detailed fuzzy TOPSIS method was used to evaluate the attractiveness of the technologies, the scores of these technologies can be considered to prioritize them and select the best technologies in the concerned district for making strategic decisions. Future researchers can propose a new approach to solve this problem.

The main problem with ACM specifying the general strategies of the matrix districts is to detect strategies placed within the boundaries of the matrix cells. It seems challenging to determine a crisp boundary for different districts to have different strategies on each side of the boundary. Accordingly, future studies can address the definition of fuzzy and probable boundaries.

7. REFERENCES

1. Akbari, M., Safaie, N., Jahani, Z. and Saadatmand, M.R., "An analytical model for confronting the omicron variant during covid-19 pandemic: A system dynamic approach", *International Journal of Engineering, Transactions B: Applications*, Vol. 35, No. 8, (2022), 1533-1546. doi: 10.5829/ije.2022.35.08b.10.
2. Ghazinoory, S., Nozari, M. and Hoshdar, F., "Cascade roadmaps as a tool for technology strategy formulation: The case of iran oil industry", *Journal of the Knowledge Economy*, (2023), 1-18. doi: 10.1007/s13132-023-01221-z.
3. Shehabuddeen, N., Probert, D. and Phaal, R., "From theory to practice: Challenges in operationalising a technology selection framework", *Technovation*, Vol. 26, No. 3, (2006), 324-335. doi: 10.1016/j.technovation.2004.10.017.
4. Heidenberger, K. and Stummer, C., "Research and development project selection and resource allocation: A review of quantitative modelling approaches", *International Journal of Management Reviews*, Vol. 1, No. 2, (1999), 197-224. doi: 10.1111/1468-2370.00012.
5. Nezhad, A.J., Nikoukar, G.H. and Habibi, M., "A suitable model for formulating technology strategy (case study: A car parts manufacturer in iran khodro company)", *International Journal of Learning and Development*, Vol. 3, No. 4, (2013), 96-107. doi: 10.5296/ijld.v3i4.4246.
6. Arasti, M.R., Mokhtarzade, N. and Khanlari, A., "Proposing an integrated technology strategy model based on positioning approach", *Journal of Industrial Management Perspective*, Vol. 3, No. 2, Summer 2013, (2013), 185-209. http://jim.p.sbu.ac.ir/article_87319.html
7. Ebrahimi, M., Baerz, A.M., Hosseini, S.H.K. and Azar, A., "A new model of petrochemical technology strategic planning", *International Journal of Business Administration*, Vol. 4, No. 2, (2013), 57. doi: 10.5430/ijba.v4n2p57.
8. Alvarado, D.C., Acha, S., Shah, N. and Markides, C.N., "A technology selection and operation (TSO) optimisation model for distributed energy systems: Mathematical formulation and case study", *Applied Energy*, Vol. 180, (2016), 491-503. doi: 10.1016/j.apenergy.2016.08.013.
9. Mohammadzadeh, S., Mokhtarzadeh, N. and Rasaei, M.R., "Strategic technologies selection for oil production: An application of attractiveness-capability matrix of technology", *Iranian Journal of Oil and Gas Science and Technology*, Vol. 10, No. 1, (2021), 66-79. doi: 10.22050/ijogst.2020.231146.1551.

10. Schuh, G., Patzwald, M. and Warzawa, T., "Turbulence-induced initiation of technology strategy development in a volatile business environment", in 2022 IEEE International Conference on Industrial Engineering and Engineering Management (IEEM), IEEE., (2022), 1399-1405.
11. Shen, Y.-C., Lin, G.T. and Tzeng, G.-H., "Combined dematel techniques with novel mcdm for the organic light emitting diode technology selection", *Expert Systems with Applications*, Vol. 38, No. 3, (2011), 1468-1481. doi: 10.1016/j.eswa.2010.07.056.
12. Moazenazadeh, D. and Hamidi, H., "Analysis and development of technology acceptance model in mobile bank field", *International Journal of Engineering, Transactions C: Aspects*, Vol. 31, No. 9, (2018), 1521-1528. doi: 10.5829/ije.2018.31.09c.07.
13. Arora, H., Naithani, A. and Gupta, S., "Distance measures of pythagorean fuzzy topsis approach for online food delivery apps", *International Journal of Engineering, Transactions A: Basics*, Vol. 35, No. 10, (2022), 1877-1886. doi: 10.5829/ije.2022.35.10a.07.
14. Gitinavard, H. and Mousavi, S., "Evaluating construction projects by a new group decision-making model based on intuitionistic fuzzy logic concepts", *International Journal of Engineering, Transactions C: Aspects*, Vol. 28, No. 9, (2015), 1312-1319. doi: 10.5829/idosi.ije.2015.28.09c.08.
15. Cil, I., Arisoy, F., Kilinc, H., Özgürbüz, E. and Cil, A.Y., "Fuzzy ahp-topsis hybrid method for indoor positioning technology selection for shipyards", in 2021 5th International Symposium on Multidisciplinary Studies and Innovative Technologies (ISMSIT), IEEE., (2021), 766-771.
16. Aliakbari Nouri, F., Khalili Esbouei, S. and Antucheviciene, J., "A hybrid mcdm approach based on fuzzy amp and fuzzy topsis for technology selection", *Informatica*, Vol. 26, No. 3, (2015), 369-388. doi: 10.15388/Informatica.2015.53.
17. Schuh, G., Patzwald, M. and Studerus, B., "Development of technology strategies under volatility and uncertainty: A concept for the continuous-iterative analysis of the firm and its environment", in 2022 Portland International Conference on Management of Engineering and Technology (PICMET), IEEE. (2022), 1-19.
18. Schuh, G., Patzwald, M. and Cardoso, M.C.I., "Resilient technology strategy in volatile environments: Derivation of requirements to enable long-term strategic positioning in times of volatility, uncertainty, complexity and ambiguity", in 2019 Portland International Conference on Management of Engineering and Technology (PICMET), IEEE. (2019), 1-15.
19. Valinejad, F., Safaie, N., Rahmani, D. and Saadatmand, M., "A hybrid model for supply chain risk management based on five-dimensional sustainability approach in telecommunication industry", *International Journal of Engineering, Transactions C: Aspects*, Vol. 35, No. 6, (2022), 1096-1110. doi: 10.5829/ije.2022.35.06c.01.
20. Zhao, F., Kuang, X., Hao, H. and Liu, Z., "Selection of emerging technologies: A case study in technology strategies of intelligent vehicles", *Engineering Management Journal*, Vol. 34, No. 1, (2022), 37-49. doi: 10.1080/10429247.2020.1839844.
21. Chen, C.-T., "Extensions of the topsis for group decision-making under fuzzy environment", *Fuzzy sets and systems*, Vol. 114, No. 1, (2000), 1-9. doi: 10.1016/S0165-0114(97)00377-1.
22. Hax, A.C. and No, M., "Linking technology and business strategies: A methodological approach and an illustration, Springer, (1993).
23. Jolly, D.R., "Development of a two-dimensional scale for evaluating technologies in high-tech companies: An empirical examination", *Journal of Engineering and Technology Management*, Vol. 29, No. 2, (2012), 307-329. doi: 10.1016/j.jengtecman.2012.03.002.
24. Wu, C.-Y. and Hu, M.-C., "The development trajectory and technological innovation capabilities in the global renewable energy industry", in 2015 Portland International Conference on Management of Engineering and Technology (PICMET), IEEE. (2015), 2574-2580.
25. Lizarralde, R., Ganzarain, J. and Zubizarreta, M., "Adaptation of the mives method for the strategic selection of new technologies at an r&d centre. Focus on the manufacturing sector", *Technovation*, Vol. 115, (2022), 102462. doi: 10.1016/j.technovation.2022.102462.
26. Ertuğrul, İ. and Karakaşoğlu, N., "Comparison of fuzzy ahp and fuzzy topsis methods for facility location selection", *The International Journal of Advanced Manufacturing Technology*, Vol. 39, (2008), 783-795. doi: 10.1016/j.ajej.2022.04.005.
27. Ahmadabadi, M.H., Keramati, M.A. and Sohrabi, T., "Emblematical pattern of main criteria to selection of foresight technology strategy in advanced aerospace industries", *Defensive Future Study Researches Journal*, Vol. 5, No. 18, (2020), 141-168. doi: 10.22034/DFSR.2021.130445.1407.

APPENDIX A

TABLE A1. Attractiveness and capability competitive scores for some technologies in district 4 (priority 1)

Code	Technology	STU	Attractiveness score	Competitiveness score	District
T99	LTE-A	Infrastructure	1.0000	0.9132	4
T161	IMS/ vIMS	Infrastructure	0.7080	0.8810	4
T63	vEPC	Infrastructure	0.9279	0.8259	4
T125	IPv6	Infrastructure	0.5419	0.8235	4
T102	Network Firewalls	Infrastructure/ security	0.7696	0.7861	4

TABLE A2. Attractiveness and competitiveness scores for some technologies in district 3 (priority 2)

Code	Technology	STU	Attractiveness score	Competitiveness score	District
T57	eSIM	Device	0.5858	0.4721	3
T93	LTE for Mission-Critical and Public Safety Networks	Infrastructure	0.5089	0.4709	3
T190	5GC	Infrastructure	0.7784	0.4686	3
T44	Cloud-Native CSP Infrastructure	Infrastructure	0.7204	0.4307	3
T91	Edge Computing for CSPs	Infrastructure	0.5202	0.4296	3

Persian Abstract

چکیده

جهانی شدن و افزایش ارتباطات مجازی، چالش های متعددی را برای شرکت های مخابراتی ایجاد کرده است. برای رفع چالش های جدید و نوظهور نظیر بار ترافیکی، امنیت سیستم های ارتباطی و بهینه سازی زیرساخت ها، سازمان ها و شرکت های تلکام به دنبال شناخت فناوری های برتر این حوزه می باشند. از طرفی، سازمان های خدمات ارتباطی از محیط های بسیار پویا و غیرقطعی برخوردار هستند و فناوری های مربوط به آنها با سرعت فزاینده ای در حال تغییر و توسعه می باشند. برای این منظور در مقاله حاضر، یک مدل کارای تدوین پورتفولیو فناوری، برای شرکت های تلکام مبتنی بر فضای پویا و غیرقطعی آنها ارائه داده است. مدل پیشنهادی یک مدل هیبریدی از رویکرد ماتریس جذابیت - توانمندی و رویکرد تصمیم گیری چندمعیاره در فضای غیرقطعی و پویا است. در این مدل، عوامل و معیارهای ارزیابی جذابیت-توانمندی مبتنی بر نیازمندی های محیط پویا و غیرقطعی این شرکتها ارائه شده است تا تصویر دقیقتری از فناوری های به شدت در حال تغییر در تدوین استراتژی فناوری ارائه دهد. در این مدل، برای کنترل عدم قطعیت ناشی از ارزیابی فناوری های نوظهور گسترده در چنین سازمانهایی از تکنیک تاپسیس فازی در ارزیابی فناوریها استفاده شده است. مدل پیشنهادی بر اساس ضرورت های شناسایی شده در MCI اجرا و نتایج آن تحلیل شده است.



Election Prediction Based on Messages Feature Analysis in Twitter Social Network

A. Yavari^a, H. Hassanpour^b

^a Department of Computer Engineering and IT, Payame Noor University, Tehran, Irann

^b Faculty of Computer Engineering and IT, Shahrood University of Technology, Shahrood, Iran

PAPER INFO

Paper history:

Received 15 February 2023

Received in revised form 27 April 2023

Accepted 06 May 2023

Keywords:

Election Prediction

Sentiment Score

Retweet Number

Twitter

ABSTRACT

With the emergence of virtual social networks, predicting social events such as elections using social network data has attracted the attention of researchers. In this paper, three indicators for election prediction have been proposed. First, the tweets are grouped based on a specific time window. Next, the indicator values for each candidate in each time window are calculated based on the sentiment scores and re-tweet numbers. In fact, the indicators are calculated based on the ratio of features related to positive to negative sentiments. Finally, using the aging estimation method, the indicator values for each party on the election date are predicted. The party with larger predicted indicator values will be considered as the winner. Investigations into Twitter data related to 2016 and 2020 US presidential elections on a four-month time span indicate that the indicator values and elections can be predicted with a high accuracy.

doi: 10.5829/ije.2023.36.06c.16

1. INTRODUCTION

Elections are one of the most important political events in most countries. People have always been interested in predicting elections. Since 1936, surveys have been an integral part of political predictions and, since 1988, numerous business corporations and news organizations have been engaged in predicting elections by using statistical techniques [1]. Academic researchers have also proposed various models for election prediction based on behavior analysis and other factors such as macro-economic conditions including employment, loan rate and inflation rate.

The appearance of Web 2 and the development of electronic communication devices such as mobile phone contributed to the development of virtual social networks. Considering the fact that the data produced in virtual social networks reflect aspects of real societies [2] and are easily accessible to the public through web crawlers, the investigation and analysis of virtual social networks has attracted researchers' attention. Many of these investigations have aimed at predicting real society events including elections based on virtual social network analysis [3]. In-time and accurate prediction of

elections is important. Because, it can contribute to the early planning of economic, international policies of the countries, and the prevention of some social crises.

Through analyzing Twitter data as the biggest news resource with over 250 million active users [4], this paper proposes three indicators for election prediction based on such factors as sentiment scores and re-tweet numbers. The first indicator, Sentiment Score ratio (SSr), is defined based on the ratio of sum of positive sentiment scores to negative sentiment scores at specific time intervals. The second indicator, ReTweet ratio (RTr), is defined based on the ratio of positive re-tweets to negative re-tweets at specific intervals. Finally, the third indicator, Sentiment Score and ReTweet ratio ($SSRTr$), is defined as a combination of the two previous indicators, and considers the number of re-tweets as a coefficient multiplied by the sentiment score of each tweet. It specifies the ratio of the sum product of sentiment scores and re-tweet numbers for positive tweets to that for negative tweets.

After specifying the indicator values at initial time intervals before the election, the indicator value at future time intervals and on the election date is predicted based on the aging estimation method [5]. Since, in all three

*Corresponding Author Email: A.Yavari@pnu.ac.ir (A. Yavari)

proposed indicators, positive emotional values are in the numerator and negative emotional values are in the denominator, any party whose predicted indicator value is higher is declared as the winner of the election.

The novelty of this paper relates to proposing three types of indicators for election prediction based on Twitter data. More especially, it relates to the possibility of specifying the different lengths of the prediction interval, depending on the need from one day to several days.

In the following sections, first, the related literature on the topic will be reviewed (section 2). Next, the proposed methods will be described (section 3). Finally, the results of the experiments on two Twitter datasets relating to 2016 and 2020 US presidential elections will be presented (section 4).

2. LITERATURE REVIEW

Election prediction on the basis of Web and virtual social network data is a relatively new line of enquiry. Election prediction in the United States of America reported in the FiveThirtyEight.com Website attracted people's attention for the first time. The 2009 German election was first predicted based on Twitter data analysis [6]. This prediction was made on the basis of comparing the tweets number for each political party in a way that the party with the larger tweet number was considered the winner. In this paper, it is argued that the number of tweets alone cannot be a good criterion for the prediction [5].

So far, various models have been proposed to improve election predictions based on Twitter features such as hashtags [6], tweet and retweet counts [7], and sentiment analysis [5]. Since social media has become a well-known platform for expressing people's feelings about various social events [8]. The indicators proposed in this paper also categorize and analyze users' tweets based on the sentiment analysis feature. Sentiment analysis in election prediction can increase the accuracy of predictions [9].

In 2015, Burnap et al. [10] predicted British election on the basis of the sentiment analysis. They considered the sum of tweet sentiment scores (-5 to +5) as a criterion for making predictions. However, the sum of tweet sentiment scores can also be liable to error [11]. Therefore, in one of the indicators proposed in this paper, the ratio of the sum of positive tweets to the sum of negative tweets is used instead of the sum of tweet sentiment scores for each political party, which contributed to the accurate prediction of 2016 and 2020 US presidential elections.

Yavari et al. [5] proposed an indicator which predicted the 2020 US presidential election with high accuracy based on the ratio of positive tweets count to negative tweets count:

$$A_i = \frac{(Positive\ Tweets\ Count)_i}{(Negative\ Tweets\ Count)_i + 1} \quad (1)$$

In Equation (1), A_i refers to the indicator value at i^{th} interval. Using the exponential averaging method, they predicted the indicator value on the election date. A larger indicator value for a political party denotes its winning the election. They assigned each tweet a sentiment score between -1 to +1, where they counted positive and negative tweets with any magnitude. Therefore, despite a considerable difference in sentiment scores, a tweet with a sentiment score of +0.01 and a tweet with a sentiment score of +1 are assigned equal values in total counts. However, in the proposed method in this paper, the sum of sentiment scores is calculated and, consequently, a tweet with a lower sentiment score will have a smaller effect compared to a tweet with a higher sentiment score.

Oueslati et al. [12], proposed a model based on sentiment analysis on influential messages to predict elections. They identified influential messages based on characteristics such as message content, time and sentiment score. Finally, based on Equation (2), they predicted the winner of the election.

$$R(A) = \frac{infpos(A) + infneg(B)}{Total\ infMessages\ count(A,B)} \quad (2)$$

In Equation (2), $infpos(A)$ and $infneg(B)$ refer to the number of influence positive messages and negative messages for A and B parties, respectively. By examining data from 2016 US election, they showed that influence messages can be a reliable feature.

Singh et al. [13] used Twitter data to predict the 2017 Punjab (a state in India) Parliament election. They used Equation (3) as an indicator for predicting the number of seats won by each party, i.e. to predict the winner of the election.

$$S(A) = \frac{pos(A) - neg(A)}{T(A) + T(B)} \quad (3)$$

In Equation (3), $S(A)$ refers to the sentiment score of A party, $pos(A)$ and $neg(A)$ refer to the sum of positive tweets and negative tweets for A party, respectively, and $T(A)$ and $T(B)$ refer to the sum of tweets for A and B parties, respectively. The party with the largest indicator value will be the winner.

Wang and Gan [14] have proposed the popularity of election candidates using Equation (4). Their proposed method has been used to predict the result of 2017 French presidential election.

$$P(A) = \left[\frac{pos(A)}{pos(A) + neg(A)} \right] \left[\frac{T(A)}{T(A) + T(B)} \right] \quad (4)$$

$P(A)$ in Equation (4) represents the popularity of party A.

Wicaksono [15] proposed a method based on sentiment analysis using Equation (5), to predict the outcome of 2016 US presidential election. Based on this

equation, the Success Rate (SR) of each party in an election is calculated, and the party that gets a higher score is predicted as the winner of the election:

$$SR(A) = \frac{pos(A)+neg(B)}{T(A)+T(B)} \quad (5)$$

where SR in Equation (5) represents the success rate of party A .

The three recent related articles introduced above have two shortcomings: firstly, they delay the prediction until election day and secondly, they are not sufficiently accurate in prediction. But as it will be shown in the next sections, these two problems have been solved in the proposed methods.

3. THE PROPOSED METHOD

This section introduces the methods proposed for election prediction. Figure 1 shows the general structure of the proposed method.

The sum of the tweets received are grouped on the basis of how many days prior to the election the prediction is made. For example, if one aims to make a prediction one week before the election, the tweets should be grouped at one-week intervals. In the next step, the intended features for each group such as sentiment scores and re-tweet numbers for each tweet are obtained. Then, based on the proposed methods, an indicator value at each interval is calculated for each party. Now, with a trace of indicator values at successive intervals, the subsequent indicator values can be predicted using the aging estimation method. Finally, the party or candidate

with larger predicted values can be introduced as the likely winner. The three newly-proposed indicators are described with details in the following sections.

3. 1. Using the Sentiment Score Feature This indicator is introduced so that the tweets with different sentiment scores will have different effects on indicator values. Therefore, in the first proposed indicator, Sentiment Score ratio (SSr), the ratio of the sum of positive scores to negative scores for each party or candidate at each interval is calculated by Equation (6).

$$SSr_i(A) = \frac{\sum_{t \in T} PSS_{i,t}(A)}{\sum_{t \in T} NSS_{i,t}(A)} \quad (6)$$

In Equation (6), $SSr_i(A)$ refers to the indicator value for A party at i^{th} interval. $PSS_{i,t}(A)$ stands for the t tweet positive sentiment score for A party at i^{th} interval and T refers to all the existing tweets at that interval. $NSS_{i,t}(A)$ stands for the t tweet negative sentiment score for A party at i^{th} interval.

3. 2. Using Re-Tweet Number A more important tweet is usually re-tweeted with a higher frequency [16]. It has been tried in the second proposed indicator, RTr (ReTweet ratio), to examine the effect of this feature on election prediction. Hence, the ratio of the sum of re-tweets for each positive tweet to the sum of re-tweets for each negative tweet is calculated for each political party at different intervals (Equation (7)).

$$RTr_i(A) = \frac{\sum_{t \in T} PRT_{i,t}(A)}{\sum_{t \in T} NRT_{i,t}(A)} \quad (7)$$

In Equation (7), $RTr_i(A)$ refers to the indicator value for A party at i^{th} interval. $PRT_{i,t}(A)$ stands for the re-tweets number related to the positive t tweet at i^{th} interval and T stands for all the existing tweets at that interval. $NRT_{i,t}(A)$ refers to the re-tweets number related to the negative t tweet at i^{th} interval. It should be pointed out that the value of this feature for the non-re-tweeted tweets is set to one.

3. 3. A Combined Indicator The third indicator is, in fact, a combination of the two previous indicators and is obtained from the ratio of the sum product of sentiment scores and the re-tweet number for positive tweets to the negative tweets at each interval (Equation (8)).

$$SSRTr_i(A) = \frac{\sum_{t \in T} PSS_{i,t}(A) * PRT_{i,t}(A)}{\sum_{t \in T} NSS_{i,t}(A) * NRT_{i,t}(A)} \quad (8)$$

In Equation (8), $SSRTr_i(A)$ refers to the indicator value for A party at i^{th} interval.

3. 4. Prediction To predict indicator values at future intervals, the aging estimation method, which is based on an exponential averaging of previous observations, is used (Equation (9)).

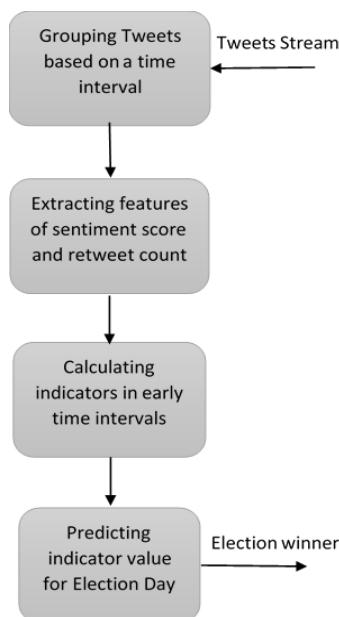


Figure 1. General structure of the proposed method

$$A_{i+1} = \alpha O_i + (1 - \alpha)A_i \quad (9)$$

In Equation (9), A_{i+1} is the predicted indicator value at the next interval ($i+1$). O_i and A_i refer to the observed value and the predicted value at the current interval, respectively. α is a parameter within $[0,1]$ which shows the effect of the observations history and the recent predictions. The closer the value of α is to one, the more weight the recent observations will have and the greater their effect will be on the predicted value. The closer it is to zero, the more the old observations, which are involved in calculating the average, will be (Equation (10)).

$$A_{i+1} = \alpha O_i + (1 - \alpha)\alpha O_{i-1} + \dots + (1 - \alpha)^{i+1}A_0 \quad (10)$$

The use of closer-to-one values for α is an advantage because the quick changes in recent observations are reflected in the indicator value more quickly, and prediction accuracy increases considerably [17]. When the predictions are to be announced, the party with the larger indicator value will be introduced as the likely winner.

4. Experiments and Results

In this section, the proposed methods are tested on two Twitter datasets related to the 2016 and 2020 US presidential elections. They are compared to the methods introduced Yavari et al. [5] Oueslati et al. [12], Singh et al. [13], Wang and Gan [14], Wicaksono [15] in terms of prediction accuracy and result. The proposed indicators and compared methods are all implemented with Python programming language in a computer system with Intel core i5 and 2 GB main memory specifications.

4.1. Dataset The first dataset includes almost 26 million tweets about 2016 US presidential election collected at the interval between August 30th to November 11th (election date)¹. A rare incident happened in 2016 election where the Republicans (Donald Trump) won the election, although they had fewer votes than the Democrats (Hillary Clinton). Therefore, this dataset can be useful for investigating the tolerance of the proposed methods.

The second dataset includes about 24 million tweets related to 2020 US presidential at the interval between July 1st to November 12th [18].

In these datasets, using the sentiment analysis method of VADER (Valence Aware Dictionary and sEntiment Reasoner) [19], each tweet has been assigned a score in the range $[-1..+1]$. A value of +1 indicates strong positive feelings, and -1 indicates strong negative feelings. VADER is actually a rule and dictionary-based sentiment analysis tool. Due to its good performance, VADER

method has been widely used for sentiment analysis of social media texts.

4.2. Results of Experiment This section reports on the prediction of 2016 and 2020 US presidential elections using the three proposed indicators and the methods introduced Yavari et al. [5] Oueslati et al. [12], Singh et al. [13], Wang and Gan [14], Wicaksono [15]. Indicator values at one-day, one-week and two-week intervals are displayed in Tables 1 and 2. As it was mentioned earlier, a larger value for a party indicates winning the election. Hence, larger indicator values are in bold face.

In Table 1, knowing that the Democratic Party won 2020 US presidential election, in addition to Singh, Wang, and Wickasono methods, one of the proposed methods in this paper (*SSRTr*) also made wrong

TABLE 1. Indicator values based on 2020 US presidential election Twitter datasets

Indicators	Number of days until the election					
	One Day		One Week		Two Weeks	
	Dem	Rep	Dem	Rep	Dem	Rep
<i>SSr</i>	2.7	1.29	1.54	1.14	1.42	1.06
<i>RTr</i>	5.31	4.65	4.27	3.25	3.5	2.72
<i>SSRTr</i>	6.5	2.58	2.32	2.33	1.8	1.88
Yavari et al. [5]	3.64	2.41	2.67	2.06	2.52	1.93
Oueslati et al. [12]	0.87	0.82	0.86	0.79	0.4	0.45
Singh et al. [13]	0.08	0.21	0.09	0.2	0.01	0.2
Wang and Gan [14]	0.16	0.49	0.17	0.49	0.17	0.47
Wicaksono [15]	0.44	0.54	0.44	0.55	0.44	0.56

TABLE 2. Indicator values based on 2016 US presidential election Twitter datasets

Indicators	Number of days until the election					
	One Day		One Week		Two Weeks	
	Dem	Rep	Dem	Rep	Dem	Rep
<i>SSr</i>	2.09	2.21	1.55	1.77	1.58	1.71
<i>RTr</i>	4.38	4.56	3.87	4.07	3.36	3.4
<i>SSRTr</i>	2.4	2.36	1.99	1.98	1.72	1.83
Yavari et al. [5]	1.76	1.74	1.43	1.58	1.46	1.55
Oueslati et al. [12]	0.52	0.65	0.95	0.85	0.48	0.32
Singh et al. [13]	0.08	0.05	0.03	0.05	0.04	0.03
Wang and Gan [14]	0.24	0.35	0.33	0.32	0.22	0.37
Wicaksono [15]	0.248	0.252	0.229	0.25	0.239	0.252

¹ <https://data.world/alexfilatov/2016-USA-presidential-election-tweets>

predictions about the election at one-week and two-week intervals. Oueslati's method has succeeded in predicting the result in the short time periods of one day and one week, but it has predicted incorrectly for the time period of two weeks. Therefore, for examining the 2020 dataset, the *SSr* and *RTr* indicators made accurate predictions at different intervals.

Table 2 displays the use of different indicators on 2016 US presidential election Twitter datasets. As it can be seen in Table 2, only the two *SSr* and *RTr* indicators managed to accurately predict the election at all intervals (In 2016, the Republicans won the election, although the Democrats had more votes!). The Yavari and Wickasono methods wrongly predicted the election only at the one-day interval with a slight difference in indicator values. Ouesati's method has also managed to make a correct prediction only in one-day interval.

Considering the results in Tables 1 and 2, it seems that the *SSr* and *RTr* indicators predicted more consistently than other indicators.

Figure 2, shows the average prediction accuracy of the three proposed indicators and method introduced by Yavari et al. [5]. The accuracy of predicting the value of the indicator for each of the parties was obtained based on Equation (11).

$$Accuracy = 1 - \text{mean} \left[\frac{abs(A-O)}{O} \right] \quad (11)$$

In Equation (11), A is the predicted values and O is the observed values.

For the two indicators *RTr* and *SSRTr*, due to the fact that they are based on the number of retweets, larger jumps and changes occur in the indicator values. Therefore, the accuracy of predicting the value of the indicator is lower than other methods. But the accuracy of predicting the value of the indicator using *SSr* and the one proposed by Yavari et al. [5] is very good.

According to the results of the experiments, the two proposed indicators, *SSr* and *RTr*, have succeeded in correctly predicting the results of the last two American elections.

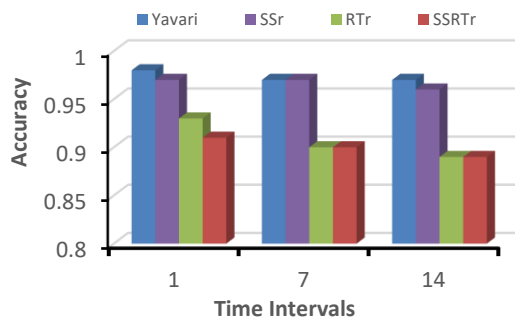


Figure 2. Average prediction accuracy of indicators for the two Republican and Democratic parties

5. CONCLUSION

In this paper, using such features as sentiment scores and re-tweet numbers for each tweet, three indicators were proposed for election prediction. The first indicator (*SSr*) is calculated based on the ratio of the sum of positive sentiment scores to negative sentiment scores at each interval. The second indicator (*RTr*) shows the ratio of the sum of positive re-tweets to negative re-tweets. Finally, the third indicator (*SSRTr*) was defined as a combination of the two previous indicators. After grouping the tweets based on an interval, the indicator values for each party at each interval are calculated. Then, using the aging estimation method, the values for these indicators on the election data are predicted. The party with the larger indicator value will be introduced as the winner. The advantages of the proposed method are the simplicity of calculations, easy understanding, and prediction of election results in arbitrary time intervals. Of course, fake messages or messages generated by social network bots can affect the proposed method as well as the methods of others. Comparisons of the proposed methods with other related methods for 2016 and 2020 US presidential elections indicate that the two *SSr* and *RTr* methods made accurate predictions for both datasets at all intervals. However, the *SSRTr* indicator and other indicators being compared did not make accurate and consistent predictions.

6. REFERENCES

- Jennings, W. and Wlezien, C., "Election polling errors across time and space", *Nature Human Behaviour*, Vol. 2, No. 4, (2018), 276-283. <https://doi.org/10.1038/s41562-018-0315-6>
- Antonakaki, D., Fragopoulou, P. and Ioannidis, S., "A survey of twitter research: Data model, graph structure, sentiment analysis and attacks", *Expert Systems with Applications*, Vol. 164, No., (2021), 114006. <https://doi.org/10.1016/j.eswa.2020.114006>
- Yavari, A., Hassanpour, H., Rahimpour Cami, B. and Mahdavi, M., "Event prediction in social network through twitter messages analysis", *Social Network Analysis and Mining*, Vol. 12, No. 1, (2022), 78. <https://doi.org/10.1007/s13278-022-00911-x>
- Erfanian, P.Y., Cami, B.R. and Hassanpour, H., "An evolutionary event detection model using the matrix decomposition oriented dirichlet process", *Expert Systems with Applications*, Vol. 189, (2022), 116086. <https://doi.org/10.1016/j.eswa.2021.116086>
- Yavari, A., Hassanpour, H., Rahimpour Cami, B. and Mahdavi, M., "Election prediction based on sentiment analysis using twitter data", *International Journal of Engineering, Transactions B: Applications*, Vol. 35, No. 2, (2022), 372-379. doi: 10.5829/IJE.2022.35.02B.13.
- Zhou, Z., Serafino, M., Cohan, L., Caldarelli, G. and Makse, H.A., "Why polls fail to predict elections", *Journal of Big Data*, Vol. 8, No. 1, (2021), 1-28.
- Wang, J. and Yang, Y., "Tweet retweet prediction based on deep multitask learning", *Neural Processing Letters*, (2022), 1-14. doi: 10.1007/s11063-021-10642-3.
- Chauhan, P., Sharma, N. and Sikka, G., "The emergence of social media data and sentiment analysis in election prediction",

- Journal of Ambient Intelligence and Humanized Computing*, Vol. 12, (2021), 2601-2627. <https://doi.org/10.1007/s12652-020-02423-y>, (2021)
9. Ceron, A., Curini, L. and Iacus, S.M., "Using sentiment analysis to monitor electoral campaigns: Method matters—evidence from the united states and italy", *Social Science Computer Review*, Vol. 33, No. 1, (2015), 3-20. doi: 10.1177/0894439314521983.
 10. Burnap, P., Gibson, R., Sloan, L., Southern, R. and Williams, M., "140 characters to victory?: Using twitter to predict the uk 2015 general election", *Electoral Studies*, Vol. 41, (2016), 230-233. doi: 10.1016/j.electstud.2015.11.017.
 11. Thelwall, M., Buckley, K., Paltoglou, G., Cai, D. and Kappas, A., "Sentiment strength detection in short informal text", *Journal of the American Society for Information Science and Technology*, Vol. 61, No. 12, (2010), 2544-2558. doi: 10.1002/asi.21416
 12. Oueslati, O., Hajhmida, M.B., Ounelli, H. and Cambria, E., "Sentiment analysis of influential messages for political election forecasting", in Computational Linguistics and Intelligent Text Processing: 20th International Conference, CICLing 2019, La Rochelle, France, April 7–13, 2019, Revised Selected Papers, Part II, Springer., (2023), 280-292.
 13. Singh, P., Dwivedi, Y.K., Kahlon, K.S., Pathania, A. and Sawhney, R.S., "Can twitter analytics predict election outcome? An insight from 2017 punjab assembly elections", *Government Information Quarterly*, Vol. 37, No. 2, (2020), 101444. doi: 10.1016/j.giq.2019.101444.
 14. Wang, L. and Gan, J.Q., "Prediction of the 2017 french election based on twitter data analysis", in 2017 9th Computer Science and Electronic Engineering (CEECE), IEEE., (2017), 89-93.
 15. Wicaksono, A.J., "A proposed method for predicting us presidential election by analyzing sentiment in social media", in 2016 2nd international conference on science in information technology (ICSITech), IEEE., (2016), 276-280.
 16. Firdaus, S.N., Ding, C. and Sadeghian, A., "Retweet prediction based on topic, emotion and personality", *Online Social Networks and Media*, Vol. 25, (2021), 100165. <https://doi.org/10.1016/j.osnem.2021.100165>
 17. Abraham, S. and Greg, G., *Operating system concepts essentials.-2nd*. 2014, Wiley.
 18. Sabuncu, İ., "USA nov. 2020 election 20 mil", *Tweets (With Sentiment And Party Name Labels) Dataset*, Vol. 20, (2020). doi: 10.21227/25te-j338.
 19. Hutto, C. and Gilbert, E., "Vader: A parsimonious rule-based model for sentiment analysis of social media text", in Proceedings of the international AAAI conference on web and social media. Vol. 8, (2014), 216-225.

Persian Abstract

چکیده

پیش بینی رویدادهای اجتماعی از جمله نتیجه انتخابات با استفاده از داده های شبکه اجتماعی، یکی از موضوعات مورد علاقه پژوهشگران در دهه اخیر بوده است. از اینرو در این مقاله، سه اندیکاتور برای پیش بینی نتیجه انتخابات پیشنهاد شده است. روش کار بدین گونه است که ابتدا توئیتهای بر اساس یک پنجره زمانی گروه بندی می شوند. سپس مقادیر اندیکاتورهای در هر پنجره زمانی و برای هر حزب یا نامزد انتخابات بر مبنای نمره احساسی و تعداد بازتوییت هر پیام در توئیتر محاسبه می شود. سپس با استفاده از روش تخمین سالمندی، مقادیر اندیکاتورهای مربوط به هر حزب در روز انتخابات پیش بینی می شوند. مقدار اندیکاتور پیش بینی شده برای هر حزب که بیشتر باشد، بعنوان پیروز انتخابات تعیین می شود. نتایج آزمایشات بر روی داده های توئیتر مرتبط با انتخابات ریاست جمهوری آمریکا در سالهای 2016 و 2020 در یک بازه زمانی چهار ماه نشان می دهد که می توان با دقت خوبی مقادیر اندیکاتور و نهایتاً نتیجه انتخابات را پیش بینی نمود.



Experimental Analysis of Square Position on Variable Displacement Electrohydraulic Actuation System by Open Loop Control

G. Kumar*, N. P. Mandal

Department of Mechanical Engineering, National Institute of Technology Patna, Patna, Biha, India

PAPER INFO

Paper history:

Received 24 February 2023

Received in revised form 04 May 2023

Accepted 06 May 2023

Keywords:

Actuator Position Control

Square Reference Position

Open-loop Control

Correlation Coefficient

ABSTRACT

Electrohydraulic actuation systems offer definitive position control and an energy-efficient solution. Such systems are widely used in mobile machinery, robotics, and various stationary systems. Achieving good control of actuator position of the variable displacement electrohydraulic actuation system by an open loop control is the objective of this study. For square position (reference position) control, amplitude is taken as 0.1 m, at 0.05, 0.15 and 0.25 Hertz of frequency. Square position control is accomplished with LabVIEW algorithm through the application of compact RIO controller having input and output module. Appropriate control of voltage supply is obtained, when response position and reference position show appropriate accuracy. A higher Pearson's correlation coefficient near to 1 and lower the Mean absolute error, Mean deviation of error and standard deviation of error represent the best response position. It is observed that highest value of correlation coefficient achieved at 0.05 Hertz of frequency for response R3. At a lower frequency, square position control is better with higher correlation coefficient and lowest values of errors.

doi: 10.5829/ije.2023.36.06c.17

1. INTRODUCTION

Electro-hydraulic actuator systems are essential in the engineering sector due to their compactness, ability to produce extremely high forces with excellent control accuracy, and high power-to-weight ratio [1]. Because of these features, there is a lot of curiosity among engineers and researchers about how to regulate force and position in an electro-hydraulic (EHA) system. Nowadays, electrohydraulic systems have become common in a wide range of manufacturing machines, Aircraft, mining equipment, fatigue testing, and various forms of automation, particularly in the automotive industry. Many applications requirements are quick responses, linear motions, and precise placement of heavy objects and these requirements are fulfilled with application of appropriate controller in the electrohydraulic actuation systems. For vehicle suspensions, Sam et al. [2] and Alleyne and Hedrick [3] have used hydraulic systems to compensate the vibrations. Physical modelling of hydraulic system was used by Alleyne and Liu [4], Liu

and Alleyne [5] successfully predicted the dynamics, including the friction model. This modelling has been done for the purpose of electro-hydraulic system modeling. In certain situations, obtaining a model might be extremely difficult or even impossible due to its high level of complexity and nonlinearity. The modelling and controller design are more challenging because of the electro-hydraulic control system's inherent nature includes a variety of uncertainties, significant nonlinearities, and time-varying features. Some causes of nonlinearity in the electro-hydraulic control system are nonlinear flow and pressure behaviors, friction inside the actuator, trapped oils in actuator chambers, and compressibility of oil. These factors make system modelling and control even more challenging.

Closed-loop and open-loop control are the two different types of control techniques that are utilized for the electrohydraulic actuation system. Several closed-loop control strategies, including back-stepping control [6-9], advanced adaptive control [10-12], sliding mode control [13], PID control [14], intelligent control [15],

*Corresponding Author Institutional Email: gulshan.me19@nitp.ac.in
(G. Kumar)

and unknown dynamics estimator control [16, 17], have been developed for use in control application of electrohydraulic systems. By combining feedback and dynamics estimation, these approaches can achieve extremely high control accuracy. However, closed-loop control for hydraulic systems is enormously complex and costly because a closed-loop electrohydraulic actuation system must include servo valves, a controller, and a variety of sensors. As a result of its complexity with expensiveness, closed-loop control is not appropriate for extreme conditions such as mining sites, so open-loop control is preferred in these cases. The open-loop control for hydraulic systems is primarily comprised of throttling valves [18], sequential valves [19, 20], and synchronous motors [21]. As a result of its ease of use and high level of dependability, this type of control is well-suited for extremely challenging working conditions. Position control of the actuator in an open loop for sinusoidal demand was discussed by Kumar and Mandal [22], and according to the results, up to 0.25 Hertz can be controlled in an open loop; after that, advanced control design is required for higher frequencies. In the research conducted by Sazonov et al. [23-25], an additive method of control for turbomachinery systems was discussed in details for the purpose of controlling the jet mesh system. This method of control is applicable in robotics and unmanned aerial vehicle systems. Manring and Fales [26] discuss the comparison of a pump control scheme to a valve control scheme. Multiple actuation demands can be fulfilled by valve control schemes, while pump-controlled schemes are safer, more robust, and more energy efficient (no throttling loss), so pump-controlled schemes are more demandable. In the present work, the VDEHA system is used, which is also a pump-controlled scheme. Sadeghi et al. [27] developed micro-position control system for shape memory alloy actuator using particle swarm optimisation. Developed control system gives excellent accuracy, which is suitable for application in micro-positioning. Fateh and Sadeghijaleh [28] developed voltage control strategy for tracking control of electric robot. Further, concluded that voltage control approach is better than the torque control approach.

In this experimental work, square position signals are used as the reference position signals for controlling the position of the hydraulic actuator of the VDEHA system in an open loop control. Square-position control is performed at 0.05 Hertz, 0.15 Hertz and 0.25 Hertz, which has an amplitude of 0.1 m. Control algorithms are prepared in LabVIEW and processed with a compact RIO controller. Control accuracy and error in position control are evaluated. Remaining part of this paper is organized as: in section 2, the VDEHA system is described in detail; in section 3, mathematical modelling is discussed; in section 4, results of position control and position error are presented; associated terms such as correlation coefficient and error calculations are described; and in

section 5, conclusions of using square position signals are discussed.

2. VARIABLE DISPLACEMENT ELECTRO HYDRO-STATIC ACTUATION (VDEHA) SYSTEM

Figure 1 presents a simplified schematic diagram of the VDEHA system. It is comprised of a symmetric hydraulic actuator, and the solenoid valves ('a' and 'b') are responsible for controlling the displacement of the actuator. The actuator moves a total length of 0.2 m in its entirety. To determine where the actuator is positioned, a linear variable differential transducer, also known as an LVDT, is utilized as a position sensor.

Figure 2 presents the experimental configuration of the VDEHA system that was used in the study. Table 1 has an overview of the components that make up the experimental rig in further detail. To interface between the personal computer (11) (LabVIEW programme) and VDEHA system, a real-time controller (12) with an input and output module is employed. NI 9215 and NI 9263 are voltage input and voltage output module, respectively.

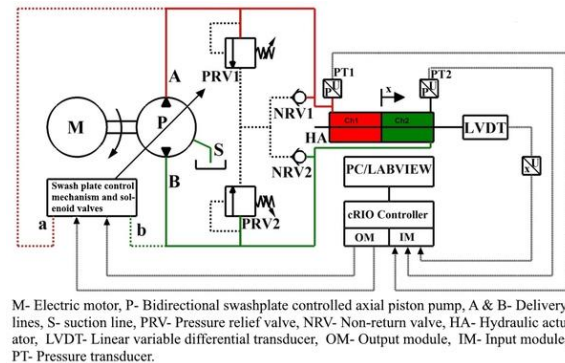
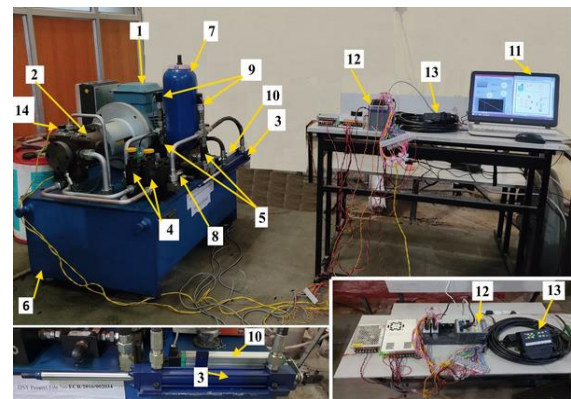


Figure 1. Schematic diagram of VDEHA system



(1) Electric motor, (2) Variable displacement axial piston pump, (3) Hydraulic actuator, (4) Pressure relief valves, (5) Non-return valves, (6) Oil tank, (7) Hydraulic accumulator, (8) Accumulator safety block, (9) Pressure transducers, (10) LVDT, (11) Personal computer, (12) Real-time controller, (13) Analogue amplifier, (14) Solenoid valves.

Figure 2. Experimental setup of VDEHA system

TABLE 1. Experimental components details

Label	Component	Remarks
1	Electric motor	3-phase Fixed rotational speed.
2	Variable displacement axial piston pump	Rexroth Flow = 119 L/min Displacement volume =28CC/Rev Max pressure = 45 MPa
3	Hydraulic actuator	Symmetric Total displacement = 0.2 m
4	Pressure-relief valves	Max operating pressure = 25MPa Max flow = 100 L/min
5	Non-return valves	
6	Oil Tank	
7	Hydraulic accumulator	Volume = 6L Pre-charge pressure = 6MPa
8	Accumulator safety block	
9	Pressure transducers	Measuring pressure =0-25MPa
10	LVDT	Measuring position = 0 - 0.2 m
11	Personal computer	
12	Real time controller	Controller – NI9030 with (IM and OM)
13	Analogue amplifier	Input = 10 to 32 V Output = 200 to 600 mA
14	Solenoid valves	Nominal resistance =23 Ω (at 20 ⁰ C)

Both of module have voltage signal range of $\pm 10V$ having sampling rate of 100kS/s/ch with resolution of 16-Bit. These modules are used with compact reconfigurable input output (c-RIO) system.

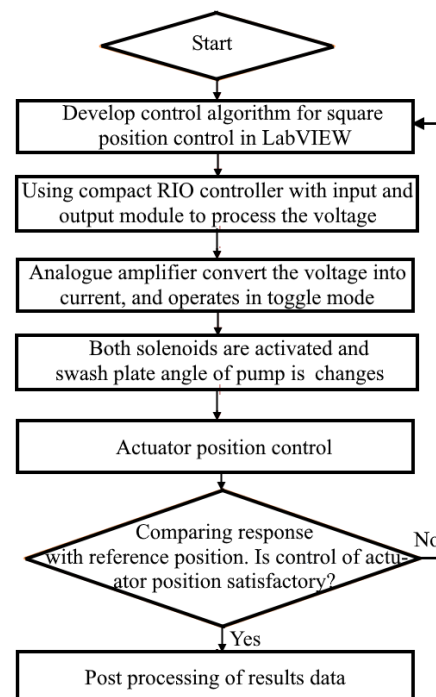
The response voltage signal from the LVDT (10), is received by the input module (NI 9215).

The output module (NI9263) sends the voltage signal to an analogue amplifier (13); it works in toggle mode of operation, and then electric current is supplied to solenoid valves (14). A variable-displacement axial piston pump (2) delivers the pressurized flow with the help of a fixed-speed electric motor (1). Pressure transducers (9) are used to measure the pressure in the actuator's (3) chambers. The hydraulic accumulator (7) is treated as a detached component, so it is not shown in the schematic diagram. The total displacement of the hydraulic actuator is 0.2 m, and its position is measured by an LVDT. Because of the LVDT is physically connected to the hydraulic actuator, the positions of the actuator and the LVDT are equivalent.

Controlling the flow of the pump is mostly dependent on the current that the amplifier generates. The flow rate and direction of actuator movement are based on the position of the spool valve (internal part) of the pump. An electric connection is established between a personal computer, an LVDT, a real-time controller, an analogue amplifier, and solenoid valves. To create a real-time control programme, a panel of control and simulation loops in LabVIEW software is used. LabVIEW is utilized in the manner of interfacing the hardware components of the controller, like the NI compact RIO controller, with software in the system to perform measurement and control actions. It has the ability to integrate hardware in a way that is unrivalled, and it comes with a large number of libraries that are already built in. These features make it ideal for performing sophisticated data processing during experimentation and simulation. The controlling action is performed in open loop control, which is based on the visualization of the response position with respect to the reference position. Several experiments are carried out, with the response and reference positions close to each other being considered. A flow chart of control methodology is shown in Figure 3.

3. MATHEMATICAL MODELING

Figure 4 shows the swash plate control mechanism and solenoid valves section of the schematic diagram (Figure 1) of the VDEHA system. The solenoid valves (14) link

**Figure 3.** Flow chart of control methodology

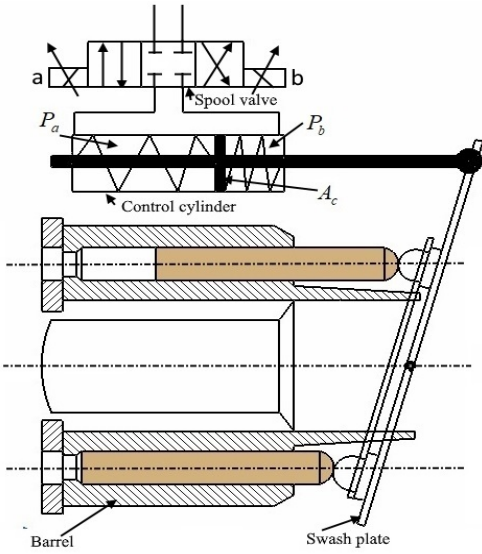


Figure 4. Swashplate control mechanism with solenoid spool valve

with the swash plate and control the pump's flow. Deflection in the swashplate either increases or decreases the displacement volume of the pump. The flow direction of the pump is determined by the direction of the deflection of the swashplate.

The control cylinder is the internal component of the pump of the VDEHA system.

In simplified form, equation of motion of control cylinder can be written as [29]:

$$m_c \ddot{x} = A_c (P_a - P_b) - F_f - F_s \tag{1}$$

where m_c is the mass of piston, A_c is the area of piston of control cylinder, P_a and P_b are chamber pressure of control cylinder, F_f is frictional force, and F_s is the self-adjusting force of controlling cylinder.

Pressure inside the chambers of control cylinder is expressed as [29]:

$$V_a \dot{P}_a = K(Q_a - A_c \dot{x} - k_{la} P_a - k_{li} (P_a - P_b)) \tag{2}$$

$$V_b \dot{P}_b = K(Q_b - A_c \dot{x} - k_{lb} P_b - k_{li} (P_b - P_a)) \tag{3}$$

where V_a and V_b are volume of chamber 'a' and 'b'.

K is the bulk modulus of the oil and are the leakage through chamber 'a' and 'b', and k_{li} is the internal leakage.

Flow through the spool valve by assuming $Q_a = Q_b$ is written as [29]:

$$Q_{sv} = Q_a = Q_b = B \cdot y \sqrt{(|P_s - \Delta P|) / 2 \text{sign}(P_s - \Delta P \text{sgn}(y))} \tag{4}$$

where $\Delta P = P_a - P_b$, B is the spool valve constant, y is the spool position of the valve, and P_s is the supply pressure.

Solenoid valves allow the percentage of flow corresponding to current supply, it is expressed as:

$$Q_{sv\%} = i / 4 - 50, \text{ when } 200\text{mA} \leq i \leq 600\text{mA} \tag{5}$$

where, $Q_{sv\%}$ is the flow through spool valve in percentage, and i is the current in mA.

An analogue amplifier is used to generate current from low voltage. In this work, the analogue amplifier operates in a toggle mode, so both solenoids operate independently. Only one solenoid is operational at any given time. Voltage and current relation are expressed as:

$$i = \begin{cases} 89.47 + 26.32 \cdot V_s, & \text{when } 4.2 \leq V_s \leq 8 \\ 0, & \text{when } 3.8 \leq V_s \leq 4.2 \\ 300 - 26.32 \cdot V_s, & \text{when } 0 \leq V_s \leq 3.8 \end{cases} \tag{6}$$

where V_s is the voltage supply to the solenoid valves.

When voltage belongs to 4.2 to 8 volts then solenoid 'a' is working, similarly for 0 to 3.8 volts, solenoid 'b' is working.

Equations (5) and (6) are the calibrated equations for the solenoid valves and analogue amplifier respectively. The behavior of actuator piston with respect to actuator position is expressed as:

$$\ddot{x}_{ap} = \frac{\pi}{4m_a} (d_{piston}^2 - d_{rod}^2) (P_A - P_B) \tag{7}$$

where x_{ap} is the actuator position, m_a is the mass of actuator, P_A and P_B are the chambers pressure of the actuator, and it is the same as the delivery pressure of the pump. To measure the pressure of chambers of actuator, pressure transducers are used.

Position of actuator is measured by LVDT, the calibration equation of the LVDT is written as:

$$x_{ap} = 0.04V_o + 0.004 \tag{8}$$

where V_o is the output voltage of LVDT.

Basically, in this work, voltage supply to the amplifier is controlled, in that voltage control actuating action of solenoid valves are performed, as a result actuator is controlled.

4. RESULT AND DISCUSSION

4. 1. Correlation Coefficient

In this work, Pearson's correlation coefficient [30] is used to determine the closeness of the response position of the actuator with the reference position of the actuator. There are three possibilities on which Pearson's correlation coefficient (r) depends: (1) both the variables (reference

and response) are either simultaneously increasing or decreasing; (2) one variable is increasing, and another is decreasing; and (3) there is no relation between these two variables. For case 1, the correlation coefficient (r) approaches a value of 1. For case 2, ' r ' approaches -1, and for case 3, ' r ' equals 0. In the current work, both variables either increase or decrease, so the ' r ' value approaches 1. According to Jothivenkatachalam et al. [31], ' r ' between 0.8 and 1.0 is highly significant, and ' r ' between 0.6 and 0.8 is moderately significant.

The equation of correlation coefficient in term of reference and response position is expressed as:

$$r = \frac{\sum (x_{ap} - \bar{x}_{ap})(x_{apr} - \bar{x}_{apr})}{\sqrt{\sum (x_{ap} - \bar{x}_{ap})^2 \sum (x_{apr} - \bar{x}_{apr})^2}} \quad (9)$$

where r is correlation coefficient between x_{ap} and x_{apr} .

Within a sample, x_{ap} is the response position and x_{apr} is the reference position of actuator, \bar{x}_{ap} is the mean of the x_{ap} , and \bar{x}_{apr} is the mean of the x_{apr} .

4. 2. Responses of Actuator Position

Closed-loop control for hydraulic systems is enormously complex and costly because it must include servo valves, a controller, and a variety of sensors. As a result of its complexity with expensiveness, closed-loop control is not appropriate for extreme conditions such as mining sites, so open-loop control is preferred in these cases. Further, when force is more essential than precision, open loop control is the preferred option. Because it is not always essential to precisely regulate the position of the actuator, open-loop control is employed in place of closed-loop control.

Numerous industrial applications have regular needs for different types of tracking requirements, such as square, sinusoidal, triangular, step, or their combination. So, application-oriented tracking requirements have been experimentally tested. In previous study of the VDEHA system by Kumar and Mandal [22], the position of the hydraulic actuator was controlled with sinusoidal demand signals in the range of 0.1 to 0.25 Hertz, and no other work was performed on this novel VDEHA system. In this experimental work, square position signals are used as the reference position signals for position control of the hydraulic actuator of the VDEHA system in an open loop control. Square-position control is performed under suggested range of frequency of 0.05, 0.15 and 0.25 Hertz, with amplitude of 0.1 m. Figures 5-7 show the results of the square position control. The equation for square position can be expressed as:

$$x_{apr} = \begin{cases} 0, & 0 \leq t < \frac{T}{4} \text{ and } \frac{3T}{4} < t \leq T \\ 1, & \frac{T}{4} \leq t \leq \frac{3T}{4} \end{cases} \quad (10)$$

where, T is the cycle time, $T = 1/f$ and t is time in second, and f is frequency in Hertz.

Equation (11) is used to determine the positional inaccuracy that is error (e).

$$e = x_{apr} - x_{ap} \quad (11)$$

Figure 5 shows the responses of actuator (Figure 5(a)), and error in position (Figure 5(b)) at 0.05 Hertz of the frequency of the square position control. In this case, response R3 gives the highest value of the correlation coefficient ($r = 0.957$), followed by other responses at the same frequency of 0.05 Hertz. The voltage supply pattern shown in Figure 5c corresponds to the better position response 'R3'.

All four variations in voltage corresponding to all four response positions are not shown because minor difference in voltage causes overlap in curve.

At 0.15 Hertz (Figure 6(a)), R3 response of the actuator position has the highest value of the correlation coefficient ($r = 0.90$). Magnitude of error (Figure 6(b)) with respect to 0.05 Hertz of frequency increases in this case.

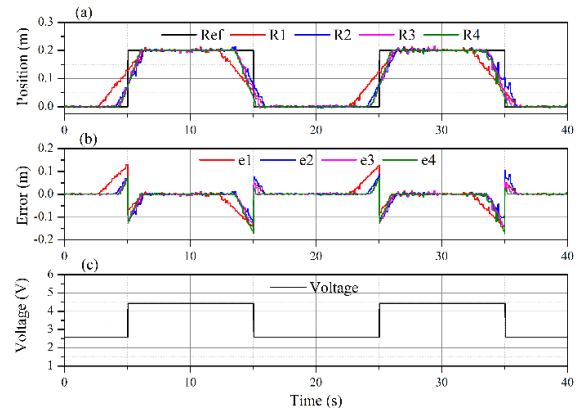


Figure 5. (a) Actuator position responses, (b) Error curve, and (c) Voltage supply, at 0.05 Hertz of frequency

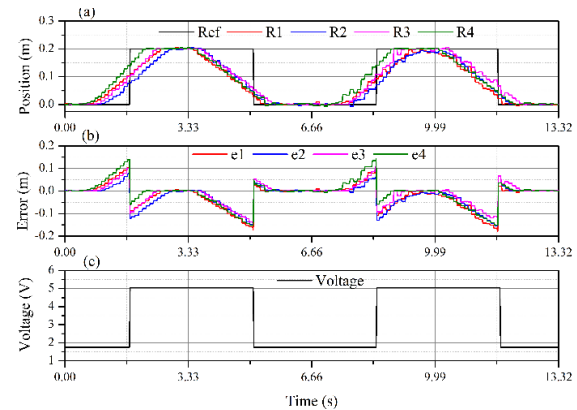


Figure 6. (a) Actuator position responses, (b) Error curve, and (c) Voltage supply, at 0.15 Hertz of frequency

At 0.25 Hertz (Figure 7(a)) of frequency in the square position, the actuator is unable to complete the total displacement of 0.2 m, and the magnitude of error (Figure 7(b)) is also higher than at 0.05 Hertz and 0.15 Hertz of frequency. At 0.25 Hertz, R4's response has a higher value of the correlation coefficient ($r = 0.849$).

Figure 8(a) shows the correlation coefficient (r) variation with respect to the responses (R1, R2, R3, and

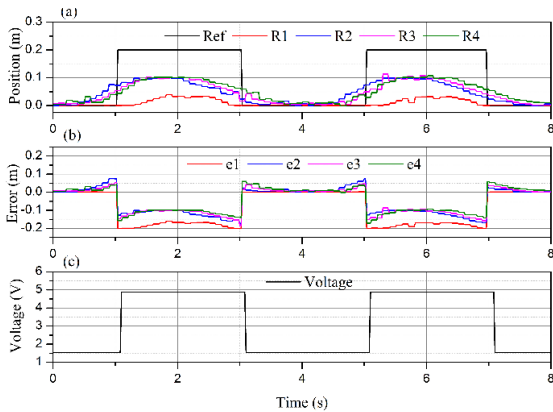


Figure 7. (a) Actuator position responses, (b) Error curve, and (c) Voltage supply, at 0.25 Hertz of frequency

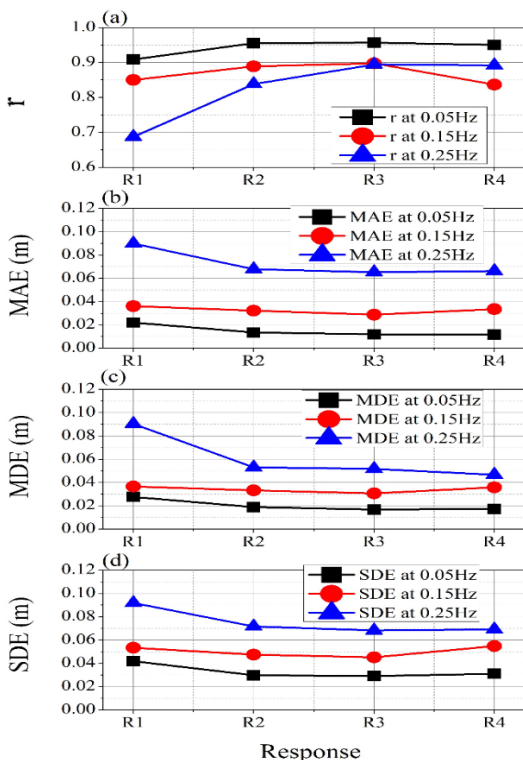


Figure 8. (a) Correlation coefficient (r), (b) Mean absolute error (MAE), (c) Mean deviation of error (MDE), and (d) Standard deviation of error (SDE)

R4) at frequencies of 0.05 Hertz, 0.15 Hertz and 0.25 Hertz, and the result shows that at 0.05 Hertz of frequency, response R3 shows a higher value of "r." It means that the position response is very close to the reference position. In Figure 8(b), mean absolute error curves are shown; their minimum value is 0.011 m; similarly, MED (Figure 8(c)) and SDE (Figure 8(d)) also have values of 0.0195 m and 0.03 m, respectively, at 0.05 Hertz of frequency.

The variation in "r" is minimum for 0.05 Hertz and maximum for 0.25 Hertz. It indicates that the accuracy of position control is better at 0.05 Hertz. MAE is maximum at 0.25 Hertz; variation in MAE between R1 and R2 is higher compared to variation of R2 with R3 and R4. In comparison of best-to-best "r" value of responses, "r" at 0.05 Hertz is 6.33% and 12.72% better than at 0.15 Hertz and 0.25 Hertz respectively. The variation in mean deviation of error (MDE) is at its minimum at 0.15 Hertz, while the minimum MDE is at 0.05 Hertz. MDE indicates how far the response signal is from the mean response signal. The minimum value of SDE indicates that the maximum number of response data is very close to its mean data, and the minimum SDE is observed at 0.05 Hertz of frequency.

5. CONCLUSIONS

The experimental results show that open loop control can perform satisfactorily under several square position controls with frequencies of 0.05, 0.15, and 0.25 Hertz and amplitudes of 0.1 m. In this study, the correlation coefficient assesses control accuracy between response and reference position curves. The best value (higher) of the correlation coefficient is achieved for lower frequencies, and as frequency increases, the value of the correlation coefficient gets reduced. In comparison of best-to-best response, the correlation coefficient at 0.05 Hertz is 6.33% and 12.72% better than that at 0.15 Hertz and 0.25 Hertz respectively. Mean absolute error (MAE), mean deviation of error (MDE), and standard deviation of error (SDE) are minimum for lower frequencies, and as frequency increases, their value also increases. From an application point of view, square position control can be used for low frequencies if used in open loop control. For higher frequencies, advanced control techniques like feedforward, fuzzy, and sliding mode control are suggested.

6. ACKNOWLEDGEMENT

This work is supported by SERB, DST India (Project file no.- ECR/2016/002034).

7. REFERENCES

- Merritt, H.E., "Hydraulic control systems, 1967", *John Wiley & Sons, Inc.*, New York
- Sam, Y.M., Osman, J.H. and Ghani, M.R.A., "A class of proportional-integral sliding mode control with application to active suspension system", *Systems & Control Letters*, Vol. 51, No. 3-4, (2004), 217-223. doi: <https://doi.org/10.1016/j.sysconle.2003.08.007>
- Alleyne, A. and Hedrick, J.K., "Nonlinear adaptive control of active suspensions", *IEEE Transactions on Control Systems Technology*, Vol. 3, No. 1, (1995), 94-101. doi: 10.1109/87.370714.
- Alleyne, A.G. and Liu, R., "Systematic control of a class of nonlinear systems with application to electrohydraulic cylinder pressure control", *IEEE Transactions on Control Systems Technology*, Vol. 8, No. 4, (2000), 623-634. doi: 10.1109/87.852908.
- Liu, R. and Alleyne, A., "Nonlinear force/pressure tracking of an electro-hydraulic actuator", *Journal of Dynamics Systems, Measurement, and Control, Trans. of ASME*, Vol. 122, No. 1, (2000), 232-236. <https://doi.org/10.1115/1.482466>
- Guo, Q., Zhang, Y., Celler, B.G. and Su, S.W., "Backstepping control of electro-hydraulic system based on extended-state-observer with plant dynamics largely unknown", *IEEE Transactions on Industrial Electronics*, Vol. 63, No. 11, (2016), 6909-6920. doi: 10.1109/TIE.2016.2585080.
- Kaddissi, C., Kenne, J.-P. and Saad, M., "Indirect adaptive control of an electrohydraulic servo system based on nonlinear backstepping", *IEEE/ASME Transactions on Mechatronics*, Vol. 16, No. 6, (2010), 1171-1177. doi: 10.1109/TMECH.2010.2092785.
- Yao, J., Jiao, Z. and Ma, D., "Extended-state-observer-based output feedback nonlinear robust control of hydraulic systems with backstepping", *IEEE Transactions on Industrial Electronics*, Vol. 61, No. 11, (2014), 6285-6293. doi: 10.1109/TIE.2014.2304912.
- Gholipour, R., Khosravi, A. and Mojallali, H., "Suppression of chaotic behavior in duffing-holmes system using back-stepping controller optimized by unified particle swarm optimization algorithm", (2013). doi: 10.5829/idosi.ije.2013.26.11b.05.
- Yao, B., Bu, F., Reedy, J. and Chiu, G.-C., "Adaptive robust motion control of single-rod hydraulic actuators: Theory and experiments", *IEEE/ASME Transactions on Mechatronics*, Vol. 5, No. 1, (2000), 79-91. doi: 10.1109/3516.828592.
- Li, C., Chen, Z. and Yao, B., "Adaptive robust synchronization control of a dual-linear-motor-driven gantry with rotational dynamics and accurate online parameter estimation", *IEEE Transactions on Industrial Informatics*, Vol. 14, No. 7, (2017), 3013-3022. doi: 10.1109/TII.2017.2773472.
- Yao, J., Jiao, Z., Ma, D. and Yan, L., "High-accuracy tracking control of hydraulic rotary actuators with modeling uncertainties", *IEEE/ASME Transactions on Mechatronics*, Vol. 19, No. 2, (2013), 633-641. doi: 10.1109/TMECH.2013.2252360.
- Ala, R. and Mehdi, S., "Systematic approach to design a finite time convergent differentiator in second order sliding mode controller", *International Journal of Engineering, Transactions B: Applications*, Vol. 26, No. 11, (2013), 1357-1368. doi: 10.5829/idosi.ije.2013.26.11b.11.
- Somasundaram, D. and Babu, S., "A closed loop control of quadratic boost converter using pid controller", *International Journal of Engineering, Transactions B: Applications*, Vol. 27, No. 11, (2014), 1653-1662. doi: 10.5829/idosi.ije.2014.27.11b.02.
- Saadat, M. and Garmsiri, N., "A new intelligent approach to patient-cooperative control of rehabilitation robots", *International Journal of Engineering, Transactions C: Aspects*, Vol. 27, No. 3, (2014), 467-474. doi: 10.5829/idosi.ije.2014.27.03c.15.
- Na, J., Li, Y., Huang, Y., Gao, G. and Chen, Q., "Output feedback control of uncertain hydraulic servo systems", *IEEE Transactions on Industrial Electronics*, Vol. 67, No. 1, (2019), 490-500. doi: 10.1109/TIE.2019.2897545.
- Huang, Y., Na, J., Wu, X. and Gao, G., "Approximation-free control for vehicle active suspensions with hydraulic actuator", *IEEE Transactions on Industrial Electronics*, Vol. 65, No. 9, (2018), 7258-7267. doi: 10.1109/TIE.2018.2798564.
- Wang, A., Kuang, L. and Zhang, X., "A study on flow coefficient of combined throttling groove in spool valves", *Journal of Zhejiang University-Science A*, Vol. 52, No. 2, (2018), 110-117.
- Abbas, R., Al-Baldawi, Y. and Abullah, F., "Theoretical and experimental study of hydraulic actuators synchronization by using flow divider valve", *Journal of Engineering and Development*, Vol. 18, No. 5, (2014), 283-293. doi: 10.1109/TIE.2018.2798564.
- Mahato, A.C., Ghoshal, S.K. and Samantaray, A.K., "Reduction of wind turbine power fluctuation by using priority flow divider valve in a hydraulic power transmission", *Mechanism and Machine Theory*, Vol. 128, (2018), 234-253. <https://doi.org/10.1016/j.mechmachtheory.2018.05.019>
- Mulyukin, V., Karelin, D. and Belousov, A., "A mathematical model of the controlled axial flow divider for mobile machines", in IOP Conference Series: Materials Science and Engineering, IOP Publishing. Vol. 134, (2016), 012039.
- Kumar, G. and Mandal, N.P., "Experimental study of position tracking control and pressure variation analysis on electrohydraulic system in open loop", *Materials Today: Proceedings*, Vol. 56, (2022), 2184-2188. <https://doi.org/10.1016/j.matpr.2021.11.497>
- Sazonov, Y.A., Mokhov, M.A., Gryaznova, I.V., Voronova, V.V., Tumanyan, K.A., Frankov, M.A. and Balaka, N.N., "Development and prototyping of jet systems for advanced turbomachinery with mesh rotor", *Emerging Science Journal*, Vol. 5, No. 5, (2021), 775-801. doi: 10.28991/esj-2021-01311.
- Sazonov, Y.A., Mokhov, M.A., Gryaznova, I.V., Voronova, V.V., Tumanyan, K.A., Frankov, M.A. and Balaka, N.N., "Designing mesh turbomachinery with the development of euler's ideas and investigating flow distribution characteristics", *Civil Engineering Journal*, Vol. 8, No. 11, (2022), 2598-2627. doi: 10.28991/CEJ-2022-08-11-017.
- Sazonov, Y.A., Mokhov, M.A., Gryaznova, I.V., Voronova, V.V., Tumanyan, K.A., Frankov, M.A. and Balaka, N.N., "Simulation of hybrid mesh turbomachinery using cfd and additive technologies", *Civil Engineering Journal*, Vol. 8, No. 12, (2022), 3815-3830. doi: 10.28991/CEJ-2022-08-12-011.
- Manring, N.D. and Fales, R.C., "Hydraulic control systems, John Wiley & Sons, (2019).
- Mir Mohammad Sadeghi, S., Hoseini, S., Fathi, A. and Mohammadi Daniali, H., "Experimental hysteresis identification and micro-position control of a shape-memory-alloy rod actuator", *International Journal of Engineering, Transactions A: Basics*, Vol. 32, No. 1, (2019), 71-77. doi: 10.5829/ije.2019.32.01a.09.
- Fateh, M.M. and Sadeghijaleh, M., "Voltage control strategy for direct-drive robots driven by permanent magnet synchronous motors", *International Journal of Engineering, Transactions B: Applications*, Vol. 28, No. 5, (2015), 709-716. doi: 10.5829/idosi.ije.2015.28.05b.09.
- Grabbel, J. and Ivantysynova, M., "An investigation of swash plate control concepts for displacement controlled actuators",

- International Journal of Fluid Power*, Vol. 6, No. 2, (2005), 19-36. <https://doi.org/10.1080/14399776.2005.10781217>
30. Bishara, A.J. and Hittner, J.B., "Reducing bias and error in the correlation coefficient due to nonnormality", *Educational and Psychological Measurement*, Vol. 75, No. 5, (2015), 785-804. <https://doi.org/10.1177/0013164414557639>
31. Jothivenkatachalam, K., Nithya, A. and Mohan, S.C., "Correlation analysis of drinking water quality in and around perur block of coimbatore district, tamil nadu, india", *Rasayan Journal of Chemistry*, Vol. 3, No. 4, (2010), 649-654.

Persian Abstract

چکیده

سیستم‌های محرک الکتروهیدرولیک، کنترل موقعیت قطعی و یک راه‌حل کارآمد انرژی را ارائه می‌دهند. چنین سیستم‌هایی به طور گسترده در ماشین آلات متحرک، رباتیک و سیستم‌های ثابت مختلف استفاده می‌شود. دستیابی به کنترل خوب موقعیت محرک سیستم تحریک الکتروهیدرولیک با جابجایی متغیر توسط یک کنترل حلقه باز هدف این مطالعه است. برای کنترل موقعیت مربع (موقعیت مرجع)، دامنه ۰.۱ متر، در فرکانس ۰.۰۵، ۰.۱۵ و ۰.۲۵ هرتز در نظر گرفته می‌شود. کنترل موقعیت مربع با الگوریتم LabVIEW از طریق استفاده از کنترلر فشرده RIO با مازول ورودی و خروجی انجام می‌شود. هنگامی که موقعیت پاسخ و موقعیت مرجع دقت مناسب را نشان می‌دهند، کنترل مناسب منبع ولتاژ به دست می‌آید. ضریب همبستگی پیرسون نزدیک به ۱ بیشتر و میانگین خطای مطلق کمتر، میانگین انحراف خطا و انحراف استاندارد خطا نشان دهنده بهترین موقعیت پاسخ هستند. مشاهده شد که بیشترین مقدار ضریب همبستگی در فرکانس ۰.۰۵ هرتز برای پاسخ R3 به دست آمد. در فرکانس پایین تر، کنترل موقعیت مربع با ضریب همبستگی بالاتر و کمترین مقادیر خطا بهتر است.



Electrolyte Temperature Dependency of Electrodeposited Nickel in Sulfate Solution on the Hardness and Corrosion Behaviors

S. Syamsuir^{*a}, B. Soegijono^b, S. D. Yudanto^c, B. Basori^d, M. K. Ajiriyanto^e, D. Nanto^f, F. B. Susetyo^a

^a *Departement of Mechanical Engineering, Universitas Negeri Jakarta, Indonesia*

^b *Department of Geoscience, Universitas Indonesia, Indonesia*

^c *Research Center for Metallurgy - National Research and Innovation Agency, Indonesia*

^d *Department of Mechanical Engineering, Universitas Nasional, Indonesia*

^e *Research Center for Nuclear Fuel Cycle and Radioactive Waste Technology - National Research and Innovation Agency, Indonesia*

^f *Department of Physics Education, UIN Syarif Hidayatullah, Indonesia*

PAPER INFO

Paper history:

Received 13 March 2023

Received in revised form 13 May 2023

Accepted 14 May 2023

Keywords:

Ni Films

Electrodeposition

Crystallite Size

Micro-strain

ABSTRACT

The hardness and corrosion resistance of nickel (Ni) deposit on a substrate could be reached by controlling electrolyte temperature during deposition. In this research, the electrodeposition of Ni at various temperatures of electrolytes was performed. Electrodeposited Ni films using an optical digital camera, X-ray diffraction (XRD), scanning electron microscope with energy-dispersive x-ray spectroscopy (SEM-EDS), microhardness test, and potentiostat were investigated. The bright deposit occurred at 25 °C; an increase in the temperature to 40 °C leads to a change of color into semi-bright. Shifting to a higher temperature would increase the deposition rate, cathodic current efficiency, grain size, and oxygen content. The X-ray reflections in the planes (111), (200), and (220) correspond to as the Ni phase with a face center cubic (FCC) crystal structure. Decreasing crystallite size and micro-strain promoted to reach high hardness. Increasing the corrosion current density implies decreasing polarization resistance. The sample at the lowest electrolyte temperature has a better hardness, and the sample formed at 25 °C sulfate solution had less corrosion rate.

doi: 10.5829/ije.2023.36.06c.18

NOMENCLATURE

$Cor\ Rate$	Corrosion rate (mmpy)	k	Shape factor ($k=0.94$)
C	Corrosion rate constant (3.27)	λ	The wavelength of the radiation source (nm)
M	Weight of the Ni atomic (g/mol)	D	The crystallite size (nm)
I_{corr}	Corrosion current density (A/cm^2)	β	Peak full width at half maximum (radians)
n	Number of Ni electrons	θ	Phase peak angle (°)
ρ	Ni density (8.908 g/cm ³)	ϵ	Micro-strain (%)
E_{corr}	Corrosion potential (V)	R_{ct}	Polarization resistance (Ω)

1. INTRODUCTION

Nickel (Ni) has many advantages of physical and other properties, such as better corrosion resistance and hardness [1, 2]. NiO formation on the Nickel surface could form the passive nickel layer and increase the corrosion resistance and hardness. Ni is widely used as a protective coating from corrosion attacks on automotive

vehicle components and accessories such as logos, door handles, and rearview handles [3]. For those reasons, hardness and corrosion resistance properties are needed.

Numerous methods could be conducted to protect the material from corrosion attacks, such as coating, electrodeposition, hot-dip galvanizing, chemical vapor deposition (CVD), and physical vapor deposition (PVD) [4, 5]. The electrodeposition process makes Ni as

*Corresponding Author Institutional Email: syamsuir@unj.ac.id
(S. Syamsuir)

protective film from corrosion attack, more promising due to being faster, cheaper, and more environmental friendly [6]. Parameters such as current density, temperature, and bath formula must be considered for better hardness and corrosion resistance.

Recently, there have been many studies on the electrodeposition of Ni to increase the hardness and corrosion resistance. Wasekar et al. [7] conducted electrodeposition by varying pulse frequency, current density, and saccharin and found saccharin significantly influences hardness. Gu et al. [8] electrodeposited Ni on a brass substrate using a choline chloride-ethylene glycol solution, producing a film's hardness of around 7.6-9.7 GPa. Furthermore, potentiodynamic polarization measurement in 3% NaCl solution showed 0.0102 mA/cm² of corrosion current. Yamamoto et al. [9] fabricated a Ni layer in a sulfamate bath with various current densities resulting in a hardness of around 380 HV when plating with 20 mA/cm². Bigos et al. [10] found Ni films hardness around 620 HV when electrodeposition in a citrate-based bath. Cheng et al. [11] observed Ni film was electrodeposited by reverse pulsed current, and varying saccharin found less grain size and corrosion current in 5 g/l saccharin addition.

The hardness and corrosion resistance could also be reached by controlled electrolyte temperature. Chung et al. [12] varied the temperature of the electrolyte solution 5, 10, 15, and 20 °C to produce a Ni film at the highest hardness at 5 °C. Jinlong et al. [13] also reported that Ni electrodeposition at 20, 50, and 80 °C temperature variations produced the lowest corrosion rates at 20 °C. Furthermore, in previous work, by varying the temperature of the electrolyte solution, 20, 30, and 50 °C found the highest hardness at 20 °C and the lowest corrosion rate at 50 °C [14].

As mentioned above, many researchers vary bath composition to reach high hardness and corrosion resistance. Varying temperatures have been conducted; other researchers also used a complex bath. This condition could raise the new problem of waste treatment before releasing it into nature.

For that reason, the electrodeposition of Ni in 0.5 M NiSO₄ solution without any additions and variations in temperature needs further investigation. In this research, the electrodeposition of Ni with various temperatures was performed using an electrolyte solution without additive addition.

2. EXPERIMENTAL

2. 1. Process and Materials

The Ni electrodeposition process used DC power supply apparatus in 0.5 M NiSO₄ solution using 10mA cm⁻² of current density. The electrodeposition was carried out in a 250 ml electrolyte plating bath at temperatures 10, 25,

and 40 °C for 1 h. The sample was designated as T10, T25, and T40 for electrolyte temperatures 10, 25, and 40 °C, respectively.

Pure Ni was used as the anode, and copper alloy [14] was used for the cathode. Before the electrodeposition process, the cathode was polished sequentially using abrasive paper of #1000 up to #3000. Moreover, the cathode was cleaned with acetone before electrodeposition was performed.

2. 2. Characterization

For visual appearance, the picture was captured using a digital camera. Afterwards, the captured figures were analyzed by visual appearance. The mass increment of the Ni films was found by weighing the substrate before and after electrodeposition. Moreover, a mass of the Ni films is inserted in the current efficiency and deposition rate equation. The cathodic current efficiency (CCE) and deposition rate (*v*) were calculated similarly by the method as previously reported [15].

The X-ray diffraction (XRD) identified the phase and crystal structure of the films Ni with the Cu K α radiation (Philips binary sweep). XRD data was collected from 30° to 80° with a step size of 0.020°.

Surface morphology and composition of Ni films were analyzed with FE-SEMFEI INSPECT F50 energy dispersive analysis of X-rays (EDAX) EDS analyzer.

The potentiodynamic polarization was carried out in an electrochemical workstation (Digi-Ivy DY 2311) at 30 °C. A three-electrode cell was used with a Pt as a counter electrode, an Ag/AgCl electrode as a reference electrode, and a 1 cm² Ni film embedded in epoxy resin as a working electrode. The potentiodynamic polarization measurement performs with a 1 mV/s scan rate in 3.5% NaCl solution.

The Tafel extrapolation methods were used to find the I_{corr} and the E_{corr} . Afterwards, the following equation was used to calculate the corrosion rate (*Cor Rate*) [16];

$$Cor Rate = C \frac{M \times I_{corr}}{n \times \rho} \quad (1)$$

The microhardness test was carried out with a MicroMet® 5100 series. The test was conducted with a load of 100 g for 10 s and according to the ATM E384 standard.

3. RESULTS AND DISCUSSION

3. 1. Visual Appearance

Based on Figure 1, the bright deposit occurred at 25°C; an increase in the temperature to 40°C leads to a change of colour into semi-bright. A decrease in the temperature to 10°C leads to a shift in the dullness. Usually, bright deposits result in lower current densities, and dull deposits at higher current densities [17]. Furthermore, additive addition also affected the appearance quality of deposition [18].

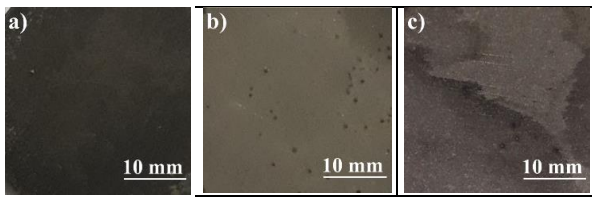


Figure 1. The visual appearance of Ni films (a) T 10, (b) T 25, and (c) T 40

3. 2. Cathodic Current Efficiency and Deposition Rate

Various sample's cathodic current efficiency results can be observed in Figure 2. This behaviour indicated that the cathodic current efficiency depends strongly on temperature. Shifting to a higher temperature would affect to increase the cathodic current efficiency. Sarac and Baykul [19] found higher temperatures lead to higher cathodic current efficiency. This condition means faster Ni^{2+} ions moving in the forward direction from the anode to the cathode and promotes increasing the cathodic current efficiency as the temperature of the electrolyte solution rises. Moreover, the shift to the higher temperature affects nearly equally the deposition of Ni and hydrogen evolution [20].

Electrolyte temperature decreased when the deposition was performed, affecting the decrease of the Ni films deposition rate. A measurement result of the deposition rate of electrodeposited Ni films is shown in Figure 2. Because the deposition rate is limited by poor mass transfer conditions at low electrolyte temperatures [21]. It would influence the movement of Ni^{2+} ions from the anode to the cathode becomes slower with decreasing electrolyte temperature. Kang et al. [22] found that elevating the electrolyte temperature increased the deposition rate when electrodeposition Ni using electrolyte temperature 40 until 60 °C.

An increased in deposition rate would also influence the film thickness. Basori et al. [15] found that increased electrolyte temperature promoted the film's thickness due to increased in deposition rate. More thickness in the Ni films could influence the hardness.

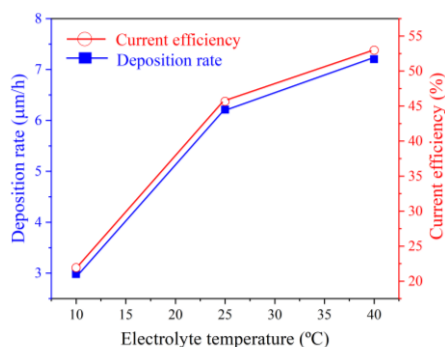


Figure 2. The cathodic current efficiency and deposition Rate of Ni films

3. 3. XRD

Figure 3 illustrates the XRD pattern of electroplated Ni film samples on Cu alloy substrates at 10 °C (T10), 25 °C (T25), and 40 °C (T40). The X-ray reflections in the planes (111), (200), and (220) are defined as the Ni phase with a face centre cubic (FCC) crystal structure. According to Donegan et al. [23], Shin et al. [24] and Zhang et al. [25] these peaks are comparable to their results.

Using the JANA2006 software, the XRD pattern of Ni film samples can be very well fitted [26]. The diffraction patterns observed and the calculated results are compared in Figure 4. The calculated lattice constants of samples T10, T25, and T40 with cubic phase and $\text{Fm}\bar{3}\text{m}$ space group are 0.3522 nm, 0.3522 nm, and 0.3521 nm, respectively.

The Monshi-Scherrer and Williamson Hall Plot methods were used to analyze the effect of deposition temperature on crystallite size based on XRD patterns. Figures 5(a) and 5(b) show the Monshi-Scherrer and Williamson Hall method of the Ni film samples with a deposition temperature of 25 °C. The crystallite size can be calculated using Equation (2) based on the intercept value obtained from the $\ln(1/\cos\theta)$ vs $\ln\beta$ curve (Figure 5 (a)) [27, 28].

$$e^{\frac{k\lambda}{D}} = \frac{k\lambda}{D} \quad (2)$$

The crystallite size values of samples T10, T25, and T40 were 22.53 nm, 23.52 nm, and 24.54 nm, respectively. Based on the intercept values, for samples T10, T25, and T40 were -5.0471, -5.0901, and -5.1326, respectively. The Williamson Hall Plot method is used to calculate the crystallite size, which is formulated as follows [29, 30].

$$\beta \cdot \cos\theta = \frac{k\lambda}{D} + 4\epsilon \sin\theta \quad (3)$$

The crystallite sizes of samples T10, T25, and T40 were 27.85 nm, 36.20 nm, and 41.38 nm, respectively. This value is derived from the linear regression results of the $4\epsilon \sin\theta$ vs $\beta \cdot \cos\theta$ curve shown in Figure 5 (b). The micro-strain values of samples T10, T25, and T40 were 0.11%,

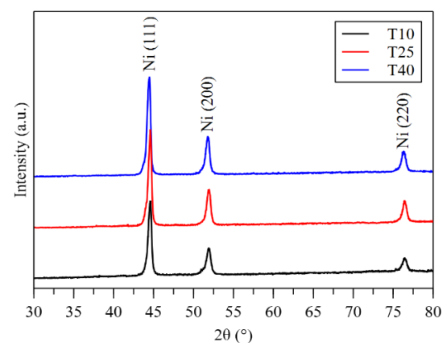


Figure 3. XRD patterns of Ni film samples with various temperature deposition

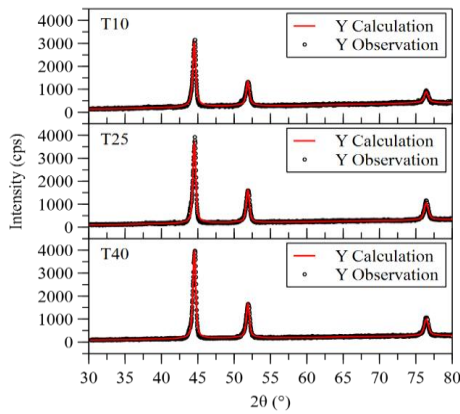


Figure 4. The observed diffraction pattern of the Ni film samples compared with the calculation results

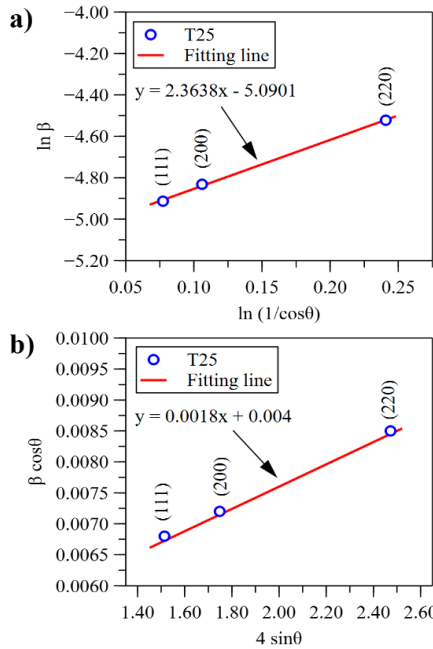


Figure 5. Calculation of the crystallite size of Ni film samples with a deposition temperature of 25 °C. (a) Monshi-Scherrer method, and (b) Williamson Hall Plot method

0.18%, and 0.20%, respectively. Increasing deposition temperature causes the peaks to broaden due to lattice strain. Crystal growth of the Ni film is directly proportional to the increase in deposition temperature, according to the Monshi-Scherrer method and the Williamson Hall Plot.

3. 4. SEM-EDS

The electrolyte temperature significantly influences the surface morphology of the Ni film. The SEM-EDS image (Figure 6) represents the outermost surface areas. The T10 sample shows a clear island-like structure [31]. Raising the temperature to 25 °C would change the island-like structure to a compact

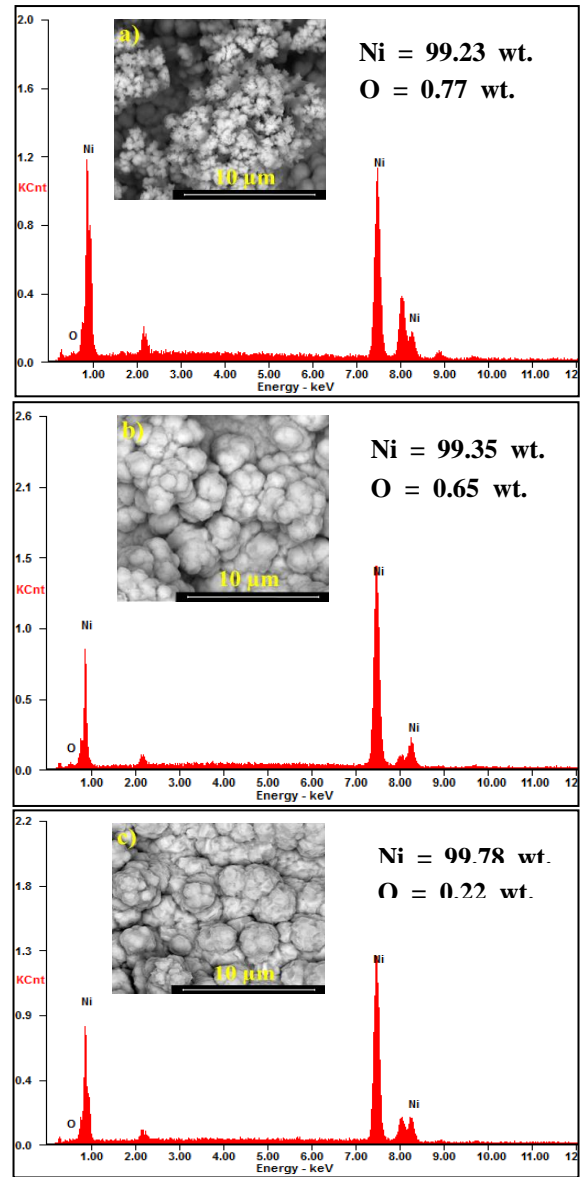


Figure 6. SEM-EDS of Ni film (a) T10, (b) T25, and (c) T40

nodule without porosity. When the electrolyte temperature increases to 40 °C, a nodule is still seen in the surface morphology, but a little porosity is shown in the grain boundary.

Raising the temperature also influences the grain size. Compared to Figure 2, it can be seen a shift to the higher temperature on electrodeposited Ni films delivering a higher cathodic current efficiency. This behaviour means higher cathodic current efficiency produces larger grain sizes [32]. Besides current efficiency, deposition rate also contributed to grain size [33]. As seen in Figure 6, an increase in the temperature creates a larger grain size due to an increase in current efficiency and deposition rate. Lin et al. [33] reported that controlling the deposition rate leads to forming of various grain sizes.

Ni and O content is seen on the EDS examination. At high temperature, less O content is visited, and in the lowest temperature, more extensive O content is seen (Figure 6). This behaviour indicated that the oxygen content depends strongly on the temperature. Various research has been found that forming a NiO would improve corrosion resistance and hardness [34, 35]. Jabbar et al. [36] found C content in the Ni films increased by an electrolyte temperature due to the exhibit of graphene 0.2 g/l in the electrolyte solution. In contrast, within Jabbar et al. [36] research, unseen O content exists on the Ni surfaces due to probably the sample transport and storage prior to EDS characterization [14].

3. 5. Microhardness The Microhardness test result of Ni films can be seen in Figure 7. The Ni film's microhardness increases, corresponding to the electrolyte temperature decrease [22]. This behaviour perfectly agrees with Chung et al. [12] research where microhardness increases linearly when electrolyte temperature is decreased.

Compared to the XRD result, it can be seen an increase in the electrolyte temperature leads to an increase in the micro-strain. An increase in the micro-strain indicates more crystal defects that are formed and could influence the physical and mechanical properties [14, 37]. Therefore, less micro-strain would increase the hardness.

The slow deposition rate at a lower temperature promoted less crystallite size [12]. Less crystallite size could result in high hardness. Bigos et al. [10] found that shifting to a larger crystallite size decreases hardness. Martínez et al. [38] also found that reducing crystallite size would increase the hardness. This statement is in alignment with the present study.

Besides crystallite size, film thickness also contributed to the influence of the hardness. Compared to Figure 2, an increase in the electrolyte temperature can increase the deposition rate, which promotes increasing the film's thickness. Therefore, more thickness of the Ni films could increase the hardness [39].

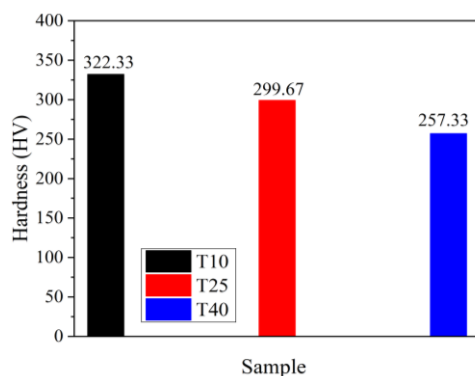


Figure 7. Microhardness test result of Ni films

The hardness of electrodeposited Ni using various bath compositions and electrolyte temperatures is summarized in Table 1.

Wasekar et al. [7] found that a saccharine in the solution significantly influences the hardness. Comparing between Figure 7 and Table 1, bath composition also contributed to high hardness besides electrolyte temperature [7]. Moreover, compared to previous work, where electrodeposited by adding H_3BO_3 , resulted less hardness than present research [14].

3. 6. Potentiodynamic Polarization The potentiodynamic polarization scan results in 3.5% NaCl solution are shown in Figure 8. Shifting to high temperatures leads to producing more negative E_{corr} . This phenomenon contradicts our previous work, which could be the boric acid effect in the electrolyte solution [14]. Adding more boric acid has increased the cathodic current efficiency so that it will affect the properties of the Ni film formed. Moreover, adding boric acid also could influence strain and stress in the Ni films [40]. Increased internal stress will cause slight cracks in the Ni films [41]. Hence, those cracks would influence the E_{corr} of the Ni films.

Based on Figure 8, it can be seen that E_{corr} has a more positive value than Gu et al. [8] results. This behaviour could have different morphological results. It is seen that Gu et al. [8] had a smaller grain size than this research. Elias and Hedge [39] reported grain size would influence E_{corr} .

Based on Table 2, sample T25 has shown less corrosion rate. Moreover, the corrosion current density increases, implying decreasing polarization resistance, which means the film will be easier to corrode [42]. Furthermore, samples T10 and T40, showing active loops, indicate uniform corrosion on the film's surface (Figure 8) [43].

Compared to SEM result, compact morphology was observed in sample T25, whereas porous morphology is found in the other samples. Xu et al. [44] found porosity could influence corrosion resistance. Higher porosity

TABLE 1. Ni film's average hardness

Bath Composition (g/l)	Temp. (°C)	Hardness (HV)
$Ni(NH_2SO_3)_2$ (450), NiCl (4), and H_3BO_3 (40)	5-20	408.9-630.2 [12]
$NiSO_4$ (450) and H_3BO_3 (45)	20-50	219-259.25 [14]
$NiSO_4$ (95-110), NiCl (15-20), H_3BO_3 (30-40), surfactant (SDS) (0.4), and graphene (0.2)	15-60	220-500 [36]
$NiSO_4$ (300), NiCl (45), H_3BO_3 (40), $C_{12}H_{25}OSO_2Na$ (0.05), and $C_7H_4NO_3SNa$ (3)	50-80	510-590 [22]

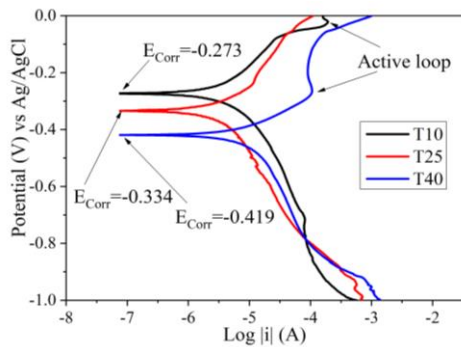


Figure 8. Potentiodynamic polarization curve of Ni films

TABLE 2. Potentiodynamic polarization of Ni films

Sample	I_{corr} (A/cm ²)	E_{corr} (V) vs Ag/AgCl	R_{ct} (Ω)	Cor Rate (mmpy)
T10	2.83×10^{-6}	-0.273	9088	0.0328
T25	2.49×10^{-6}	-0.334	10330	0.0280
T40	6.76×10^{-6}	-0.419	3800	0.0784

would increase the corrosion rate. Therefore sample T25 has a higher corrosion resistance than other samples.

Elias and Hedge [39] reported nodule form of the grain size would influence corrosion resistance. Based on Figure 6, nodule forms are shown in the T25 and T40 samples. Unfortunately, porosity is seen in the T40 sample. Therefore sample T25 is resulting better corrosion resistance. All conditions mentioned above can be corroborated by sample T25 has better corrosion resistance.

4. CONCLUSIONS

The characteristic of Ni films at various deposition temperature was investigated. The surface morphology of the sample looks different as the change of the electrolyte temperature. Increased electrolyte temperature is related to increase in grain size, deposition rate, cathodic current efficiency, micro-strain, and crystallite size. Moreover, decreased electrolyte temperature is related to increase in oxygen content and hardness. Sample T25 has better corrosion resistance than the other samples. Furthermore, the sample with the lowest electrolyte temperature has better hardness than the other samples.

5. ACKNOWLEDGMENTS

This work was financially supported by the Engineering Faculty of Universitas Negeri Jakarta under grant No. 065a/5.FT/PP/V/2020.

6. REFERENCES

- Toocharoen, S., Kaewkuekool, S., and Peasura, P. "Rejuvenation heat treatment of nickel base superalloy grade GTD111 after long-term service via taguchi method for optimization." *International Journal of Engineering, Transactions A: Basics*, Vol. 34, No. 4, (2021), 956-965. <https://doi.org/10.5829/ije.2021.34.04a.22>
- Patil, V. G., Somasundaram, B., Kandaiah, S., Ramesh, M. R., and Kumar, S. "High Temperature Corrosion Behavior of High Velocity Oxy Fuel Sprayed NiCrMoFeCoAl-30%SiO₂ and NiCrMoFeCoAl-30%Cr₂O₃ Composite Coatings on ASTM SA213-T22 Steel in a Coal-fired Boiler Environment." *International Journal of Engineering, Transactions A: Basics*, Vol. 35, No. 7, (2022), 1416-1427. <https://doi.org/10.5829/ije.2022.35.07a.19>
- Susetyo, F. B., Faridh, A., and Soegijono, B. "Stirring Effect on Surface Morphology, Structure, and Electrochemical Behavior of Electrodeposited Nickel Film on Copper Substrates." *IOP Conference Series: Materials Science and Engineering*, Vol. 694, No. 1, (2019), 1-5. <https://doi.org/10.1088/1757-899X/694/1/012040>
- Poursaiedi, E., and Salarvand, A. "Comparison of properties of Ti/TiN/TiCN/TiAlN Film deposited by cathodic arc physical vapor and plasma-assisted chemical vapor deposition on custom 450 steel substrates." *International Journal of Engineering, Transactions A: Basics*, Vol. 29, No. 10, (2016), 1459-1468. <https://doi.org/10.5829/idosi.ije.2016.29.10a.17>
- Moosaei, H. R., Zareei, A. R., and Salemi, N. "Elevated Temperature Performance of Concrete Reinforced with Steel, Glass, and Polypropylene Fibers and Fire-proofed with Coating." *International Journal of Engineering, Transactions B: Applications*, Vol. 35, No. 5, (2022), 917-930. <https://doi.org/10.5829/ije.2022.35.05b.08>
- Bazzaoui, M., Martins, J. I., Bazzaoui, E. A., and Albourine, A. "Environmentally friendly process for nickel electroplating of ABS." *Applied Surface Science*, Vol. 258, No. 20, (2012), 7968-7975. <https://doi.org/10.1016/j.apsusc.2012.04.146>
- Wasekar, N. P., Haridoss, P., Seshadri, S. K., and Sundararajan, G. "Influence of mode of electrodeposition, current density and saccharin on the microstructure and hardness of electrodeposited nanocrystalline nickel coatings." *Surface & Coatings Technology*, Vol. 291, (2016), 130-140. <https://doi.org/10.1016/j.surfcoat.2016.02.024>
- Gu, C. D., You, Y. H., Yu, Y. L., Qu, S. X., and Tu, J. P. "Microstructure, nanoindentation, and electrochemical properties of the nanocrystalline nickel film electrodeposited from choline chloride-ethylene glycol." *Surface and Coatings Technology*, Vol. 205, No. 21-22, (2011), 4928-4933. <https://doi.org/10.1016/j.surfcoat.2011.04.098>
- Yamamoto, T., Igawa, K., Tang, H., Chen, C. Y., Chang, T. F. M., Nagoshi, T., Kudo, O., Maeda, R., and Sone, M. "Effects of current density on mechanical properties of electroplated nickel with high speed sulfamate bath." *Microelectronic Engineering*, Vol. 213, (2019), 18-23. <https://doi.org/10.1016/j.mee.2019.04.012>
- Bigos, A., Wolowicz, M., Janusz-Skuza, M., Starowicz, Z., Szczerba, M. J., Bogucki, R., and Beltowska-Lehman, E. "Citrate-based baths for electrodeposition of nanocrystalline nickel coatings with enhanced hardness." *Journal of Alloys and Compounds*, Vol. 850, (2021), 156857. <https://doi.org/10.1016/j.jallcom.2020.156857>
- Cheng, W., Ge, W., Yang, Q., and Qu, X. "Study on the corrosion properties of nanocrystalline nickel electrodeposited by reverse pulse current." *Applied Surface Science*, Vol. 276, (2013), 604-608. <https://doi.org/10.1016/j.apsusc.2013.03.139>

12. Chung, C. K., Chang, W. T., Chen, C. F., and Liao, M. W. "Effect of temperature on the evolution of diffusivity, microstructure and hardness of nanocrystalline nickel films electrodeposited at low temperatures." *Materials Letters*, Vol. 65, No. 3, (2011), 416-419. <https://doi.org/10.1016/j.matlet.2010.10.064>
13. Jinlong, L., Tongxiang, L., and Chen, W. "Effect of electrodeposition temperature on grain orientation and corrosion resistance of nanocrystalline pure nickel." *Journal of Solid State Chemistry*, Vol. 240, (2016), 109-114. <https://doi.org/10.1016/j.jssc.2016.05.025>
14. Susetyo, F. B., Fajrah, M. C., and Soegijono, B. "Effect of Electrolyte Temperature on Properties of Nickel Film Coated onto Copper Alloy Fabricated by Electroplating." *e-Journal of Surface Science and Nanotechnology*, Vol. 18, (2020), 223-230. <https://doi.org/10.1380/ejsnt.2020.223>
15. Basori, Soegijono, B., and Susetyo, F. B. "Magnetic field exposure on electroplating process of ferromagnetic nickel ion on copper substrate." *Journal of Physics: Conference Series*, Vol. 2377, No. 012002, (2022), 1-7. <https://doi.org/10.1088/1742-6596/2377/1/012002>
16. Yang, Z., Liu, X., and Tian, Y. "Fabrication of super-hydrophobic nickel film on copper substrate with improved corrosion inhibition by electrodeposition process." *Colloids and Surfaces A: Physicochemical and Engineering Aspects*, Vol. 560, (2019), 205-212. <https://doi.org/10.1016/j.colsurfa.2018.10.024>
17. SEKAR, R. "Synergistic effect of additives on electrodeposition of copper from cyanide-free electrolytes and its structural and morphological characteristics." *Transactions of Nonferrous Metals Society of China (English Edition)*, Vol. 27, No. 7, (2017), 1665-1676. [https://doi.org/10.1016/S1003-6326\(17\)60189-4](https://doi.org/10.1016/S1003-6326(17)60189-4)
18. Fukumoto, K., Oue, S., Kikuchi, Y., Akamatsu, S., Takasu, T., and Nakano, H. "Effect of organic additives on the electrodeposition behavior of Zn from an alkaline zincate solution and its microstructure." *Materials Transactions*, Vol. 61, No. 3, (2020), 497-505. <https://doi.org/10.2320/matertrans.MT-M2019316>
19. Sarac, U., and Baykul, M. C. "Morphological and microstructural properties of two-phase Ni-Cu films electrodeposited at different electrolyte temperatures." *Journal of Alloys and Compounds*, Vol. 552, (2013), 195-201. <https://doi.org/10.1016/j.jallcom.2012.10.071>
20. Kamel, M. M., Anwer, Z. M., Abdel-Salam, I. T., and Ibrahim, I. S. "Nickel electrodeposition from novel lactate bath." *Transactions of the IMF*, Vol. 88, No. 4, (2010), 191-197. <https://doi.org/10.1179/002029610X12696136822437>
21. Chung, C. K., Chang, W. T., and Hung, S. T. "Electroplating of nickel films at ultra low electrolytic temperature." *Microsystem Technologies*, Vol. 16, No. 8-9, (2010), 1353-1359. <https://doi.org/10.1007/s00542-009-0955-6>
22. Kang, J. X., Zhao, W. Z., and Zhang, G. F. "Influence of electrodeposition parameters on the deposition rate and microhardness of nanocrystalline Ni coatings." *Surface and Coatings Technology*, Vol. 203, No. 13, (2009), 1815-1818. <https://doi.org/10.1016/j.surfcoat.2009.01.003>
23. Donegan, K. P., Godsell, J. F., Otway, D. J., Morris, M. A., Roy, S., and Holmes, J. D. "Size-tuneable synthesis of nickel nanoparticles." *Journal of Nanoparticle Research*, Vol. 14, No. 1, (2012), 1-10. <https://doi.org/10.1007/s11051-011-0670-y>
24. Shin, S. M., Lee, D. W., and Wang, J. P. "Fabrication of nickel nanosized powder from LiNiO₂ from spent lithium-ion battery." *Metals*, Vol. 8, No. 1, (2018), 1-6. <https://doi.org/10.3390/met8010079>
25. Zhang, J., Leung, P., Qiao, F., Xing, L., Yang, C., Su, H., and Xu, Q. "Balancing the electron conduction and mass transfer: Effect of nickel foam thickness on the performance of an alkaline direct ethanol fuel cell (ADEFEC) with 3D porous anode." *International Journal of Hydrogen Energy*, Vol. 45, No. 38, (2020), 19801-19812. <https://doi.org/10.1016/j.ijhydene.2020.05.119>
26. Petricek, V., Dušek, M., and Palatinus, L. "Crystallographic computing system JANA2006: General features." *Zeitschrift für Kristallographie*. <https://doi.org/10.1515/zkri-2014-1737>
27. Yudanto, S. D., Chandra, S. A., Roberto, R., Utama, D. P., Herlina, V. O., and Lusiana. "Phase and electrical properties of Ca₃Co₄O₉ ceramic prepared by a citrate sol-gel route." *Journal of Ceramic Processing Research*, Vol. 67, No. 2, (2022), 248-256. <https://doi.org/10.31857/s0044457x22020076>
28. Monshi, A., Foroughi, M. R., and Monshi, M. R. "Modified Scherrer Equation to Estimate More Accurately Nano-Crystallite Size Using XRD." *World Journal of Nano Science and Engineering*, Vol. 02, No. 03, (2012), 154-160. <https://doi.org/10.4236/wjnse.2012.23020>
29. Mote, V., Purushotham, Y., and Dole, B. "Williamson-Hall analysis in estimation of lattice strain in nanometer-sized ZnO particles." *Journal of Theoretical and Applied Physics*, Vol. 6, No. 1, (2012), 2-9. <https://doi.org/10.1186/2251-7235-6-6>
30. Yudanto, S. D., Dewi, Y. P., Sebayang, P., Chandra, S. A., Imaduddin, A., Kurniawan, B., and Manaf, A. "Influence of CNTs addition on structural and superconducting properties of mechanically alloyed MgB₂." *Journal of Metals, Materials and Minerals*, Vol. 30, No. 3, (2020), 9-14. <https://doi.org/10.14456/jmmm.2020.32>
31. Wang, Y. M., Zhao, D. D., Zhao, Y. Q., Xu, C. L., and Li, H. L. "Effect of electrodeposition temperature on the electrochemical performance of a Ni(OH)₂ electrode." *RSC Advances*, Vol. 2, No. 3, (2012), 1074-1082. <https://doi.org/10.1039/c1ra00613d>
32. Wasekar, N. P., O'Mullane, A. P., and Sundararajan, G. "A new model for predicting the grain size of electrodeposited nanocrystalline nickel coatings containing sulphur, phosphorus or boron based on typical systems." *Journal of Electroanalytical Chemistry*, Vol. 833, (2019), 198-204. <https://doi.org/10.1016/j.jelechem.2018.11.057>
33. Lin, Y., Pan, J., Zhou, H. F., Gao, H. J., and Li, Y. "Mechanical properties and optimal grain size distribution profile of gradient grained nickel." *Acta Materialia*, Vol. 153, (2018), 279-289. <https://doi.org/10.1016/j.actamat.2018.04.065>
34. Abdallah, M., Zaafarany, I. A., Abd El Wanees, S., and Assi, R. "Breakdown of passivity of nickel electrode in sulfuric acid and its inhibition by pyridinone derivatives using the galvanostatic polarization technique." *International Journal of Corrosion and Scale Inhibition*, Vol. 4, No. 4, (2015), 338-352. <https://doi.org/10.17675/2305-6894-2015-4-4-4>
35. Zhou, J., and Kong, D. "Effects of Ni addition on corrosion behaviors of laser cladded FeSiBNi coating in 3.5% NaCl solution." *Journal of Alloys and Compounds*, Vol. 795, (2019), 416-425. <https://doi.org/10.1016/j.jallcom.2019.05.012>
36. Jabbar, A., Yasin, G., Khan, W. Q., Anwar, M. Y., Korai, R. M., Nizam, M. N., and Muhyodin, G. "Electrochemical deposition of nickel graphene composite coatings effect of deposition temperature on its surface morphology and corrosion resistance." *RSC Advances*, Vol. 7, No. 49, (2017), 31100-31109. <https://doi.org/10.1039/c6ra28755g>
37. Susetyo, F. B., Soegijono, B., Yusmaniar, and Fajrah, M. C. "Deposition of nickel films on polycrystalline copper alloy with various current densities from watts solution." *AIP Conference Proceedings*, Vol. 2331, (2021). <https://doi.org/10.1063/5.0041640>
38. Martínez, C., Briones, F., Aguilar, C., Araya, N., Iturriza, I., Machado, I., and Rojas, P. "Effect of hot pressing and hot isostatic pressing on the microstructure, hardness, and wear behavior of nickel." *Materials Letters*, Vol. 273, (2020). <https://doi.org/10.1016/j.matlet.2020.127944>

39. Elias, L., and Hegde, A. C. "Effect of magnetic field on corrosion protection efficacy of Ni-W alloy coatings." *Journal of Alloys and Compounds*, Vol. 712, (2017), 618-626. <https://doi.org/10.1016/j.jallcom.2017.04.132>
40. Tsuru, Y., Nomura, M., and Foulkes, F. R. "Effects of boric acid on hydrogen evolution and internal stress in films deposited from a nickel sulfamate bath." *Journal of Applied Electrochemistry*, Vol. 32, No. 6, (2002), 629-634. <https://doi.org/10.1023/A:1020130205866>
41. Liu, S., Ji, R., Liu, Y., Zhang, F., Jin, H., Li, X., Zheng, Q., Lu, S., and Cai, B. "Effects of boric acid and water on the deposition of Ni/TiO₂ composite coatings from deep eutectic solvent." *Surface and Coatings Technology*, Vol. 409, (2021), 126834. <https://doi.org/10.1016/j.surfcoat.2021.126834>
42. Munasir, N., Triwikantoro, Zainuri, M., Bäßler, R., and Darminto. "Corrosion polarization behavior of Al-SiO₂ composites in 1M and related microstructural analysis." *International Journal of Engineering, Transactions A: Basics*, Vol. 32, No. 7, (2019), 982-990. <https://doi.org/10.5829/ije.2019.32.07a.11>
43. Krawczyk, B., Cook, P., Hobbs, J., and Engelberg, D. L. "Corrosion behavior of cold rolled type 316L stainless steel in HCl-containing environments." *Corrosion*, Vol. 73, No. 11, (2017), 1346-1358.
44. Xu, W., Lu, X., Zhang, B., Liu, C., Lv, S., Yang, S., and Qu, X. "Effects of porosity on mechanical properties and corrosion resistances of PM-fabricated porous Ti-10Mo Alloy." *Metals*, Vol. 8, No. 3, (2018). <https://doi.org/10.3390/met8030188>

Persian Abstract

چکیده

سختی و مقاومت به خوردگی رسوب نیکل (Ni) روی یک بستر را می توان با کنترل دمای الکترولیت در طول رسوب به دست آورد. در این تحقیق، رسوب الکتریکی نیکل در دماهای مختلف الکترولیت ها انجام شد. فیلم های نیکل با استفاده از دوربین دیجیتال نوری، پراش اشعه ایکس (XRD)، میکروسکوپ الکترونی روبشی با طیفسنجی پرتو ایکس پراکنده انرژی (SEM-EDS)، تست ریزسختی و پتانسیواستات مورد بررسی قرار گرفتند. رسوب روشن در ۲۵ درجه سانتیگراد رخ داده است. افزایش دما تا ۴۰ درجه سانتیگراد منجر به تغییر رنگ به نیمه روشن می شود. جایجایی به دمای بالاتر نرخ رسوب، راندمان جریان کاتدی، اندازه دانه و محتوای اکسیژن را افزایش می دهد. بازتاب اشعه ایکس در صفحات (۱۱۱)، (۲۰۰)، و (۲۲۰) به عنوان فاز Ni با ساختار کریستالی مکعبی مرکز صورت (FCC) مطابقت دارد. کاهش اندازه کریستالیت و ریز کرنش برای رسیدن به سختی بالا ارتقا یافته است. افزایش چگالی جریان خوردگی به معنی کاهش مقاومت پلازماسیون است. نمونه در پایین ترین دمای الکترولیت دارای سختی بهتری است و نمونه تشکیل شده در محلول سولفات ۲۵ درجه سانتی گراد سرعت خوردگی کمتری داشت.

AIMS AND SCOPE

The objective of the International Journal of Engineering is to provide a forum for communication of information among the world's scientific and technological community and Iranian scientists and engineers. This journal intends to be of interest and utility to researchers and practitioners in the academic, industrial and governmental sectors. All original research contributions of significant value focused on basics, applications and aspects areas of engineering discipline are welcome.

This journal is published in three quarterly transactions: Transactions A (Basics) deal with the engineering fundamentals, Transactions B (Applications) are concerned with the application of the engineering knowledge in the daily life of the human being and Transactions C (Aspects) - starting from January 2012 - emphasize on the main engineering aspects whose elaboration can yield knowledge and expertise that can equally serve all branches of engineering discipline.

This journal will publish authoritative papers on theoretical and experimental researches and advanced applications embodying the results of extensive field, plant, laboratory or theoretical investigation or new interpretations of existing problems. It may also feature - when appropriate - research notes, technical notes, state-of-the-art survey type papers, short communications, letters to the editor, meeting schedules and conference announcements. The language of publication is English. Each paper should contain an abstract both in English and in Persian. However, for the authors who are not familiar with Persian, the publisher will prepare the latter. The abstracts should not exceed 250 words.

All manuscripts will be peer-reviewed by qualified reviewers. The material should be presented clearly and concisely:

- *Full papers* must be based on completed original works of significant novelty. The papers are not strictly limited in length. However, lengthy contributions may be delayed due to limited space. It is advised to keep papers limited to 7500 words.
- *Research notes* are considered as short items that include theoretical or experimental results of immediate current interest.
- *Technical notes* are also considered as short items of enough technical acceptability with more rapid publication appeal. The length of a research or technical note is recommended not to exceed 2500 words or 4 journal pages (including figures and tables).

Review papers are only considered from highly qualified well-known authors generally assigned by the editorial board or editor in chief. Short communications and letters to the editor should contain a text of about 1000 words and whatever figures and tables that may be required to support the text. They include discussion of full papers and short items and should contribute to the original article by providing confirmation or additional interpretation. Discussion of papers will be referred to author(s) for reply and will concurrently be published with reply of author(s).

INSTRUCTIONS FOR AUTHORS

Submission of a manuscript represents that it has neither been published nor submitted for publication elsewhere and is result of research carried out by author(s). Presentation in a conference and appearance in a symposium proceeding is not considered prior publication.

Authors are required to include a list describing all the symbols and abbreviations in the paper. Use of the international system of measurement units is mandatory.

- On-line submission of manuscripts results in faster publication process and is recommended. Instructions are given in the IJE web sites: www.ije.ir-www.ijeir.info
- Hardcopy submissions must include MS Word and jpg files.
- Manuscripts should be typewritten on one side of A4 paper, double-spaced, with adequate margins.
- References should be numbered in brackets and appear in sequence through the text. List of references should be given at the end of the paper.
- Figure captions are to be indicated under the illustrations. They should sufficiently explain the figures.
- Illustrations should appear in their appropriate places in the text.
- Tables and diagrams should be submitted in a form suitable for reproduction.
- Photographs should be of high quality saved as jpg files.
- Tables, Illustrations, Figures and Diagrams will be normally printed in single column width (8cm). Exceptionally large ones may be printed across two columns (17cm).

PAGE CHARGES AND REPRINTS

The papers are strictly limited in length, maximum 8 journal pages (including figures and tables). For the additional to 8 journal pages, there will be page charges. It is advised to keep papers limited to 3500 words.

Page Charges for Papers More Than 8 Pages (Including Abstract)

For International Author ***	\$55 / per page
For Local Author	100,000 Toman / per page

AUTHOR CHECKLIST

- Author(s), bio-data including affiliation(s) and mail and e-mail addresses).
- Manuscript including abstracts, key words, illustrations, tables, figures with figure captions and list of references.
- MS Word files of the paper.



THOMSON REUTERS

WEB OF SCIENCE



Scopus®



CAS®

A DIVISION OF THE
AMERICAN CHEMICAL SOCIETY



Scientific Indexing Services

Google
Scholar